frontiers | Research Topics

# Functional pavement and advanced material testing technology

**Edited by**
Han-Cheng Dan, Hui Yao, Weina Meng and Kai Liu

**Published in**
Frontiers in Materials

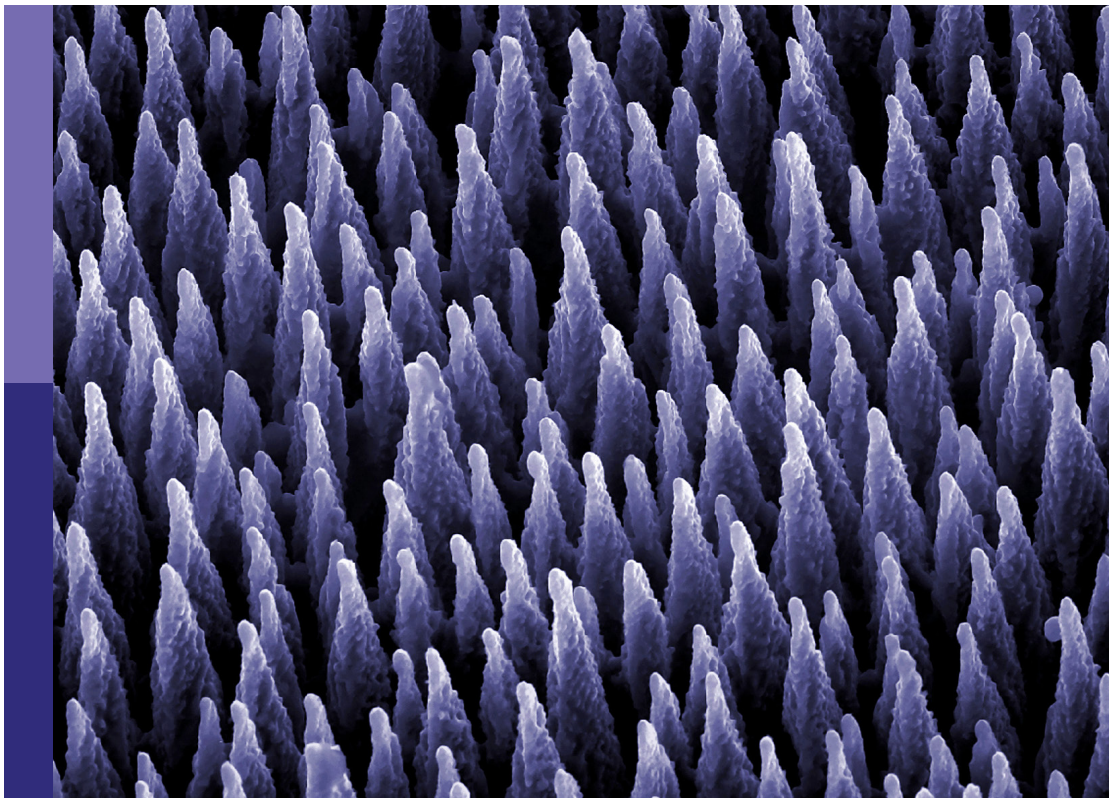

ISSN 1664-8714
ISBN 978-2-83251-392-7
DOI 10.3389/978-2-83251-392-7

## About Frontiers

Frontiers is more than just an open access publisher of scholarly articles: it is a pioneering approach to the world of academia, radically improving the way scholarly research is managed. The grand vision of Frontiers is a world where all people have an equal opportunity to seek, share and generate knowledge. Frontiers provides immediate and permanent online open access to all its publications, but this alone is not enough to realize our grand goals.

## Frontiers journal series

The Frontiers journal series is a multi-tier and interdisciplinary set of open-access, online journals, promising a paradigm shift from the current review, selection and dissemination processes in academic publishing. All Frontiers journals are driven by researchers for researchers; therefore, they constitute a service to the scholarly community. At the same time, the *Frontiers journal series* operates on a revolutionary invention, the tiered publishing system, initially addressing specific communities of scholars, and gradually climbing up to broader public understanding, thus serving the interests of the lay society, too.

## Dedication to quality

Each Frontiers article is a landmark of the highest quality, thanks to genuinely collaborative interactions between authors and review editors, who include some of the world's best academicians. Research must be certified by peers before entering a stream of knowledge that may eventually reach the public - and shape society; therefore, Frontiers only applies the most rigorous and unbiased reviews. Frontiers revolutionizes research publishing by freely delivering the most outstanding research, evaluated with no bias from both the academic and social point of view. By applying the most advanced information technologies, Frontiers is catapulting scholarly publishing into a new generation.

## What are Frontiers Research Topics?

Frontiers Research Topics are very popular trademarks of the *Frontiers journals series*: they are collections of at least ten articles, all centered on a particular subject. With their unique mix of varied contributions from Original Research to Review Articles, Frontiers Research Topics unify the most influential researchers, the latest key findings and historical advances in a hot research area.

Find out more on how to host your own Frontiers Research Topic or contribute to one as an author by contacting the Frontiers editorial office: frontiersin.org/about/contact

# Functional pavement and advanced material testing technology

**Topic editors**

Han-Cheng Dan — Central South University, China
Hui Yao — Beijing University of Technology, China
Weina Meng — Stevens Institute of Technology, United States
Kai Liu — Hefei University of Technology, China

**Citation**

Dan, H.-C., Yao, H., Meng, W., Liu, K., eds. (2023). *Functional pavement and advanced material testing technology*. Lausanne: Frontiers Media SA.
doi: 10.3389/978-2-83251-392-7

# Table of contents

frontiers | Frontiers in Materials

TYPE Editorial
PUBLISHED 09 January 2023
DOI 10.3389/fmats.2022.1117075



OPEN ACCESS

EDITED AND REVIEWED BY
John L. Provis,
The University of Sheffield,
United Kingdom

*CORRESPONDENCE
Hui Yao,
huiyao@mtu.edu

SPECIALTY SECTION
This article was submitted to Structural Materials,
a section of the journal
Frontiers in Materials

RECEIVED 06 December 2022
ACCEPTED 28 December 2022
PUBLISHED 09 January 2023

CITATION
Yao H, Dan H-C, Liu K and Meng W (2023), Editorial: "Functional pavement and advanced material testing technology". *Front. Mater.* 9:1117075.
doi: 10.3389/fmats.2022.1117075



# Editorial: "Functional pavement and advanced material testing technology"

Hui Yao[1]*, Han-Cheng Dan[2], Kai Liu[3] and Weina Meng[4]

[1]Beijing University of Technology, Beijing, China, [2]Central South University, Changsha, China, [3]Hefei University of Technology, Hefei, China, [4]Stevens Institute of Technology, Hoboken, NJ, United States

KEYWORDS

**civil engineering, pavement materials, advanced compaction and sensoring methods, characterization method, numerical simulation**

Editorial on the Research Topic
"Functional pavement and advanced material testing technology"

Pavement quality and its maintenance technologies have been intensively researched recently, as road condition significantly affects daily traveling. However, how to build high-quality pavement or/and when to maintain the pavement is needed remain concerns. Innovative pavement materials and technologies are therefore essential to address the existing engineering challenges.

"Frontiers in Materials" is a high-visibility and well-known international journal, that mainly publishes rigorously peer-reviewed research articles in the field of materials science and engineering. This Research Topic "Functional Pavement and Advanced Material Testing Technology" summarizes the recent or emerging technologies of pavement engineering. The Research Topic covers three sections: "Advanced Materials, Advanced Compaction and Sensoring Methods, and Simulation Models".

(1) Advanced Materials: The carbon black with different contents was used and added to the rapid-hardening cement grouting paste. Different properties were examined with different tests, including fluidity, color difference, spectrum reflectance, thermal conductivity, and flexural and compressive strength. The results show that the fluidity remained high while the conductivity, flexural strength, and compressive strength exhibited reduction compared to the control (Haibin et al.). Recently, a new "gussasphalt" modified binder was developed using styrene-butadiene-styrene, terpene resin, furfural extraction oil, and other related materials with Qingchuan Rock Asphalt (QRA). The key properties of the modified asphalt, such as the rheological properties, microstructure, and thermal stability were studied. The optimum ratio of different components in the modified asphalt was also determined Li et al. The use of Reclaimed Asphalt Pavement (RAP) for pavement maintenance is also fully discussed. The different tests of asphalt mixtures with different proportions of RAP were employed for the performance evaluation, including the dynamic modulus, rutting resistance, dynamic creep, semicircular bending, and freeze-thaw splitting tests. The rejuvenator was identified as effectively enhancing the low-temperature performance and moisture susceptibility of modified asphalt mixtures with RAP. The research results show that the maximum content of RAP can be used up to 50% (Ma et al.). The crumb rubber was added to the asphalt to improve the compatibility between the rubber and asphalt through the dry process with various treatments. Three kinds of treatments (i.e., high-temperature, pre-swelling, and microwave treatments) were adopted

and evaluated with different measurements for the modified asphalt, including the viscosity, rutting resistance, and microstructures. The results show that these treatments all work effectively for the improvement of performance in rubber-modified asphalt (Liang et al.).

(2) Advanced Compaction and Sensoring Methods: The dynamic response of asphalt pavement was investigated under the vibration rolling compaction. The Dynamic Stiffness Method (DSM) with the multidimensional Fourier transform was proposed and used to solve 3D pavement response under compaction. The stiffness matrix and 3D solution were derived and validated. The field test was also conducted and verified through sensors and tests, including the SmartRock sensor, acceleration sensor, temperature sensors, and non-nuclear density meter. The research results show that the thickness and acceleration keep a linear trend during the compaction. The compaction mechanism relates to the modulus and vibration acceleration (Shan et al.). Recently, the graphene platelets and carbon nanotubes (CNTs) with different surface areas were added to the epoxy composites for the investigation of the morphological, electrical, and mechanical properties, and the strain-electrical resistance. From the test results, it is possible that the modified epoxy composite can be treated as a strain sensor for pavement monitoring (Xin et al.). Besides, the toll station and video surveillance data can be integrated together to help with pavement maintenance and management. The traffic or toll station information includes vehicle type, axle load, lane, speed, and temporal information. The Bayesian method was used to train the traffic data and recover data. The research results provide a reference for preventive pavement maintenance (Dan et al.).

(3) Simulation Models: The Discrete Element Method (DME) is a promising simulation method to analyze materials at the microscale. A comprehensive literature review on the application of DEM in asphalt mixtures was elucidated. The development history of DEM was mentioned and the test results were also used to verify the models. Different modeling methods were developed to construct digital samples, such as the methods of user-defined, image-based, and random modeling. The loading model and modeling procedure were discussed and some thoughts and discussions on the development of DEM were also elaborated. The review paper will advance the simulation of pavement materials (Yao et al.). In addition, a workflow with the photogrammetry and Fourier transform method was proposed to accurately express the natural pore morphology of porous rocks, such as acquiring, characterizing, and regenerating pores. The uniaxial compression simulations were carried out to study the influences of porosity and pore morphology on the strength and stiffness of rocks. The simulation results indicate that the porosity shows a first-order control on the mechanical properties of rocks and pore orientation affects the Fourier descriptors D2. The pore morphology influences the rock failure and mechanical properties like the rock strength and Young's modulus (Zhao et al.).

Nine manuscripts were received and considered for possible publication in the Research Topic. All manuscripts were rigorously, fairly, and anonymously reviewed. Both the quality and originality of these papers were thoroughly examined and checked. Finally, nine research articles were accepted and approved for publication.

Our editorial team members thank all reviewers for their professional and dedicated support and help, and also, appreciate all the authors for their efforts and contributions to this Research Topic. In addition, we all are grateful to the editorial and support teams from the Journal of Frontiers in Materials, especially to Prof. John L. Provis, Prof. Antonio Caggiano, Prof. Hugo M. Silva, Prof. Dongshuai Hou, Julius Alesiunas, Petia Apostolova, and Elie Abdel Ahad.

## Author contributions

HY and H-CD drafted the editorial, and KL and WM helped revise the draft.

## Conflict of interest

The authors declare that the research was conducted in the absence of any commercial or financial relationships that could be construed as a potential conflict of interest.

## Publisher's note

frontiers in Materials

ORIGINAL RESEARCH
published: 03 February 2022
doi: 10.3389/fmats.2022.824364

# The Innovative Self-Sensing Strain Sensor for Asphalt Pavement Structure: Substitutability and Synergy Effects of Graphene Platelets With Carbon Nanotubes in Epoxy Composites

*Xue Xin[1], Xuehao Luan[1], Linping Su[1], Chuanyi Ma[2], Ming Liang[1]*, Ximao Ding[3] and Zhanyong Yao[1]**

[1]School of Qilu Transportation, Shandong University, Jinan, China, [2]Shandong HI-SPEED Group, Jinan, China, [3]Shandong HI-SPEED Jiwei Expressway Co., Ltd., Jinan, China

OPEN ACCESS

**Edited by:**
Han-Cheng Dan,
Central South University, China

**Reviewed by:**
Huaping Wang,
Lanzhou University, China
Ping Xiang,
Central South University, China

***Correspondence:**
Ming Liang
ming.liang@sdu.edu.cn
Zhanyong Yao
zhanyong-y@sdu.edu.cn

**Specialty section:**
This article was submitted to Structural Materials, a section of the journal Frontiers in Materials

**Received:** 29 November 2021
**Accepted:** 03 January 2022
**Published:** 03 February 2022

**Citation:**
Xin X, Luan X, Su L, Ma C, Liang M, Ding X and Yao Z (2022) The Innovative Self-Sensing Strain Sensor for Asphalt Pavement Structure: Substitutability and Synergy Effects of Graphene Platelets With Carbon Nanotubes in Epoxy Composites. Front. Mater. 9:824364. doi: 10.3389/fmats.2022.824364

Situ sensors with high accuracy, long durability, and high survival rate are crucial for the health monitoring of asphalt pavement. Due to the harsh environment during the construction period and service life, the monitoring components which can be buried synchronously with the construction period of the road surface become a difficult problem to be solved urgently. The development of functional composites sheds a new insight for pavement strain detection with remarkable self-sensing behavior. In this paper, the substitutability and synergy effect of graphene platelets with carbon nanotubes (CNTs), the effect of CNT types with different specific surface areas in epoxy composites to the morphological, electrical, and mechanical properties, and the strain-electrical resistance response peculiarity of composites were evaluated. The performance of developed composite sensors with epoxy encapsulation was investigated through laboratory experiments. The morphologies showed that CNT-GNP hybrids in composites present a better dispersion state because of the size effect and synergetic effect whereas the pure CNTs are prone to entangle with each other. Composites with CNT(SSA500) display the most amounts of conductive units in same dosage. CNTs and GNP can strengthen the elastic modulus of the epoxy matrix to basically the same as that of asphalt mixture within the range of 1100–1500 MPa. At last, Laboratory experiments have proved the promising prospect for CNTs-GNP/epoxy composites serving as the strain sensor. The developed composites-based strain sensor can provide a new prospect for asphalt pavement monitoring.

**Keywords: self-sensing property, asphalt pavement structure, strain sensor, composites, substitutability and synergy effects**

## INTRODUCTION

With the development of road construction and design, asphalt pavement is supposed to be an intelligent infrastructure with properties of intelligence, automation, and informatization (Ko and Ni, 2005; Abdo, 2014). As the important development direction and basic elements for the intelligent road, the sensing network should be endowed with the abilities of active perception (Soong and Cimellaro, 2009; Ku-Herrera et al., 2016; Sony et al., 2019). It is regarded that keeping the health monitoring abreast with the pavement construction and service period among the whole life cycle are crucial for the design, maintenance management, and assessment. In general, the strain of asphalt pavement structure is much smaller within hundreds or even ten times the micro strain. Therefore, situ sensors with good monitoring accuracy, long durability, and high survival rate are very important for asphalt pavement. In recent years, the optical fibre-based sensors for strain monitoring of asphalt pavement has attracted the attention of many scholars. The transverse and longitudinal directions and distresses, such as cracks, ruts, and settlements can be efficiently measured by distributed optical fibre sensing technology (Xiang and Wang, 2016; Wang et al., 2018; Xiang and Wang, 2018; Wang et al., 2020). However, with the effect of complex construction conditions, such as heavy compaction and high-temperature of asphalt concrete, heavy vehicles, and extreme environments over its life-span, the traditional strain sensors are usually difficult to maintain in the asphalt pavement structure (Hasni et al., 2017; Escalona-Galvis and Venkataraman, 2021). Besides, the poor durability and deformation incompatibility of conventional sensing elements also restrict the development of intelligent monitoring for road engineering. Moreover, the insufficient service period is much less than the designed life of the road, further resulting in high maintenance costs (Cheng and Miyojim, 1998; Dai, 2017; Han et al., 2020).

In recent years, the development of composites sheds new insight on the strain detection of pavement (Li et al., 2004; Gao et al., 2009; Hu et al., 2010; Eswaraiah et al., 2012; Xi and Chung, 2020). With the remarkable self-sensing and special functional ability, composite smart materials are responsive to the effect of deformation, force, or other factors (Xi and Chung, 2020; Yang et al., 2021). Application of self-sensing composites in the field of civil engineering can mainly be divided into two categories based on the matrix materials, one is the common civil engineering materials of cement or asphalt and the other is polymer (Thostenson and Chou, 2006; Wang et al., 2015; Can-Ortiz et al., 2019). Considering the advantages of high reactivity and controllable mechanical properties, epoxy resins are widely used in the composites. Conducting materials in the composites play a vital role for the self-sensing characteristics with the electrical signal sensitivity peculiarity as the deformation of composite materials (Xin et al., 2022). Among the diverse conductive materials, carbon materials such as carbon nanotubes (CNTs), carbon blacks (CB), graphenes (GNPs), and carbon fibers have been the predominant conductive materials due to the good conductivity and mechanical properties (Li et al., 2018; Park et al., 2020). The conductive fillers are dispersed in the polymer matrix and can form a conductive system. The optimizations of conducting systems and accurate evaluation of composites' properties have attracted considerable interest from researchers (Chen et al., 2007; Han et al., 2009; Campo et al., 2015; Bisht et al., 2020; Koo and Tallman, 2020). In our previous studies, the aligned multiwall carbon nanotubes with excellent electrical conductivity were used to prepare the epoxy matrix composites for a novel strain sensor, which can effectively monitor the micro-strain in the field of road engineering (Xin et al., 2020). CNTs exhibit excellent mechanical, electrical, and thermodynamic properties due to the special volume effect, tunneling effect, and size effect, which makes the development and innovation of micro-strain sensor possible (Li et al., 2004; Gao et al., 2009; Chung, 2012). However, it is generally acknowledged that the combination of more than one filler can improve the electrical properties or mechanical properties for the composites because of the synergistic effect (Wei et al., 2010). Some studies investigated the influence of two or three fillers on the mechanical, electrical, or morphological behavior of polymers. Li et al. (Li et al., 2013a) developed the hybrid fillers composed of CNTs grown on GNPs and dispersed them into epoxy matrix. They presented that the embedding of CNT–GNP hybrids into pristine epoxy endows optimum dispersion of CNTs and GNPs as well as better interfacial adhesion between the carbon fillers and matrix, which results in a significant improvement in load transfer effectiveness. I. Kranauskaite et al. (Kranauskaitė et al., 2018) investigated the enhancing electrical conductivity of CNTs/epoxy composites by mixing the GNPs at a fixed content of 0.3 wt%. They found that the mixed particles did not interfere with the percolative behavior of CNTs but can improve the overall electrical performances. Jan Sumfleth et al. (Sumfleth et al., 2011) evaluated the comparison of rheological and electrical percolation phenomena in carbon black and carbon nanotube filled epoxy polymers, which demonstrated that the differences between the rheological and electrical percolation thresholds are dependent on the curing conditions. These interesting works have proved the advantages of hybrids fillers. But few studies have been carried out to introduce the self-sensing properties at such a small micro-strain range as the *in situ* sensor. The substitution effects of GNP with CNTs by the same content have not been investigated in detail. Moreover, most researchers have mainly focused on the properties of composite materials, but have not taken the engineering applications into consideration.

In the present research, the developed strain sensors based on CNT-GNP hybrids/epoxy composites were investigated. The influences of CNTs types with different aspect ratios/specific surface areas (SSA) on the CNT-GNP hybrids/epoxy composites were evaluated simultaneously (Li et al., 2013b; Zakaria et al., 2017). Based on ultrasonic dispersion and micro-nano conducting structure analysis, the dispersion behavior of CNT-GNP hybrids in epoxy resin and its influence to the electrical, mechanical properties, and strain-electrical resistance response peculiarity of composites were respectively analyzed. In addition, with the aims of ultra-high detection accuracy and micro-strain sensitivity for the pavement applications, the self-sensing composite materials were

**TABLE 1 |** Basic information of CNTs with different SSA and laminar GNP.

| | CNT(SSA165) | CNT(SSA500) | CNT(SSA60) | Laminar GNP | |
|---|---|---|---|---|---|
| Purity (wt%) | 95 | >98 | 98 | D50 diameter (um) | 7~10 |
| Out Diameter (nm) | 10–20 | 4~6 | >50 | Stacking density (g/ml) | 0.08~0.13 |
| Length (μm) | 50–100 | 10–20 | <15 | Tablet resistance (mΩ·cm) | 5.6 |
| Special surface area ($m^2$/g) | 165 | ~500 | >60 | Carbon content (wt%) | >98 |
| Electric Conductivity (s/cm) | >100 | >100 | >100 | | |
| ASH (wt%) | <5 | <1.5 | <5 | | |

conducted with encapsulation and formed the studied process. At last, the sensor installed with the specific T-shaped aluminum structure was subjected to the asphalt mixture experiment to simulate the pavement environment and verify the applicability.

# EXPERIMENTAL

## Materials

The polymer matrix used in this study is thermosetting epoxy resin compounded by bisphenol A and epichlorohydrin, which have the advantages of high reactivity and controllable mechanical properties. The epoxy resin and polyamide curing agent were achieved commercially (Xingcheng Co.Ltd., Nantong, China and Xiangshan Company, Beijing, China) and matched in a mass ratio of 100:30. Three types of CNTs with different SSA and the laminar GNP were supplied by JCNANO Technology Company, China. The basic information of the conducting carbon fillers are summarized in **Table 1**.

## Preparation of the Composites

Three types of CNTs with different special surface areas and laminar GNPs of specific mass were grinded and dispersed respectively in the N, N-dimethyl -formamide (DMF) using mechanical agitation with 300 rpm for 10 min and ultrasonic instrument (UH450, Oulior) with 5 s ON and 3 s OFF cycle for 10 min. Then the CNTs suspension and the laminar GNP suspension were blended and sonicated for 20 min. The two steps were performed to obtain the uniform fillers suspensions. Considering the CNTs size of nanoscale and the GNP size of microscale, the dispersion degree of CNT-GNP will directly determine the conductive behavior of the composites, the preparation of suspension is the crucial step. After that, epoxy resin was poured into the blended suspensions along the container wall for minimizing the introduction of bubbles. Then the samples were stirred mechanically for 30 min at 1000 rpm and sonicated for 90 min. What calls for special attention is that the mixture of epoxy resin and suspensions presents high viscosity during sonicating, so stirring was conducted at the same time while sonicating to ensure the effective dispersion of the conductive fillers. Furthermore, the samples were maintained with water cooling so as to prevent a temperature rise in the ultrasonic state, which may lead to the aggregation of conductive fillers. The mixture was then conducted in the vacuum drying oven at 80°C for 60 min to eliminate the DMF solvent completely. After cooling down to room temperature, polyamide curing agent was added into the samples and stirred mechanically for 10 min at 300 rpm. Then the produced composites were poured into the dumbbell-shaped polytetrafluoroethylene mold and the self-developed silicone tube mold. After being cured at room temperature for 24 h and 80°C for 2 h, samples were de-molded and further cured at 120°C for 4 h. The schematic of **Figure 1** shows the preparation process of the epoxy composites. Descriptions of the compositions of samples in naming are listed in **Table 2**. The CNTs were partially substituting by GNP at same dosage.

## Characterizations

### Morphology

The morphologies of CNT(SSA165), CNT(SSA500), CNT(SSA60), and laminar GNP were observed by the scanning electron microscopy (SEM, Hitachi SU8010). Powders of three CNTs with different special surface areas and GNP were treated by oven drying and spray-gold and observed under an accelerating voltage of 10 KV. The SEM for the fractured surfaces of the 12 epoxy composites samples were all conducted, in order to illuminate conductive structure formed by the CNTs and GNP and the interfacial interaction between the epoxy and carbon fillers. Combining with the morphologies, the electrical conductivity, strain-electrical resistance response and toughening mechanism of the epoxy composites can be analyzed and verified deeply.

### Electrical Conductivity and Strain-Electrical Resistance Response

The electrical conductivity of epoxy composites was measured by the digital voltage-current meter of Keithley DAQ 6510 with the maximum resistance range of 100 MΩ using a two-probe method. Wires were embedded into the composites directly by the self-developed silicone tube mold, which will be introduced in detail in *Sensor Encapsulation and Bending Strain Test in Asphalt Concrete Beam Section*. Data of electrical resistance R can be acquired directly from the instrument and the electrical conductivity $\rho$ can be calculated by the formula of $\rho = \frac{RS}{L}$, where S and L are the cross sectional area and length of composites sample, respectively. In the present study, the samples were prepared with 4 mm in diameter and 100 mm in length. All the electrical conductivity data are the average of three measurements.

Strain-electrical resistance response was measured using a self-developed test system, see **Figure 2**. Differing from other research, the test system was specially designed for obtaining

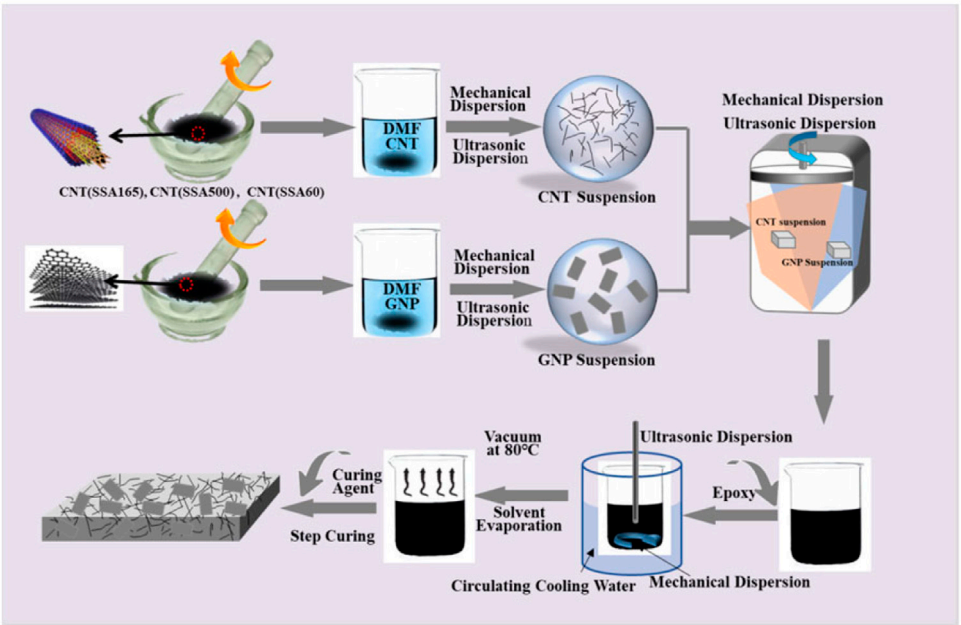


**FIGURE 1 |** Preparation process schematic of the composites for asphalt pavement strain monitoring.

**TABLE 2 |** Descriptions of the compositions samples in naming.

| Epoxy composites | Descriptions |
|---|---|
| $CNT(SSA165)_{0.8}$/EP | Epoxy filled with 0.8 wt% CNT(SSA165) |
| $CNT(SSA165)_{0.7}GNP_{0.1}$/EP | Epoxy filled with 0.7 wt% CNT(SSA165) and 0.1 wt% GNP |
| $CNT(SSA165)_{0.6}GNP_{0.2}$/EP | Epoxy filled with 0.6 wt% CNT(SSA165) and 0.2 wt% GNP |
| $CNT(SSA165)_{0.5}GNP_{0.3}$/EP | Epoxy filled with 0.5 wt% CNT(SSA165) and 0.3 wt% GNP |
| $CNT(SSA500)_{0.8}$/EP | Epoxy filled with 0.8 wt% CNT(SSA500) |
| $CNT(SSA500)_{0.7}GNP_{0.1}$/EP | Epoxy filled with 0.7 wt% CNT(SSA500) and 0.1 wt% GNP |
| $CNT(SSA500)_{0.6}GNP_{0.2}$/EP | Epoxy filled with 0.6 wt% CNT(SSA500) and 0.2 wt% GNP |
| $CNT(SSA500)_{0.5}GNP_{0.3}$/EP | Epoxy filled with 0.5 wt% CNT(SSA500) and 0.3 wt% GNP |
| $CNT(SSA60)_{0.8}$/EP | Epoxy filled with 0.8 wt% CNT(SSA60) |
| $CNT(SSA60)_{0.7}GNP_{0.1}$/EP | Epoxy filled with 0.7 wt% CNT(SSA60) and 0.1 wt% GNP |
| $CNT(SSA60)_{0.6}GNP_{0.2}$/EP | Epoxy filled with 0.6 wt% CNT(SSA60) and 0.2 wt% GNP |
| $CNT(SSA60)_{0.5}GNP_{0.3}$/EP | Epoxy filled with 0.5 wt% CNT(SSA60) and 0.3 wt% GNP |

the accurate micro-strain with the scale less than 100 με, which is the general strain range in asphalt pavement. With the samples clamping fixed on the strain control device (see **Figure 2A**), the variation of strain will be measured by the strain extensometer and displayed in the PC interface when rotating the hand wheel. At the same time, the electrical resistance R is automatically recorded by Keithley DAQ 6510 and illustrated in another PC interface. The parameter of resistance variation rate can be calculated by $\triangle R/R_0 = (R-R_0)/R_0*100\%$.

### Mechanical Property

Dumbbell-shaped epoxy composites samples were prepared with the PVDF molds. The quasi-static tensile tests were conducted in the universal testing machine of SANS at room temperature. Direct tensile test loaded with a constant displacement rate of 0.2 mm/min until the samples were broken. The strain-stress curves, mechanical property parameters of tensile elastic modulus, elongation at break, and breaking strength can be obtained from the direct tensile test. Three replicates for one sample were measured to obtain the average value of mechanical property parameters.

## RESULTS AND DISCUSSION

### SEM Morphology of Carbon Fillers and Composites

SEM images of the three types of CNTs with different special surface areas (SSA) of CNT (SSA165), CNT (SSA500), CNT (SSA60), and GNP are shown in **Figure 3**. SSA are defined as the total area (S) of the CNTs per unit mass (m), i.e., SSA = S/m or can be calculated by the formula of SSA = S/V, in which S means

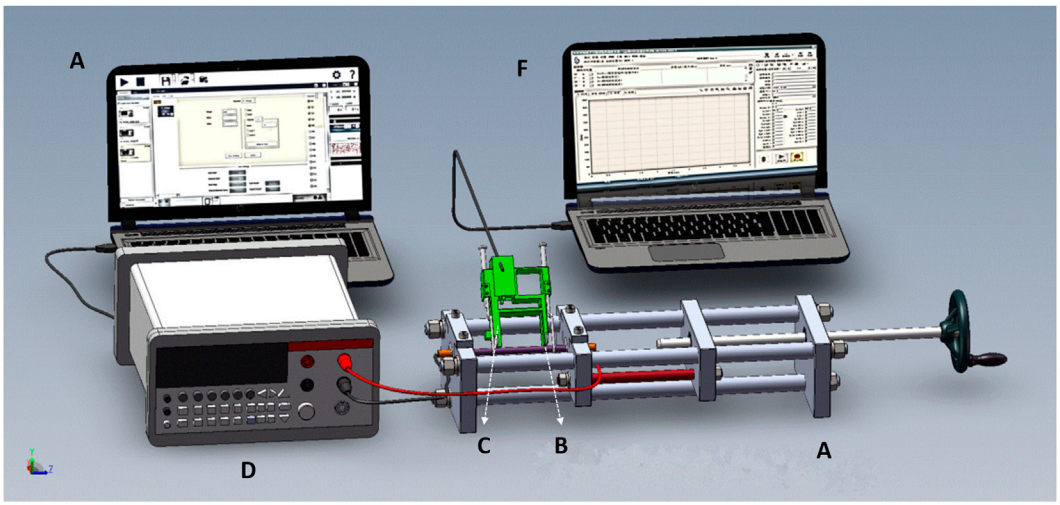


**FIGURE 2 |** Self-developed test system for strain-electrical resistance response, **(A)** Strain control device, **(B)** Specimen, **(C)** Extensometer, **(D)** Digital multimeter, **(E, F)** data record computer.

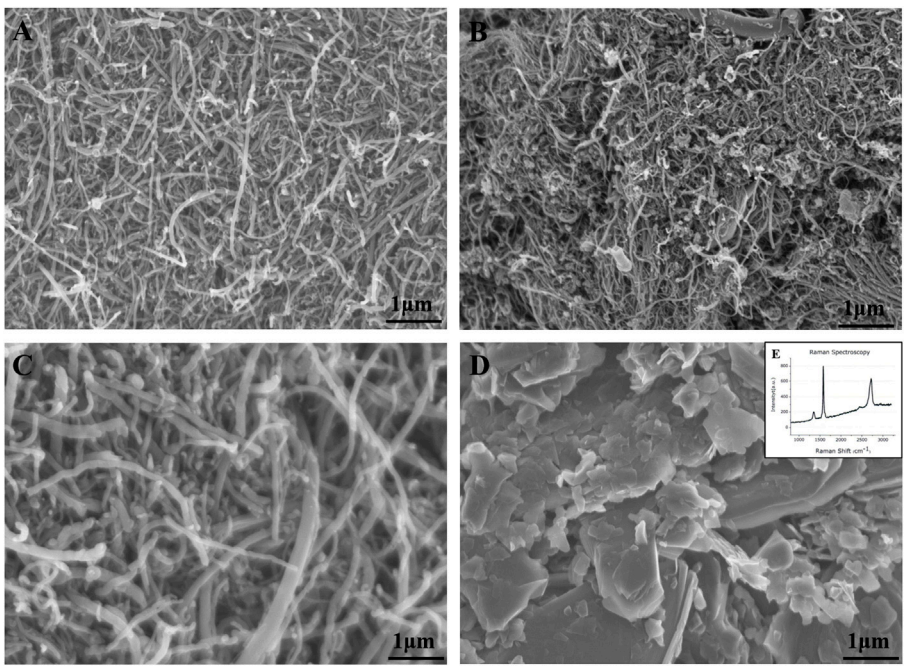


**FIGURE 3 |** SEM images of **(A)** CNT (SSA165), **(B)** CNT (SSA500), **(C)** CNT (SSA60), **(D)** GNP.

the total area, V means the volume of CNTs. It can be seen that the tortuous and sinuate CNTs entangled with each other because of the elongated tubular structure and strong Van der Waals forces. Furthermore, the entanglement degree appears much more tightly with the higher SSA, seen in **Figure 2B**. However, the larger the value of SSA, the more carbon nanotubes per unit volume. Thus, the total interface area with the epoxy resin matrix will decline sharply in the composites. On the other hand, the surface of the CNTs is hydrophobic and CNTs tend to aggregate into bundles in solution. Based on this, it is crucial to disperse CNTs in the epoxy resin matrix effectively and uniformly, in order to optimize the mechanical and electrical

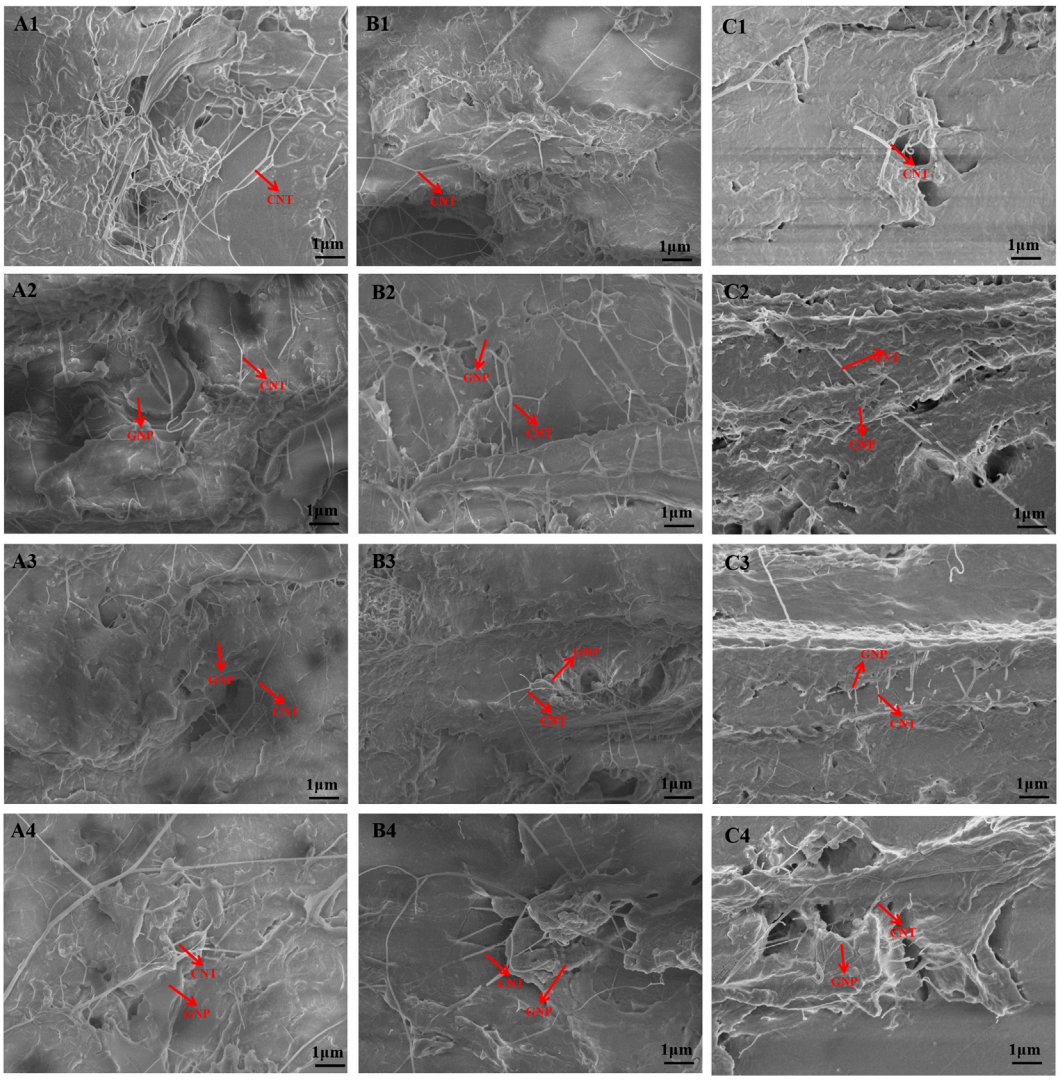


**FIGURE 4 |** SEM of the fracture surfaces for epoxy composites with different fillers, **(A1)** CNT(SSA165)0.8/EP, **(A2)** CNT(SSA165)$_{0.7}$GNP$_{0.1}$/EP, **(A3)** CNT(SSA165)$_{0.6}$GNP$_{0.2}$/EP, **(A4)** CNT(SSA165)0.5GNP0.3/EP, **(B1)** CNT(SSA500)0.8/EP, **(B2)** CNT(SSA500)0.7GNP0.1/EP, **(B3)** CNT(SSA500)0.6GNP0.2/EP, **(B4)** CNT(SSA500)0.5GNP0.3/EP, **(C1)** CNT(SSA60)0.8/EP, **(C2)** CNT(SSA60)0.7GNP0.1/EP, **(C3)** CNT(SSA60)0.6GNP0.2/EP, **(C4)** CNT(SSA60)0.5GNP0.3/EP.

performance and prevent the stress concentration areas. Similar viewpoints were also reported in previous studies (Liu et al., 2017; Liu and An, 2018; Han et al., 2019). Considerable interests have been put forward by modifying the CNTs structure or introducing other fillers to promote the dispersion and directional arrangement. **Figure 3D** demonstrates the SEM image of the GNP. The GNP displays laminar and plate-like structure and the size of sheet varies. The sheet of GNP shows a coarse surface, so it is expected to be beneficial in connecting with the CNTs.

SEM morphologies of the fracture surfaces of CNT/GNP/EP composites were investigated to measure the dispersion of CNTs-GNP fillers (displayed in **Figure 4**). It can be seen that a CNT-GNP hybrid (see **Figures 4A2–C4**) shows a better dispersion state (Li et al., 2013b; Xi and Chung, 2020). Unlike the pure CNTs which are entangled with each other, most of the CNTs are well dispersed in the composites in the presence of GNP and ultrasonication. The previous tortuous CNTs are separated individually and formed directional alignment in the composites. In the case of a CNT-GNP hybrid conductive structure, CNTs are arranged among the adjacently laminar GNP and the original configuration of pure CNTs or GNP are disrupted and rearranged. In most instances, the CNTs or GNP tend to aggregate because of the high Van der Waals forces (Thostenson and Chou, 2006). However, when the GNP was introduced into the composites, CNTs in nano scale are easily prone to be dispersed homogenously and filled among GNP with micro dimensions. Thus, GNP absorbs the molecules of CNTs

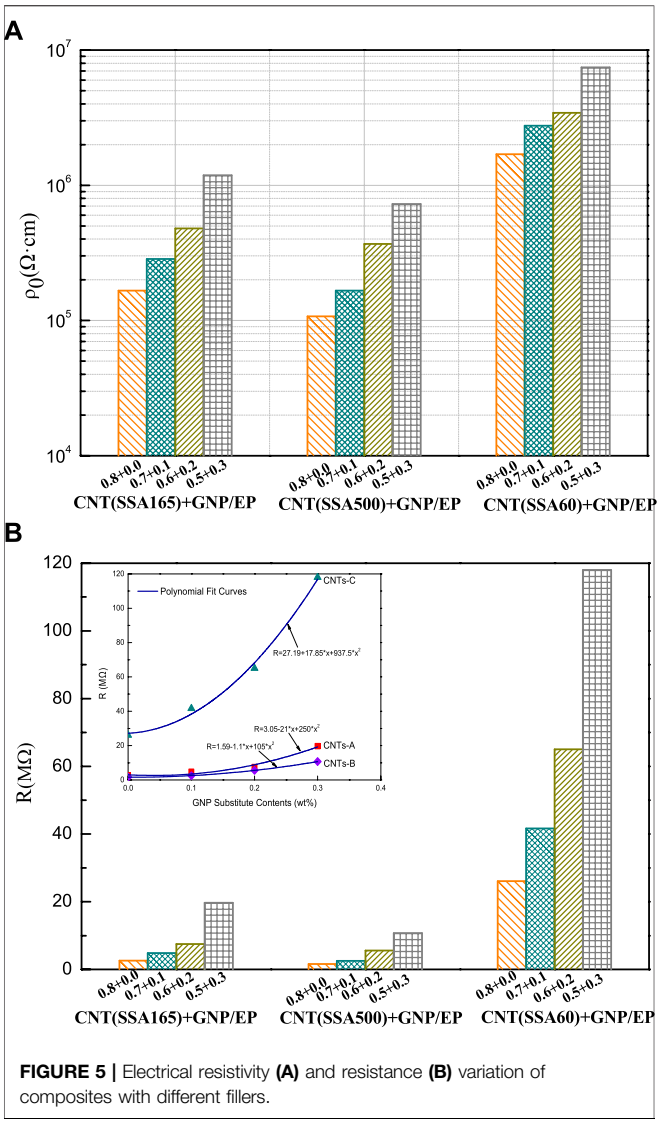


**FIGURE 5 |** Electrical resistivity **(A)** and resistance **(B)** variation of composites with different fillers.

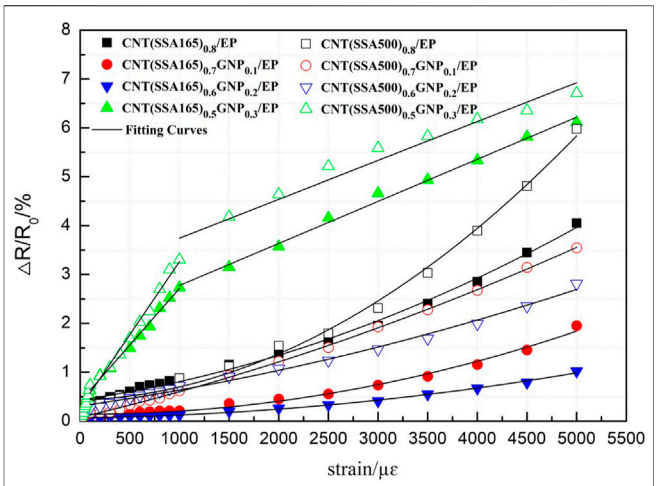


**FIGURE 6 |** Strain-electrical resistance response peculiarity.

and prevents their aggregations. Moreover, the sandwiched CNTs among the GNP plates bridge the separated plates of GNP from nano scale to micro dimensions, which are expected to further improve the electrical conductivity and sensing sensitivity of the composite. In addition, the approximately oriented conductive network and well dispersed CNTs and GNP fillers in the composites will promote the interaction efficiency and enhance more contact area among carbon fillers and epoxy matrix, which is further expected to lead to better electrical properties, strain-electrical resistance response, and mechanical properties of the composites (Abot et al., 2010; Sengupta et al., 2011; Yang et al., 2020).

By comparing **Figures 4A–C**, it can be found that the SSA of CNTs plays an important role in the dispersion state of CNT-GNP. Composites with CNTs (SSA500) display the most amounts of CNTs and contact points within the same field of vision at the same dosage, seen in **Figures 4B1–B4**. Moreover, the high aspect ratio further resulted in the well-established 3D conductive network. So it is reasonable to conclude that composites with CNT(SSA500) will show the best electrical properties and strain-electrical resistance response peculiarity. On the contrary, composites with CNT(SSA60) appear to have the least CNT conjunction points between the laminar GNP together with the shortest tubular structure. This will lead to the poor electricity conduction, in other words, a much higher dosage of CNT (SSA60) should be required if we want to achieve the same conductivity with other kinds of CNTs.

## Electrical and Self-Sensing Peculiarity of the Composites

The electrical resistivity and resistance variation of composites with the SSA change of CNTs and fraction between CNTs and GNP (total filler loading is 0.8 wt%) are displayed in **Figure 5**. The *in situ* electrical resistivity of composites, $\rho_0$ can be calculated by the formula of $\rho_0 = \frac{R_0 S}{L}$, in which R, S, and L respectively represent the resistance, cross sectional area, and length of the composites specimen. It is clearly seen that composites with CNT(SSA500) display least $\rho_0$ and $R_0$ when at the same fraction between CNTs and GNP, which means the optimal electrical conductivity because of the highest SSA and most conductive paths. It is generally believed that the conductivity of CNTs largely depends on the tube diameter and the helix angle of the tube wall (Han et al., 2019). Researchers (Tian et al., 2019) found that CNTs can be regarded as one-dimensional quantum wires with good conductivity when the tube diameter is less than 6 nm, nevertheless, the conductivity of CNTs will decrease when the diameter is larger than 6 nm. On the other hand, $\rho_0$ and $R_0$ show a trend of gradual increase with the introduction of GNP when the SSA of CNTs is constant. Furthermore, the growth trend is various for different CNTs, see the small diagram in **Figure 5B**. The increasing data shows exponential growth by fitting, for CNTs-B, $R = 1.59–1.1*x+105x^2$, for CNTs-C, $R = 27.19 + 17.85*x+937.5\ x^2$.

This is related to the lower electrical conductivity of GNP comparing to CNTs. It is worth noting that composites with

**TABLE 3 |** The fitting parameters of three stages for composites with $CNT(SSA165)_{0.5}GNP_{0.3}$ and $CNT(SSA500)_{0.5}GNP_{0.3}$.

| | $CNT(SSA165)_{0.5}GNP_{0.3}$/EP | $CNT(SSA500)_{0.5}GNP_{0.3}$/EP |
|---|---|---|
| Stage 1($0 < x < 200$ με) | $\triangle R/R_0$ = -0.005 + 6.04E-3×strain | $\triangle R/R_0$ = -0.034 + 7.23E-3×strain |
| Stage 2($200 < x < 1000$ με) | $\triangle R/R_0$ = 0.401 + 2.31E-3×strain | $\triangle R/R_0$ = 0.275 + 2.99E-3×strain |
| Stage 3($1000 < x < 5000$με) | $\triangle R/R_0$ = 1.913 + 8.61E-4×strain | $\triangle R/R_0$ = 2.947 + 7.96E-4×strain |

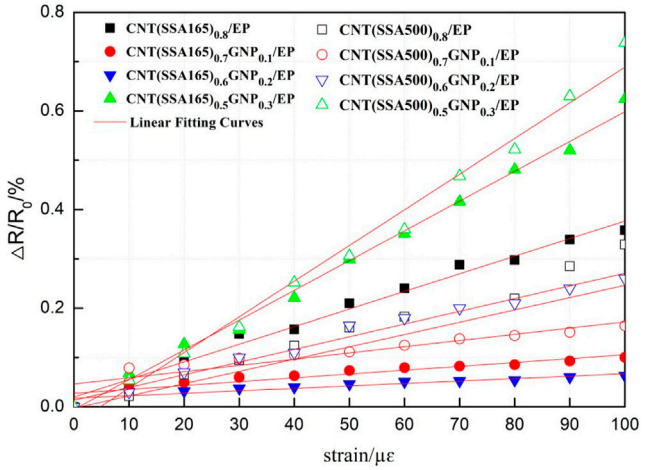


**FIGURE 7 |** Strain-electrical resistance response peculiarity at strain range of 0-100 με

CNT(SSA60) are shown to be much higher and more unstable $R_0$ than composites with CNT(SSA165) and CNT(SSA500), so the composites with CNT (SSA60) will not be considered in the following discussions of strain-electrical resistance response peculiarity.

The electrical resistance variation of composites with different CNTs and GNP as the quasi-static tensile loading were recorded in real-time by the self-developed test system. The *in situ* electrical resistance response peculiarity as a function of strain is depicted in **Figure 6**, in which the solid dot represents composites with CNT(SSA165) and the hollow dot represents composites with CNT(SSA500). It is clearly seen that the resistance change rate $\triangle R/R_0$ of all the epoxy composites shows an increasing trend as the increment of tensile within the tested strain range, indicating good self-sensing property. The increase patterns of $\triangle R/R_0$ as strain were remarkably different. For pure CNTs and GNT substituting CNTs by 0.1 wt% and 0.2 wt%, the resistance change rate $\triangle R/R_0$ of epoxy composites displays a trend of linear growth at small strain (less than 1000 με) followed by exponential growth at high elongation strain. Nevertheless, when the substitution of CNT by GNP reaches up to 0.3 wt %, $\triangle R/R_0$ of epoxy composites shows three linear stages with various growth slopes. The slope was highest within the initial strain range (less than 100 με), implying the most sensitivity of strain sensing and ideal monitoring accuracy for asphalt pavement. As the strain increases, the value of the slope drops in the second and third stages. To depict these variations quantitatively, the curves were fitted by piecewise function. The fitting results of the three stages are presented in **Table 3**.

Considering the small structure deformation in asphalt pavement, more emphasis is put on the strain-electrical resistance response peculiarity of the developed composites at micro strain range of 0-100 με. The variations of $\triangle R/R_0$ with strain are presented in **Figure 7**. Apparently, the $\triangle R/R_0$ has a linear relationship with the applied strain. These linear relationships between $\triangle R/R_0$ and strain provide the core foundation for our research and development of sensors. Furthermore, the absolute value of slope increases with the increase of GNP substitution dosage. In this case, the internal structure of conductive domains consisting of CNTs and GNP are difficult to deform at such a small micro strain in the effect of intense connection with the epoxy matrix and codependence between the CNTs and GNP (Spitalsky et al., 2010; Chung, 2019). Deformation is transmitted to the conductive structure through the matrix material when the external force is applied to the composites, which results in less contact among conductive domains and thus the significant increment of resistance. Once the deformation occurs, the conductive domains will separate and have less contact with each other. The corresponding results are the evident increase of resistance. The changes of resistance become more obvious with the increase of GNP, since more GNP in conductive domains will lead to the more diminished contact under tensile. That is why sensing sensitivity improves as the substituting GNP increases.

Besides the synergy effect of CNTs and GNP, the substitutability effect of GNP with CNTs in epoxy composites for asphalt pavement strain monitoring is also focused on for consideration in this study, which can be further explained by the schematic diagram of conducting network structure, see **Figure 8**. To overcome the drawback of the aggregation tendency of CNTs and GNP, the combined advantage is made full use of to further improve the electricity conduction capacity of composites. However, whether there is a better critical substitution between the two carbon fillers is a significant issue. In order to gain an insight into the general tendency of electrical and mechanical properties to change with dosage variation between the two fillers, increasing GNP contents and correspondingly reducing the same CNTs contents are designed with the total filler content which remains fixed. Combining with the comparation of the longitudinal SEM images, it can be observed that the GNP proportion in the total conductive system is increasing from the top to the bottom (see **Figure 4**), corresponding to the decreasing CNTs proportion. However, even though the amounts of CNTs between the adjacent GNP reduce distinctly, the conductivity of CNTs-GNP/epoxy composites will not be lead to a sharp decline

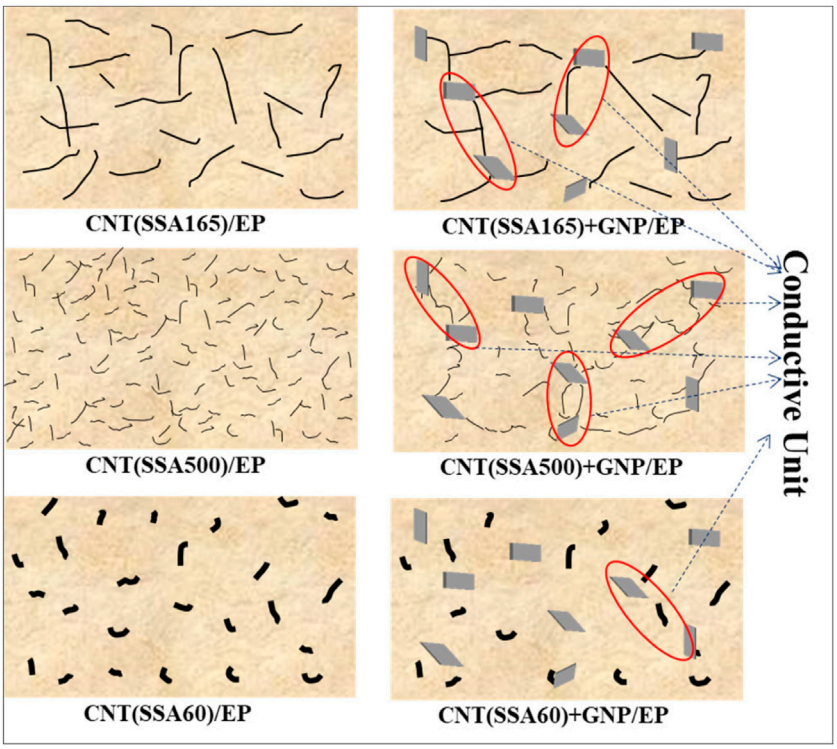


**FIGURE 8 |** Schematic diagram of conducting network structure.

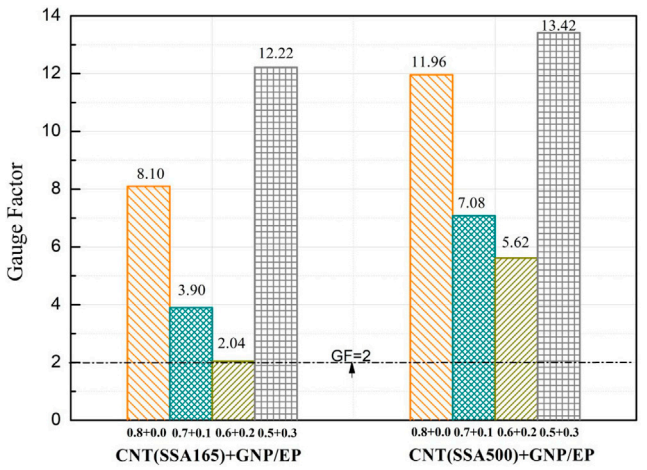


**FIGURE 9 |** The self-sensing gauge factor of composites under 5000 με.

under the influence of increasing GNP. In the conductive system constituted of GNP and CNTs, the two carbon fillers can prevent aggregation with each other (Ghaleb et al., 2014; Dos Reis et al., 2018; Fang et al., 2020). CNTs dispersed among the GNP and formed conductive units. These conductive units contact with each other and finally construct a three-dimensional conductive network structure. When GNP equivalently replaces the CNT, the amounts of conductive units will increase and the CNTs in each conductive unit will reduce correspondingly. Under the combined influence of the two aspects, the change rate of resistance increases when the external stretch is applied although the conductance decreases slightly.

Furthermore, the $\triangle R/R_0$ of composites with CNT(SSA500) is shown to be obviously higher than that of composites with CNT(SSA165) in the case of composites with CNT(SSA165) and CNT(SSA500) at same filler proportion, which indicates better self-sensing behavior. Comparing to the CNT(SSA165), CNT(SSA500) with smaller out diameter and shorter length presents more numbers of carbon tubes at the same mass fraction. This indicates that more conductive paths will be established in the composites.

In order to gain an insight into the influence of SSA on the sensing sensitivity coefficient, the gauge factor (GF), i.e. sensitivity coefficient, was defined as the following equation, $GF = \frac{\Delta R/R_0}{\varepsilon}$. The calculated GF values are shown in **Figure 9**. It is found that the GF is affected by both CNTs' SSA and GNP substitution dosage. Composites with higher GNP substitution dosage present, first, decreasing and then increasing GF, which is beneficial to the development of self-sensing sensors. Considerable interests have been aroused to explore the potential mechanism for the phenomenon (Bisht et al., 2020). As indicated previously, the strain-electrical resistance response peculiarity of the composites strongly depends on the formed conductive structure and networks. With the increase of GNP substitution dosage, the contents and volume fraction of CNTs reduce correspondingly. The amounts of conductive domains constructed with GNP and CNTs increase in the composites,

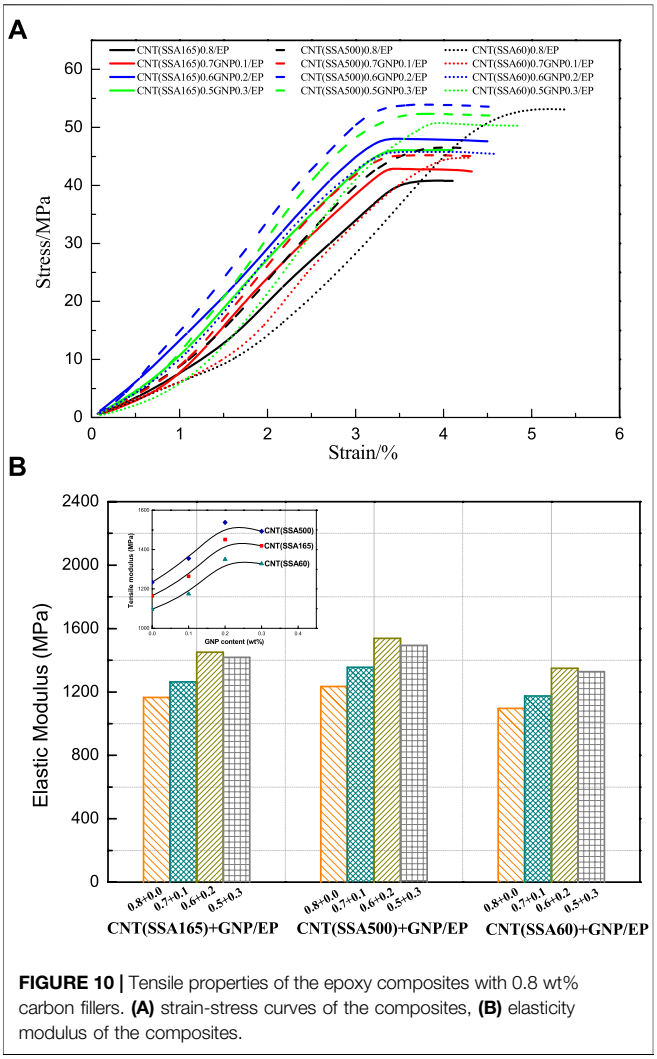


**FIGURE 10 |** Tensile properties of the epoxy composites with 0.8 wt% carbon fillers. **(A)** strain-stress curves of the composites, **(B)** elasticity modulus of the composites.

despite the quantity of CNTs in each conductive domain dropping off. Just like the conductance of a single copper wire is almost the same as that of unwound multistrand copper wire, the CNTs between the adjacent GNP existing in the form of an independent and dispersed state will present approximate resistance values. However, parts of CNTs among the GNP exist in the interlocking state, which will give rise to the increasing resistance with the combined action of higher GNP substitution dosage. With the gradually increasing applied strain, the deformation transferred to the conductive network structure through the epoxy matrix will be greater due to the micron scale effect of GNP. That is why the higher the GNP substitution dosage, the more obvious the resistance change rate at the same applied strain.

## Tensile Properties of the Epoxy Composites

The mechanical properties of the epoxy composites with total 0.8 wt% carbon fillers composed of CNTs and GNP were investigated under quasi-static tensile properties to verify the suitability of the composite modulus for asphalt mixture. **Figure 10** displays the stress-strain curves and the calculated elasticity modulus of all the composites. With the increasing applied stress, all of the composites present approximately linear growth tendency with strain. When the strain reaches a certain value, the stress will remain nearly constant until the breakage of composites, in which the constant stress represents the ultimate tensile strength and the breakup strain represents the maximum tensile strain. The introduced GNP partial substitution of CNTs has brought about a noticeable change to the composites' mechanical behavior. The ultimate tensile strength of the CNTs-GNP reinforced composites is much higher than that of CNTs reinforced composites. This was due to the enhancement of the interface adhesion between CNTs and epoxy matrix after the addition of GNP (Yang et al., 2020). The addition of multilayer GNP promotes the dispersion of CNTs in the epoxy matrix, and the bonding between CNTs and GNP can further inhibit the aggregation and entanglement of CNTs. On the other hand, the CNTs can also restrain the build-up of GNP to avoid re-aggregation with each other. Under the above-mentioned mechanism, CNTs and GNP reinforce the epoxy matrix by the means of the formed three-dimensional network in the matrix. However, composites with GNP substitution dosage of 0.3 wt% are lower than that of 0.2 wt%, which is because of the density difference between CNTs and GNP. The GNP substitution dosage shows the highest value in modulus as the GNP increases.

**Figure 10B** displays the elastic modulus of composites with different carbon fillers. It is well known that the higher the degree of the load transfer between the monitoring sensor and the detected materials, the monitoring accuracy will be better. So the elastic modulus of the self-sensing composites should be equivalent to that of the asphalt mixture. As shown in **Figure 10B**, although the elastic modulus varies with the different carbon filler, it generally falls within the range of 1100 MPa to 1500 MPa (modulus range of asphalt mixture). The elastic modulus of composites basically overlaps with that of the asphalt mixture, which keeps the same deformation between composites sensor and asphalt mixtures. The collaborative deformation among sensor and asphalt pavement structure ensure the accuracy of the monitoring results.

## Sensor Encapsulation and Bending Strain Test in Asphalt Concrete Beam

The most common forming methods of conductive composites include surface conductive film formation method, conductive filler dispersion and cladding method, conductive material lamination method, etc. However, when these methods are used for conducting property tests after the samples are prepared, the conductive glue such as silver adhesive electrode, aluminum foil adhesive electrode, or tin welding method, is generally used to connect wires. Some disadvantages are inescapable, such as the decreased smoothness of the specimen's surface, the long curing time of conductive adhesive, the insufficient bonding effect of conductive adhesive and the unstable contact electrical signal. In order to solve the above problems, we developed the new manufacturing method and the integrated forming mould of composites material with embedded conductive electrode, seen as **Figure 11A**. In the manufacturing device, the conductive wires will be pre-embedded in the mould through the cap plugs at both

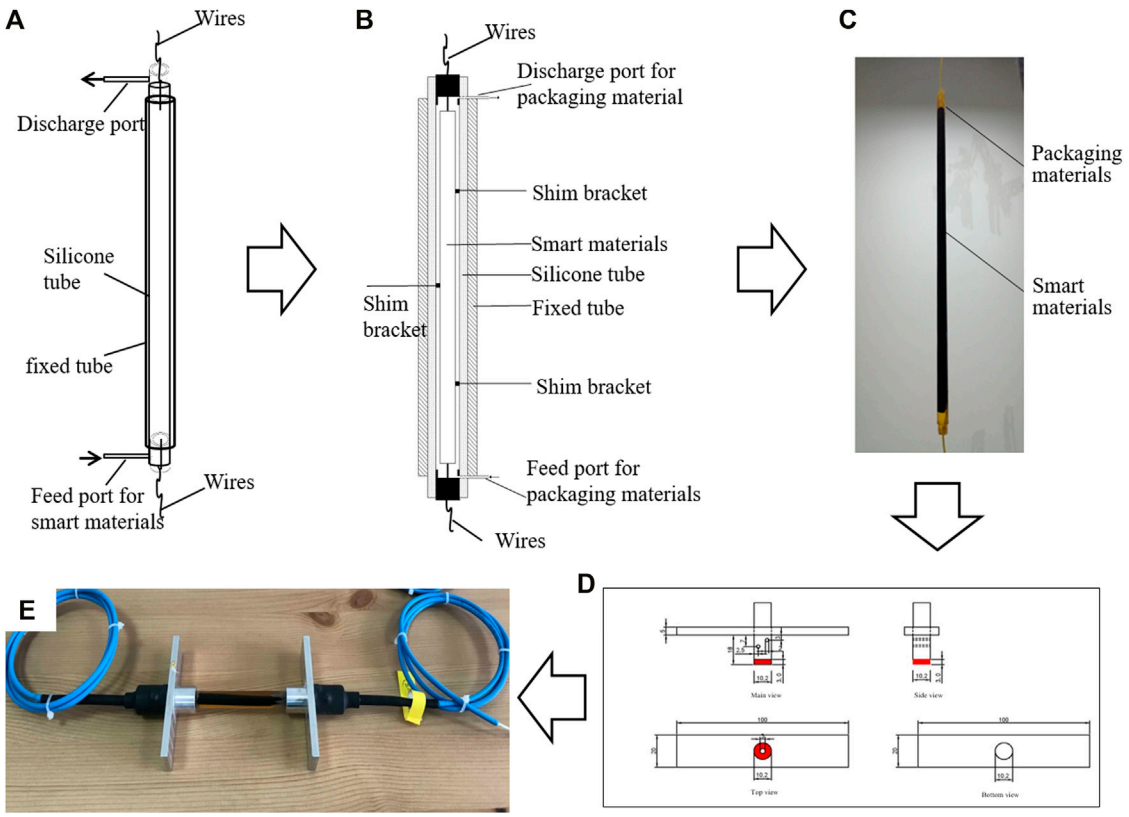


**FIGURE 11 |** The encapsulation and installation of sensor. **(A)**. Integrated forming mould of composites material with conductive electrode, **(B)**. Encapsulation mould of the sensor, **(C)**. The encapsulated sensor, **(D)**. Schematic diagram of I-beam design, **(E)**. schematic of the installed sensor.

ends of the silicone tube. A feed port and a discharge port are arranged on both sides of the cap plug for the inflow and outflow of composite materials. The fixed acrylic tube with the inner diameter close to the external diameter of the silicone tube is tailored to keep the cured composites vertical. After preparation of the self-sensing composites, the encapsulation mould of the sensor is carried out for the protection of composites, seen as **Figure 11B**. Three semi-circular shaped shim brackets with the inner diameter the same as the self-sensing composites and same thickness as the encapsulated layer are pasted on the composites specimen to ensure composites strip in the center. After the mold is assembled, epoxy resin will be injected as the encapsulated material and the encapsulated sensor is displayed as **Figure 11C**. With the advantage of convenient and easy production and high production efficiency, the developed methods for the sensor's moulding and encapsulation can bring considerable benefits as compared to traditional methods. Afterwards, the aluminum I-beam is designed and installed for the sensors, in order to embed in the asphalt concrete.

To assess the monitoring effectiveness and applicability of the self-sensing composites sensor, the bending strain test was further conducted on the asphalt mixture beam embedded with a developed sensor. The self-sensing composites sensor based of $CNT(SSA500)_{0.5}GNP_{0.3}$/EP was embedded in the bottom of the double-layer plate rutting specimen with the size of 300 mm × 300 mm×100 mm and then AC13 asphalt mixture was compacted in the rutting mould according to the experimental specification (Ministry of Transport, 2011). After 24 h of curing, the rutting specimens were cut into beam with the size of 300 × 100 × 100 mm. The beam with self-sensing composites sensor embedded at the bottom (see **Figure 12B**) was conducted with the three point bending load test (see **Figure 12A**). The three point bending load test was controlled under the program displacement control mode of 0.1 mm/min (see **Figure 12C**). At the same time, three parallel strain gauges with the same length as the self-sensing composites sensor were pasted at the bottom of the beam in order to compare and verify the strain values. During the three point bending load test, the electrical resistance was collected and recorded synchronously (see **Figure 12D** and **Figure 12E**). According to the results of the three-point bending test, the resistance change rate $\triangle R/R_0$ of self-sensing composites sensor also shows the similar increase trend as calibrated by the self-developed test system, except that the increase slope decreased slightly. Through the embedment test in the laboratory, the developed polymer composite sensor displays quite good survival rate under the high temperature and high pressure compacting condition of asphalt mixture. Most importantly, the developed sensor shows high accuracy in strain monitoring for asphalt mixture, even though the asphalt beam underwent very small deformation. The $\triangle R/R_0$ of the self-sensing composite sensor based off $CNT(SSA500)_{0.5}GNP_{0.3}$/EP

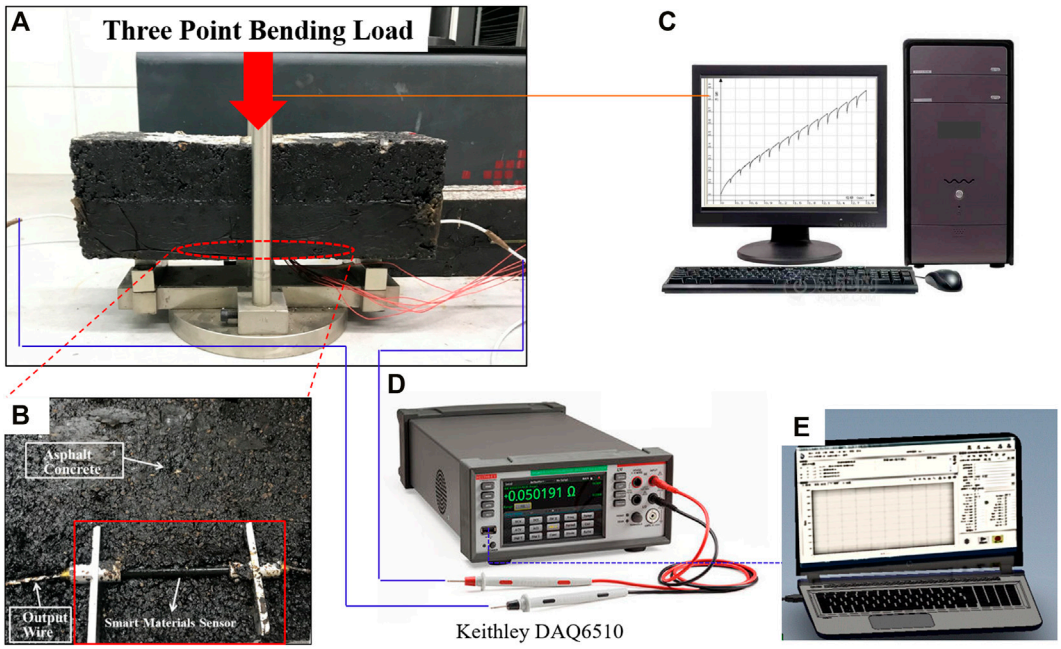


**FIGURE 12 |** Bending strain test of the self-sensing composites sensor in asphalt concrete beam.

also shows a linear growth trend within 200 με, but the growth slope is 80% of that measured by the laboratory calibration table experiment.

## CONCLUSION

The self-sensing strain sensors for asphalt pavement were developed novelly based on the composites with CNT and GNP. The effect of CNTs with different SSA on the CNT-GNP hybrids/epoxy composites were investigated simultaneously. The results showed that CNTs-GNP hybrid in composites presented better dispersion state because of the size effect and synergetic effect comparing to the pure CNTs which were entangled with each other. In the case of CNTs-GNP hybrid conductive structure, CNTs are distributed among the adjacent laminar GNP and the original configuration of pure CNTs or GNP are disrupted and rearranged. Composites with CNT (SSA500) display most amounts of conductive domains within the uniform scale field of vision at same dosage. Moreover, the higher aspect ratio will result in the well-established 3D conductive network. $\triangle R/R_0$ of all the epoxy composites shows an increasing trend as the increment of external tensile in the experimental range, which indicates good self-sensing property. The $\triangle R/R_0$ of composites with CNT (SSA500) is shown to be obviously higher than that of composites with CNT (SSA165), indicating better self-sensing behaviors. CNTs and GNP reinforced the epoxy matrix by forming a three-dimensional network in the matrix. The modulus of composite sensors is in accordance with that of asphalt mixture, which ensures the collaborative deformation among sensor and asphalt pavement structure, and thus the accuracy of monitoring results. Laboratory experiments, by means of a three-point bending test for an asphalt mixture beam-embedded developed polymer composite sensor, verified the durability of the sensor and its high accuracy in strain monitoring for asphalt pavement.

## DATA AVAILABILITY STATEMENT

The original contributions presented in the study are included in the article/Supplementary material, further inquiries can be directed to the corresponding authors.

## AUTHOR CONTRIBUTIONS

XX: Data curation, Writing - original draft, Writing—review and editing. XL: Methodology. LS: Investigation. ML: Writing–original draft, Writing—review and editing, Funding acquisition. ZY: Project administration, Supervision. CM and XD: Investigation. All authors have read and agreed to the published version of the manuscript. We confirm that the order of authors listed in the manuscript has been approved by all named authors.

## FUNDING

The authors acknowledge the financial support of the National Natural Science Foundation of China (No. 51908330), the Qilu Young Scholars Program of Shandong University (No. 202099000060), Natural Science Foundation of Shandong Province (CN) (No. ZR2020ME244) and the Fundamental Research Funds of Shandong University (No. 2020GN059).

## REFERENCES


Abdo, M. (2014). *Structural Health Monitoring, History, Applications and Future, A Review Book*. San Francisco: Open Science.

Abot, J. L., Song, Y., Vatsavaya, M. S., Medikonda, S., Kier, Z., Jayasinghe, C., et al. (2010). Delamination Detection with Carbon Nanotube Thread in Self-Sensing Composite Materials. *Composites Sci. Tech.* 70 (7), 1113–1119. doi:10.1016/j.compscitech.2010.02.022

Bisht, A., Dasgupta, K., and Lahiri, D. (2020). Evaluating the Effect of Addition of Nanodiamond on the Synergistic Effect of Graphene-Carbon Nanotube Hybrid on the Mechanical Properties of Epoxy Based Composites. *Polym. Test.* 81, 106274. doi:10.1016/j.polymertesting.2019.106274

Campo, M., Jiménez-Suárez, A., and Ureña, A. (2015). Effect of Type, Percentage and Dispersion Method of Multi-Walled Carbon Nanotubes on Tribological Properties of Epoxy Composites. *Wear* 324-325, 100–108. doi:10.1016/j.wear.2014.12.013

Can-Ortiz, A., Abot, J. L., and Avilés, F. (2019). Electrical Characterization of Carbon-Based Fibers and Their Application for Sensing Relaxation-Induced Piezoresistivity in Polymer Composites. *Carbon* 145, 119–130. doi:10.1016/j.carbon.2018.12.108

Chen, H., Jacobs, O., Wu, W., Rüdiger, G., and Schädel, B. (2007). Effect of Dispersion Method on Tribological Properties of Carbon Nanotube Reinforced Epoxy Resin Composites. *Polym. Test.* 26 (3), 351–360. doi:10.1016/j.polymertesting.2006.11.004

Cheng, H. D., and Miyojim, M. (1998). Novel System for Automatic Pavement Distress Detection. *J. Comput. Civil Eng.* 12 (3), 145–152. doi:10.1061/(asce)0887-3801(1998)12:3(145)

Chung, D. D. L. (2019). A Review of Multifunctional Polymer-Matrix Structural Composites. *Composites B: Eng.* 160, 644–660. doi:10.1016/j.compositesb.2018.12.117

Chung, D. D. L. (2012). Carbon Materials for Structural Self-Sensing, Electromagnetic Shielding and thermal Interfacing. *Carbon* 50 (9), 3342–3353. doi:10.1016/j.carbon.2012.01.031

Dai, H. (2017). An Innovative Sensing Approach Using Carbon Nanotube-Based Somposites for Structural Health Monitoring of concrete Structures. Doctoral Dissertation. Newark, DE(USA): University of Delaware Library.

Dos Reis, J., Oliveira Costa, C., and Sá da Costa, J. (2018). Strain Gauges Debonding Fault Detection for Structural Health Monitoring. *Struct. Control Health Monit.* 25 (12), e2264. doi:10.1002/stc.2264

Escalona-Galvis, L. W., and Venkataraman, S. (2021). Optimum Reduction of Sensing Electrodes for Delamination Identification with Electrical Resistance Tomography. *Struct. Control Health Monit.* 28 (6), e2726. doi:10.1002/stc.2726

Eswaraiah, V., Balasubramaniam, K., and Ramaprabhu, S. (2012). One-pot Synthesis of Conducting Graphene-Polymer Composites and Their Strain Sensing Application. *Nanoscale* 4 (4), 1258–1262. doi:10.1039/c2nr11555g

Fang, Y., Li, L.-Y., and Jang, S.-H. (2020). Calculation of Electrical Conductivity of Self-Sensing Carbon Nanotube Composites. *Composites Part B: Eng.* 199, 108314. doi:10.1016/j.compositesb.2020.108314

Gao, L., Thostenson, E. T., Zhang, Z., and Chou, T.-W. (2009). Coupled Carbon Nanotube Network and Acoustic Emission Monitoring for Sensing of Damage Development in Composites. *Carbon* 47, 1381e1388. doi:10.1016/j.carbon.2009.01.030

Ghaleb, Z. A., Mariatti, M., and Ariff, Z. M. (2014). Properties of Graphene Nanopowder and Multi-Walled Carbon Nanotube-Filled Epoxy Thin-Film Nanocomposites for Electronic Applications: The Effect of Sonication Time and Filler Loading. *Composites A: Appl. Sci. Manufacturing* 58, 77–83. doi:10.1016/j.compositesa.2013.12.002

Han, B., Yu, X., and Kwon, E. (2009). A Self-Sensing Carbon Nanotube/cement Composite for Traffic Monitoring. *Nanotechnology* 20 (44), 445501. doi:10.1088/0957-4484/20/44/445501

Han, S., Meng, Q., Araby, S., Liu, T., and Demiral, M. (2019). Mechanical and Electrical Properties of Graphene and Carbon Nanotube Reinforced Epoxy Adhesives: Experimental and Numerical Analysis. *Composites Part A: Appl. Sci. Manufacturing* 120, 116–126. doi:10.1016/j.compositesa.2019.02.027

Han, S., Meng, Q., Xing, K., Araby, S., Yu, Y., Mouritz, A., et al. (2020). Epoxy/graphene Film for Lifecycle Self-Sensing and Multifunctional Applications. *Composites Sci. Tech.* 198, 108312. doi:10.1016/j.compscitech.2020.108312

Hasni, H., Alavi, A. H., Chatti, K., Lajnef, N., and Lajnef, C. N. (2017). A Self-Powered Surface Sensing Approach for Detection of Bottom-Up Cracking in Asphalt concrete Pavements: Theoretical/numerical Modeling. *Construction Building Mater.* 144, 728–746. doi:10.1016/j.conbuildmat.2017.03.197

Hu, N., Karube, Y., Arai, M., Watanabe, T., Yan, C., Li, Y., et al. (2010). Investigation on Sensitivity of a Polymer/carbon Nanotube Composite Strain Sensor. *Carbon* 48 (3), 680–687. doi:10.1016/j.carbon.2009.10.012

Ko, J. M., and Ni, Y. Q. (2005). Technology Developments in Structural Health Monitoring of Large-Scale Bridges. *Eng. Struct.* 27 (12), 1715e1725. doi:10.1016/j.engstruct.2005.02.021

Koo, G. M., and Tallman, T. N. (2020). Higher-order Resistivity-Strain Relations for Self-Sensing Nanocomposites Subject to General Deformations. *Composites Part B: Eng.* 190, 107907. doi:10.1016/j.compositesb.2020.107907

Kranauskaitė, I., Macutkevič, J., Borisova, A., Martone, A., and Banys, J. (2018). Enhancing Electrical Conductivity of Multiwalled Carbon Nanotube/epoxy Composites by Graphene Nanoplatelets. *Lith. J. Phys.* 57 (4), 232–242. doi:10.3952/physics.v57i4.3602

Ku-Herrera, J. J., Pacheco-Salazar, O. F., Rios-Soberanis, C. R., Dominguez-Rodriguez, G., and Aviles, F. (2016). Self-sensing of Damage Progression in Unidirectional Multiscale Hierarchical Composites Subjected to Cyclic Tensile Loading. *Sensors* 16, 400e412. doi:10.3390/s16030400

Li, W., Dichiara, A., and Bai, J. (2013). Carbon Nanotube-Graphene Nanoplatelet Hybrids as High-Performance Multifunctional Reinforcements in Epoxy Composites. *Composites Sci. Tech.* 74, 221–227. doi:10.1016/j.compscitech.2012.11.015

Li, W., He, D., and Bai, J. (2013). The Influence of Nano/micro Hybrid Structure on the Mechanical and Self-Sensing Properties of Carbon Nanotube-Microparticle Reinforced Epoxy Matrix Composite. *Composites Part A: Appl. Sci. Manufacturing* 54, 28–36. doi:10.1016/j.compositesa.2013.07.002

Li, Y., Liao, Y., and Su, Z. (2018). Graphene-functionalized Polymer Composites for Self-Sensing of Ultrasonic Waves: An Initiative towards "Sensor-free" Structural Health Monitoring. *Composites Sci. Tech.* 168, 203–213. doi:10.1016/j.compscitech.2018.09.021

Li, Z., Dharap, P., Nagarajaiah, S., Barrera, E. V., and Kim, J. D. (2004). Carbon Nanotube Film Sensors. *Adv. Mater.* 16 (7), 640–643. doi:10.1002/adma.200306310

Liu, F., Hu, N., Ning, H., Atobe, S., Yan, C., Liu, Y., et al. (2017). Investigation on the Interfacial Mechanical Properties of Hybrid Graphene-Carbon Nanotube/polymer Nanocomposites. *Carbon* 115, 694–700. doi:10.1016/j.carbon.2017.01.039

Liu, J. K., and An, L. (2018). An, Synthesis and Properties of Graphene/carbon Nanotube/epoxy Resin Composites. *Chem. Eng. Trans. (CET Journal)* 71, 949–954. doi:10.3303/CET1871159

Ministry of Transport (2011). *JTG E20-2011, Standard Test Methods of Bitumen and Bituminous Mixtures for Highway Engineering*.

Park, K., Scaccabarozzi, D., Sbarufatti, C., Jimenez-Suarez, A., Ureña, A., Ryu, S., et al. (2020). Coupled Health Monitoring System for CNT-Doped Self-Sensing Composites. *Carbon* 166, 193–204. doi:10.1016/j.carbon.2020.04.060

Sengupta, R., Bhattacharya, M., Bandyopadhyay, S., Bhowmick, A. K., and Bhowmick, A. K. (2011). A Review on the Mechanical and Electrical Properties of Graphite and Modified Graphite Reinforced Polymer Composites. *Prog. Polym. Sci.* 36 (5), 638–670. doi:10.1016/j.progpolymsci.2010.11.003

Sony, S., Laventure, S., and Sadhu, A. (2019). A Literature Review of Next-Generation Smart Sensing Technology in Structural Health Monitoring. *Struct. Control Health Monit.* 26 (3), e2321. doi:10.1002/stc.2321

Soong, T. T., and Cimellaro, G. P. (2009). Future Directions in Structural Control. *Struct. Control. Health Monit.* 16 (1), 7–16. doi:10.1002/stc.291

Spitalsky, Z., Tasis, D., Papagelis, K., and Galiotis, C. (2010). Carbon Nanotube-Polymer Composites: Chemistry, Processing, Mechanical and Electrical Properties. *Prog. Polym. Sci.* 35, 357–401. doi:10.1016/j.progpolymsci.2009.09.003

Sumfleth, J., Buschhorn, S. T., and Schulte, K. (2011). Comparison of Rheological and Electrical Percolation Phenomena in Carbon Black and Carbon Nanotube Filled Epoxy Polymers. *J. Mater. Sci.* 46 (3), 659–669. doi:10.1007/s10853-010-4788-6

Thostenson, E. T., and Chou, T.-W. (2006). Carbon Nanotube Networks: Sensing of Distributed Strain and Damage for Life Prediction and Self Healing. *Adv. Mater.* 18 (21), 2837–2841. doi:10.1002/adma.200600977

Tian, Z., Li, Y., Zheng, J., and Wang, S. (2019). A State-Of-The-Art on Self-Sensing concrete: Materials, Fabrication and Properties. *Composites Part B: Eng.* 177, 107437. doi:10.1016/j.compositesb.2019.107437

Wang, H.-P., Xiang, P., and Jiang, L.-Z. (2020). Optical Fiber Sensing Technology for Full-Scale Condition Monitoring of Pavement Layers. *Road Mater. Pavement Des.* 21 (5), 1258–1273. doi:10.1080/14680629.2018.1547656

Wang, H., Xiang, P., and Jiang, L. (2018). Optical Fiber Sensor Based In-Field Structural Performance Monitoring of Multilayered Asphalt Pavement. *J. Lightwave Technol.* 36 (17), 3624–3632. doi:10.1109/jlt.2018.2838122

Wang, P.-N., Hsieh, T.-H., Chiang, C.-L., and Shen, M.-Y. (2015). Synergetic Effects of Mechanical Properties on Graphene Nanoplatelet and Multiwalled Carbon Nanotube Hybrids Reinforced Epoxy/carbon Fiber Composites. *J. Nanomater.* 2015, 1–9. doi:10.1155/2015/838032

Wei, T., Song, L., Zheng, C., Wang, K., Yan, J., Shao, B., et al. (2010). The Synergy of a Three Filler Combination in the Conductivity of Epoxy Composites. *Mater. Lett.* 64 (21), 2376–2379. doi:10.1016/j.matlet.2010.07.061

Xi, X., and Chung, D. D. L. (2020). Electret Behavior of Carbon Fiber Structural Composites with Carbon and Polymer Matrices, and its Application in Self-Sensing and Self-Powering. *Carbon* 160, 361–389. doi:10.1016/j.carbon.2020.01.035

Xiang, P., and Wang, H. P. (2016). Strain Transfer Analysis of Optical Fiber Based Sensors Embedded in an Asphalt Pavement Structure. *Meas. Sci. Technol.* 27 (7), 075106. doi:10.1088/0957-0233/27/7/075106

Xiang, P., and Wang, H. (2018). Optical Fibre-Based Sensors for Distributed Strain Monitoring of Asphalt Pavements. *Int. J. Pavement Eng.* 19 (9), 842–850. doi:10.1080/10298436.2016.1211872

Xin, X., Liang, M., Yao, Z., Su, L., Zhang, J., Li, P., et al. (2020). Self-sensing Behavior and Mechanical Properties of Carbon Nanotubes/epoxy Resin Composite for Asphalt Pavement Strain Monitoring. *Construction Building Mater.* 257, 119404. doi:10.1016/j.conbuildmat.2020.119404

Xin, X., Rong, Y., Su, L., Qiu, Z., Yang, C., Liang, M., et al. (2022). Dynamic Mechanical and Chemorheology Analysis for the Blended Epoxy System with Polyurethane Modified Resin. *J. Renew. Mater.* 10 (4), 1081–1095. doi:10.32604/jrm.2022.018021

Yang, H., Yuan, L., Yao, X., Zheng, Z., and Fang, D. (2020). Monotonic Strain Sensing Behavior of Self-Assembled Carbon Nanotubes/graphene Silicone Rubber Composites under Cyclic Loading. *Composites Sci. Tech.* 200, 108474. doi:10.1016/j.compscitech.2020.108474

Yang, Q. L., Qian, Y., Fan, Z., Lin, J., Wang, D., Zhong, J., et al. (2021). Exploiting the Synergetic Effects of Graphene and Carbon Nanotubes on the Mechanical Properties of Bitumen Composites. *Carbon* 172 (2021), 402–413. doi:10.1016/j.carbon.2020.10.020

Zakaria, M. R., Abdul Kudus, M. H., Md. Akil, H., and Mohd Thirmizir, M. Z. (2017). Comparative Study of Graphene Nanoparticle and Multiwall Carbon Nanotube Filled Epoxy Nanocomposites Based on Mechanical, thermal and Dielectric Properties. *Composites Part B: Eng.* 119, 57–66. doi:10.1016/j.compositesb.2017.03.023

**Conflicts of Interest:** Author CM was employed by Shandong HI-SPEED Group. Author XD was employed by Shandong HI-SPEED Jiwei Expressway Co. LTD.

The remaining authors declare that the research was conducted in the absence of any commercial or financial relationships that could be construed as a potential conflict of interest.

**Publisher's Note:** All claims expressed in this article are solely those of the authors and do not necessarily represent those of their affiliated organizations, or those of the publisher, the editors and the reviewers. Any product that may be evaluated in this article, or claim that may be made by its manufacturer, is not guaranteed or endorsed by the publisher.

frontiers in Materials

ORIGINAL RESEARCH
published: 08 February 2022
doi: 10.3389/fmats.2021.842809

# Investigation on the Effects of RAP Proportions on the Pavement Performance of Recycled Asphalt Mixtures

*Xiang Ma*, Jiaqing Wang and Yinyin Xu*

*College of Civil Engineering, Nanjing Forestry University, Nanjing, China*

In-plant hot mix recycling technology has been widely used in maintenance and reconstruction due to its good recycling performance. However, the utilization rate of recycled asphalt pavement (RAP) is still only 10–25%, resulting in excessive accumulation and landfilling of RAP materials, which fails to promote the sustainable value of RAP in recycling. Therefore, this paper comprehensively explores the pavement performance of AC-20 ordinary asphalt recycled mixture and AC-13 modified asphalt recycled mixture with different proportions of RAP. The pavement performance test includes the dynamic modulus, rutting, dynamic creep, semicircular bending, and freeze-thaw splitting tests. The results show that, with the increase of RAP content, the mechanical properties and high-temperature properties of the two types of recycled asphalt mixtures are improved, the low temperature properties and moisture susceptibility properties are enhanced first and then weakened, and the best performance is reached when RAP content is 20 and 40%, respectively. According to the entire pavement performance test results, the influence of RAP content on AC-13 recycled modified asphalt mixtures is relatively smaller than that of AC-20 normal recycled asphalt mixtures. The addition of rejuvenator can improve the low-temperature performance and moisture susceptibility of recycled asphalt mixtures to a certain extent, especially for AC-20 ordinary recycled asphalt mixture. Consequently, it is suggested to use AC-13 recycled modified asphalt mixture in the upper layer of road; the RAP content can reach 20%, and rejuvenator can be used to improve its moisture susceptibility and low-temperature performance. AC-20 ordinary recycled asphalt mixture can be used in the middle surface layer, and the RAP content can reach 40%, or using AC-13 recycled modified asphalt mixture, the RAP content can reach 50%.

**Keywords: hot in-plant reclaimed, RAP proportions, pavement performance, high-temp stability, low-temp cracking resistance, moisture susceptibility performance**

OPEN ACCESS

***Edited by:***
*Han-Cheng Dan,*
*Central South University, China*

***Reviewed by:***
*Jizhe Zhang,*
*Shandong University, China*
*Qiao Dong,*
*Southeast University, China*

****Correspondence:***
*Xiang Ma*
*max@njfu.edu.cn*

***Specialty section:***
*This article was submitted to Structural Materials, a section of the journal Frontiers in Materials*

***Received:*** *24 December 2021*
***Accepted:*** *27 December 2021*
***Published:*** *08 February 2022*

***Citation:***
*Ma X, Wang J and Xu Y (2022) Investigation on the Effects of RAP Proportions on the Pavement Performance of Recycled Asphalt Mixtures. Front. Mater. 8:842809. doi: 10.3389/fmats.2021.842809*

## 1 INTRODUCTION

In the United States in 1975, the recycling of asphalt pavement reached 50,000 tons; in 1978, it reached more than 5 million tons, and through the end of the 1980s, the use of recycled asphalt mixes in the United States occupied 50% of the national production of asphalt mixes and furthered related research, such as the development of regenerative agents and the mechanism of asphalt aging.

Although the requirements of the major U.S. states (Thakur, 2010) on the proportion of old material blending are different, the blending rate is roughly 10–50%, and the survey found that most of the asphalt pavement maintained by plant mix hot regeneration technology has a better road performance to meet the requirements of use. In the United States, the plant mix hot regeneration maintenance and repair technology is mainly used in road and airport runway paving (Kandhal et al., 1995). Germany, Finland, and other European countries in the mid-1970s also began to carry out research and exploration of asphalt pavement regeneration technology; the first country to apply asphalt recycled mixture in pavement maintenance and repair was Germany, and the effect is remarkable. In 1978, the recycling rate of old pavement materials reached 100%. In Finland, the government called on all towns to actively carry out the recycling of pavement waste materials, and now the application of recycled materials has gradually expanded from low-to high-grade highway pavement. The most representative is the research report of NCHRP (Kandhal and Foo, 1997) (NCHRP Report452), which suggests that RAP not only plays the role of "black stone," but also the old asphalt coating on the surface still plays the role of bonding. Gaitan et al. (2013) studied the use of RAP in cold and hot recycled asphalt mixtures and analyzed the asphalt mastic in cold and hot recycled asphalt mixes, and the test results showed that the old material cold recycled was more active than hot recycled, and the degree of integration of new and old asphalt in hot recycled asphalt mixes was only 50–70%, whereas cold recycled material was 20% higher, so a more in-depth study on the degree of integration of new and old asphalt in hot recycling is needed. Navaro et al. (2012) conducted a stratified extraction of asphalt in recycled asphalt mixes and used a combination of ultraviolet and infrared spectroscopy to determine the proportion of old and new asphalt in the mix. Experimental studies showed that the test process, temperature, and mixing time were the main factors affecting the mass fraction of old and new asphalt. Shane (Gundla and Underwood, 2017) mixed new and old asphalt and new and old aggregates in different proportions, and Arshad (Hussain and Yanjun, 2013) extracted and recovered the old asphalt from the RAP material and mixed it with different proportions of old and new asphalt and evaluated its performance. Luis (Loria et al., 2011) conducted a study on the road performance of hot mix asphalt pavements with up to 50% RAP in a region of Canada, and the results showed that the water damage resistance and low temperature crack resistance of high-RAP recycled materials could meet the requirements.

Since 2000, the aging phenomenon of asphalt pavement binders has been studied in depth in China, and its regeneration mechanism has also been systematically investigated. Jin et al. (2001) studied the changes in the composition and properties of road asphalt by using the thin film thermal aging method, and the test results showed that the aromatic fraction and gum content of the mixture decreased after aging, whereas the asphaltene content increased, and also, this change was in accordance with the macroscopic kinetic law. Chen and Chen (2008) found that the reactive groups in the internal molecules of asphalt react with oxygen in the air to form polar molecules, and oxygen and sulfur atoms are mostly present in asphalt molecules as carbonyl groups, sulfoxide functional groups, thioethers, and thiols, which he considered as the main cause of asphalt aging. The chemical composition and physical properties of asphalt are analyzed from two perspectives; in the chemical composition of asphalt after aging, the gum content is decreasing, asphalt content is increasing, and the physical indicators of the asphalt softening point has increased. Viscosity is also becoming larger, and needle penetration and ductility have decreased to a certain extent. Most domestic regeneration methods are based on the addition of light oil regenerants, but this regeneration method generally suffers from a lack of aging resistance (Ding, 2013). Domestic microscopic studies on asphalt are still mainly focused on the analysis of asphalt functional group changes using infrared spectroscopy and other means, and the research on microscopic analysis using atomic force microscopy is still relatively limited. Yang et al. (2015) and others studied the effect of three factors on the microstructure of asphalt by AFM, namely, the type of asphalt, short-term aging, and cooling rate during sample preparation, and found that the bee-type structures of different asphalts were very different, the quantities were somewhat different, and the sensitivity to short-term aging was also different. Zhao (Fan, 2016) used carbonyl and sulfoxide coefficients as the microscopic evaluation index of asphalt aging, which correlated well with the macroscopic mechanical index and could reasonably explain and evaluate the difference in performance of asphalt before and after aging.

Yang and Ma (2011) studied the effective regeneration rate of aging asphalt hot regeneration through experiments and found that there is a close relationship between the regeneration rate and aging asphalt preheating temperature, regenerant diffusion ability, and regenerated asphalt mixture mixing and time. Chen Yunqing (Chen, 2015) found that the moisture content of RAP material increased after aging, whereas the asphalt content decreased and the gradation occurred significantly refined. Meanwhile, the abrasion value and angularity of coarse aggregates in RAP material decreased to some extent, and the decline of limestone was small compared with basalt, but its wear resistance was obviously inferior to basalt. Shen (Shen and Wang, 2015) concluded that the RAP fineness modulus is the main factor affecting the volume parameters of asphalt recycled mixes, and the larger the RAP fineness modulus, the worse the high-temperature stability of the recycled material, whereas the degree of aging of asphalt has a small effect on the volume parameters of recycled mixes, but the effect on the mechanical properties of recycled material is greater, and the higher the degree of aging of asphalt in RAP material can improve the high-temperature stability of recycled material. The high temperature stability of the recycled material can be improved with higher aging of RAP material, but it is not good for moisture susceptibility. Zhao (2014) used the rutting test and Hamburg rutting test to evaluate and analyze the high-temperature performance of the recycled asphalt mixture, and it was found that the greater the amount of old material blended, the better the high temperature stability of the asphalt mixture. The moisture

**TABLE 1 |** Results of recovered AC-20 common asphalt mix components.

| Grouping | Passing percentage of each sieve size (mm) (%) | | | | | | | | | | | Asphalt content (%) |
|---|---|---|---|---|---|---|---|---|---|---|---|---|
| | 19.0 | 16.0 | 13.2 | 9.5 | 4.75 | 2.36 | 1.18 | 0.6 | 0.3 | 0.15 | 0.075 | |
| RAP | 97.3 | 86.3 | 73.4 | 60.7 | 42.6 | 23.7 | 16.3 | 11.7 | 6.9 | 5.1 | 3.9 | 3.8 |
| Coarse RAP | 97.9 | 85.2 | 72.5 | 60.3 | 39.7 | 24.6 | 15.8 | 10.8 | 5.8 | 4.9 | 3.7 | 3.6 |
| Fine RAP | 100 | 100 | 100 | 100 | 100 | 49.8 | 33.9 | 25.6 | 14.1 | 10.7 | 7.5 | 4.1 |

susceptibility was evaluated by using the water immersion Marshall test and freeze-thaw splitting test, and when the old material admixture ratio was lower than 50, there was little difference in moisture susceptibility performance compared with that of the brand new asphalt mixture. Yan and Xiao (2016) found through their study that increasing the RAP admixture can improve the high-temperature stability and water damage resistance of recycled asphalt mixes but has a negative impact on its low-temperature performance. Therefore, whereas increasing the proportion of RAP ensures its road performance meets the actual use requirements, the appropriate amount of regenerant can be introduced to improve the recycled asphalt mixture. At this stage, for a large amount of RAP material, recycled asphalt concrete and the synergistic mechanism between the regenerant is still to be clarified and the combination of different RAP and regenerant on the comprehensive road performance of recycled asphalt mixture research to be carried out.

The effect of the variation of RAP content on the road performance of different types of recycled asphalt mixes is considered for two different types of recycled asphalt mixes with high RAP content. The mechanical properties, high-temperature properties, low-temperature crack resistance, and moisture susceptibility are comprehensively studied by the variation of RAP admixture. The effect of the introduction of the regenerant on the road performance at higher RAP content (40%) was also considered. The results show that the RAP content ratio can be appropriately increased in AC-13 modified recycled asphalt mix and AC-20 normal recycled asphalt mix to meet the requirements of the road, and the targeted addition of recyclers further improves its low-temperature performance and moisture susceptibility properties. The research results can provide an effective scientific basis and theoretical foundation for the efficient resource utilization of RAP admixture in practical projects.

# 2 RAP COMPONENT ANALYSIS AND MIX RATIO DESIGN

## 2.1 RAP Component Analysis

In this test, a milling speed of 15 m/min was used to recycle the used materials. The old materials recovered in this study were AC-20 common asphalt mixture and AC-13 modified asphalt mixture, and the extraction test was carried out using a fully automatic asphalt extraction instrument. At the same time, considering the large variability of the gradation of the old material, the uniformity of the mix design could not be guaranteed, so the old material was also divided into two grades: coarse and fine. First, the coarse and fine aggregates in the old material were separated as much as possible by heating, and then the separated old material was sieved into two components: coarse material (greater than 4.75 mm) and fine material (less than 4.75 mm). The sieving results of two kinds of asphalt mixes and the asphalt content of the mixes are shown in **Tables 1**, **2**.

It can be seen that the asphalt content in the RAP materials both decreased to some extent (4.3 and 4.9% for AC-20 and AC-13 of the original pavement, respectively), indicating that the asphalt content continued to decrease during the aging process. Due to the adhesion property of the asphalt itself, it causes some of the fines to adhere to the surface of the coarse RAP material. Comparing the RAP test results with the coarse and fine RAP integration results, it can be found that the error between them is very small, indicating that the grade composition of the test and its asphalt content results are more reasonable.

## 2.2 Recycled Asphalt Properties

The 70# common asphalt and SBS modified asphalt from the above recycled old material were used as the research objects. The mixture of extracted old asphalt and trichloroethylene was processed using a Swiss BuchiR-215V rotary evaporator, and the trichloroethylene in the mixture was removed by distillation and recycled. Then, the remaining pure asphalt was evaluated and analyzed, and the results were compared with the original values as shown in **Tables 3**, **4**.

From **Tables 3**, **4**, in the recovery of two asphalt indicators it can be seen that needle penetration and ductility of the two old asphalts is significantly reduced and no longer meets the requirements of engineering technical indicators, whereas the softening point compared with the original indicators continues to increase. This is due to the asphalt in the aging process in the conversion between the components, the asphalt content is reduced, gum and asphaltene content increased, and asphalt molecular mass increased, making the recovered asphalt viscosity decreased, brittle, and hard.

## 2.3 Optimal Asphalt Content

The aggregate sieving tests for two types of recycled aggregates with different RAP admixtures were carried out based on the Aggregate Test Procedure for Highway Engineering (JTG E42-2005) with RAP admixtures of 20, 30, 40, and 50%, respectively.

At the same time, the Marshall mix design method was used to determine the OAC, and the five asphalt contents used were 4.0,

**TABLE 2 |** Results of recovered AC-13 modified asphalt mix components.

| Grouping | Passing percentage of each sieve size (mm) (%) | | | | | | | | | | Asphalt content (%) |
|---|---|---|---|---|---|---|---|---|---|---|---|
| | 16.0 | 13.2 | 9.5 | 4.75 | 2.36 | 1.18 | 0.6 | 0.3 | 0.15 | 0.075 | |
| RAP | 100 | 94.1 | 79.5 | 49.5 | 34.2 | 23.8 | 16.3 | 13.1 | 9.7 | 6.1 | 4.5 |
| Coarse RAP | 100 | 94.8 | 79.0 | 45.8 | 32.1 | 22.5 | 15.2 | 12.0 | 8.6 | 4.5 | 4.2 |
| Fine RAP | 100 | 100 | 100 | 100 | 76.1 | 51.9 | 34.1 | 24.8 | 16.9 | 10.3 | 4.8 |

**TABLE 3 |** Test index of recovered 70# asphalt.

| Test index | Test results | Original value | Technical requirements | Test method (Ministry of Transport of the People's Republic of China, 2004) |
|---|---|---|---|---|
| Penetration (25°C 100 g 5 s) (0.1 mm) | 23.6 | 71.3 | 60–80 | T0604-2000 |
| Ductility (15°C 5 cm/min) (cm) | 55.4 | >100 | ≥100 | T0605-1993 |
| Softening point (°C) | 62.5 | 46.5 | ≥46 | T0606-2000 |

**TABLE 4 |** Test index of recovered SBS modified asphalt.

| Test index | Test results | Original value | Technical requirements | Test method (Ministry of Transport of the People's Republic of China, 2004) |
|---|---|---|---|---|
| Penetration (25°C 100 g 5 s) (0.1 mm) | 30.8 | 66.2 | 50–80 | T0604-2000 |
| Ductility (5°C 5 cm/min) (cm) | 6.9 | 34.8 | ≥30 | T0605-1993 |
| Softening point (°C) | 85.5 | 82.0 | ≥60 | T0606-2000 |

**TABLE 5 |** Summary results of the OAC for each asphalt recycled mixture.

| Mixture type | Optimal asphalt content (%) | | | |
|---|---|---|---|---|
| | 20% RAP | 30% RAP | 40% RAP | 50% RAP |
| AC-20 | 4.2 | 4.2 | 4.3 | 4.2 |
| AC-13 | 4.8 | 4.9 | 4.9 | 4.8 |

4.5, 5.0, 5.5, and 6.0%. Marshall specimens of 63.5 mm in height and 101.6 mm in diameter were formed. According to JTG F40-2004 (Ministry of Transport of the People's Republic of China, 2004), the OAC can be calculated based on the relationship between the asphalt content and the Marshall test indexes, including bulk density, air void, voids in the mineral aggregate (VMA), voids filled with asphalt (VFA), Marshall stability, and Marshall flow as shown in **Table 5**.

# 3 TEST METHOD

## 3.1 Dynamic Modulus Test

The test were conducted on the mechanical properties of AC-20 ordinary asphalt recycled mix and AC-13 modified asphalt recycled mix with different blending ratios (0, 20, 40, and 50%, respectively) in which 5% of the same recycler is added to both recycled materials with 40% RAP blending for performance comparison. The heating temperature of RAP is 120°C for the best compaction characteristics of the mix (Ma et al., 2020), and the test at this temperature has a molding diameter of 150 mm, height of 150 mm rotary compaction specimens and the number of compaction for 100 times, dynamic modulus test; the test process is shown in **Figures 1A–C**. Loading frequencies of 0.1, 0.5, 1, 5, 10, and 25 Hz were used for repeated loading tests under temperature conditions of -10°C, 5°C, 20°C, 35°C, and 50°C, respectively, and the temperature was carried out from low to high temperatures, in turn, whereas the frequency was carried out from high to low frequency, in turn; the load and deformation curves of the last five waveforms were collected for the test, and the average of the three was taken for each specimen type as the final result. The average value of the three waveforms for each specimen type is taken as the final result. The test preparation and procedure are shown in **Figure 1**.

The dynamic modulus of the asphalt mixture at different temperatures can be established as a master curve with frequency at the same reference temperature, and the shift factor can be calculated from the corresponding model, of which the most commonly used is the WLF equation, as shown in **Eq. 1**.

$$\log \alpha_T = \frac{C_1 (T - T_s)}{C_2 + T - T_s} \tag{1}$$

where $\alpha_T$ is the shift factor at $T$ temperature conditions; $C_1$, $C_2$ are constants; $T_S$ is the reference temperature; and $T$ is the temperature of the individual test.

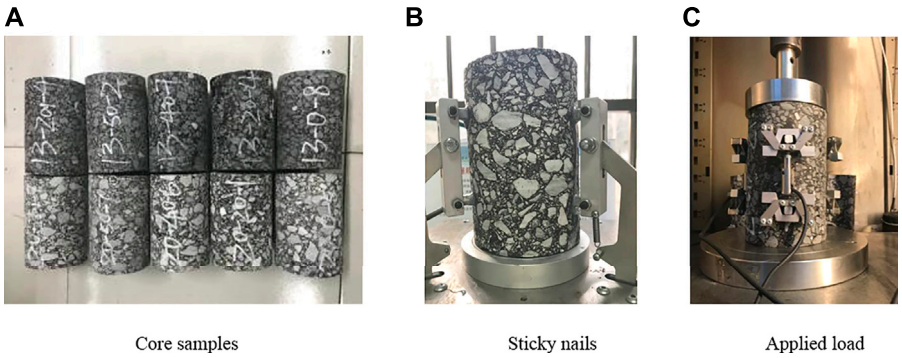


**FIGURE 1 |** Dynamic modulus test procedure.

Pellinen (Pellinen et al., 2002) of the University of Maryland applied the least squares method to fit the sigmoidal equation and obtained the master curve by superposition of shift factors as in **Eq. 2**.

$$\lg|E^*| = \delta + \frac{\alpha}{1 + e^{\beta+\gamma*\lg(fr)}} \tag{2}$$

where $|E^*|$ is the dynamic modulus value; $\delta$ is the minimum dynamic modulus value; $\alpha$ is the range of dynamic modulus values; $\beta$, $\gamma$ are the regression parameters; and $fr$ is scaling down the frequency, where the scaled-down frequency $fr$ and the frequency $f$ can be converted by the equation as in **Eq. 3**.

$$\lg(fr) = \lg(f) + \lg(a_T) \tag{3}$$

where f is the test frequency and $a_T$ is the time–temperature conversion factor, representing the translation distance of the dynamic modulus curve at each temperature to the curve at the reference temperature.

## 3.2 High-Temperature Stability Test

The high-temperature rutting and dynamic creep tests were used to evaluate the high-temperature performance of asphalt recycled mixes with different RAP content ratios. The rutting specimens were prepared based on the density of Marshall specimens, and the heating temperature of RAP is 120°C. The high-temperature rutting test is used to characterize the high-temperature performance of the mixture by dynamic stability, and the average value of three for each specimen type is taken as the final result.

The dynamic creep test uses 150-mm-diameter and 150-mm-height rotating compacted specimens (forming conditions, specimen type, and dynamic modulus test are the same); 60°C is the test temperature, axial pressure is set at 700 kPa, surrounding pressure is 0, loading cycle is 1 s until the specimen is damaged or the test time reaches 3 h, and each specimen type takes the average value of the three specimen types as the final result.

## 3.3 Low-Temperature Crack Resistance Test

A−10°C semicircular splitting test was conducted by using a semicircular specimen of 150 mm in diameter and 50 mm in height at the test temperature of −10°C. For the SCB test, the distance S between the two round rod pivot points was also 12 cm (0.8 times the semicircular specimen), and the loading rate was 50 mm/min. The semicircular specimen was continuously loaded until its destruction in the test, and the load and displacement were recorded. The test was carried out by a UTM-25 multifunctional testing machine, and the average value of three for each specimen type was taken as the final result.

The stress and modulus equations for semicircular specimens are used as shown in **Eqs 4, 5** (Molnernaar et al., 2002).

$$\sigma_t = \frac{4.8F}{BD} \tag{4}$$

$$M_r = \frac{1.84F}{BV} \tag{5}$$

where $\sigma t$ is the bottom tensile stress (MPa), $F$ is the vertical direction load (N), $D$ is the diameter of the specimen (mm), B is the thickness of the specimen (mm), $V$ is the vertical displacement at the bottom of the specimen (mm), and $M_r$ is the modulus (MPa).

## 3.4 Moisture Susceptibility (Freeze-Thaw Splitting Test)

The freeze-thaw splitting test was carried out with 150 mm diameter, 50 mm height, and 20 and 40% RAP content of recycled mixture semicircular specimens. The air void of the asphalt mixture is related to the compaction times and heating temperatures of RAP and influences the moisture susceptibility, so compaction times and heating temperature were considered during the test. The specimens were divided into two groups, one of which was first treated with freeze-thaw cycles and then put into a constant temperature water bath at 25°C for 2 h, together with the other group of specimens for splitting test with a loading rate of 5 mm/min. The average value of the three tests was taken as the final result for each specimen type.

# 4 ANALYSIS OF TEST RESULTS

## 4.1 Dynamic Modulus

In this test, the test temperature of 20°C was used as the reference temperature, and $a_T$ was taken as 0. The dynamic modulus values

**TABLE 6 |** Master curve fitting equations for different asphalt recycled mixes at 20°C.

| Recycled material type | RAP ratio (%) | Master curve fitting equation | $R^2$ |
|---|---|---|---|
| AC-20 General | 0 | $\lg\|y\| = -0.5327 + \frac{5.1838}{1+e^{-1.7923-0.2127*\lg x}}$ | $R^2$ = 0.9993 |
| | 20 | $\lg\|y\| = 1.6286 + \frac{3.0361}{1+e^{-1.0695-0.2293*\lg x}}$ | $R^2$ = 0.9994 |
| | 40 | $\lg\|y\| = 2.1933 + \frac{2.5760}{1+e^{-0.9036-0.1994*\lg x}}$ | $R^2$ = 0.9994 |
| | 50 | $\lg\|y\| = -0.7126 + \frac{5.4748}{1+e^{-1.9831-0.1909*\lg x}}$ | $R^2$ = 0.9983 |
| | 40 + regenerant | $\lg\|y\| = -0.5910 + \frac{5.4560}{1+e^{-1.8524-0.1774*\lg x}}$ | $R^2$ = 0.9992 |
| AC-13 modified | 0 | $\lg\|y\| = 2.1123 + \frac{2.4605}{1+e^{-0.7344-0.2172*\lg x}}$ | $R^2$ = 0.9996 |
| | 20 | $\lg\|y\| = 0.6008 + \frac{3.9909}{1+e^{-1.4949-0.1952*\lg x}}$ | $R^2$ = 0.9991 |
| | 40 | $\lg\|y\| = -0.8353 + \frac{5.4766}{1+e^{-1.8391-0.1869*\lg x}}$ | $R^2$ = 0.9978 |
| | 50 | $\lg\|y\| = 1.0657 + \frac{3.6196}{1+e^{-1.5355-0.2469*\lg x}}$ | $R^2$ = 0.9980 |
| | 40 + regenerant | $\lg\|y\| = 2.3046 + \frac{2.3719}{1+e^{-0.6720-0.2679*\lg x}}$ | $R^2$ = 0.9992 |

obtained for different loading frequencies at this temperature were first fitted to obtain the initial fitting equations. The initially obtained $\delta$, $\alpha$, $\beta$, and $\gamma$ were used as the initial values, fitted to determine the $a_T$ values corresponding to other test temperatures (Ma et al., 2008), and then the test values of frequency–dynamic modulus at different temperature conditions were leveled to finally obtain the master curve fitting equation at the reference temperature of 20°C as shown in **Table 6**. The results of comparing the master curves of two types of asphalt recycled mixes under different RAP admixtures are shown in **Figures 2**, **3**, respectively.

The dynamic modulus values of the two types of asphalt recycled mixes increased with the increase of loading frequency, but the degree of change was different for different RAP admixture mixes, indicating that the recycled material was sensitive to temperature changes. For the AC-20 common asphalt recycled mix, the temperature stability of the mix is as follows: RAP0%<RAP20% < RAP50% < RAP40% + regenerator < RAP40%, which indicates that, compared with the new material, the recycled material has a better temperature stability after adding RAP material with the increase of RAP content showing a trend of increasing first and then decreasing in the content. The temperature stability of AC-13 modified asphalt recycled mix is as follows: RAP40% + regenerator < RAP50% < RAP20% < RAP0% < RAP40%, in which the sensitivity of the mix to temperature after adding RAP material is not significantly different compared with the new material, but the temperature sensitivity of the recycled mixture was slightly better when the RAP content was 40%, and the addition of the recycler was not conducive to the improvement of the temperature stability of the mixture. In addition, comparing the results of AC-13 and AC-20, it can be seen that the temperature sensitivity of AC-20 normal recycled asphalt mixture is influenced by the RAP content. The temperature sensitivity of AC-13 modified recycled asphalt mixture is weaker compared with AC-20 normal asphalt mixture. The results of dynamic modulus values of AC-20 ordinary asphalt recycled mix at high frequency (low temperature) with different RAP admixtures are: RAP0%

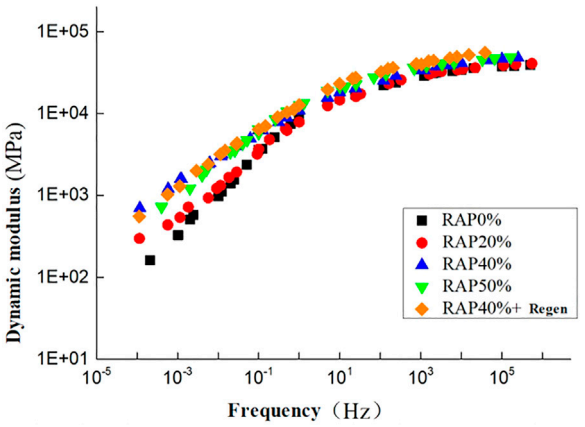


**FIGURE 2 |** Master curve of five different AC-20 normal asphalt recycled mixes.

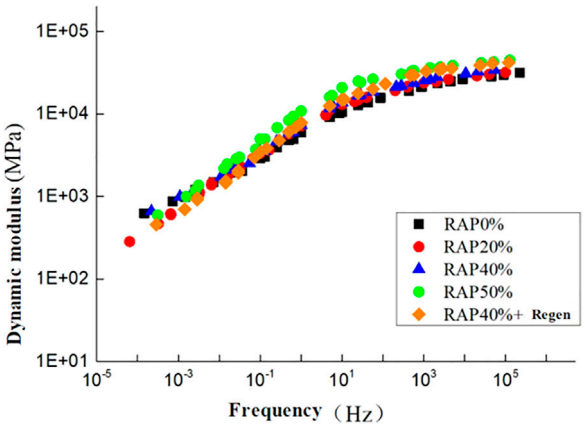


**FIGURE 3 |** Master curve of five different AC-13 modified asphalt recycled mixes.

<RAP20% < RAP40% < RAP40% + regenerator < RAP50%, while the results of AC-13 modified asphalt recycled mix are: RAP0%<RAP20% < RAP40% < RAP50% < RAP40% + regenerant. For the two different types of asphalt recycled mixes, the addition of the old material and the regenerant improved the mechanical strength of the mixes to some extent under high-frequency (low-temperature) conditions, and the higher the RAP content, the higher the strength, but considering the reduced flexibility of the recycled material, its anticracking performance at low temperature still needs further study. In addition, the RAP doping under low-frequency (high-temperature) conditions had a significant effect on the high-temperature stability of the AC-20 common asphalt recycled mix and had less effect on the AC-13 modified asphalt recycled mix. Meanwhile, the dynamic modulus values of AC-13 modified asphalt recycled mix with the same RAP content are basically higher than those of AC-20 ordinary asphalt recycled mix, indicating that the mechanical strength of AC-13 modified asphalt recycled mix is higher than that of AC-20 ordinary asphalt recycled mix.

## 4.1 High-Temperature Stability

### 4.1.1 Dynamic Stability

The dynamic stability test results are shown in **Figure 4**. The dynamic stability of the recycled asphalt mixes with different RAP content met the technical requirements (≥1,000 times/min). With the increase of RAP, the dynamic stability of the two types of recycled asphalt gradually increased, and when the RAP mixture increased from 40 to 50%, the growth rate became significantly larger, indicating that its high-temperature rutting resistance significantly improved. The softening point and viscosity of the recycled asphalt increase, thus showing increasing high-temperature performance. Comparing the two types of recycled material, it can be seen that the high-temperature stability of the AC-13 modified asphalt recycled mix is better than that of the AC-20 normal asphalt recycled mix as a whole.

### 4.1.2 Dynamic Creep Cumulative Strain

The dynamic creep cumulative strain curves of AC-20 normal asphalt recycled mix and AC-13 modified asphalt recycled mix with different RAP content are shown in **Figures 5**, **6**. For the AC-20 common asphalt recycled mix, the new material is the earliest to be damaged, the slope of the second stage is the largest, and the number of rheology is the smallest, only about 1,000 times. In addition, it can also be seen that the slope and strain of the second stage of the recycled material with 50% RAP is slightly greater than that of the recycled material with the addition of the recycler, and the performance of the two is similar, whereas both are significantly greater than the slope and strain of the recycled material with 40% RAP. For AC-13 modified asphalt recycled mixes, the third stage did not appear in any of the five different mixes, and the high-temperature rutting resistance of AC-13 modified asphalt recycled mixes with the same RAP content was better than that of AC-20 normal asphalt recycled mixes. Compared with the new material, the high-temperature rutting resistance of both types of recycled mixes with RAP was significantly improved, and the best high-temperature performance was achieved at 40% of RAP, and the high-temperature performance of AC-20 normal asphalt recycled mixes with this amount was close to that of AC-13 modified asphalt recycled mixes. In addition, the high-temperature rutting test and dynamic creep results are different, indicating that, for the high RAP mixture, it is not suitable to use a single index of dynamic stability and evaluate its high-temperature performance. It should be integrated with the dynamic creep test comprehensive evaluation.

## 4.2 Low-Temperature Crack Resistance

The critical value of bending strain energy density (Shan et al., 2019) was used as the main evaluation index of low-temperature performance. The semicircular splitting test indexes of 10 different asphalt recycled mixes at −10°C low temperature are shown in **Table 7**. Under the same RAP content conditions, the

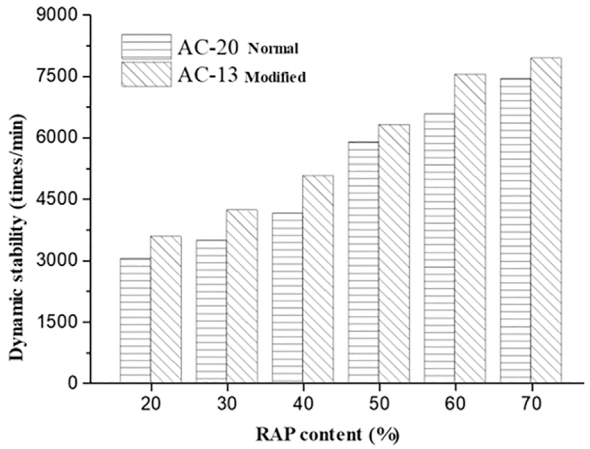


**FIGURE 4 |** Dynamic stability of asphalt recycled material with different RAP content.

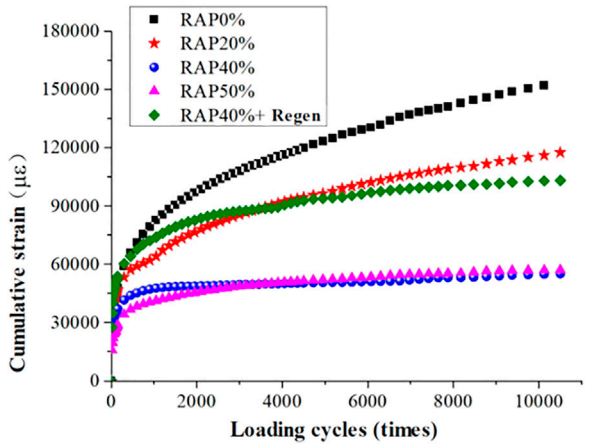


**FIGURE 6 |** Dynamic creep curves of five different AC-13 modified asphalt recycled mixes.

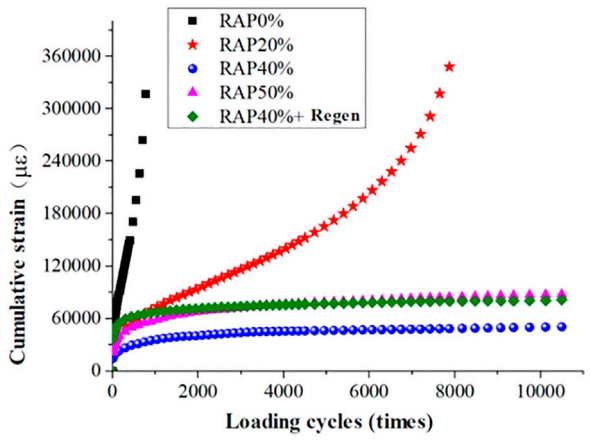


**FIGURE 5 |** Dynamic creep curves of five different AC-20 ordinary asphalt recycled mixes.

four indexes of the AC-13 modified asphalt recycled mix are greater than the performance indexes of the AC-20 common asphalt recycled mix, which proves that the low-temperature performance of AC-13 modified asphalt recycled mix is more superior. The trend of bending and tensile strength and modulus of stiffness of both types of recycled mixes is the same: RAP0% <RAP20% < RAP40% < RAP40% + regenerator < RAP50%, whereas the trend of bending and tensile strain value is the opposite: RAP0%>RAP20% > RAP40% + regenerator > RAP40% > RAP50%, which finally leads to the trend of strain energy density change: RAP20% > RAP0%>RAP40% + regenerator > RAP40% > RAP50%. Compared with the new material, only the low-temperature performance of the mixture with 20% RAP doping is improved, whereas continuing to increase the RAP doping will instead make its anticracking performance worse, and the higher the RAP doping, the worse the anticracking performance. In addition, the proportion of RAP at 40% of the recycled mix after adding the regenerant four indicators have different degrees of increase, the regenerant in a certain degree makes the old and new asphalt mix combined more fully, and makes the brittle asphalt softened to a certain extent so as to enhance the toughness of the recycled mix and low-temperature cracking resistance.

## 4.3 Moisture Susceptibility Performance

The experimental results after freeze-thaw splitting tests with different RAP admixtures under different compaction times and heating temperatures are shown in **Figure 7A–D**. Considering the effect of heating temperature on the freeze-thaw splitting strength ratio TSR, it can be seen that, with the increase of heating temperature of the old material, the water damage resistance of the recycled asphalt mixture is significantly higher, and the difference between the performance of the mixture with the heating temperature of the old material above 120°C and that of the new material (RAP content is 0%) is small, which indicates that increasing the heating temperature of the old material can effectively improve the moisture susceptibility of the mixture. Considering the effect of the RAP admixture on the moisture susceptibility performance of the recycled mix, it can be seen that, with the increase of the RAP admixture from 20 to 40%, the freeze-thaw splitting tensile strength ratio of the mix increased slightly, and its water damage resistance increased slightly, but the enhancement effect on the moisture susceptibility performance was weak compared with the heating temperature. When considering the number of rotational compactions, the increase makes a small increase in the TSR value of the mix, which is due to the fact that the increase in the amount of compaction reduces the void ratio to a certain extent, improves the compactness of the mix, reduces the water infiltrated inside the mix during freeze-thaw, and shows better moisture susceptibility. Compared with the AC-20 ordinary asphalt recycled mix, the AC-13 modified asphalt recycled mix has higher splitting strength before and after freeze-thaw and has better resistance to water damage.

**TABLE 7 |** Semicircular splitting test results of different asphalt recycled mixes (–10°C).

| Mix type | RAP content (%) | Bending and tensile strength (MPa) | Bending tensile strain (με) | Modulus of rigidity (MPa) | Strain energy density (KJ/m$^3$) |
|---|---|---|---|---|---|
| AC-20 General | 0% | 10.82 | 2,385 | 2,916 | 9.35 |
| | 20% | 11.46 | 2,328 | 3,602 | 9.67 |
| | 40% | 12.55 | 2,143 | 4,709 | 8.84 |
| | 50% | 13.63 | 2000 | 5,244 | 8.65 |
| | 40% + regenerant | 13.32 | 2,259 | 4,909 | 9.06 |
| AC-13 modified | 0% | 12.17 | 2,853 | 3,647 | 13.35 |
| | 20% | 12.95 | 2,822 | 3,964 | 13.60 |
| | 40% | 13.39 | 2,768 | 4,985 | 13.16 |
| | 50% | 13.98 | 2,683 | 5,610 | 12.92 |
| | 40% + regenerant | 13.75 | 2,804 | 5,273 | 13.31 |

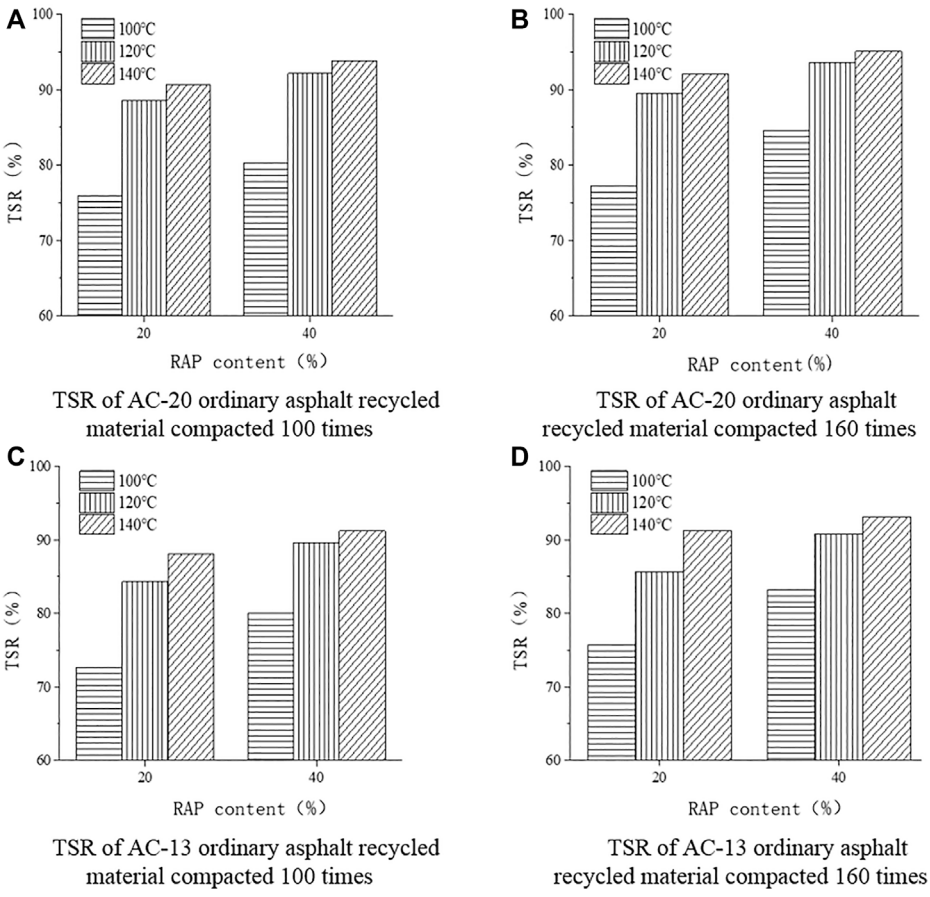


**FIGURE 7 |** TSR values of each asphalt recycled mix.

## 5 CONCLUSION

The effects of RAP content (0, 20, 40, and 50% respectively) on the road performance of two different types of mixes, AC-20 normal asphalt recycled mix and AC-13 modified asphalt recycled mix, based on dynamic modulus, high- and low-temperature performance, and moisture susceptibility performance were investigated, and the main findings can be summarized as follows.

1 The addition of RAP and regenerant improved the dynamic modulus and mechanical strength of the recycled mixture, and

the higher the RAP content, the higher the strength. Under low-frequency (high-temperature) conditions, the RAP content had a greater effect on the mechanical properties of AC-20 ordinary asphalt recycled mixes, but the mechanical properties of AC-13 modified asphalt recycled mixture has less effect.

2 Compared with the virgin asphalt mixture, the high-temperature rutting resistance of both types of recycled mixes with RAP were significantly improved, and the introduction of regenerant did not significantly improve the high-temperature rutting resistance. Compared with AC-20 ordinary asphalt recycled mix, the high-temperature rutting resistance of AC-13 modified asphalt recycled mix was better at the same RAP content level.

3 The low-temperature cracking resistance of the two different types of asphalt recycled mixes tended to increase with the increase of RAP content (from 0 to 50%) and then weakened, and the best low-temperature performance was achieved when the RAP content was 20%.

4 The moisture susceptibility of the two types of recycled mixtures showed a trend of increasing and then decreasing with the increase of RAP and reached the best state when the RAP was 40%.

5 Under the high RAP content condition, the regenerant for road performance needs to be systematically analyzed according to the specific situation, and a single regenerant has a negative impact on the mechanical properties and high-temperature performance of the recycled mixture. Systematic analysis is needed to determine the appropriate RAP content and regenerant use according to the actual project characteristics.

It is noteworthy that the content of RAP influences the performance of the recycled asphalt mixture, mainly because of interaction between virgin and aged asphalt binder. So, for future research, the blending between the virgin and aged asphalt binder is required to shed more light on the reasons.

## DATA AVAILABILITY STATEMENT

The original contributions presented in the study are included in the article/Supplementary Material, further inquiries can be directed to the corresponding author.

## AUTHOR CONTRIBUTIONS

Conceptualization, XM and JW; methodology, XM and JW; validation, XM and JW; formal analysis, XM; investigation, JW and YX; data curation, XM; writing—original draft preparation, YX; writing—review and editing, JW.

## FUNDING

The research was funded by the Jiangsu Transportation Scientific Research Project, Grant number 2017-21.

## REFERENCES

Chen, H. X., and Chen, S. F. (2008). Aging Behavior and Aging Mechanism of Substrate Asphalt. *J. Shandong Univ. Eng. Edition* 38, 13–19. doi:10.3969/j.issn.1671-5381.2009.01.004

Chen, Y. Q. (2015). *Influence of Different Layers of Old Material Characteristics on the Road Performance of Hot Recycled Asphalt Mixtures*. Master dissertation. Nanjing: Southeast University.

Ding, Z. (2013). *Development and Application Research of Asphalt Mixture Regenerant for Waste Rubber Reuse*. Master dissertation. Xi'an: Chang'an University.

Fan, Z. F. (2016). *Microscale Study on the Evaluation of Asphalt Aging Performance*. Master dissertation. Changsha: South China University of Technology.

Gaitan, L., Mehta, Y., Nolan, A., Dubois, E., Coffey, S., McCarthy, L., et al. (2013). Evaluation of the Degree of Blending and Polymer Degradation of Reclaimed Asphalt Pavement (RAP) for Warm Mix Asphalt. *J. Solid Waste Technol. Mngmnt* 39, 101–113. doi:10.5276/jswtm.2013.101

Gundla, A., and Underwood, S. (2017). Evaluation of *In Situ* RAP Binder Interaction in Asphalt Mastics Using Micromechanical Models. *Int. J. Pavement Eng.* 18, 798–810. doi:10.1080/10298436.2015.1066003

Hussain, A., and Yanjun, Q. (2013). Effect of Reclaimed Asphalt Pavement on the Properties of Asphalt Binders. *Proced. Eng.* 54, 840–850. doi:10.1016/j.proeng.2013.03.077

Jin, M. L., Yang, J. H., and Shi, M. R. (2001). Analysis of the Aging Mechanism of Road Asphalt. *J. Shanghai Inst. Appl. Tech. (Natural Sci. Edition)* 1, 14–17. doi:10.3969/j.issn.1671-7333.2001.01.003

Kandhal, P. S., and Foo, K. Y. (1997). *Designing Recycled Hot Mix Asphalt Mixtures Using Superpave Technology*. Alabama: National Center for Asphalt Technology, 1–18.

Kandhal, P. S., Rao, S. S., Watson, D. E., and Young, B. (1995). Performance of Recycled Hot Mix Asphalt Mixtures in State of Georgia. *Transportation Res. Rec.* 1507, 67–77.

Loria, L., Hajj, E. Y., Sebaaly, P. E., Barton, M., Kass, S., and Liske, T. (2011). Performance Evaluation of Asphalt Mixtures with High Recycled Asphalt Pavement Content. *Transportation Res. Rec.* 2208, 72–81. doi:10.3141/2208-10

Ma, X., Leng, Z., Wang, L., and Zhou, P. (2020). Effect of Reclaimed Asphalt Pavement Heating Temperature on the Compactability of Recycled Hot Mix Asphalt. *Materials* 13 (16), 3621. doi:10.3390/ma13163621

Ma, X., Ni, F. J., and Chen, R. S. (2008). Dynamic Modulus Test of Asphalt Mixture and Prediction Model. *China J. Highw. Transport* 21, 35–39. doi:10.19721/j.cnki.1001-7372.2008.03.007

Ministry of Transport of the People's Republic of China (2004). *Technical Specifications for Construction of Highway Asphalt Pavements: JTG F40-2004*. Beijing, China: China Communications Press.

Molnernaar, A., Scarpas, A., Liu, X., and Erkens, S. (2002). Semi-circular Bending Test; Simple but Useful. *Asphalt Paving Technol. Assoc. Asphalt Paving Technologists-Proceedings Tech. Sessions* 71, 794–815.

Navaro, J., Bruneau, D., Drouadaine, I., Pouteau, B., Colin, J., and Dony, A. (2012). Analyzing the Influence of Manufacturing Conditions of Reclaimed Asphalt concrete on the Characteristics of the Asphalt Binder: Development of a Gradual Binder Extraction Method. *Eur. Phys. J. Appl. Phys.* 58, 1–14. doi:10.1051/epjap/2012110102

Pellinen, T. K., Witczak, M. W., Marasteanu, M., Chehab, G., and Dongré, R. (2002). Stress Dependent Master Curve Construction for Dynamic (Complex) Modulus. *Asphalt Paving Technol. Assoc. Asphalt Paving Technologists-Proceedings Tech. Sessions* 71, 281–309.

Shan, M., Wang, L., and Zhang, B. (2019). Low Temperature Properties of Warm-Mixed Crumb Rubber Asphalt Mixture under Salt and Freeze-Thaw Cycles. *J. Building Mater.* 22, 467–473. doi:10.3969/j.issn.1007-9629.2019.03.20

Shen, J., and Wang, X. H. (2015). Research on the Influence of Old Material Characteristics on the Performance of Plant-Mixed Hot Recycled Mixes. *Inner Mongolia Road and Transportation* 4, 48–51. doi:10.3969/j.issn.1005-0574.2015.04.016

Thakur, S. C. (2010). *Laboratory Evaluation of Characteristics of Recycled Asphalt Pavement (RAP) in Kansas. Doctoral Dissertation*. Lawrence: University of Kansas.

Yan, X. Y., and Xiao, L. J. (2016). Research on the Road Performance of High-Dose RAP Plant-Mixed Hot Recycled Asphalt Mixes. *Road Eng.* 6, 76–77.

Yang, J., Gong, M. H., and Troy, P. (2015). Atomic Force Microscopy-Based Microstructure Study of Bitumen. *J. Pet. (Petroleum Plus)* 4, 959–965. doi:10.3969/j.issn.1001-8719.2015.04.018

Yang, Y. W., and Ma, T. (2011). Detection Method of Effective Regeneration Rate of Aged Asphalt Hot Regeneration[J]. *J. Construction Mater.* 14, 418–422. doi:10.3969/j.issn.1007-9629.2011.03.025

Zhao, B. (2014). *Research on the Mechanism and Technical Performance of Hot Regeneration of Asphalt Mixture*. Master dissertation. Xi'an: Chang'an University.

**Conflict of Interest:** The authors declare that the research was conducted in the absence of any commercial or financial relationships that could be construed as a potential conflict of interest.

frontiers in Materials

ORIGINAL RESEARCH
published: 11 February 2022
doi: 10.3389/fmats.2021.816949

# Theoretical and Experimental Investigation on Dynamic Response of Asphalt Pavement Under Vibration Compaction

*Hong-Yu Shan*[1,2], *Han-Cheng Dan*[1]*, *Shi-Ping Wang*[1], *Xiang Liu*[3]* and *Hao Wang*[4]

[1]School of Civil Engineering, Central South University, Changsha, China, [2]Power China Guiyang Engineering Corporation Limited, Guiyang, China, [3]School of Traffic and Transportation Engineering, Central South University, Changsha, China, [4]Department of Civil and Environmental Engineering, Rutgers, The State University of New Jersey, Piscataway, China

This study aims to investigate the dynamic response regulation by combining the theoretical analysis and field test under the vibration rolling condition. Based on the viscoelastic theory of a multilayer system, the dynamic stiffness method (DSM) incorporating multidimensional Fourier transform is proposed to solve the 3-dimensional (3D) dynamic response of pavement under vibration compaction. The stiffness matrix of each pavement layer and the global stiffness matrix of the whole pavement structure are obtained. By combining vibration load with boundary conditions, the 3D exact solution is obtained and validated by the finite element method. In addition, the field test is also conducted using a series of sensors and equipment (e.g., SmartRock sensor, acceleration sensor, temperature sensors, and non-nuclear density meter) to calibrate the theoretical model to determine the wave number and dynamic modulus during the vibration rolling process. Then, considering the factors during compaction, the rules of displacement variation and pavement acceleration are investigated in terms of modulus, thickness, and density. The results show that the 3D displacement and acceleration components both vibrate with high frequencies during compaction, and peak acceleration in the vertical direction prevails. For the vertical displacement, its distribution beneath the drum of the roller is almost even except that it drops to zero abruptly around the drum edge. The relationship between thickness and acceleration follows a linear function, and the acceleration on the pavement surface rises when the thickness increases. Although the density and modulus increase with rolling times, the effect of modulus on acceleration is more obvious and prominent than that of density. In summary, the DSM presented in this article provides a robust method to calculate the dynamic response of pavement under vibratory compaction and to back-calculate the modulus of compacted pavement layers. Moreover, the regulation also sheds insight on the understanding of vibration compaction mechanism that there is a potentially strong correlation between compaction state, modulus, and vibration acceleration.

**Keywords: asphalt pavement, vibration compaction, dynamic response, dynamic stiffness method (DSM), vibration acceleration**

OPEN ACCESS

***Edited by:***
*Dongshuai Hou,*
*Qingdao University of Technology, China*

***Reviewed by:***
*Pengfei Liu,*
*RWTH Aachen University, Germany*
*Peiwen Hao,*
*Chang'an University, China*

***Correspondence:**
*Han-Cheng Dan*
*danhancheng@csu.edu.cn*
*Xiang Liu*
*xiangliu06@gmail.com*

***Specialty section:***
*This article was submitted to Structural Materials, a section of the journal Frontiers in Materials*

***Received:*** *17 November 2021*
***Accepted:*** *28 December 2021*
***Published:*** *11 February 2022*

***Citation:***
*Shan H-Y, Dan H-C, Wang S-P, Liu X and Wang H (2022) Theoretical and Experimental Investigation on Dynamic Response of Asphalt Pavement Under Vibration Compaction. Front. Mater. 8:816949. doi: 10.3389/fmats.2021.816949*

# 1 INTRODUCTION

It is widely known that compaction is a key procedure in the construction process of asphalt pavement. Generally speaking, insufficient strength and poor durability are important reasons for asphalt pavement distresses, such as rutting, cracking, and water damage (Wang et al., 2009; Dan et al., 2022; Dan et al., 2020a; Hosseini et al., 2020). To a large extent, these distresses have been closely correlated with pavement compaction quality (Coleri et al., 2012; Xu and Chang, 2016; Jia et al., 2019; Wu et al., 2019; Jing et al., 2020). Although the importance of compaction is widely acknowledged nowadays, study on the compaction mechanism is still troubled with simplification and one-sidedness. In the field, the pavement construction process is affected by many complicating factors, such as exciting force, compaction work, amplitude, vibration frequency, and rolling speed (Coleri et al., 2012; Fares et al., 2014; Xu and Chang, 2016; Jia et al., 2019; Liu et al., 2019; Jing et al., 2020; Paulmichl et al., 2020; Liu et al., 2022). Specifically, there is little quantitative study as to how these factors affect the compaction and to what degree the effects are significant. It is, therefore, challenging to accurately reveal the compaction mechanism due to so many complex influencing factors. Additionally, it is difficult to detect the feedback information of pavement structure and analyze the physical and mechanical processes contained in the feedback information. In summary, there is a big gap between theory and practice for improving the compaction technology of asphalt pavement (Dan et al., 2020b).

Asphalt mixture is a type of pavement material with rheological properties and, thus, is generally compacted using the vibratory roller in engineering. In the compaction process, the vibratory roller not only runs on the pavement surface at a certain speed but also vibrates up and down at a certain frequency. Therefore, compared with traffic loading, the dynamic response of asphalt pavement in the process of vibration rolling is definitely different and requires special treatment. Many researchers carried out investigations on the dynamic response of asphalt pavement under various types of loading, and those methods can be roughly categorized into analytical approach and numerical simulation (Grundmann et al., 1999; Lu and Jeng, 2007; Lefeuvemesgouez and Mesgouez, 2008; Xu et al., 2008; Souza and Castro, 2012; Beskou et al., 2016; Dong and Ma, 2018; Roozbahany and Partl, 2019; Lv et al., 2020; Qian et al., 2020), with very limited experimental studies in the literature (Dong et al., 2012; Chen X et al., 2015; Shan et al., 2019; Li et al., 2020). In the analytical approach, the differential governing equation was usually established, and the analytical/semi-analytical solutions of pavement dynamic response were obtained by means of integral transformation (Bierer and Bode, 2007; Zhenning et al., 2016; Zhan et al., 2018; Liu et al., 2021a; Liu et al., 2021b). Most solutions treated the traffic loading as a moving concentrated, constant load or a moving load that changed harmonically with time. The studies on vibration of pavement mainly considered pavement roughness (Li et al., 2012; Lv et al., 2020), but few investigated the characteristics of dynamic response in the process of vibration compaction of pavement because the use of the analytical method is strongly affected by the complexity of the model itself (Lv et al., 2020; Zhao and Wang, 2020). In order to consider more complex situations, many researchers applied the finite element method to simulate the response of pavement under various dynamic loading. In addition, the discrete element method (DEM) is increasingly applied to quantify the internal stresses of aggregates during compaction from a microscopic perspective (Chen J et al., 2015; Liu et al., 2019; Si et al., 2019; Qian et al., 2020). Despite the general applicability of the finite and discrete element methods, the numerical simulation of dynamic pavement responses is usually time-consuming and inefficient (Wang et al., 2021). At present, the literature on the dynamic response of asphalt pavement structure under the combined action of moving and vibratory loading is relatively scarce, especially the theoretical aspects of vibration compaction.

Hence, taking into account the moving and vibratory characteristics of compaction loading, this work aims to study the three-dimensional (3D) dynamic response regulation in the compaction process and the influencing factors. A 3D model is to be established based on viscoelasticity theory for the pavement multilayer system, and the dynamic stiffness method will be used to derive the analytical solution for the purpose of a fast and efficient calculation. Furthermore, the dynamic response of asphalt pavement under the action of the vibratory roller is investigated in terms of displacement, acceleration, temperature, modulus, and compaction degree of the asphalt pavement.

# 2 METHODOLOGY

## 2.1 Assumptions

Although asphalt mixture is a complex three-phase material, the pavement is generally regarded as a multilayer elastic structure with infinite length in theoretical considerations (Bierer and Bode, 2007; Liu et al., 2021b). Previous research has pointed out that plastic deformation within the finite acting time of the vibratory roller is negligibly small, and the dynamic response process is, thus, regarded as a viscoelastic vibration (Wang et al., 2021). In addition, before the establishment of the model, the following assumptions need to be introduced:

(1) The roller–pavement vibration system is linear.
(2) The structure layers underneath the surface course are homogenous and isotropically elastic.
(3) The constitutive relationships of the structural layers satisfy Hook's law.
(4) The displacement at a certain depth in the pavement is zero.
(5) The load vibrates freely on the road surface with a sinusoidal waveform, and the loading point is kept fixed. The pavement response with time can be illustrated according to different positions, which is expressed by $x = vt$ ($v$ is the moving speed of the road roller, $t$ is the sampling time, and $x$ is the distance to the observation point) (Dan et al., 2015; Wang et al., 2021).

## 2.2 Governing Equations

The 3D pavement with the Cartesian coordinate can be defined as follows. The origin is located at the pavement surface, and the $z$-,

*y*- and *x*-axes are along the pavement depth direction, transverse direction, and longitudinal direction (driving of the vibratory roller), respectively.

Considering an asphalt pavement under vibration loading, the force equilibrium equation can be written as

$$\begin{cases} \dfrac{\partial \sigma_x}{\partial x} + \dfrac{\partial \tau_{xy}}{\partial y} + \dfrac{\partial \tau_{zx}}{\partial z} = \rho \dfrac{\partial^2 u_x}{\partial t^2} \\ \dfrac{\partial \sigma_y}{\partial y} + \dfrac{\partial \tau_{zy}}{\partial z} + \dfrac{\partial \tau_{yx}}{\partial x} = \rho \dfrac{\partial^2 u_y}{\partial t^2} \\ \dfrac{\partial \sigma_z}{\partial z} + \dfrac{\partial \tau_{xz}}{\partial x} + \dfrac{\partial \tau_{yx}}{\partial y} = \rho \dfrac{\partial^2 u_z}{\partial t^2} \end{cases}, \tag{1}$$

where $u_z$, $u_y$, and $u_x$ are the displacement components in the *z*-, *y*-, and *x*- direction, respectively; $\sigma_z$, $\sigma_y$, and $\sigma_x$ are the normal stress components accordingly; $\rho$ is the density of the pavement material, and $\tau$ represents the shear stresses.

The strain–displacement and constitutive relationships are

$$\begin{cases} \varepsilon_x = \dfrac{\partial u_x}{\partial x}, \gamma_{xy} = \dfrac{\partial u_x}{\partial y} + \dfrac{\partial u_y}{\partial x} \\ \varepsilon_y = \dfrac{\partial u_y}{\partial y}, \gamma_{yz} = \dfrac{\partial u_y}{\partial z} + \dfrac{\partial u_z}{\partial y} \\ \varepsilon_z = \dfrac{\partial u_z}{\partial z}, \gamma_{xz} = \dfrac{\partial u_x}{\partial z} + \dfrac{\partial u_z}{\partial x} \end{cases}, \tag{2}$$

$$\begin{cases} \varepsilon_x = \dfrac{1}{E}\left[\sigma_x - \mu\left(\sigma_y + \sigma_z\right)\right] \\ \varepsilon_y = \dfrac{1}{E}\left[\sigma_y - \mu\left(\sigma_x + \sigma_z\right)\right] \\ \varepsilon_z = \dfrac{1}{E}\left[\sigma_z - \mu\left(\sigma_y + \sigma_x\right)\right] \\ \gamma_{xy} = \dfrac{1}{G}\tau_{xy}, \gamma_{xz} = \dfrac{1}{G}\tau_{xz}, \gamma_{zy} = \dfrac{1}{G}\tau_{zy} \end{cases}, \tag{3}$$

where $\nu$, $E$, and $G$ are Poisson's ratio, Young's elastic modulus, and shear modulus of the material.

Subsequently, **Eqs 1–3** in the time domain are transformed into the frequency domain according to the Fourier transform method, as shown in **Eqs 4–6**,

$$\begin{cases} \dfrac{\partial \tilde{\sigma}_x}{\partial x} + \dfrac{\partial \tilde{\tau}_{xy}}{\partial y} + \dfrac{\partial \tilde{\tau}_{zx}}{\partial z} + \rho \xi^2 \tilde{u}_x = 0 \\ \dfrac{\partial \tilde{\sigma}_y}{\partial y} + \dfrac{\partial \tilde{\tau}_{zy}}{\partial z} + \dfrac{\partial \tilde{\tau}_{yx}}{\partial x} + \rho \xi^2 \tilde{u}_y = 0 \\ \dfrac{\partial \tilde{\sigma}_z}{\partial z} + \dfrac{\partial \tilde{\tau}_{xz}}{\partial x} + \dfrac{\partial \tilde{\tau}_{yx}}{\partial y} + \rho \xi^2 \tilde{u}_z = 0 \end{cases}, \tag{4}$$

$$\begin{cases} \tilde{\varepsilon}_x = \dfrac{\partial \tilde{u}_x}{\partial x}, \tilde{\gamma}_{xy} = \dfrac{\partial \tilde{u}_x}{\partial y} + \dfrac{\partial \tilde{u}_y}{\partial x} \\ \tilde{\varepsilon}_y = \dfrac{\partial \tilde{u}_y}{\partial y}, \tilde{\gamma}_{yz} = \dfrac{\partial \tilde{u}_y}{\partial z} + \dfrac{\partial \tilde{u}_z}{\partial y} \\ \tilde{\varepsilon}_z = \dfrac{\partial \tilde{u}_z}{\partial z}, \tilde{\gamma}_{xz} = \dfrac{\partial \tilde{u}_x}{\partial z} + \dfrac{\partial \tilde{u}_z}{\partial x} \end{cases}, \tag{5}$$

$$\begin{cases} \tilde{\varepsilon}_x = \dfrac{1}{E}\left[\tilde{\sigma}_x - \mu\left(\tilde{\sigma}_y + \tilde{\sigma}_z\right)\right] \\ \tilde{\varepsilon}_y = \dfrac{1}{E}\left[\tilde{\sigma}_y - \mu\left(\tilde{\sigma}_x + \tilde{\sigma}_z\right)\right] \\ \tilde{\varepsilon}_z = \dfrac{1}{E}\left[\tilde{\sigma}_z - \mu\left(\tilde{\sigma}_y + \tilde{\sigma}_x\right)\right] \\ \tilde{\gamma}_{xy} = \dfrac{1}{G}\tilde{\tau}_{xy}, \tilde{\gamma}_{xz} = \dfrac{1}{G}\tilde{\tau}_{xz}, \tilde{\gamma}_{zy} = \dfrac{1}{G}\tilde{\tau}_{zy} \end{cases}, \tag{6}$$

with

$$\begin{cases} \lambda = \dfrac{\mu E}{(1+\mu)(1-2\mu)} \\ G = \dfrac{E}{2(1+\mu)} \end{cases}. \tag{7}$$

Combining **Eqs 5–7**, the following equations can be obtained:

$$\tilde{\sigma}_x = (\lambda + 2G)\frac{\partial \tilde{u}_x}{\partial x} + \lambda\left(\frac{\partial \tilde{u}_y}{\partial y} + \frac{\partial \tilde{u}_z}{\partial z}\right). \tag{8}$$

$$\tilde{\sigma}_y = (\lambda + 2G)\frac{\partial \tilde{u}_y}{\partial y} + \lambda\left(\frac{\partial \tilde{u}_x}{\partial x} + \frac{\partial \tilde{u}_z}{\partial z}\right). \tag{9}$$

$$\tilde{\sigma}_z = (\lambda + 2G)\frac{\partial \tilde{u}_z}{\partial z} + \lambda\left(\frac{\partial \tilde{u}_y}{\partial y} + \frac{\partial \tilde{u}_x}{\partial x}\right). \tag{10}$$

$$\tilde{\tau}_{xy} = G\left(\frac{\partial \tilde{u}_x}{\partial y} + \frac{\partial \tilde{u}_y}{\partial x}\right), \tilde{\tau}_{xz} = G\left(\frac{\partial \tilde{u}_x}{\partial z} + \frac{\partial \tilde{u}_z}{\partial x}\right), \quad \tilde{\tau}_{zy} = G\left(\frac{\partial \tilde{u}_z}{\partial y} + \frac{\partial \tilde{u}_y}{\partial z}\right). \tag{11}$$

Taking the derivative of **Eq. 10** with respect to *x*, we have

$$\frac{\partial^2 \tilde{u}_z}{\partial x \partial z} = \frac{1}{(\lambda + 2G)}\frac{\partial \tilde{\sigma}_z}{\partial x} - \frac{\lambda}{(\lambda + 2G)}\left(\frac{\partial^2 \tilde{u}_y}{\partial x \partial y} + \frac{\partial^2 \tilde{u}_x}{\partial x^2}\right). \tag{12}$$

Likewise, taking derivative of **Eq. 8** with respect to *x* and then combining with **Eq. 12**, we obtain

$$\frac{\partial \tilde{\tau}_{xz}}{\partial z} = -\frac{4G(\lambda + G)}{\lambda + 2G}\frac{\partial^2 \tilde{u}_x}{\partial x^2} - \frac{3\lambda G + 2G^2}{\lambda + 2G}\frac{\partial^2 \tilde{u}_y}{\partial x \partial y} - G\frac{\partial^2 \tilde{u}_x}{\partial y^2} - \frac{\lambda}{\lambda + 2G}\frac{\partial \tilde{\sigma}_z}{\partial x} - \rho \xi^2 \tilde{u}_x. \tag{13}$$

Similarly, taking derivative of **Eqs 9, 10** with respect to *y*, we have

$$\frac{\partial \tilde{\tau}_{yz}}{\partial z} = -\frac{4G(\lambda + G)}{\lambda + 2G}\frac{\partial^2 \tilde{u}_y}{\partial y^2} - \frac{3\lambda G + 2G^2}{\lambda + 2G}\frac{\partial^2 \tilde{u}_x}{\partial x \partial y} - G\frac{\partial^2 \tilde{u}_y}{\partial x^2} - \frac{\lambda}{\lambda + 2G}\frac{\partial \tilde{\sigma}_z}{\partial y} - \rho \xi^2 \tilde{u}_y. \tag{14}$$

In addition, the following equations can be obtained as well:

$$\frac{\partial \tilde{u}_z}{\partial z} = \frac{1}{\lambda + 2G}\tilde{\sigma}_z - \frac{\lambda}{\lambda + 2G}\frac{\partial \tilde{u}_x}{\partial x} - \frac{\lambda}{\lambda + 2G}\frac{\partial \tilde{u}_y}{\partial y}. \tag{15}$$

$$\frac{\partial \tilde{\sigma}_z}{\partial z} = -\frac{\partial \tilde{\tau}_{zx}}{\partial x} - \frac{\partial \tilde{\tau}_{zy}}{\partial y} - \rho \xi^2 \tilde{u}_z. \tag{16}$$

$$\frac{\partial \tilde{u}_x}{\partial z} = \frac{1}{G}\tilde{\tau}_{xz} - \frac{\partial \tilde{u}_z}{\partial x}. \tag{17}$$

$$\frac{\partial \tilde{u}_y}{\partial z} = \frac{1}{G}\tilde{\tau}_{zy} - \frac{\partial \tilde{u}_z}{\partial y}. \tag{18}$$

For **Eqs 13–18** in the space domain, transforming into the frequency domain by performing the Fourier transform and then the governing equation can be given as follows

$$\begin{cases} \frac{\partial \tilde{\sigma}_z}{\partial z} = -k \cdot j\tilde{\tau}_{zx} - s \cdot j\tilde{\tau}_{zy} - \rho\xi^2 \cdot \tilde{u}_z \\ \frac{\partial j\tilde{\tau}_{xz}}{\partial z} = \left[\frac{4G(\lambda+G)}{\lambda+2G}k^2 + Gs^2 - \rho\xi^2\right] \cdot j\tilde{u}_x + \frac{3\lambda G + 2G^2}{\lambda+2G}ks \cdot j\tilde{u}_y + \frac{\lambda}{\lambda+2G}k \cdot \tilde{\sigma}_z \\ \frac{\partial j\tilde{\tau}_{yz}}{\partial z} = \left[\frac{4G(\lambda+G)}{\lambda+2G}s^2 + Gk^2 - \rho\xi^2\right] \cdot j\tilde{u}_y + \frac{3\lambda G + 2G^2}{\lambda+2G}ks \cdot j\tilde{u}_x + \frac{\lambda}{\lambda+2G}s \cdot \tilde{\sigma}_z \\ \frac{\partial \tilde{u}_z}{\partial z} = \frac{1}{\lambda+2G}\tilde{\sigma}_z - \frac{\lambda}{\lambda+2G}k \cdot j\tilde{u}_x - \frac{\lambda}{\lambda+2G}s \cdot j\tilde{u}_y \\ \frac{\partial j\tilde{u}_x}{\partial z} = \frac{1}{G}j\tilde{\tau}_{xz} + k \cdot \tilde{u}_z \\ \frac{\partial j\tilde{u}_y}{\partial z} = \frac{1}{G}j\tilde{\tau}_{zy} + s \cdot \tilde{u}_z \end{cases}. \tag{19}$$

The abovementioned can be rearranged into a matrix form:

$$\frac{\partial}{\partial z}\begin{bmatrix} \tilde{\sigma}_z \\ j\tilde{\tau}_{xz} \\ j\tilde{\tau}_{yz} \\ \tilde{u}_z \\ j\tilde{u}_x \\ j\tilde{u}_y \end{bmatrix} = \begin{bmatrix} 0 & -k & -s & -\rho\xi^2 & 0 & 0 \\ \frac{\lambda k}{\lambda+2G} & 0 & 0 & 0 & \frac{4G(\lambda+G)k^2}{\lambda+2G} + Gs^2 - \rho\xi^2 & \frac{(3\lambda G+2G^2)ks}{\lambda+2G} \\ \frac{\lambda s}{\lambda+2G} & 0 & 0 & 0 & \frac{(3\lambda G+2G^2)ks}{\lambda+2G} & \frac{4G(\lambda+G)s^2}{\lambda+2G} + Gk^2 - \rho\xi^2 \\ \frac{1}{\lambda+2G} & 0 & 0 & 0 & -\frac{\lambda k}{\lambda+2G} & -\frac{\lambda s}{\lambda+2G} \\ 0 & 1/G & 0 & k & 0 & 0 \\ 0 & 0 & 1/G & s & 0 & 0 \end{bmatrix} \begin{bmatrix} \tilde{\sigma}_z \\ j\tilde{\tau}_{xz} \\ j\tilde{\tau}_{yz} \\ \tilde{u}_z \\ j\tilde{u}_x \\ j\tilde{u}_y \end{bmatrix}. \tag{20}$$

## 2.3 Stiffness Matrix for Multilayer Pavement System

On the basis of the established governing **Eq. 20**, it is necessary to simplify the governing equation to derivate the solution. First, we define

$$B = \begin{bmatrix} 0 & -k & -s & -\rho\xi^2 & 0 & 0 \\ \frac{\lambda k}{\lambda+2G} & 0 & 0 & 0 & \frac{4G(\lambda+G)k^2}{\lambda+2G} + Gs^2 - \rho\xi^2 & \frac{(3\lambda G+2G^2)ks}{\lambda+2G} \\ \frac{\lambda s}{\lambda+2G} & 0 & 0 & 0 & \frac{(3\lambda G+2G^2)ks}{\lambda+2G} & \frac{4G(\lambda+G)s^2}{\lambda+2G} + Gk^2 - \rho\xi^2 \\ \frac{1}{\lambda+2G} & 0 & 0 & 0 & -\frac{\lambda k}{\lambda+2G} & -\frac{\lambda s}{\lambda+2G} \\ 0 & 1/G & 0 & k & 0 & 0 \\ 0 & 0 & 1/G & s & 0 & 0 \end{bmatrix}, \tag{21}$$

and **Eq. 20** can be rewritten as

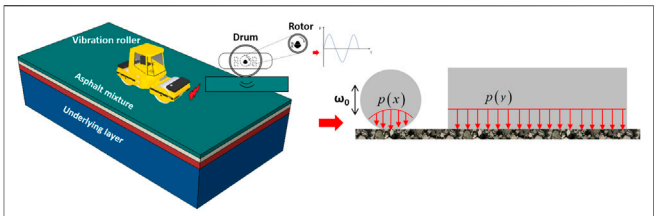


**FIGURE 1 |** Simplified model of vibration load.

$$\frac{\partial}{\partial z}\left[\tilde{\sigma}_z \quad j\tilde{\tau}_{xz} \quad j\tilde{\tau}_{yz} \quad \tilde{u}_z \quad j\tilde{u}_x \quad j\tilde{u}_y\right]^T = B \cdot \left[\tilde{\sigma}_z \quad j\tilde{\tau}_{xz} \quad j\tilde{\tau}_{yz} \quad \tilde{u}_z \quad j\tilde{u}_x \quad j\tilde{u}_y\right]^T. \tag{22}$$

According to the boundary condition shown in **Figure 1**, **Eq. 22** can be solved readily.

$$\left[\tilde{\sigma}_z^1 \quad j\tilde{\tau}_{xz}^1 \quad j\tilde{\tau}_{yz}^1 \quad \tilde{u}_z^1 \quad j\tilde{u}_x^1 \quad j\tilde{u}_y^1\right]^T = e^{Bh_1}\left[\tilde{\sigma}_z^0 \quad j\tilde{\tau}_{xz}^0 \quad j\tilde{\tau}_{yz}^0 \quad \tilde{u}_z^0 \quad j\tilde{u}_x^0 \quad j\tilde{u}_y^0\right]^T, \tag{23}$$

where $\left[\tilde{\sigma}_z^1 \quad j\tilde{\tau}_{xz}^1 \quad j\tilde{\tau}_{yz}^1 \quad \tilde{u}_z^1 \quad j\tilde{u}_x^1 \quad j\tilde{u}_y^1\right]^T$ and $\left[\tilde{\sigma}_z^0 \quad j\tilde{\tau}_{xz}^0 \quad j\tilde{\tau}_{yz}^0 \quad \tilde{u}_z^0 \quad j\tilde{u}_x^0 \quad j\tilde{u}_y^0\right]^T$ represent the boundary condition at $h = h_1$ and surface, respectively, and $h_1$ is the layer thickness.

Defining $T = e^{Bh_1}$ and combining with the block matrix algorithm, **Eq. 24** is obtained directly as follows:

$$\begin{bmatrix} \tilde{\sigma}_z^0 \\ j\tilde{\tau}_{xz}^0 \\ j\tilde{\tau}_{yz}^0 \\ \tilde{\sigma}_z^1 \\ j\tilde{\tau}_{xz}^1 \\ j\tilde{\tau}_{yz}^1 \end{bmatrix} = \begin{bmatrix} -T_{21}^{-1}T_{22} & T_{21}^{-1} \\ T_{12} - T_{11}T_{21}^{-1}T_{22} & T_{11}T_{21}^{-1} \end{bmatrix} \times \begin{bmatrix} \tilde{u}_z^0 \\ j\tilde{u}_x^0 \\ j\tilde{u}_y^0 \\ \tilde{u}_z^1 \\ j\tilde{u}_x^1 \\ j\tilde{u}_y^1 \end{bmatrix}. \tag{24}$$

Based on the relationship between the stress and displacement in the coordinate system, the following equations hold true:

$$\begin{bmatrix} -\tilde{\sigma}_z^0 \\ -j\tilde{\tau}_{xz}^0 \\ -j\tilde{\tau}_{yz}^0 \\ \tilde{\sigma}_z^1 \\ j\tilde{\tau}_{xz}^1 \\ j\tilde{\tau}_{yz}^1 \end{bmatrix} = \begin{bmatrix} -T_{21}^{-1}T_{22} & T_{21}^{-1} \\ T_{12} - T_{11}T_{21}^{-1}T_{22} & T_{11}T_{21}^{-1} \end{bmatrix} \times \begin{bmatrix} \tilde{u}_z^0 \\ j\tilde{u}_x^0 \\ j\tilde{u}_y^0 \\ \tilde{u}_z^1 \\ j\tilde{u}_x^1 \\ j\tilde{u}_y^1 \end{bmatrix}. \tag{25}$$

Here, the stiffness matrix can be defined as follows:

$$[S] = \begin{bmatrix} -T_{21}^{-1}T_{22} & T_{21}^{-1} \\ T_{12} - T_{11}T_{21}^{-1}T_{22} & T_{11}T_{21}^{-1} \end{bmatrix} = \begin{bmatrix} [S_{11}] & [S_{12}] \\ [S_{21}] & [S_{22}] \end{bmatrix}. \tag{26}$$

Any two layers of structure, layer $i$ and layer $i$+1, are selected to obtain the global stiffness matrix of the multilayer pavement structure.

For layer $i$,

$$\begin{bmatrix} -\tilde{\sigma}_z^{i-1} \\ -j\tilde{\tau}_{xz}^{i-1} \\ -j\tilde{\tau}_{yz}^{i-1} \\ \tilde{\sigma}_z^i \\ j\tilde{\tau}_{xz}^i \\ j\tilde{\tau}_{yz}^i \end{bmatrix} = \begin{bmatrix} [S_{11}^i] & [S_{12}^i] \\ [S_{21}^i] & [S_{22}^i] \end{bmatrix} \times \begin{bmatrix} \tilde{u}_z^{i-1} \\ j\tilde{u}_x^{i-1} \\ j\tilde{u}_y^{i-1} \\ \tilde{u}_z^i \\ j\tilde{u}_x^i \\ j\tilde{u}_y^i \end{bmatrix}. \tag{27}$$

For layer $i$+1,

$$\begin{bmatrix} -\tilde{\sigma}_z^i \\ -j\tilde{\tau}_{xz}^i \\ -j\tilde{\tau}_{yz}^i \\ \tilde{\sigma}_z^{i+1} \\ j\tilde{\tau}_{xz}^{i+1} \\ j\tilde{\tau}_{yz}^{i+1} \end{bmatrix} = \begin{bmatrix} [S_{11}^{i+1}] & [S_{12}^{i+1}] \\ [S_{21}^{i+1}] & [S_{22}^{i+1}] \end{bmatrix} \times \begin{bmatrix} \tilde{u}_z^i \\ j\tilde{u}_x^i \\ j\tilde{u}_y^i \\ \tilde{u}_z^{i+1} \\ j\tilde{u}_x^{i+1} \\ j\tilde{u}_y^{i+1} \end{bmatrix}. \tag{28}$$

On the basis of the assumption that the layers are in complete contact with each other, combining **Eqs 27, 28**, we have

$$\begin{bmatrix} -\tilde{\sigma}_z^{i-1} \\ -j\tilde{\tau}_{xz}^{i-1} \\ -j\tilde{\tau}_{yz}^{i-1} \\ 0 \\ 0 \\ 0 \\ \tilde{\sigma}_z^{i+1} \\ j\tilde{\tau}_{xz}^{i+1} \\ j\tilde{\tau}_{yz}^{i+1} \end{bmatrix} = \begin{bmatrix} [S_{11}^i] & [S_{12}^i] & 0 \\ [S_{21}^i] & [S_{22}^i] + [S_{11}^{i+1}] & [S_{12}^{i+1}] \\ 0 & [S_{21}^{i+1}] & [S_{22}^{i+1}] \end{bmatrix} \times \begin{bmatrix} \tilde{u}_z^{i-1} \\ j\tilde{u}_x^{i-1} \\ j\tilde{u}_y^{i-1} \\ \tilde{u}_z^i \\ j\tilde{u}_x^i \\ j\tilde{u}_y^i \\ \tilde{u}_z^{i+1} \\ j\tilde{u}_x^{i+1} \\ j\tilde{u}_y^{i+1} \end{bmatrix}. \tag{29}$$

For the multilayer pavement system, the bottom layer is in complete contact with the rigid foundation bed. It thus can be regarded that the boundary condition at the bottom is zero for both stress and displacement. Therefore, the global stiffness matrix of the multilayer pavement system is given as follows:

$$\begin{bmatrix} f_1 \\ 0 \\ 0 \\ \vdots \\ 0 \\ f_{n+1} \end{bmatrix} = \begin{bmatrix} [S_{11}^1] & [S_{12}^1] & 0 & \cdots & 0 & 0 \\ [S_{21}^1] & [S_{22}^1 + S_{11}^2] & [S_{12}^2] & \cdots & 0 & 0 \\ 0 & [S_{21}^2] & [S_{22}^2 + S_{11}^3] & \cdots & 0 & 0 \\ \vdots & \vdots & \vdots & \ddots & \vdots & \vdots \\ 0 & 0 & 0 & \cdots & [S_{22}^{n-1} + S_{11}^n] & [S_{12}^n] \\ 0 & 0 & 0 & \cdots & [S_{21}^n] & [S_{22}^n] \end{bmatrix} \begin{bmatrix} d_1 \\ d_2 \\ d_3 \\ \vdots \\ d_n \\ d_{n+1} \end{bmatrix}, \tag{30}$$

where $f_1 = [\,-\tilde{\sigma}_z^0 \quad -i\tilde{\tau}_{xz}^0 \quad -i\tilde{\tau}_{yz}^0\,]^T$ and $d_i = [\,\tilde{u}_z^{i-1} \quad i\tilde{u}_x^{i-1} \quad i\tilde{u}_y^{i-1}\,]^T$.

## 2.4 Vibration Load

Generally speaking, load distribution at the bottom of the vibratory roller drum is not uniform. For the sake of simulating the response of asphalt pavement as realistic as possible, the contact force between the pavement and drum is simplified as a semi-ellipse model in this study (Herrera et al., 2018). In addition, it is assumed that the eccentric block in the roller drum rotates around the rotating shaft at a certain angular speed $\omega_0$, as shown in **Figure 1**.

Accordingly, description of the vibratory roller load can be simplified as follows:

$$P = G_r + p = G_r + \frac{2b}{L}\sqrt{\frac{L^2}{4} - (x - v_0 t)^2}\sin(\omega_0 t), \tag{31}$$

in which, $-\frac{L}{2} < x < \frac{L}{2}$; $-\frac{W}{2} < y < \frac{W}{2}$, $G_r$ is the roller gravity; $L$ and $W$ are widths along the $x$- and $y$-axes, respectively; $b$ is load amplitude; $v_0$ is the speed of the vibratory roller, and $\omega_0$ is the angular frequency.

In the practice of vibratory compaction, the moving speed of the roller is about 4.5 km/h, which can be neglected in the calculation and as such the exciting force is represented by (Bratu and Dobrescu, 2019)

$$p_c = \frac{2b}{L}\sqrt{\frac{L^2}{4} - x^2}\sin(\omega_0 t). \tag{32}$$

Thus, the vibratory roller load is further simplified as follows:

$$P_c = G_r + p_c = G + \frac{2b}{L}\sqrt{\frac{L^2}{4} - x^2}\sin(\omega_0 t). \tag{33}$$

# 3 MODEL VALIDATION AND CALIBRATION

## 3.1 Numerical Comparison

For validating the analytical solution, the finite element method (FEM) is used to calculate the response of the pavement under the same conditions. For a balance between computational cost and accuracy, a 3D pavement model with 1310576 nodes is established, and the DLOAD subroutine is applied to simulate the vibration load. The mesh and model geometrics are illustrated in **Figure 2**, and the structural parameters are listed in **Table 1**.

Comparison of solutions by the FEM and analytical method is presented in **Figure 3**. It can be seen that the displacement profiles in the $z$- and $x$-directions, as well as the peaks at the pavement midline obtained by the two methods, are consistent with each other. Furthermore, the spatial range of response to the vibration load is the same, between 15 m and 25 m. These agreements demonstrate the reliability and accuracy of the analytical method proposed in this article. Moreover, it should be pointed out that the FEM approach is highly time-consuming, which took over 2 hours in calculation in the present case. On the contrary, the developed analytical method only needed 143 s to obtain the solution in the frequency domain, and the inverse Fourier transform took another 5 s. Use of the analytical method enjoys a great advantage in computational efficiency while maintaining an equivalent accuracy.

## 3.2 Field Test and Calibration

In order to use the analytical method to analyze the dynamic response of asphalt mixture, the model parameters need to be calibrated by field test results because the modulus of loose asphalt mixture cannot be obtained during the rolling process. The pavement vibration rolling field test is performed on an asphalt bottom layer with a thickness of 8 cm in the Zheng–Xi Expressway in Guizhou Province, China. The asphalt mixture is a conventional AC-25 material. **Table 2** shows the structural and material parameters for the test pavement. The vibratory roller is Dynapac CC624HF with double drums of which the operating weight is 13,600 kg, and the static weight at the front drum is 6,000 kg, with the drum dimension 1,300 mm (diameter) × 2,130 mm (width). The loading frequency of the drum is

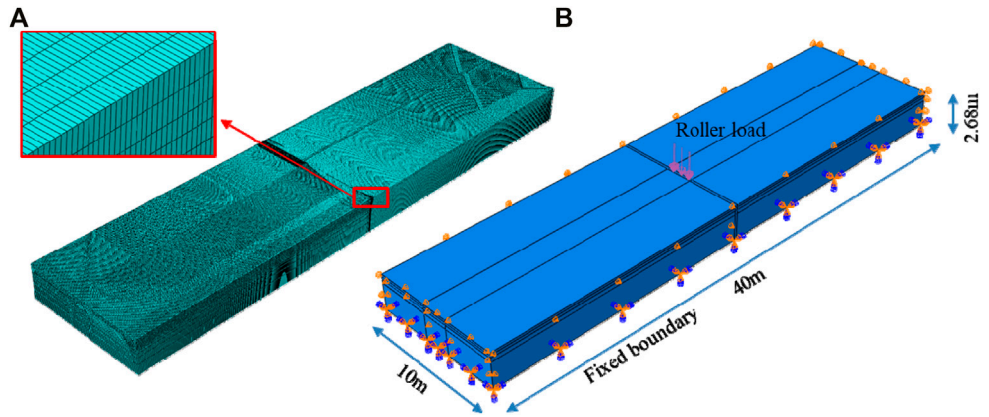


**FIGURE 2 |** FEM model: **(A)** meshing and **(B)** geometric and boundary conditions.

**TABLE 1 |** Structure and material information for the FEM model.

| Materials | Thickness (cm) | Modulus (MPa) | Poisson's ratio | Density (kg/m$^3$) |
|---|---|---|---|---|
| Asphalt mixture | 18 | 1,400 | .3 | 2,400 |
| Cement-stabilized macadam | 20 | 1,500 | .2 | 2,300 |
| Lime soil | 30 | 550 | .35 | 2,000 |
| Subgrade soil | 200 | 48 | .4 | 1,900 |

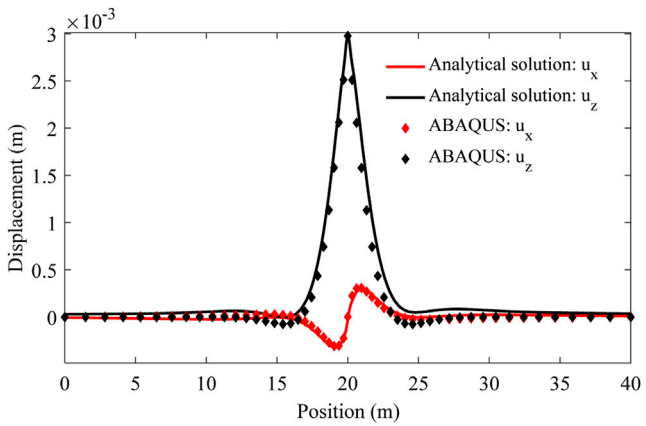


**FIGURE 3 |** Comparison between the FEM and analytical method.

51 Hz and excited force is about 166 kN. In the compaction process, the driving speed of the vibratory roller is 4.5 km/h.

During the vibration rolling process, SmartRock is placed in the mixture, and the field test data are collected *via* Bluetooth into a computer (Dan et al., 2020c). In the rolling direction, the data record area is selected approximately 25 m before and after the measuring point. After each rolling, a non-nuclear density meter is used to detect the compactness of the compacted mixture near the measuring point. In addition, to ensure the accuracy of the test, the roller moved at a constant speed when passing the observation point to mitigate the fluctuation of the signal. **Figure 4** outlines the field test setup, sensor installation, and rolling process.

However, there are many types of equipment (paver, vibration roller, rubber-tired roller, etc.) in the field, which leads to interfering signals collected by SmartRock in the field test data. Hence, the band-pass filtering program is utilized to handle this issue. The acceleration curve of asphalt mixture after filtering is shown in **Figure 5**. Based on the pavement parameters substituted into the analytical model, the relationship between the peak acceleration and modulus is shown in **Figure 6**. In addition, using the field data,

**TABLE 2 |** Structural and material information for the test pavement.

| Materials | Thickness (cm) | Modulus (MPa) | Poisson's ratio | Density (kg/m$^3$) |
|---|---|---|---|---|
| Asphalt mixture (bottom layer) | 8 | calibration | .3 | 2,635 |
| Cement-stabilized macadam | 26 | 3,500 | .2 | 2,600 |
| Graded aggregate | 16 | 550 | .35 | 2,550 |
| Subgrade soil | 100 | 48 | .4 | 1,850 |

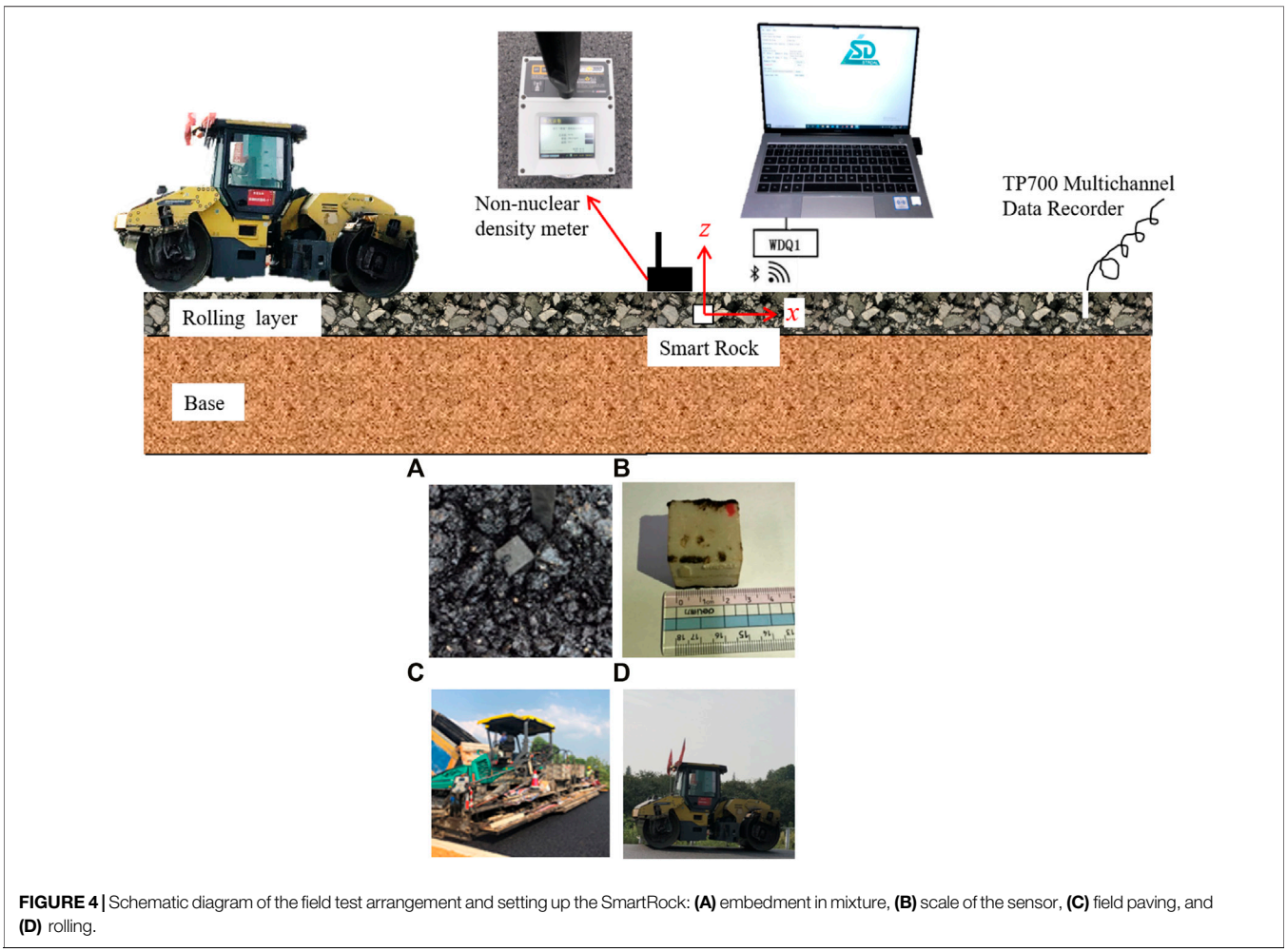


**FIGURE 4 |** Schematic diagram of the field test arrangement and setting up the SmartRock: **(A)** embedment in mixture, **(B)** scale of the sensor, **(C)** field paving, and **(D)** rolling.

the dynamic modulus of asphalt mixture is back-calculated as 99 and 2057 MPa for the first and last rolling, respectively.

The first rolling data of the field test are used to calibrate the model parameters in this study, and the calibrated acceleration is shown in **Figure 7**. The statistics criteria used in calibration are that the variance of acceleration in the $z$-direction reaches the minimum, and meanwhile, the root mean square error is minimized in all three directions between the calculated and measured accelerations. The comparison shows that the analytical solution agrees quite well with the field test data. The analytical solution captures the vibrations in acceleration over time. Also, the errors in fitting the peak values of all directions are minor, which are $9.5 \times 10^{-3}$ g, $2.26 \times 10^{-2}$ g, and $9 \times 10^{-4}$ g in the $z$-, $y$-, and $x$-directions, respectively.

# 4 ANALYSIS AND DISCUSSION

## 4.1 Vibration Displacement

It is well known that displacement is one of the noticeable dynamic responses of a pavement during the rolling process. Thus, a model is established to obtain the analytical solution of displacement for the structural and material parameters as shown earlier in **Table 2**.

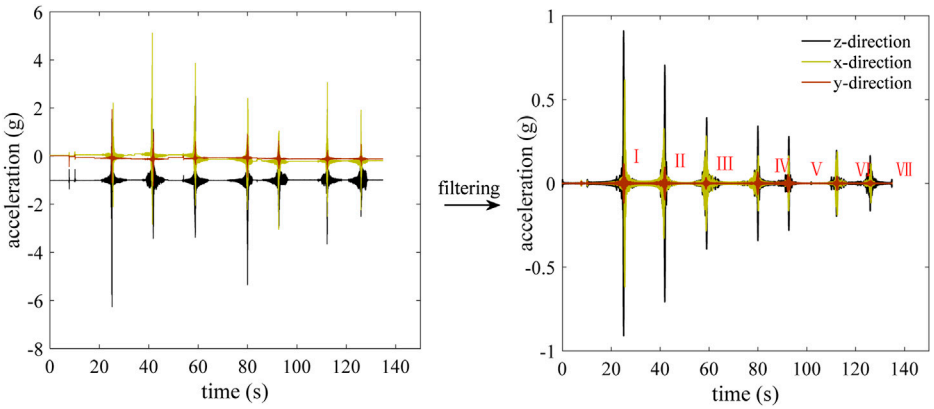


**FIGURE 5 |** Time histories of acceleration in the field test.

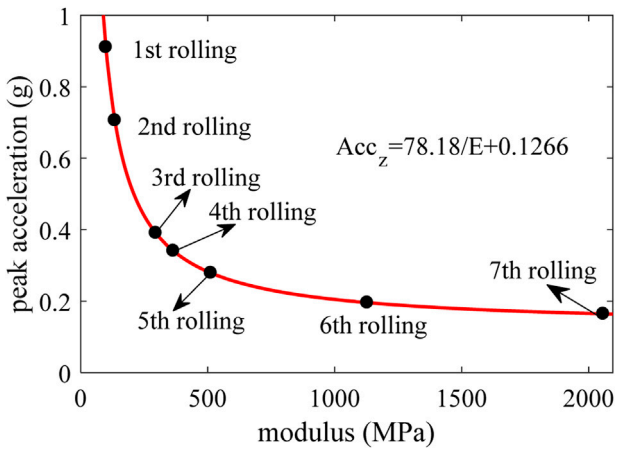


**FIGURE 6 |** Fitting curve of the relationship between peak acceleration and modulus.

**Figure 8A** presents the vertical displacement profiles of the pavement surface along the rolling and transverse directions. It can be seen in **Figure 8A** that the displacement is pronounced within the response range, and the displacement achieves the peak value at the loading point. The displacement beyond the load range vanishes rapidly.

**Figure 8B** shows *y*-axis displacement of the pavement surface, which is apparently different from vertical displacement. The displacement is zero at the load center and peaks immediately on the two sides with different signs, which agrees with the fact that asphalt mixture tends to move toward both sides of the contacting strip under rolling in the field. **Figure 8C** provides *x*-axis displacement of the pavement surface, which is generally similar with that in the *y*-direction.

During the rolling process, the dynamic response of the origin *O* changes with the moving roller. Based on the global stiffness matrix method, the displacement–time curves are obtained and shown in **Figure 9**.

Under the moving vibration load along the *x*-direction, the displacement of the observation point is shown in **Figures 9B–D** for the *z*-, *y*-, and *x*-directions. First, it can be found that the displacement of each direction vibrates along with the vibrating load. Then, in **Figure 9B**, it can be seen that $u_z$ increases slowly with the approaching load and achieves peak value when the load moves toward the center. Moreover, in **Figures 9C,D**, it can be observed that the response regulation of displacement in the *x*- and *y*-directions is different from vertical displacement. Both $u_y$ and $u_x$ increase initially and decrease to zero at the center, and the displacement is opposite when the load moves away.

Apparently, the vertical displacement $u_z$ is the largest and $u_y$ is the smallest. It shows that the internal response is concentrated on the *z*-direction mostly during the rolling process. At the same time, the force is the smallest in the *y*-direction, which leads to the smallest displacement.

## 4.2 Vibration Acceleration

In the field test, it is impossible to detect the real-time displacement in the rolling process, but the acceleration can be monitored by the sensor. Thus, the acceleration of the observation point is calculated by the model, which is shown in **Figure 10**.

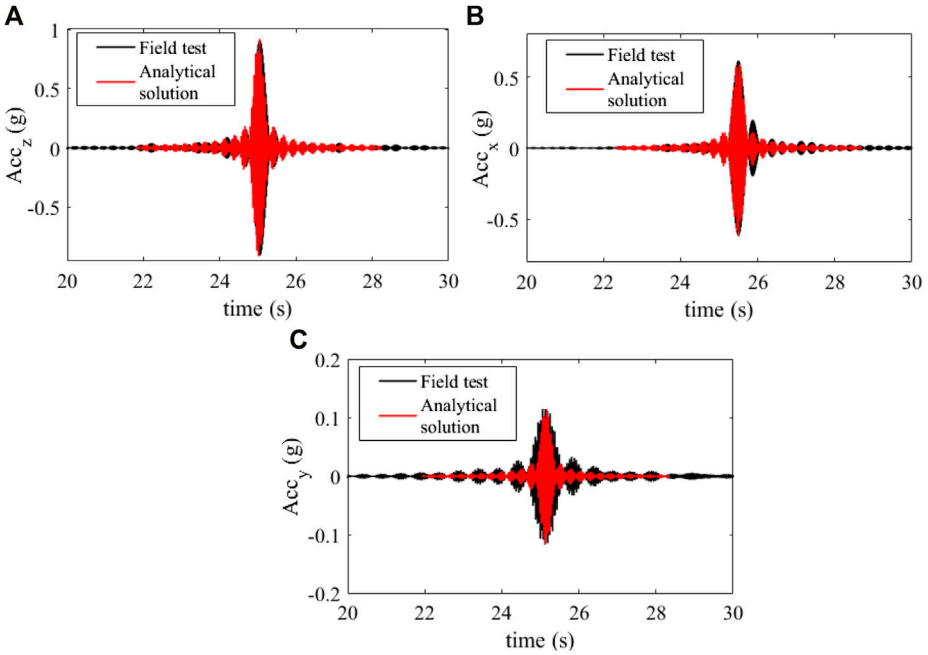


**FIGURE 7 |** Acceleration–time curve by calculation and test.

**Figure 10** shows the acceleration curves of observation point *O* in *z*-, *y*-, and *x*-directions. It can be seen from the figure that there are many similarities in the acceleration of the three directions. The accelerations vibrate with the high frequency of the vibration load, and they all show a trend of increasing gradually when the load approaches and gradually decrease when the load moves away from the observation point. In addition, by comparing the peak values of accelerations in three directions, it is found that the peak value of *z*-direction acceleration is the largest (about 0.6362 g), and that of the *y*-direction is the smallest (about 0.08243 g), about 13% of the peak value of *z*-direction.

Essentially, acceleration may be affected by many factors, including the thickness of the compacted materials. For example, the thickness of the asphalt pavement is commonly between 4 and 8 cm, **Figure 11** shows the relationship between thickness and acceleration, following a linear function, and the acceleration on the pavement surface rises when the thickness increases. It can be found that the acceleration in the *z*-direction increases from 0.1645 to 0.1797 g when the pavement thickness changes from 4 to 8 cm, respectively, and the increase percentage is about 9.2%.

## 4.3 Modulus of the Pavement

During the rolling process of asphalt mixture, the modulus of pavement varies dramatically with the increase of rolling times, and the internal response of SmartRock embedded in asphalt mixture in the field experiment also changes dramatically. For further exploring the relationship between the internal response of asphalt mixture and the increase of compaction times, the peak values of acceleration in three directions during each rolling in the field test results (**Figure 6**) are plotted as scatter plots, as shown in **Figure 12**.

It can be seen from **Figure 12A** that the peak acceleration decreases with the number of compaction times in general. The variation regulation of peak acceleration in the *z*- and *x*-directions is strongly correlated with the number of compaction times, and yet the peak acceleration in the *y*-direction is not. Generally, when the rolling times increase, the compactness of the mixture and, thus, its modulus gradually increase. Therefore, in order to analyze the influence of modulus on acceleration, the acceleration peak values in *z*- and *y*-directions are obtained by changing the material modulus parameters in the theoretical model, and the curve fitting is shown in **Figure 12B**. It can be understood from the figure that the peak accelerations in the *z*- and *x*-directions decrease sharply in the early stage with modulus. The reduction becomes gradual, and the accelerations tend to be stable with further modulus increase.

## 4.4 Pavement Compaction Degree

In general, during the rolling process, the density/compactness of the asphalt mixture also changes dramatically with the increase of compaction times. In the field test, the test points are marked after embedding SmartRock so that the non-nuclear densitometer is used to measure the density/compactness of the mixture in each pass.

**Figure 13A** demonstrates that the compactness of asphalt mixture gradually increases from 89.77% to 96.99%, with the increase of compaction times. After the asphalt mixture paved by the paver, the degree of compaction is 89.77%, when the asphalt mixture is in a relatively loose state. In early rolling, the degrees of compaction are 92.66% and 95.16% after the first and second rolling and the growth ratios are 3.2% and 2.7%, respectively. On

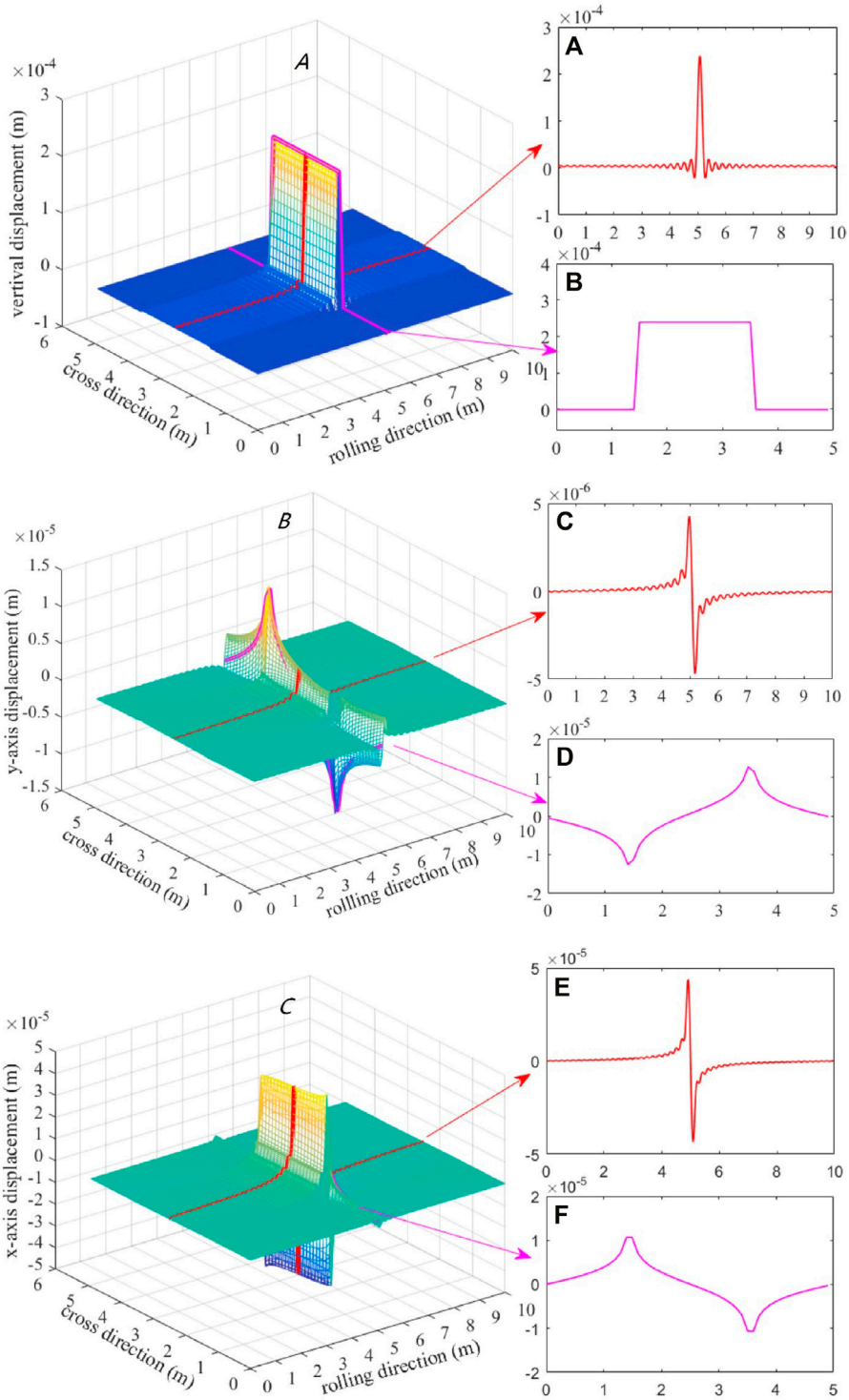


**FIGURE 8 |** Displacement profile in three directions, **(A)** vertical; **(B)** *y*-axis; and **(C)** *x*-axis.

the other hand, after the sixth and seventh rolling, the degrees of compaction are 97.19% and 96.99% and the increase percentages are 0.6% and −0.2%, respectively. Thus, the compaction degree increases rapidly initially and tends to be gentle subsequently, and the peak acceleration has the same variation regulation. Consequently, for further analyzing the influence of compactness on acceleration, the accelerations are calculated under different densities.

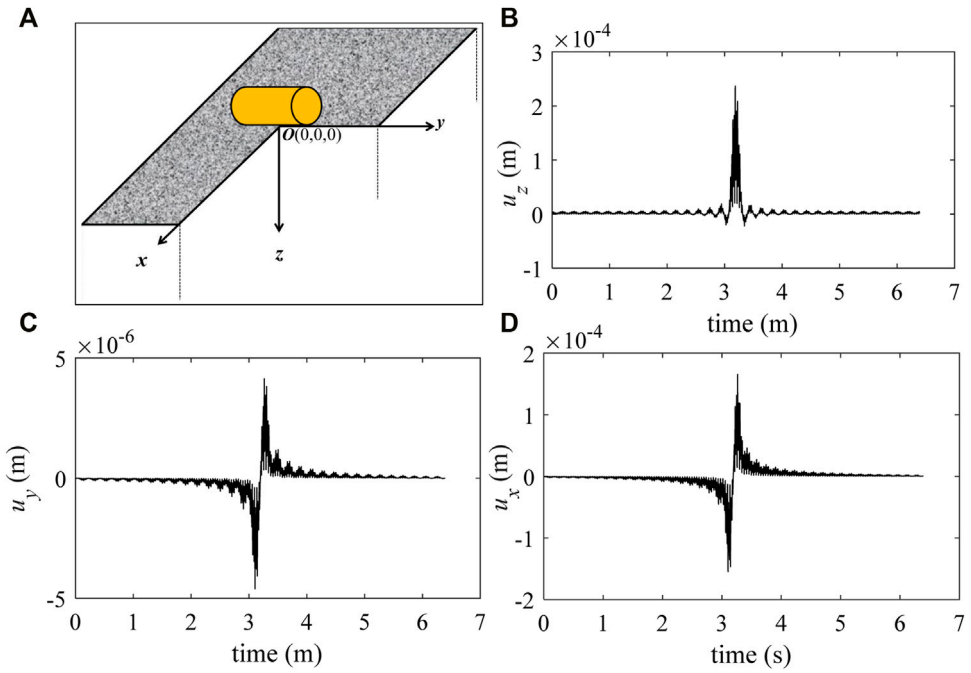


**FIGURE 9 |** The time histories of the displacement response at the origin.

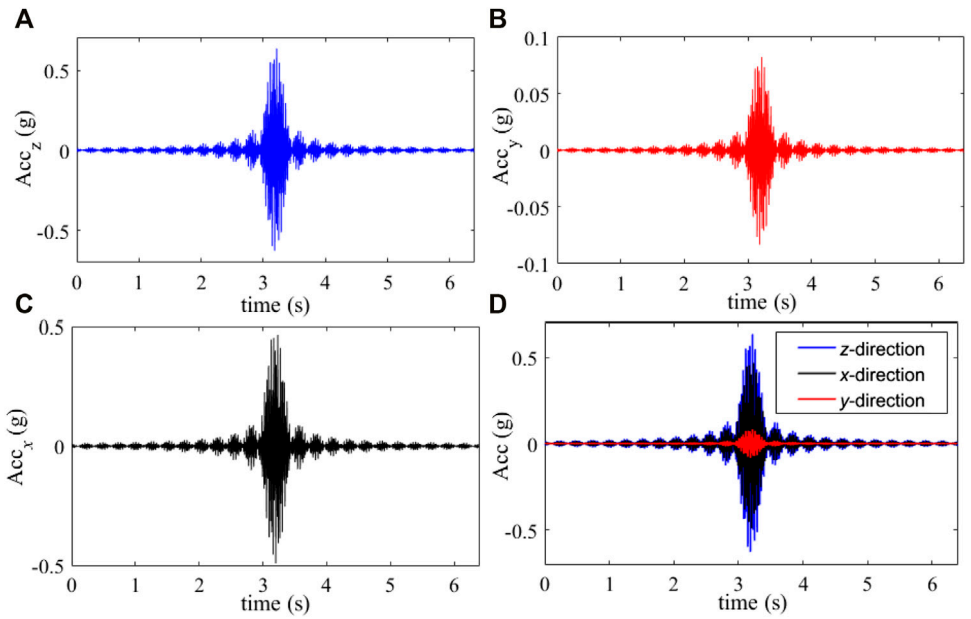


**FIGURE 10 |** Acceleration of point *O* in the rolling process.

It can be seen from **Figure 13B** that the accelerations in all directions are almost identical under different densities, which is inconsistent with the field test (**Figure 13A**) in which acceleration decreases with increase in density. Based on the governing equation, it can be revealed that there are only three polynomials containing density $\rho$ in the matrix $B$, that is, $\rho\xi^2$, $\frac{4G(\lambda+G)k^2}{\lambda+2G} + Gs^2 - \rho\xi^2$ and $\frac{4G(\lambda+G)s^2}{\lambda+2G} + Gk^2 - \rho\xi^2$, where $G$ is the shear modulus. Obviously, when only the density $\rho$ varies, $\Delta\rho$ is minor relative to the shear modulus $G$, and then $\Delta\rho$ is also very small for the matrix $B$, which leads to the calculated acceleration showing little variation. Hence, in the engineering practice, it can be concluded that although the density (degree of compaction)

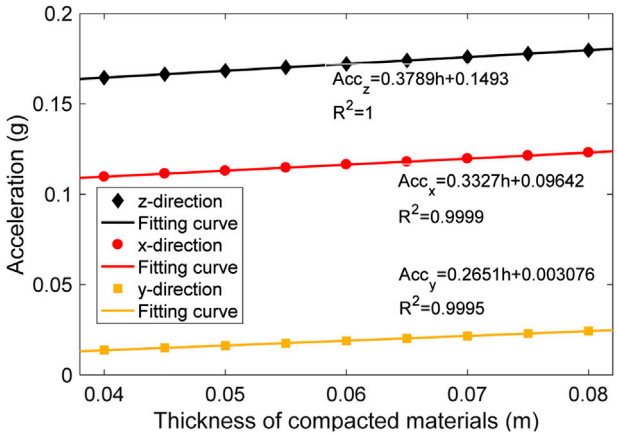


**FIGURE 11 |** Relationship between acceleration and thickness of compacted materials.

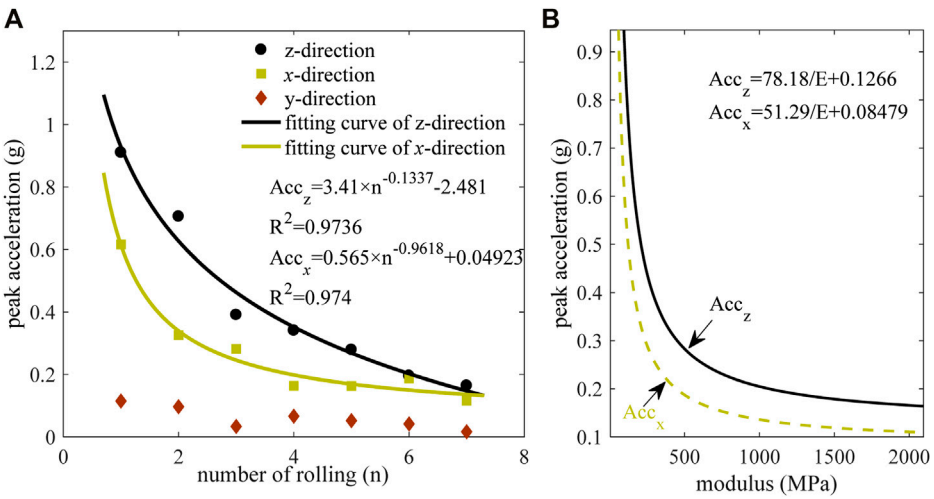


**FIGURE 12 | (A)** Peak value of acceleration; **(B)** relation curve between modulus and acceleration.

and modulus increase with the rolling times, the effect of modulus on acceleration is more obvious and prominent than that of density.

## 5 SUMMARY AND CONCLUSION

(1) In this study, investigations have been carried out to study the three-dimensional dynamic response of pavement under vibrating load. Based on the viscoelastic theory of the layered system and Fourier transform method, a set of differential governing equations of dynamic response is established under the vibration rolling load, which is simplified into a matrix form.

(2) Furthermore, the stiffness matrices of the multilayer system of asphalt pavement are derived, and the dynamic stiffness method is applied to solve the governing equation of the pavement structure under vibrating load. The proposed solution is validated by the FEM simulation and proven to be more efficient. Furthermore, the theoretical model is calibrated by the field test to determine the wave number and dynamic modulus during the vibration rolling process.

(3) The displacement always fluctuates under vibration loading with high frequency. The variation characteristics is that the displacement in *z*-direction increases sharply to a peak and then decreases sharply to zero, whereas the displacements in *x*- and *y*-directions rise to a peak value and then decrease to zero and subsequently increase reversely to a negative peak and then decrease to zero.

(4) For the vertical displacement, its distribution beneath the drum of the roller is almost even, except around the location of the drum edge, at which the displacement drops to zero sharply. For the displacements in the *x*- and *y*- directions, they reach the maximum not when the roller reaches the

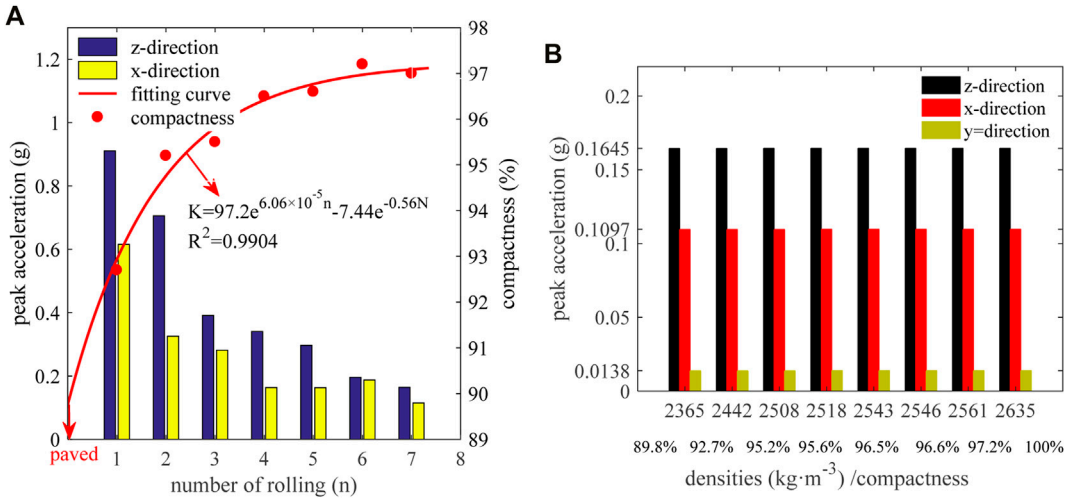


**FIGURE 13 | (A)** Compactness during the rolling process; **(B)** influence of density on acceleration.

observation point but at a certain distance from it. Overall, vertical displacement dominates the deformation under vibration loading.

(5) The acceleration of the observation point has noticeable vibration state as the displacement, and the accelerations in the three directions gradually increase when the load approaches and gradually decrease when the load moves away. In addition, it can be found that the responses of peak acceleration in *z*- and *x*- directions are obviously dominant compared to those in the *y*- direction.

(6) Combined with the field test and the calculation results of the theoretical model in this study, it is found that the peak accelerations in *z*- and *x*-directions decrease and are correlated well with the modulus, while the peak acceleration in *y*-direction does not show a clear trend. In addition, although the density (degree of compaction) and modulus increase with the rolling times, the effect of modulus on acceleration is more obvious and prominent than that of density.

## DATA AVAILABILITY STATEMENT

The original contributions presented in the study are included in the article/Supplementary Material; further inquiries can be directed to the corresponding authors.

## AUTHOR CONTRIBUTIONS

H-YS: conceptualization, methodology, investigation, and writing—original draft preparation; H-CD: conceptualization, methodology, investigation, writing—review and editing, and funding acquisition; S-PW: methodology and writing—original draft preparation; XL: methodology, investigation, and writing—review and editing; HW: writing—review and editing, supervision, and resources.

## FUNDING

This work was partially funded by the Natural Science Foundation of Hunan Province (CN) (Grant No. 2020JJ4702), the Jiangxi Transportation Science and Technology Foundation (CN) (Grant No. 2020H0028), and the Guizhou Transportation Science and Technology Foundation (CN) (Grant No. 2019-122-006).

## ACKNOWLEDGMENTS

The authors especially appreciate Zhonghai Construction Co., Ltd. for assistance in the field test.

## REFERENCES

Beskou, N. D., Hatzigeorgiou, G. D., and Theodorakopoulos, D. D. (2016). Dynamic Inelastic Analysis of 3-D Flexible Pavements under Moving Vehicles: A Unified FEM Treatment. *Soil Dyn. Earthquake Eng.* 90, 420–431. doi:10.1016/j.soildyn.2016.09.018

Bierer, T., and Bode, C. (2007). A Semi-analytical Model in Time Domain for Moving Loads. *Soil Dyn. Earthquake Eng.* 27 (12), 1073–1081. doi:10.1016/j.soildyn.2007.03.008

Bratu, P., and Dobrescu, C. (2019). Dynamic Response of Zener-Modelled Linearly Viscoelastic Systems under Harmonic Excitation. *Symmetry* 11 (8), 1050. doi:10.3390/sym11081050

Chen, J., Huang, B., Shu, X., and Hu, C. (2015). DEM Simulation of Laboratory Compaction of Asphalt Mixtures Using an Open Source Code. *J. Mater. Civ. Eng.* 27 (3), 04014130. doi:10.1061/(asce)mt.1943-5533.0001069

Chen, X., Zhang, J., and Wang, X. (2015). Full-scale Field Testing on a Highway Composite Pavement Dynamic Responses. *Transportation Geotechnics* 4, 13–27. doi:10.1016/j.trgeo.2015.05.002

Coleri, E., Harvey, J. T., Yang, K., and Boone, J. M. (2012). A Micromechanical Approach to Investigate Asphalt concrete Rutting Mechanisms. *Construction Building Mater.* 30, 36–49. doi:10.1016/j.conbuildmat.2011.11.041

Dan, H.-C., He, L.-H., Zhao, L.-H., and Chen, J.-Q. (2015). Coupled Hydro-Mechanical Response of Saturated Asphalt Pavement under Moving Traffic Load. *Int. J. Pavement Eng.* 16 (2), 125–143. doi:10.1080/10298436.2014.937712

Dan, H.-C., Zeng, H.-F., Zhu, Z.-H., Bai, G.-W., and Cao, W. (2022). Methodology for Interactive Labeling of Patched Asphalt Pavement Images Based on U-Net Convolutional Neural Network. *Sustainability* 14, 861. doi:10.3390/su14020861

Dan, H.-C., Yang, D., Liu, X., Peng, A.-P., and Zhang, Z. (2020). Experimental Investigation on Dynamic Response of Asphalt Pavement Using SmartRock Sensor under Vibrating Compaction Loading. *Construction Building Mater.* 247, 118592. doi:10.1016/j.conbuildmat.2020.118592

Dan, H.-C., Yang, D., Zhao, L.-H., Wang, S.-P., and Zhang, Z. (2020). Meso-scale Study on Compaction Characteristics of Asphalt Mixtures in Superpave Gyratory Compaction Using SmartRock Sensors. *Construction Building Mater.* 262, 120874. doi:10.1016/j.conbuildmat.2020.120874

Dan, H. C., He, L. H., and Zhao, L. H. (2020). Experimental Investigation on the Resilient Response of Unbound Graded Aggregate Materials by Using Large-Scale Dynamic Triaxial Tests. *Road Mater. Pavement Des.* 21 (2), 434–451. doi:10.1080/14680629.2018.1500300

Dong, Z., and Ma, X. (2018). Analytical Solutions of Asphalt Pavement Responses under Moving Loads with Arbitrary Non-uniform Tire Contact Pressure and Irregular Tire Imprint. *Road Mater. Pavement Des.* 19 (8), 1887–1903. doi:10.1080/14680629.2017.1354776

Dong, Z., Tan, Y., Cao, L., and Li, S. (2012). Rutting Mechanism Analysis of Heavy-Duty Asphalt Pavement Based on Pavement Survey, Finite Element Simulation, and Instrumentation. *J. Test. Eval.* 40 (7), 1228–1237. doi:10.1520/jte20120162

Fares, B., Sesh, C., and Musharraf, Z. (2014). Dynamical Response of Vibratory Rollers during the Compaction of Asphalt Pavements. *J. Eng. Mech.* 140 (7), 04014039. doi:10.1061/(asce)em.1943-7889.0000730

Grundmann, H., Lieb, M., and Trommer, E. (1999). The Response of a Layered Half-Space to Traffic Loads Moving along its Surface. *Archive Appl. Mech. (Ingenieur Archiv)* 69 (1), 55–67. doi:10.1007/s004190050204

Herrera, C., Alves Costa, P., and Caicedo, B. (2018). Numerical Modelling and Inverse Analysis of Continuous Compaction Control. *Transportation Geotechnics* 17, 165–177. doi:10.1016/j.trgeo.2018.09.012

Hosseini, A., Faheem, A., Titi, H., and Schwandt, S. (2020). Evaluation of the Long-Term Performance of Flexible Pavements with Respect to Production and Construction Quality Control Indicators. *Construction Building Mater.* 230, 116998. doi:10.1016/j.conbuildmat.2019.116998

Jia, T., He, T., Qian, Z., Lv, J., and Cao, K. (2019). An Improved Low-Cost Continuous Compaction Detection Method for the Construction of Asphalt Pavement. *Adv. Civil Eng.* 2019, 1–11. doi:10.1155/2019/4528230

Jing, C., Zhang, J., and Song, B. (2020). An Innovative Evaluation Method for Performance of In-Service Asphalt Pavement with Semi-rigid Base. *Construction Building Mater.* 235, 117376. doi:10.1016/j.conbuildmat.2019.117376

Lefeuvemesgouez, G., and Mesgouez, A. (2008). Ground Vibration Due to a High-Speed Moving Harmonic Rectangular Load on a Poroviscoelastic Half-Space. *Int. J. Sol. Struct.* 45 (11), 3353–3374. doi:10.1016/j.ijsolstr.2008.01.026

Li, H., Wang, G., Qin, L., Wang, Q., and Wang, X. (2020). A Spectral Analysis of the Dynamic Frequency Characteristics of Asphalt Pavement under Live Vehicle Loading. *Road Mater. Pavement Des.* 21 (2), 486–499. doi:10.1080/14680629.2018.1506815

Li, S., Yang, S., Chen, L., and Lu, Y. (2012). Effects of Parameters on Dynamic Responses for a Heavy Vehicle-Pavement-Foundation Coupled System. *Ijhvs* 19 (2), 207–224. doi:10.1504/ijhvs.2012.046835

Liu, K., Xu, P., Wang, F., You, L., Zhang, X., and Fu, C. (2022). Assessment of Automatic Induction Self-Healing Treatment Applied to Steel Deck Asphalt Pavement. *Automation in Construction* 133, 104011. doi:10.1016/j.autcon.2021.104011 Accepted in 10 October 2021

Liu, W., Gong, X., Gao, Y., and Li, L. (2019). Microscopic Characteristics of Field Compaction of Asphalt Mixture Using Discrete Element Method. *J. Test. Eval.* 47 (6), 4579–4594. doi:10.1520/jte20180633

Liu, X., Li, Y., Lin, Y., and Banerjee, J. R. (2021). Spectral Dynamic Stiffness Theory for Free Vibration Analysis of Plate Structures Stiffened by Beams with Arbitrary Cross-Sections. *Thin-Walled Structures* 160, 107391. doi:10.1016/j.tws.2020.107391

Liu, X., Zhao, X., Adhikari, S., and Liu, X. (2021). Stochastic Dynamic Stiffness for Damped Taut Membranes. *Comput. Structures* 248, 106483. doi:10.1016/j.compstruc.2021.106483

Lu, J.-F., and Jeng, D.-S. (2007). A Half-Space Saturated Poro-Elastic Medium Subjected to a Moving point Load. *Int. J. Sol. Structures* 44 (2), 573–586. doi:10.1016/j.ijsolstr.2006.05.020

Lv, Z., Qian, J. G., Shi, Z. H., and Gao, Q. (2020). Dynamic Responses of Layered Poroelastic Ground under Moving Traffic Loads Considering Effects of Pavement Roughness. *Soil Dyn. Earthq. Eng.* 130, 105996. doi:10.1016/j.soildyn.2019.105996

Paulmichl, I., Adam, C., and Adam, D. (2020). Parametric Study of the Compaction Effect and the Response of an Oscillation Roller. *Proc. Inst. Civil Eng. - Geotechnical Eng.* 173 (4), 285–301. doi:10.1680/jgeen.19.00209

Qian, G., Hu, K., Li, J., Bai, X., and Li, N. (2020). Compaction Process Tracking for Asphalt Mixture Using Discrete Element Method. *Construction Building Mater.* 235, 117478. doi:10.1016/j.conbuildmat.2019.117478

Roozbahany, E. G., and Partl, M. N. (2019). Investigation of Asphalt Joint Compaction Using Discrete Element Simulation. *Road Mater. Pavement Des.* 20 (7), 1722–1734. doi:10.1080/14680629.2019.1594055

Shan, J., Shao, H., Li, Q., and Sun, P. (2019). Comparison of Real Response and Theoretical Modeling of Pavement with Thick Asphalt Layers under Heavy Traffic Load. *Adv. Civil Eng.* 2019 (2), 1–11. doi:10.1155/2019/8097890

Si, C., Zhou, X., You, Z., He, Y., Chen, E., and Zhang, R. (2019). Micro-mechanical Analysis of High Modulus Asphalt concrete Pavement. *Construction Building Mater.* 220, 128–141. doi:10.1016/j.conbuildmat.2019.06.019

Souza, F. V., and Castro, L. S. (2012). Effect of Temperature on the Mechanical Response of Thermo-Viscoelastic Asphalt Pavements. *Construction Building Mater.* 30, 574–582. doi:10.1016/j.conbuildmat.2011.11.048

Wang, H., Zhang, Q., and Tan, J. (2009). Investigation of Layer Contributions to Asphalt Pavement Rutting. *J. Mater. Civ. Eng.* 21 (4), 181–185. doi:10.1061/(asce)0899-1561(2009)21:4(181)

Wang, S.-P., Dan, H.-C., Li, L., Liu, X., and Zhang, Z. (2021). Dynamic Response of Asphalt Pavement under Vibration Rolling Load: Theory and Calibration. *Soil Dyn. Earthquake Eng.* 143, 106633. doi:10.1016/j.soildyn.2021.106633

Wu, H., Li, P., Nian, T., Zhang, G., He, T., and Wei, X. (2019). Evaluation of Asphalt and Asphalt Mixtures' Water Stability Method under Multiple Freeze-Thaw Cycles. *Construction Building Mater.* 228, 117089. doi:10.1016/j.conbuildmat.2019.117089

Xu, B., Lu, J.-F., and Wang, J.-H. (2008). Dynamic Response of a Layered Water-Saturated Half Space to a Moving Load. *Comput. Geotechnics* 35 (1), 1–10. doi:10.1016/j.compgeo.2007.03.005

Xu, Q., and Chang, G. K. (2016). Adaptive Quality Control and Acceptance of Pavement Material Density for Intelligent Road Construction. *Automation in Construction* 62, 78–88. doi:10.1016/j.autcon.2015.11.004

Zhan, Y., Yao, H., and Lu, Z. (2018). Dynamic Response of the 3D Pavement-Transversely Isotropic Poroelastic Ground System to a Rectangular Moving Load. *Soil Dyn. Earthquake Eng.* 115, 394–401. doi:10.1016/j.soildyn.2018.06.037

Zhao, J., and Wang, H. (2020). Dynamic Pavement Response Analysis under Moving Truck Loads with Random Amplitudes. *J. Transp. Eng. Part. B: Pavements* 146 (2), 04020020. doi:10.1061/jpeodx.0000173

Zhenning, B. A., Liang, J., Lee, V. W., and Ji, H. (2016). 3D Dynamic Response of a Multi-Layered Transversely Isotropic Half-Space Subjected to a Moving point Load along a Horizontal Straight Line with Constant Speed. *Int. J. Sol. Struct.* 100, 427–445. doi:10.1016/j.ijsolstr.2016.09.016

**Conflict of Interest:** Author H-YS was employed by Power China Guiyang Engineering Corporation Limited.

The remaining authors declare that the research was conducted in the absence of any commercial or financial relationships that could be construed as a potential conflict of interest.

frontiers in Materials

ORIGINAL RESEARCH
published: 21 February 2022
doi: 10.3389/fmats.2022.816247

# Matching the Color Difference Between Asphalt Mixture and Cement Grouting Paste Used in Semi-flexible Pavement

*Deng Haibin*[1], *Wang Shungui*[2], *Liu Yingchen*[1], *Du Yinfei*[2]* *and Wei Tangzhong*[3]

[1]Highway and Transportation Administration Center of Huzhou, Huzhou, China, [2]School of Civil Engineering, Central South University, Changsha, China, [3]Nanjing Xingyou Transportation Technology Co., Ltd., Nanjing, China

In order to match the color difference between black asphalt mixture and light-colored cement grouting paste in semiflexible pavement, carbon black (CB) with four mass ratios (i.e., 2, 4, 6, and 8%) was incorporated into a rapid-hardening cement grouting paste. The fluidity, color difference, spectrum reflectance, thermal conductivity, and flexural and compressive strength of the aforementioned cement pastes were experimentally investigated. The results show that the mass ratios of the component in cement paste could ensure the good fluidity of cement grouting paste. Three parameters such as thermal conductivity, flexural strength, and compressive strength all reduced, compared with control paste. However, the compressive strength of the 8% CB paste was still much higher than that of the asphalt mixture. According to the color difference results, CB significantly improved the black color of cement paste, of which the black color of the asphalt mixture was between that of 6 and 8% CB cement paste. Besides, the spectrum reflectance of all the pastes reduced, especially the average reflectance of 2% CB cement paste was 51.7% lower than that of control paste. The findings in this study are expected to help design more advanced cement grouting materials to improve the optical and mechanical performances of semiflexible asphalt pavement.

**Keywords: cement grouting paste, carbon black, color difference, thermal conductivity, strength**

OPEN ACCESS

***Edited by:***
*Weina Meng,*
*Stevens Institute of Technology, United States*

***Reviewed by:***
*Wenke Huang,*
*Guangzhou University, China*
*Peiwen Hao,*
*Chang'an University, China*

***Correspondence:**
*Du Yinfei*
*yfdu_csu@csu.edu.cn*

***Specialty section:***
*This article was submitted to Structural Materials, a section of the journal Frontiers in Materials*

***Received:*** *16 November 2021*
***Accepted:*** *06 January 2022*
***Published:*** *21 February 2022*

***Citation:***
*Haibin D, Shungui W, Yingchen L, Yinfei D and Tangzhong W (2022) Matching the Color Difference Between Asphalt Mixture and Cement Grouting Paste Used in Semi-flexible Pavement. Front. Mater. 9:816247. doi: 10.3389/fmats.2022.816247*

## 1 INTRODUCTION

Asphalt pavement is the most used pavement type because of its high driving comfort, easy maintenance, low cost, and so on. In summer, the maximum temperature of asphalt pavement can reach up to 60–70°C because of its low solar reflectance (generally lower than 0.1) (Santamouris, 2013; Qin, 2015). The temperature-sensitive asphalt mixture will generate permanent deformation or rutting, which is one of the two most serious pavement distresses (Du et al., 2018). The rutting distress is generally solved by improving the high-temperature performance of the asphalt mixture, including applying high modulus asphalt (Zou et al., 2015) and optimizing aggregate gradation (Aragão et al., 2016). Optimizing the asphalt pavement structure was also proved to be able to reduce rutting depth (Lee et al., 2015).

A novel composite pavement which is paved using a semiflexible mixture was proved to have a rather high ability to resist rutting, compared to conventional hot mix asphalt (Cai et al., 2017; Gong et al., 2019; Hassani et al., 2020; Luo et al., 2020). This kind of mixture usually uses a porous asphalt mixture (air voids content of over 20%) as a flexible aggregate skeleton to carry rigid cement paste or

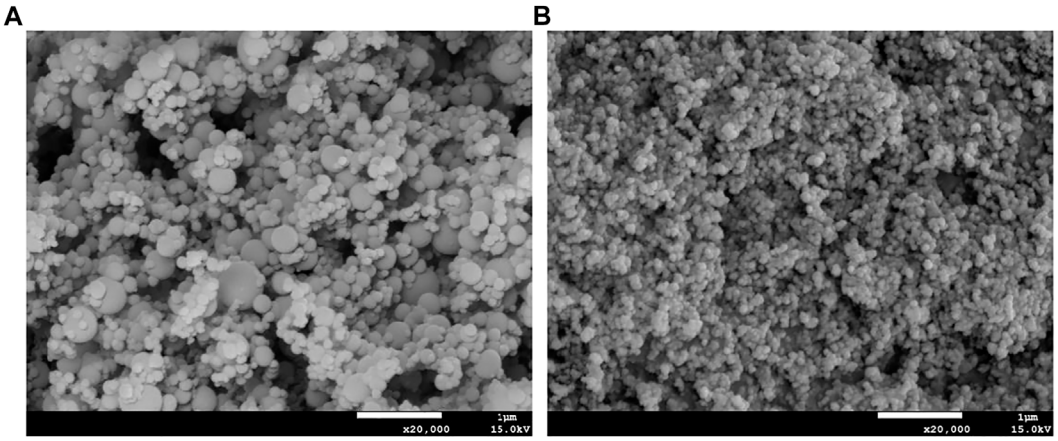


**FIGURE 1 |** SEM image of **(A)** silica fume and **(B)** CB.

mortar (Fang et al., 2016; Pei et al., 2016; Zhang et al., 2016; Wang et al., 2018). However, these published works usually used ordinary Portland cement as a binder to prepare light-colored grouting material, which resulted in the following two deficiencies: first, the resultant semiflexible pavement needs a very long curing period before it opens to traffic (Chen et al., 2020), second, the color inconsistence between the light-colored grouting material and black asphalt mixture led to the very poor appearance of the pavement surface (An et al., 2018).

To this end, this work aims at preparing a special kind of cement grouting paste, which is featured of black color and rapid hardening. Additionally, the cement paste should also have a high flow degree, which allows the cement paste to be easily grouted in the porous asphalt mixture. For this purpose, four mass contents of carbon black (CB) are blended with a kind of rapid-hardening cement. To achieve an equivalent color with the asphalt mixture, the color of the cement paste with different contents of CB was measured using a color-difference meter. Due to the color change, the spectrum reflectance of cement paste was then evaluated. The thermal properties of cement paste were evaluated by an indicator of thermal conductivity. Compressive and flexural strength tests of the paste at different curing ages were performed to investigate the influence of CB addition.

## 2 MATERIALS AND TEST METHODS

### 2.1 Materials

A kind of rapid-hardening cement was used as a binder to prepare cement grouting paste. This cement could increase the early-age strength of cement grouting paste and then rapidly open to traffic. The water-reducing agent β -naphthalene sulfonic acid was used to increase the workability of the composite. Tributyl phosphate defoamer was used to decrease the number of air bubbles. In total, four contents of CB (2–8 wt% of cement (Li et al., 2008)) were used as a functional filler to change the color and thermal property of the grouting material. The scanning electron microscope (SEM) images of silica fume and CB were compared, as shown in **Figure 1**. It can be found that the used CB had smaller particle sizes than silica fume. Additionally, the micromorphology of CB was similar to that of silica fume.

**TABLE 1 |** Mass ratios of the component in cement paste (wt%).

| Cement | Water | Silica fume | Water-reducing agent | Defoamer | CB |
|---|---|---|---|---|---|
| 100 | 40 | 10 | 1.5 | 0.2 | 2 |
| | 43 | | 1.8 | | 4 |
| | 48 | | 2.2 | | 6 |
| | 53 | | 2.5 | | 8 |

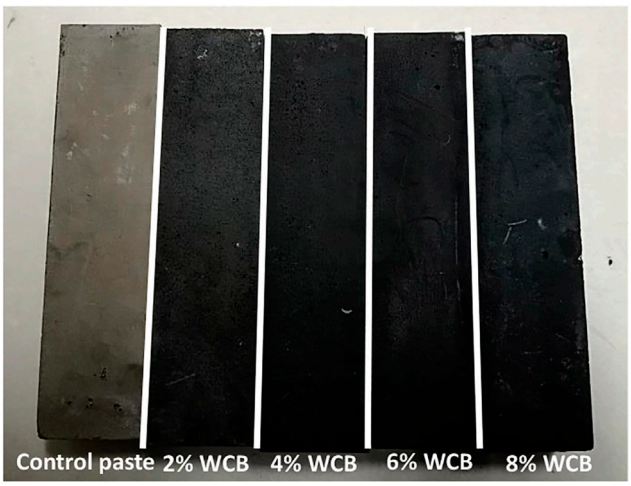


**FIGURE 2 |** Prepared cement paste specimens.

### 2.2 Preparation of Cement Grouting Paste

The detailed component proportions of cement paste are shown in **Table 1**.

CB and other additives were first added into cement and mixed together in a dry state for 2 min, and then water was added

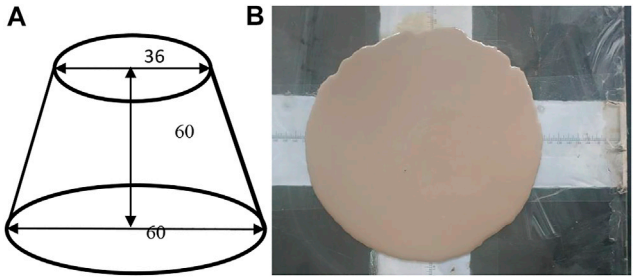


**FIGURE 3 |** Illustration of fluidity test. **(A)** Paste cone and **(B)** example of fluidity recording.

to the dry mix. The total mixing time was kept at 5 min to ensure homogenous mixing. The paste was casted into a prismatic mold (size of 40 mm × 40 mm × 160 mm) and vibrated to prepare the cement paste specimen, as shown in **Figure 2**. After 2 h, the specimen was demolded and ready to cure in the standard curing conditions (temperature of 20°C and humidity of more than 90%). For each kind of component proportion, three specimens were prepared as a group for the same experiment.

## 2.3 Test Methods

### 2.3.1 Fluidity Test

The just-mixed paste was first casted into a cone as shown in **Figure 3A**. The redundant paste was craped to ensure the cone was filled up with paste, and then the cone was placed onto a glass board and lifted vertically to allow the paste to flow freely for 30 s (**Figure 3B**). The averaged diameter was referred to as the measured fluidity.

### 2.3.2 Scanning Electron Microscope (SEM) Test

An SEM (Quanta 200, FEI Co. Ltd., America) was used to characterize the microscope images of the control, 2, 4, and 6% CB cement pastes. The broken paste samples were immersed into ethyl alcohol to prevent the hydration process. The samples were then sprayed with gold. In order to obtain clear SEM images, the voltage was maintained at 20.00 kV. All the images were magnified by 10,000 times.

### 2.3.3 Color-Difference Test

The color of each paste sample (at the age of 7 days) was measured using a potable color-difference meter (NR20XE, 3nh Technology Co., Ltd. of Shenzhen, China). The color could be described by three parameters of L*, a*, and b*. Specifically, L* represented the lightness. The negative value of L* means that the color was more like black. a* represented the degree of redness (-a* greenness) and b* of yellowness (-b* blueness). A reference plate that had known absolute color values was introduced to compare the color of the cement paste. The relative color values (i.e., ΔL, Δa, and Δb) could be automatically obtained (Zhang et al., 2018).

### 2.3.4 Thermal Conductivity Test

A thermal conductivity meter (DRE-2C, Xiangtan Instruments and Meters, China), which is based on the transient plane heat source method, was used to measure the thermal conductivity of the CSA paste. The fractured specimens after the flexural strength test were cut into small pieces (thickness of about 5 cm) with smooth surfaces. A test probe was sandwiched between two sample pieces.

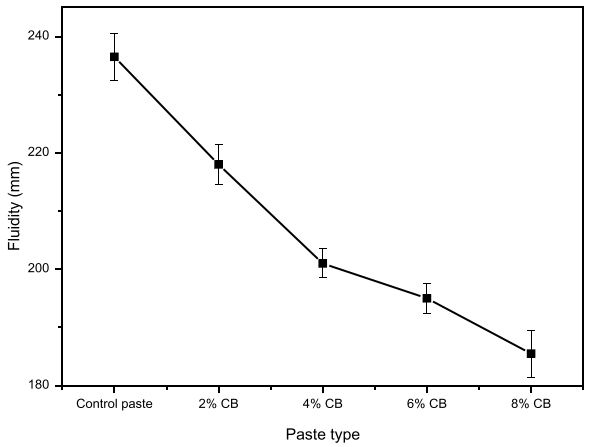


**FIGURE 4 |** Fluidity results of cement paste.

### 2.3.5 Spectrum Reflectance Test

The fractured prismatic cement paste specimens were cut into small samples with a thickness of less than 2 cm. A UV–VIS–NIR spectrophotometer (Cary 5,000, Agilent Technologies (Malaysia) Company) was used to measure the global (direct + diffuse) spectrum reflectance in the range of 190–2,500 nm. The samples were clamped in the integrating sphere to receive light radiation. The specific solar reflectance in the UV–VIS–NIR band was computed in accordance with the ASTM Standard G173-03 (ASTM, 2012).

### 2.3.6 Mechanical Performance Test

The three prismatic samples (size of 40 mm × 40 mm × 160 mm) of each kind of paste were used for the flexural strength test after having been cured for 4 h, 1, 3, and 7 days. The fractured samples were then cut into cubic samples with smooth surfaces for the compressive strength test. The aforementioned two mechanical tests were performed in accordance with the Chinese national standard method T 0506-2005 in JTG E30-2005.

# 3 RESULTS AND DISCUSSION

## 3.1 Fluidity

The fluidity results of different cement pastes are shown in **Figure 4**. It can be found that the fluidity basically reduced with the increase of the CB content. When 8% CB was added in the cement paste, the fluidity was only about 21% of that of control paste. The result indicates that the influence of CB addition on paste fluidity should be carefully considered in order to easily grout cement paste into a porous asphalt mixture, and the mass ratios of the component in cement

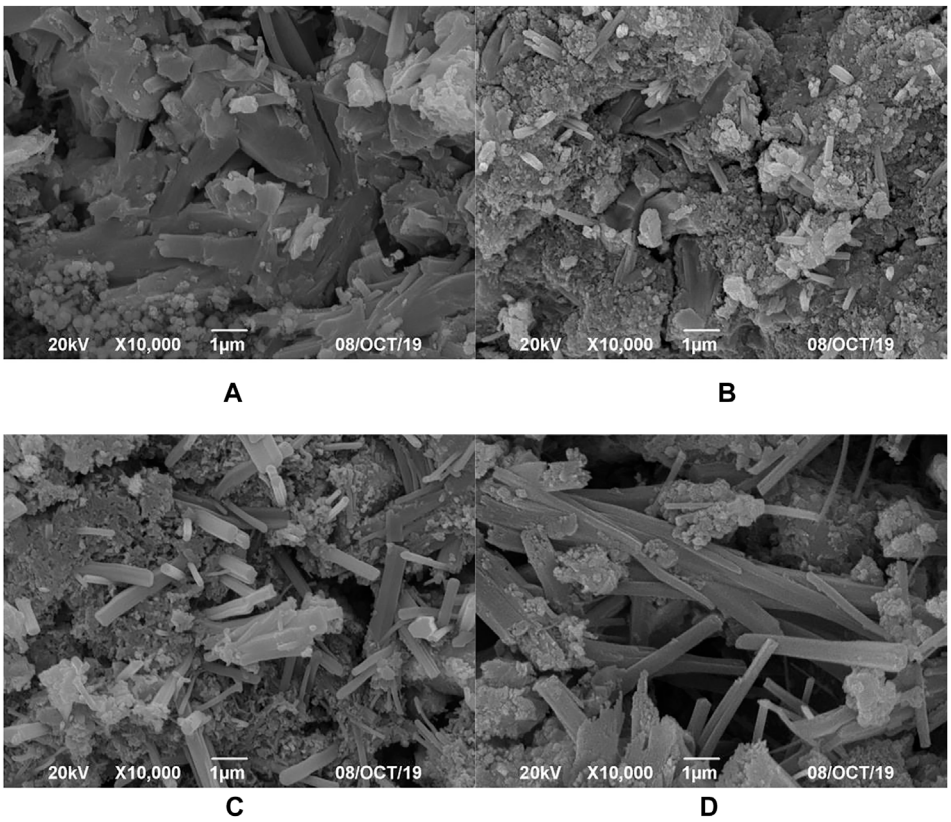


**FIGURE 5 |** SEM images of cement paste. **(A)** Control paste, **(B)** 2% CB, **(C)** 4% CB, and **(D)** 6% CB.

paste shown in **Table 1** could be optimized to have a desirable fluidity for cement pastes with different CB additions. In future studies, the appropriate CB content should be determined by observing the paste distribution in a porous asphalt mixture.

## 3.2 Microstructure

In order to illustrate the influence of CB addition on the microstructure of cement paste, the SEM images (×10,000) of control paste, 2, 4, and 6% CB are presented, as shown in **Figure 5**.

Obviously, the microstructure of control paste looked much denser than those of other pastes. The hydration products connected with each other to form a relatively stable microstructure. The silica fume filled into the micro-voids, which would reduce the micro–air voids, thus increasing the strength of control paste. The addition of CB changed the hydration process of cement paste. By comparing the images shown in **Figures 5B,D**, it can be found that the microstructure of cement paste became looser with a higher CB addition content. In addition, many CB particles adhered to the cement hydration products, especially the phenomenon of CB gathering took place in 4 and 6% CB cement pastes.

## 3.3 Color Characteristic

The color consistence between cement paste and asphalt mixture is one of the main subjects in this study. As a result, the color characteristics of different cement pastes were evaluated. The absolute values of the reference sample are shown in **Table 2**, and the color difference results of cement pastes are shown in **Table 3**.

**TABLE 2 |** Color values of the reference sample.

| Parameter | L* | a* | b* |
|---|---|---|---|
| Specific value | 94.24 | 1.61 | 1.09 |

It can be found that the parameter ΔL showed the largest varying rate for different cement pastes, compared with the other two parameters Δa and Δb. Additionally, this study focused on discussing the black color difference between cement paste and asphalt mixture. As a result, only ΔL was discussed in the following paragraph.

Compared with the reference plate, all the cement pastes looked more like the black color because of their negative values of ΔL. With the increase of the CB content, ΔL gradually reduced, indicating that CB could improve the black color of cement paste. The color of asphalt mixture was between that of 6 and 8% CB. It should be noted that after a period of service, asphalt generally experiences aging, where an asphalt pavement presents lighter color and higher solar reflectance (Sen and Roesler, 2016). From the prospective of color consistence between cement paste and asphalt mixture, the ΔL of cement

**TABLE 3 |** Color-difference results of cement pastes.

| Parameter | Control paste | 2% CB | 4% CB | 6% CB | 8% CB | Asphalt mixture |
|---|---|---|---|---|---|---|
| ΔL | −26.52 | −44.55 | −50.34 | −53.95 | −58.02 | −57.90 |
| Δa | 1.44 | −0.43 | −0.56 | −0.64 | −0.72 | −0.67 |
| Δb | 4.99 | 1.85 | 1.06 | 0.26 | −0.63 | 0.11 |

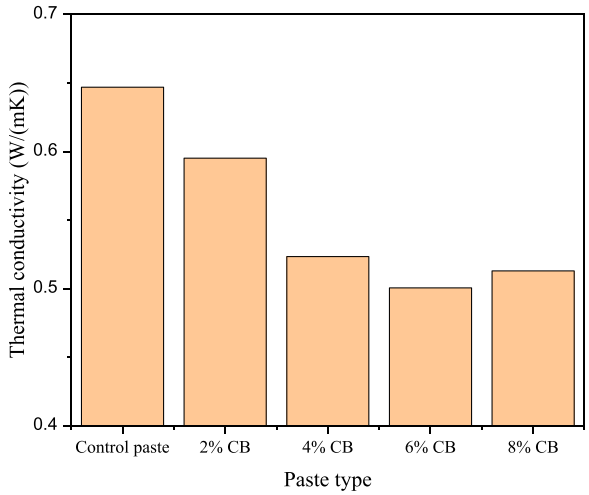


**FIGURE 6 |** Thermal conductivity of cement paste.

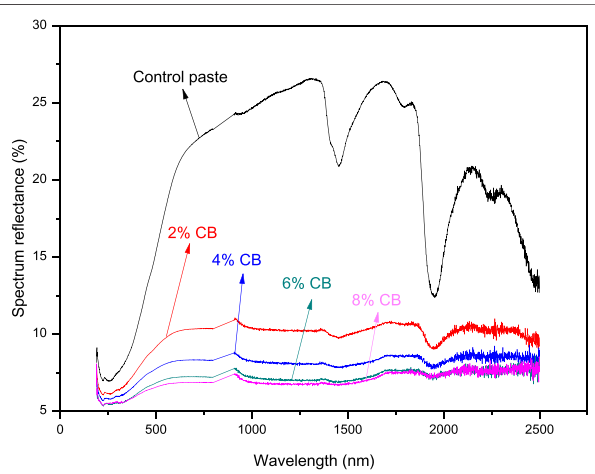


**FIGURE 7 |** Spectrum reflectance of cement paste in the UV–VIS–NIR band.

paste can be determined to be lower than that of the fresh asphalt mixture. In future studies, this result can be considered to optimize the mix design.

## 3.4 Thermal Conductivity

The thermal conductivity results of different cement pastes are shown in **Figure 6**. It can be found that the thermal conductivity of cement paste decreased first and then increased with the increase of the CB content. As discussed in **Section 3.2**, the addition of CB increased the air voids content of cement paste. So, when the content of CB was lower than 6%, the thermal conductivity of cement paste gradually reduced, although the thermal conductivity of CB was generally higher than that of cement hydration products (Dong et al., 2019). The ultimate thermal conductivity indicated that the high thermal conductivity of CB had a higher influence on the thermal conductivity of cement paste than the increasing air voids content.

## 3.5 Spectrum Reflectance

The spectrum reflectance of different cement pastes in the UV–VIS–NIR band is shown in **Figure 7**, according to which the specific reflectance was calculated and shown in **Table 4**. The detailed calculation method can be found in ASTM Standard G173-03 (ASTM, 2012).

Overall, the spectrum reflectance of cement pastes decreased with the increase of CB content. This is because the addition of CB caused the color of cement paste to be more like black. Generally, the materials with black color had lower spectrum reflectance (Xie et al., 2019).

Specifically, the UV reflectance of the five cement pastes was similar to each other, indicating that CB had a small influence on this parameter. By contrast, the VIS reflectance and IR reflectance of these cement pastes changed with a relatively large range. For example, after adding 2% CB, the IR reflectance reduced by over 50%, and in terms of average reflectance, CB also reduced this parameter to a large extent. The addition of 2% CB reduced the average reflectance from 0.203 to 0.098. The reducing ratio was 51.7%. After that, the reflectance changed very little with the increase of CB content.

The semiflexible asphalt pavement comprises asphalt mixture and cement paste. The influence of CB addition on the overall spectrum reflectance of asphalt pavement should be further studied.

## 3.6 Mechanical Performances

From the results discussed in the aforementioned sections, it can be found that CB addition could indeed influence the optical and thermal performances of cement paste. In order to investigate the mechanical performances of these pastes, two indicators of flexural and compressive strength were used. The results are shown in **Figure 8**.

Overall, the flexural and compressive strength of cement pastes both increased with increasing curing time. In particular, the two kinds of strength increased with a very high rate during the curing time of 4 h–1 day, while they changed in a very small range during the curing time of

**TABLE 4 |** Computed spectrum reflectance of different cement pastes.

| Paste type | UV reflectance | VIS reflectance | IR reflectance | Average reflectance |
|---|---|---|---|---|
| Control paste | 0.076 | 0.181 | 0.221 | 0.203 |
| 2% CB | 0.064 | 0.095 | 0.102 | 0.098 |
| 4% CB | 0.060 | 0.079 | 0.083 | 0.081 |
| 6% CB | 0.056 | 0.069 | 0.074 | 0.072 |
| 8% CB | 0.056 | 0.066 | 0.072 | 0.070 |

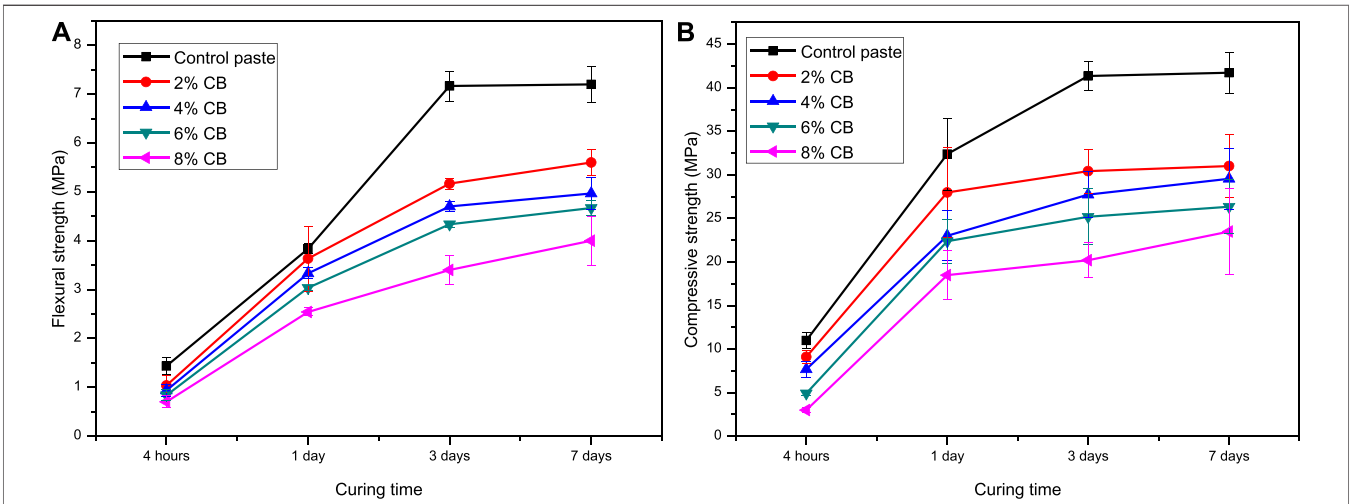


**FIGURE 8 |** Mechanical performances of cement paste. **(A)** Flexural strength and **(B)** compressive strength.

3–7 days. The results might be attributed to the early hydration characteristic of the used cement. The flexural and compressive strength of control paste at the curing time of 4 h reached up to 1.4 and 11.0 MPa, respectively.

The addition of CB had negative effects on the flexural and compressive strength of cement paste, which is in part because CB addition increased the air voids content of cement paste. Take the 1 day-strength for example. When 6% CB paste was added in cement paste, the flexural and compressive strength reduced by 20.9 and 30.9%, respectively. Nevertheless, these strength values could meet the compressive strength requirement of asphalt pavement. It was reported that the compressive strength of an in-service asphalt mixture was approximately 6 MPa (Wu et al., 2018). By contrast, the 1-day compressive strength of 8% CB paste was 18.5 MPa. This indicates that the semiflexible asphalt pavement grouted with the cement paste prepared in this study could be open to traffic in less than 1 day, and the composite asphalt pavement may have higher strength than conventional asphalt pavement.

## 4 CONCLUSION

Traditional semiflexible asphalt pavement presents a bad appearance because of the color inconsistence between black asphalt mixture and light-colored cement paste. Carbon black (CB) was introduced in this study to prepare black cement paste that was grouted in a porous asphalt mixture. The optical, thermal, and mechanical performances of the aforementioned cement pastes were then investigated. The following conclusions were drawn:

(1) By designing the mass ratios of the component, the fluidity of cement grouting paste containing CB could be ensured in a high level. When 8% CB was added to the cement paste, the fluidity was only about 21% of that of control paste.
(2) According to the SEM images of the cement paste, CB caused the microstructure to become looser, and when the CB content was higher than 4%, the CB particles began to gather.
(3) CB improved the black color of cement paste. As a result, the cement paste presented lower spectrum reflectance. The 2% CB cement paste had an average reflectance 51.7% lower than that of control paste.
(4) Due to having higher air voids contents, the cement pastes with CB had lower thermal conductivity, although the thermal conductivity of CB is higher than that of cement hydration products.
(5) The addition of CB reduced the flexural and compressive strength of cement pastes. Nevertheless, the compressive strength value was still much higher than that of the asphalt mixture, indicating that the prepared composite asphalt pavement may have higher strength than conventional asphalt pavement.

## DATA AVAILABILITY STATEMENT

The original contributions presented in the study are included in the article/Supplementary Material, further inquiries can be directed to the corresponding author.

## AUTHOR CONTRIBUTIONS

DY contributed to methodology; DH and WS contributed to validation; DH contributed to formal analysis; DH, WS, and LY contributed to the investigation; WS contributed to data curation; DH and LY contributed to writing—original draft preparation; DY contributed to writing—review and editing; WT contributed to supervision; WT contributed to project administration; and LY contributed to funding acquisition. All authors have read and agreed to the published version of the manuscript.

## FUNDING

This research was funded by the Science and Technology Project of Zhejiang Highway and Transportation Administration Center, China (Grant number 2020H05), National Natural Science Foundation of China (Grant number 51808562), and Natural Science Foundation of Hunan Province, China (Grant number 2020JJ5723).

## REFERENCES

An, S., Ai, C., Ren, D., Rahman, A., and Qiu, Y. (2018). Laboratory and Field Evaluation of a Novel Cement Grout Asphalt Composite. *J. Mater. Civ. Eng.* 30 (8), 04018179. doi:10.1061/(asce)mt.1943-5533.0002376

Aragão, F. T. S., Pazos, A. R. G., Motta, L. M. G. d., Kim, Y.-R., and Nascimento, L. A. H. d. (2016). Effects of Morphological Characteristics of Aggregate Particles on the Mechanical Behavior of Bituminous Paving Mixtures. *Constr. Build. Mater.* 123, 444–453. doi:10.1016/j.conbuildmat.2016.07.013

ASTM (2012). *Standard Tables for Reference Solar Irradiance: Direct normal and Hemispherical on 37 Tilted Surface*. West Conshohocken, PA: ASTM International.

Cai, J., Pei, J., Luo, Q., Zhang, J., Li, R., and Chen, X. (2017). Comprehensive Service Properties Evaluation of Composite Grouting Materials with High-Performance Cement Paste for Semi-flexible Pavement. *Constr. Build. Mater.* 153, 544–556. doi:10.1016/j.conbuildmat.2017.07.122

Chen, X., Wang, Y., Chong, H., and Huang, J. (2020). Use of Sulphoaluminate Cement in Grouted Macadam as Sustainable Pavement Material. *J. Transp. Eng. Part. B Pavements* 146 (2), 04020018. doi:10.1061/jpeodx.0000167

Dong, W., Li, W., Lu, N., Qu, F., Vessalas, K., and Sheng, D. (2019). Piezoresistive Behaviours of Cement-Based Sensor with Carbon Black Subjected to Various Temperature and Water Content. *Compos. B: Eng.* 178, 107488. doi:10.1016/j.compositesb.2019.107488

Du, Y., Chen, J., Han, Z., and Liu, W. (2018). A Review on Solutions for Improving Rutting Resistance of Asphalt Pavement and Test Methods. *Constr. Build. Mater.* 168, 893–905. doi:10.1016/j.conbuildmat.2018.02.151

Fang, B., Xu, T., and Shi, S. (2016). Laboratory Study on Cement Slurry Formulation and its Strength Mechanism for Semi-flexible Pavement. *J. Test. Eval.* 44 (2), 907–913. doi:10.1520/jte20150230

Gong, M., Xiong, Z., Chen, H., Deng, C., Chen, X., Yang, J., et al. (2019). Evaluation on the Cracking Resistance of Semi-flexible Pavement Mixture by Laboratory Research and Field Validation. *Constr. Build. Mater.* 207, 387–395. doi:10.1016/j.conbuildmat.2019.02.064

Hassani, A., Taghipoor, M., and Karimi, M. M. (2020). A State of the Art of Semi-flexible Pavements: Introduction, Design, and Performance. *Constr. Build. Mater.* 253, 119–196. doi:10.1016/j.conbuildmat.2020.119196

Lee, J., Kim, Y. R., and Lee, J. (2015). Rutting Performance Evaluation of Asphalt Mix with Different Types of Geosynthetics Using MMLS3. *Int. J. Pavement Eng.* 16 (10), 894–905. doi:10.1080/10298436.2014.972916

Li, H., Xiao, H., and Ou, J. (2008). Electrical Property of Cement-Based Composites Filled with Carbon Black under Long-Term Wet and Loading Condition. *Compos. Sci. Tech.* 68 (9), 2114–2119. doi:10.1016/j.compscitech.2008.03.007

Luo, S., Yang, X., Zhong, K., and Yin, J. (2020). Open-graded Asphalt concrete Grouted by Latex Modified Cement Mortar. *Road Mater. Pavement Des.* 21 (1), 61–77. doi:10.1080/14680629.2018.1479290

Pei, J., Cai, J., Zou, D., Zhang, J., Li, R., Chen, X., et al. (2016). Design and Performance Validation of High-Performance Cement Paste as a Grouting Material for Semi-flexible Pavement. *Constr. Build. Mater.* 126, 206–217. doi:10.1016/j.conbuildmat.2016.09.036

Qin, Y. (2015). A Review on the Development of Cool Pavements to Mitigate Urban Heat Island Effect. *Renew. Sust. Energ. Rev.* 52, 445–459. doi:10.1016/j.rser.2015.07.177

Santamouris, M. (2013). Using Cool Pavements as a Mitigation Strategy to Fight Urban Heat Island-A Review of the Actual Developments. *Renew. Sust. Energ. Rev.* 26, 224–240. doi:10.1016/j.rser.2013.05.047

Sen, S., and Roesler, J. (2016). Aging Albedo Model for Asphalt Pavement Surfaces. *J. Clean. Prod.* 117, 169169–175175. doi:10.1016/j.jclepro.2016.01.019

Wang, D., Liang, X., Jiang, C., and Pan, Y. (2018). Impact Analysis of Carboxyl Latex on the Performance of Semi-flexible Pavement Using Warm-Mix Technology. *Constr. Build. Mater.* 179, 566–575. doi:10.1016/j.conbuildmat.2018.05.173

Wu, J., Li, D., Zhu, B., and Wu, C. (2018). Milling Process Simulation of Old Asphalt Mixture by Discrete Element. *Constr. Build. Mater.* 186, 996–1004. doi:10.1016/j.conbuildmat.2018.08.015

Xie, N., Li, H., Abdelhady, A., and Harvey, J. (2019). Laboratorial Investigation on Optical and thermal Properties of Cool Pavement Nano-Coatings for Urban Heat Island Mitigation. *Building Environ.* 147, 231–240. doi:10.1016/j.buildenv.2018.10.017

Zhang, J., Cai, J., Pei, J., Li, R., and Chen, X. (2016). Formulation and Performance Comparison of Grouting Materials for Semi-flexible Pavement. *Constr. Build. Mater.* 115, 582–592. doi:10.1016/j.conbuildmat.2016.04.062

Zhang, Y., Sun, Q., and Yang, X. (2018). Changes in Color and thermal Properties of Fly Ash Cement Mortar after Heat Treatment. *Constr. Build. Mater.* 165, 72–81. doi:10.1016/j.conbuildmat.2018.01.029

Zou, X., Sha, A., Jiang, W., and Huang, X. (2015). Modification Mechanism of High Modulus Asphalt Binders and Mixtures Performance Evaluation. *Constr.Build. Mater.* 90, 53–58. doi:10.1016/j.conbuildmat.2015.04.048

**Conflict of Interest:** Author WT is employed by Nanjing Xingyou Transportation Technology Co., Ltd.

The remaining authors declare that the research was conducted in the absence of any commercial or financial relationships that could be construed as a potential conflict of interest.

**Publisher's Note:** All claims expressed in this article are solely those of the authors and do not necessarily represent those of their affiliated organizations, or those of the publisher, the editors, and the reviewers. Any product that may be evaluated in this article, or claim that may be made by its manufacturer, is not guaranteed or endorsed by the publisher.

frontiers in Materials

ORIGINAL RESEARCH
published: 28 February 2022
doi: 10.3389/fmats.2022.840380

# Performance Optimization of Modified Gussasphalt Binder Prepared Using Natural Asphalt

*Tao Li[1†], Qing Jin[2*†], Peng Jiang[2*], Huadong Sun[3*], Yongling Ding[3*], Zongyao Yan[1] and Nan Shi[1]*

[1]Shandong Hi-speed Construction Management Group Co., Ltd., Jinan, China, [2]School of Civil Engineering, Shandong University, Jinan, China, [3]School of Civil Engineering, Shandong Jiaotong University, Jinan, China

OPEN ACCESS

**Edited by:**
Han-Cheng Dan,
Central South University, China

**Reviewed by:**
Dongdong Ge,
Changsha University of Science and Technology, China
Yuchao Lyu,
China University of Petroleum (East China), China

***Correspondence:**
Qing Jin
jinqing@sdu.edu.cn
Peng Jiang
jiangp2020@163.com
Huadong Sun
sunhuadong2004@163.com
Yongling Ding
204130@sdjtu.edu.cn

[†]These authors have contributed equally to this work and share first authorship

**Specialty section:**
This article was submitted to Structural Materials, a section of the journal Frontiers in Materials

**Received:** 21 December 2021
**Accepted:** 31 January 2022
**Published:** 28 February 2022

**Citation:**
Li T, Jin Q, Jiang P, Sun H, Ding Y, Yan Z and Shi N (2022) Performance Optimization of Modified Gussasphalt Binder Prepared Using Natural Asphalt. Front. Mater. 9:840380. doi: 10.3389/fmats.2022.840380

The advantageous thermal stability and construction workability of gussasphalt, a type of asphalt concrete, has drawn increasing attention. To prepare a type of superior gussasphalt concrete using Qingchuan rock asphalt (QRA), a modified gussasphalt binder was prepared with modifiers made up by different dose of styrene-butadiene-styrene, terpene resin, furfural extraction oil and SAW. Then, the rheological properties, microstructure, and thermal stability of gussasphalt binder were studied. The results indicated that the modifier #1 had significant effects on the other indexes but for the ductility, it was less effective in improving the low-temperature performance of the asphalt binder. The low-temperature performance of the binder with modifier #2 was superior compared with that of binder with modifier #1. The binder with 12.5% QRA and 5% modifier #2 can be regarded as an optimal collocation, which had a superior compatibility, high-temperature performance, and comprehensive temperature susceptibility.

**Keywords: gussasphalt, rock asphalt, rheological properties, compatibility, thermal stability**

## 1 INTRODUCTION

Gussasphalt concrete presents a flowing state at an appropriate construction temperature (220–250°C), which can autonomously reach the required density and flatness without compaction (Wang et al., 2011). Therefore, it is more suitable for bridge deck paving and other construction that heavy compaction machinery can't get involved. The overlay of bridge deck requires asphalt concrete with good durability, fatigue resistance, and water resistance (Pouget et al., 2010; Chen et al., 2011a; Gao et al., 2015; Jia et al., 2016). Some of steel box girder bridge exposed to sunlight could cause the overlay temperature to reach 70°C or higher, which shows the need for an overlay with good thermal stability (Chen et al., 2011a; Gao et al., 2015). Gussasphalt concrete not only meets these performance requirements, but can also effectively resist the stress caused by the partial deflection of the steel plate. It also possesses excellent adhesion and compliance with the steel deck (Qiu et al., 2019; Wang et al., 2019). Thus, gussasphalt concrete is suitable for deck paving, especially for long-span and medium-span steel bridges (Chen et al., 2011b; Sang Luo et al., 2018; Ke et al., 2019).

Numerous studies have been conducted on gussasphalt, which have made it possible to produce gussasphalt concrete with high quality. Wang and Li (2015), Liu (2019), and Zou et al. (2020) determined the effects of different factors like the gradation, preparation technique, and asphalt and modifier contents on the performance of gussasphalt and thereby obtained an optimum formula, which suggests the TLA content of 25–30%. Xin et al. (2017) and Jin et al. (2014) analyzed the effects of different temperatures, asphalt types, and filler-asphalt ratios on the high-temperature properties using

laboratory testing. The correlation between the performance of gussasphalt and its composition, and the relationship between the high-temperature deformation and generalized shear modulus, were explored. Zhang et al. (2010), Qian et al. (2013), and Wu et al. (2013) focused on the influences of different strain levels of loading on the fatigue performance of a gussasphalt mix. The fatigue resistance of the gussasphalt was analyzed and evaluated based on a four-point flexural fatigue test. By modifying the mechanical model of the Burgers model, Xie et al. (2017) and Luo R. et al. (2018) derived the viscoelastic material parameters using laboratory tests and theoretical equations. The pivotal factors leading to significant permanent deformation were discovered and summarized. With the progress of science and technology, additional functional research and development will help to improve the serviceability of basic transportation. A conductive gussasphalt (CGA) mix that can melt snow on a bridge deck is a good example of optimizing pavement rideability. Wang et al. (2018b) evaluated the ice melting efficiencies of CGA concrete prepared using various material combinations and studied the effects of the conductive material and asphalt concrete type on the engineering performance. Chen et al. (2019) systemically investigated the effects of the mix type, working conditions, and environmental factors of a CGA mix on the corrosion of a steel bridge deck. Wang et al. (2018a) proposed and evaluated a heat conduction estimation method and derived and verified a theoretical equation for a CGA combination structure. These studies revealed that CGA may have great potential applications in the field of steel deck overlays. However, Zhao et al. (2020) claimed that the gussasphalt applied on the Jiangyin Bridge had a weak high-temperature stability and a lower modulus (Bo Yao et al., 2013), according to an analysis of long-term maintenance data. Thus, there is an urgent need to optimize gussasphalt concrete to tolerate various application scenarios.

The mix proportion design of the gussasphalt binder is characterized by a high content of mineral powder and asphalt binder, high mixing temperature, and low coarse aggregate content. The asphalt binder plays the role of the skeleton, which is completely different from other asphalt concretes with coarse aggregates as the skeleton. The cohesion determines the strength of the gussasphalt concrete (Artamendi et al., 2017; Huang et al., 2019). The acquisition or improvement of each specific property of the asphalt binder can be realized through changes in its microstructure (Mazumder et al., 2018). The identification of the origin of the microstructure and chemical components associated with the formation of this microstructure can reveal the rheology (Yu et al., 2015; Das et al., 2016; Singh and Sawant, 2016). Physical properties such as the stiffness, elasticity, plasticity, adhesion, surface energy, and healing mainly depend on the microstructure of the asphalt (Grover Allen et al., 2014; Kim et al., 2017a). At present, most asphalt mix design methods adopt macroscopic parameters as the design indexes (Bo Yao et al., 2013; Wang and Li, 2015; Singh and Sawant, 2016; Shadkam et al., 2017; Zhang et al., 2018). However, many engineering practices have proved that the current design method cannot effectively control the material performance. In some cases, the statistical indicators are the same, but the performance varies greatly, which implies that some macroscopic design indicators do not conform to the material damage mode (Du, 2014; Cavalli et al., 2016; Kim et al., 2016; Yao and You, 2016). Understanding the properties of asphalt binders at the microscale may be beneficial for improving the knowledge of their macro-performance (Yang et al., 2020).

The use of different techniques to study the microstructure of asphalt is conducive to establishing the relationship between its microstructure and physical properties. Based on foundational laboratory tests, fluorescent microscope tests, and Superpave$^{TM}$ tests, the compatibility of components at the microscale, thermal properties, and rheological properties of a composite natural asphalt modified gussasphalt (CNAMGA) binder were revealed. The optimal collocation of the CNAMGA binder was determined and verified.

# 2 MATERIALS AND METHODS

## 2.1 Materials

### 2.1.1 Base Asphalt

The base asphalt was 90# Kunlun asphalt, and the relevant performance tests were conducted strictly according to Chinese standard E20-2011, Standard Test Methods of Bitumen and Bituminous Mixtures for Highway Engineering (Code of China, 2011). The results are listed in **Table 1**.

### 2.1.2 Natural Asphalt

In recent years, natural asphalt has been extensively studied and widely used in asphalt pavements. To explore more substitutes with high yield, stable properties, and low cost, Chinese Qingchuan rock asphalt (QRA) was employed for the preparation of gussasphalt in this study, according to T0614-2011 and T0618-1993 of Chinese standard E20-2011 (Code of China, 2011). The ash content of QRA was 4.5%, asphalt aromatic was 31.49%, saturate was 29.45%, resin was 34.44% and asphaltene was 4.62%.

### 2.1.3 Modifying Agent

Different modifying agents were adopted in this study (**Table 2**), it is widely acknowledged that Styrene-butadiene-styrene (SBS) can enhance the elasticity of binder at high temperatures and increase flexibility of binder at low temperatures, terpene resin (TR) is easy to mix with asphalt after heating and melting, and during this process, the initial adhesion and aging resistance of asphalt were greatly improved as well. Furfural extraction oil (FEO) can improve the elongation of asphalt at low temperature (Liu et al., 2018; Bai et al., 2019). It can be used as a blending component in asphalt to optimize the composition and make thermoplastic elastomers more compatible in asphalt. SAW modifier can reduce the high-temperature asphalt viscosity and the mixing temperature, and improve the high-temperature performance of asphalt mix.

## 2.2 Test Method

### 2.2.1 Fluorescent Microscope

The CNAMGA binder was heated to a flowing state, and a drop of the sample was taken with a needle and placed on a glass slide

**TABLE.1 |** Technical indexes of 90# base asphalt.

| Test index | | Unit | Specified value | Test results | Test method |
|---|---|---|---|---|---|
| Penetration | 15°C, 100 g, 5 s | 0.1 mm | — | 40 | T0604 |
| | 25°C, 100 g, 5 s | | 80–100 | 92 | |
| | 30°C, 100 g, 5 s | | — | 151 | |
| Softening point (R and B) | | °C | ≥45 | 50.5 | T0606 |
| Ductility (15°C, 5 cm/min) | | cm | ≥100 | 108 | T0605 |
| Density (25°C) | | g/cm$^3$ | Actual measurement | 1.109 | T0603 |
| Thin film oven test (TFOT) (163°C, 300min) | Mass loss | % | −0.8–0.8 | 0.04 | T0610 |
| | Penetration ratio (25°C) | % | ≥57 | 67 | T0604 |
| | Ductility (10°C, 5 cm/min) | cm | ≥8 | 16.7 | T0605 |

**TABLE 2 |** Properties of modifying agents.

| Modifying agent | Property and characteristic |
|---|---|
| SBS | Molecular weight: 220–260 kD, block styrene content: 40.4%, Shore A hardness: 82, white granular |
| TR | Molecular weight: 650–2,600 kD, specific gravity: 0.97, softening point: 110°C, glass transition temperature: 84°C, yellowish viscous liquid or transparent brittle solid |
| FEO | Density (20°C): 0.994 g/cm$^3$, flash point: 251°C, aniline point: 30°C, kinematic viscosity (100°C):35.36, aromatic hydrocarbon content: 82%, dark green liquid |
| SAW | Melting point: 115°C, flash point: 290°C, white or pale-yellow solid |

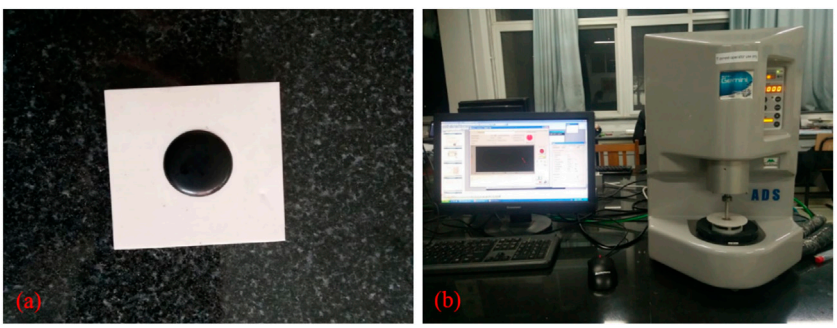


**FIGURE 1 | (A)** The preparation of specimens and **(B)** the DSR test.

washed with absolute ethyl alcohol. Cover slips were gently placed on the slide, which was placed in an oven at 135°C for 10 min. After removing and cooling, a suitable multiple objective lens (×400) was selected for microscopic observation.

### 2.2.2 Dynamic Shear Rheometer Test

Based on AASHTO T 315 (American Association of State Highway and Transportation Officials, 2012), dynamic shear rheometer (DSR) tests were conducted with a Gemini II ADS dynamic shear rheometer, selecting the strain-controlled mode with a frequency of 10 rad/s (1.59 Hz). Five test temperatures from 64 to 88°C at increments of 6°C were applied in the Superpave grading system. The applied strain values, γ, for the original specimen, rolling thin film oven test (RTFO-aged) specimen, and pressure aging vessel test (PAV-aged) specimen were 12, 10, and 1%, respectively. The original specimen and RTFO-aged specimen had a diameter of 25 mm and thickness of 1 mm, while those of the PAV-aged specimen were 8 and 2 mm, respectively. The test process was depicted in **Figure 1**.

### 2.2.3 Bending Beam Rheometer Test

Bending beam rheometer (BBR) tests were conducted using a CANNON bending beam rheometer to evaluate the low-temperature rheological properties, in accordance with the procedures outlined in AASHTO T 313 (2016). When the loads were applied to asphalt beams (125 × 6.25 × 12.5 mm) during the detection process at test temperature of −12, −18 and −24°C, the deflection of the beams was recorded, and the deflection–time curve was obtained and analyzed using a software program to calculate creep stiffness *S* and creep rate *m*. The test process was depicted in **Figure 2**.

## 2.3 Preparation Scheme

Composite modifier #1 was obtained by mixing SBS, SAW, and TR in a 2:1:2 ratio. The 90# base asphalt, QRA, and composite modifier

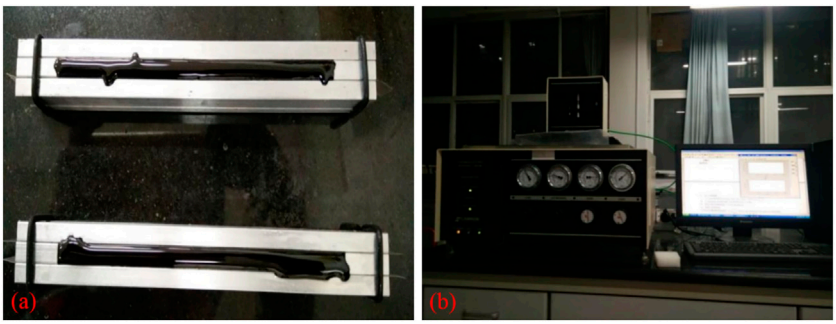


**FIGURE 2 | (A)** The preparation of specimens and **(B)** the BBR test.

**TABLE 3 |** Scheme design of CNAMGA binder.

| Factor specimen | A: QRA content (%) | B: Composite modifier #1 content (%) |
|---|---|---|
| 1 | 1 (10.0) | 1 (0) |
| 2 | 1 | 2 (3) |
| 3 | 1 | 3 (5) |
| 4 | 2 (12.5) | 1 |
| 5 | 2 | 2 |
| 6 | 2 | 3 |
| 7 | 3 (15.0) | 1 |
| 8 | 3 | 2 |
| 9 | 3 | 3 |

were used for specimen preparation. The standby base asphalt was heated to reach a flowing state in a constant-temperature oven at 135°C. Then, an appropriate amount of base asphalt was heated to 160°C in the magnetic stirring electric heating mantle, and SBS was added bit by bit until all the SBS was added while stirring the binder for 40–50 min. Reference (Lu et al., 2009) showed that the 8% content of QRA had no considerably adverse influence on low temperature performance. In view of the addition of modifier, 10, 12.5 and 15% QRA for 90 # base asphalt were determined. According to the different QRA contents, a small amount of asphalt was weighed, and small amounts of SAW, TR, and QRA were added until all the needed components were added while stirring for 1 h. Next, the asphalt binder was stirred by a homomixer at a speed of 3,500 rpm for 40–50 min, maintaining the mixing temperature at 160°C. Finally, the CNAMGA binder specimens were prepared.

# 3 RESULTS AND DISCUSSION

## 3.1 Fundamental Property Measurements

### 3.1.1 Orthogonal Test

The specimens were prepared according to the preparation scheme for the CNAMGA binder. Factor A (the QRA content) had three levels (10, 12.5, and 15.0%) and factor B (the composite modifier #1 content) had three levels (0, 3, and 5%), and various combinations were adopted to analyze the binder properties. The interaction between the factors was not considered, as the test arrangement shown in **Table 3** indicates.

Asphalt penetration test (25°C, 100 g, 5 s), ductility test (10°C, 5 cm/min), softening point test (R&B), and rolling thin film oven test (RTFOT) (163°C, evaporation for 5 h) were performed according to T0604-2011, T0605-2011, T0606-2011, and T0608-1993 of E20-2011 (Code of China, 2011), respectively. The results are shown in **Figure 3**.

As the results shown in **Figure 3** indicate, when the QRA content is the same, the softening point increases and the mass loss decreases, the penetration increases and then decreases, and the ductility gradually decreases (except for specimen 6) with an increase in the modifier #1 content. Referring to the technical requirements for modified hard asphalt binder in the *Technical* Guide on Design and Construction of Bridge Deck Paving of Highway Steel Box Girder, the specimen with the 10% QRA content and less than 5% modifier #1 content does not meet the penetration requirements (1–4 mm). The specimen with 10% QRA and 5% modifier #1 or specimen with 15% QRA and any content of modifier #1, does not meet the ductility requirement (≥10 mm). When the QRA content is 7.5% and the modifier #1 content is less than 5%, or the QRA content is 15% and the modifier #1 content is less than 3%, the specimen doesn't meet the softening point requirement (≥72°C). All the specimens meet the mass-loss requirement (<0.5%). According to the above analysis, specimens with a 12.5% QRA content and 5% modifier #1 content meet the all the index requirements.

### 3.1.2 Variance Analysis

Furthermore, given the test results and rules for different collocations of the CNAMGA binder in **Figure 3**, a variance analysis (Jamshidi et al., 2012) was adopted to investigate the influencing factors of different technical indexes. The results are presented in **Table 4**.

According to the one-tailed hypothesis test in mathematical statistics, with a confidence interval ($\alpha$ = 0.05), when the factor degree of freedom is 2 and the error degree of freedom is 4, it can be seen from the $F$ distribution table that the critical value is $F_{0.05}(2, 4) = 6.9$. That is, there is a 95% certainty that $F \leq 6.9$ will appear, which can be judged to have no significant impact on the experimental index (acceptable region). If $F > 6.9$ happens with only a 5% certainty, this indicates that the null hypothesis is not

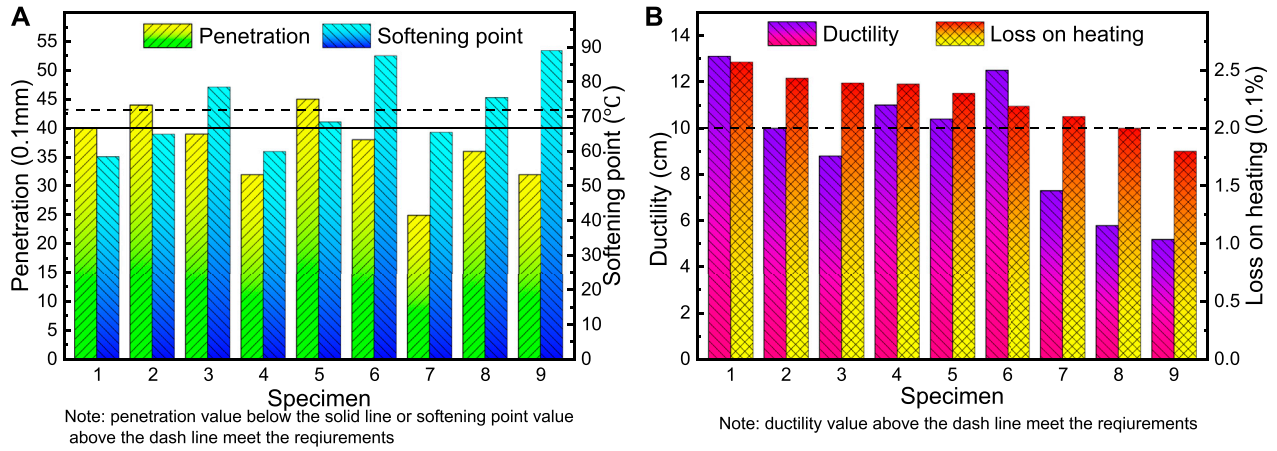


**FIGURE 3 |** Results of **(A)** penetration test and softening point test, **(B)** ductility test and RTFOT.

**TABLE 4 |** Variance analysis results.

| Performance index | Variation source | Degree of freedom | Quadratic sum | Mean squares | *F* Value | Critical value |
|---|---|---|---|---|---|---|
| Penetration | A | 2 | 160.89 | 80.44 | 11.05 | $F_{0.05}$ (2, 4) = 6.9 |
| | B | 2 | 131.56 | 65.78 | 9.04 | $F_{0.01}$ (2, 4) = 18.0 |
| | E (Error) | 4 | 29.11 | 7.28 | — | — |
| | T (Total) | 8 | 321.56 | — | — | — |
| Softening point | A | 2 | 130.67 | 65.33 | 14.39 | $F_{0.05}$ (2, 4) = 6.9 |
| | B | 2 | 864.67 | 432.33 | 95.19 | $F_{0.01}$ (2, 4) = 18.0 |
| | E | 4 | 18.17 | 4.54 | — | — |
| | T | 8 | 1,013.50 | — | — | — |
| Ductility | A | 2 | 48.04 | 24.02 | 10.86 | $F_{0.05}$ (2, 4) = 6.9 |
| | B | 2 | 5.68 | 2.84 | 1.28 | $F_{0.01}$ (2, 4) = 18.0 |
| | E | 4 | 8.84 | 2.21 | — | — |
| | T | 8 | 62.56 | — | — | — |
| Mass loss | A | 2 | 0.00381 | 0.00191 | 96.93 | $F_{0.05}$ (2, 4) = 6.9 |
| | B | 2 | 0.00075 | 0.00037 | 19.03 | $F_{0.01}$ (2, 4) = 18.0 |
| | E | 4 | 0.00008 | 0.00002 | — | — |
| | T | 8 | 0.00464 | — | — | — |

valid, and that this factor has a significant impact on the experimental index (rejection region). The critical value is $F_{0.01}$ (2, 4) = 18.0, with a confidence interval ($\alpha = 0.01$). That is, there is a 99% certainty that $6.9 < F < 18.0$ will appear, which can be judged to have a significant impact on the experimental index (acceptable region). If $F > 18.0$ occurs with only a 1% certainty, this indicates that the null hypothesis "this factor has a significant effect on the experimental index" is invalid, and this factor has a strongly significant impact on the experimental index (rejection region).

Note that because $6.9 < F_B < F_A < 18.0$ with regard to penetration, it can be considered that the QRA and modifier #1 contents have a significant impact on the penetration of the binder. From $F_B < 6.9 < F_A < 18.0$ for the ductility, it can be seen that the QRA content has a significant effect, while the modifier #1 content has no significant effect on the ductility. The $6.9 < F_A < 18.0 < F_B$ for softening point indicates that the QRA content has a significant effect on the softening point, and the modifier #1 content has a strongly significant effect on it. That $18.0 < F_B < F_A$ for the mass loss illustrates that the QRA and modifier #1 contents have a strongly significant impact on the mass loss.

The modifier #1 has a significant effect on the other indexes, but for the ductility, it is slightly less effective in improving the low-temperature performance of the asphalt. It is speculated that the modifier #1 component may affect the compatibility and performance of the modified asphalt. The collocation of the modifier #1 is adjusted to SBS: SAW: TR: FEO = 2: 2: 0.5: 0.5, the TR content is reduced, and FEO, which can enhance the ductility at low temperature, is added. The objective of this new modifier (#2) is to reduce the consistency, improve the compatibility between the modifier and asphalt, and improve the low-temperature performance of the binder.

## 3.2 Fluorescent Microscope Test

### 3.2.1 Qualitative Analysis

The microstructure of the modified asphalt significantly affects the properties of the modified asphalt. To confirm whether

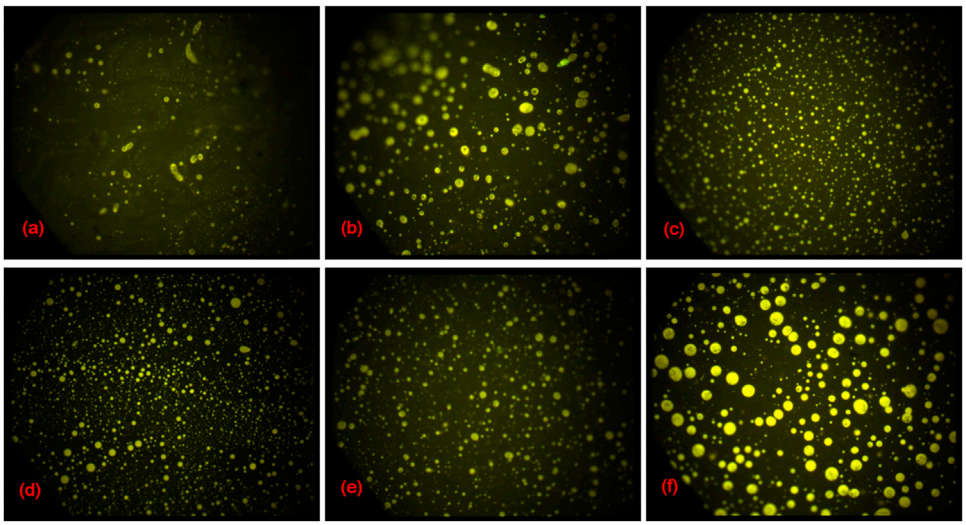


**FIGURE 4 |** Fluorescent microscope images, **(A)** specimen 2', **(B)** specimen 3', **(C)** specimen 5', **(D)** specimen 6', **(E)** specimen 8', **(F)** specimen 9'.

modifier #2 could live up to the expectations mentioned above, a fluorescent microscope is employed to observe and analyze the dispersibility and compatibility of the QRA and modifier in the binder. Six specimens (specimens 2', 3', 5', 6', 8', and 9') are remade with modifier #2 according to the collocation in **Table 3**. They are then subjected to fluorescent microscope tests, and the results are shown in **Figure 4**.

Specimens presents different swollen polymer-rich phase from the vision of fluorescent microscope. In these pictures, the swollen polymer-rich phase has a bright yellow appearance and the dark region denotes the asphalt-rich phase. The QRA contents of specimens 2' and 3' are 10%, those of specimens 5' and 6' are 12.5%, and those of specimen 8' and 9' are 15%. The modifier #2 contents of specimens 3', 6', and 9' are 5%, and those of specimens 2', 5', and 8' are 3%. The irregular shape of polymer-rich phase in **Figure 4A** indicates the poor compatibility of the components in specimen 2'. **Figure 4C** shows that many polymer-rich phase in small size evenly distribute in specimen 5', implying better swelling comparing to specimen 2'. The distribution of polymers tends to sparse and inconspicuous in **Figure 4E**, indicating poor compatibility with higher content of QRA, the increasing addition of heavy fractions obstructs polymers swelled by light fractions. Compared with **Figures 4A,B** depicts the dispersed polymer-rich phase is proned to be spherical but distributes unevenly, implying modifier #2 plays a certain role in compatibility. The compatibility shown in **Figure 4D** is slightly poorer than that seen in **Figure 4C**, which is not yet obvious. It is not difficult to see the shape of polymer-rich phase is large in size, indicating agglomeration with higher content of modifier #2 and QRA from **Figure 4F**, and a potential phase separation may occur. The above phenomena prove that the modifier and QRA contents should coordinate with each other; mismatching will affect the dispersion of the different components in the binder. It can be concluded that the compatibility of the binders with the 12.5% QRA and 3% or 5% content of modifier #2 is better.

### 3.2.1 Quantitative Analysis

The pictures in aforementioned statement are only partial visions under fluorescent microscope, which are representative, while sometimes a partial vision is hard to depict all-inclusive information. Extensive binarization treatment and mathematical statistics in fluorescent photomicrograph can present a more comprehensive result. Image-Pro Plus software (version 6.0), a powerful 2D and 3D image processing software, was employed to implement quantitative analysis. The area of the fluorescent part (that is, the pixels with gray values ≥175) in the photomicrograph was analyzed. Taking specimens 5' and 6' as examples, **Figure 5** presents the process of binarization treatment.

With binarization treatment, the sparse and uneven distribution of polymer-rich phase in specimen 5' tends to be more conspicuous than that of specimen 6'. In this way, the proportions of the fluorescence areas in the total areas of observation of different specimens could be quantitatively compared. Samples are observed multiple times using different fields of view, and mathematical statistics are used to determine the results, which are shown in **Figure 6**.

As shown in **Figure 6**, with the increase addition of modifier #2 in the specimens with 10% content of QRA and specimens with 15% contents of QRA, the fluorescence spots area gradually decreases, while that of specimens with 12.5% content of QRA increases with the addition of modifier #2. This proves that higher modifier and QRA contents do not yield better results, the role of modifier #2 on the specimens with 12.5% content of QRA can be played to the better extent. Note that the fluorescence spots of the specimen with 12.5% QRA and 5% modifier #2 are the densest and the area proportion is the largest, as a result of the sufficient cross-linking and grafting reactions occurring in the binder. Therefore, the QRA and modifier contents should match each other, or the larger agglomeration or no fluorescent spots can be found under the sampling field. The statistical results show that the compatibility of the binder with the 12.5% QRA content and

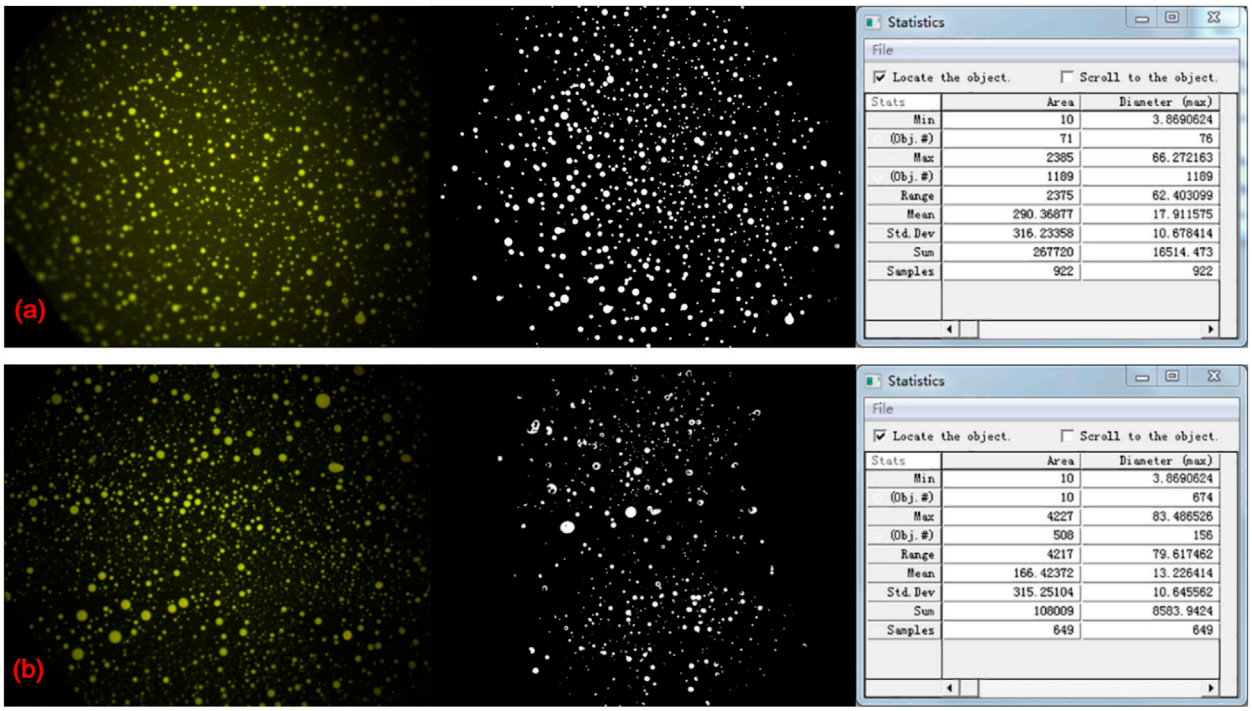


**FIGURE 5 |** Binarization treatment results of **(A)** specimen 5' and **(B)** specimen 6'.

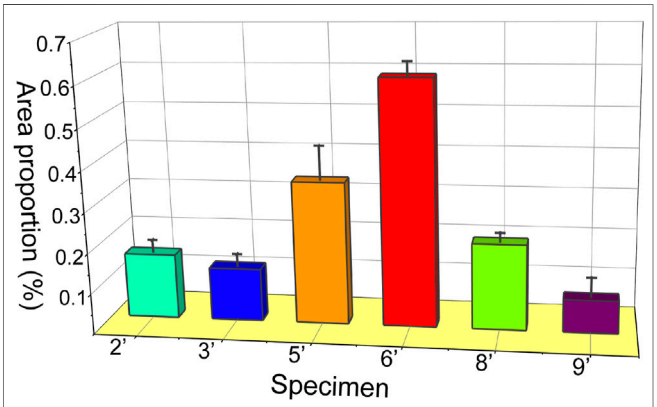


**FIGURE 6 |** Area ratio of modifier and QRA.

5% modifier #2 is superior, which could be considered as the main research object in next characterization of macro-properties.

## 3.3 Superpave$^{TM}$ Asphalt Binder Tests

### 3.3.1 High-Temperature Performance

The shear strength of asphalt concrete mainly depends on the bonding force caused by the interaction between the binder and aggregate and the internal friction angle caused by the intercalation of the aggregates in the asphalt mix. When the temperature goes up and shear stress increases, the asphalt binder viscosity decreases and the flow mobility increases, and the migration of binder to the pavement surface leads to a reduction on the internal friction angle of asphalt mix. The integrity and shear strength of the mix deteriorate, leading to pavement rutting and other pavement diseases (Al-Khateeb and Al-Akhras, 2011; Ali et al., 2017), therefore high-temperature performance is important for the serviceability of asphalt concrete. The rutting factor $G^*/\sin\delta$ can be considered to be a characterization parameter for the high-temperature performance. A larger value indicates a worse high-temperature fluidity, and a higher anti-rutting performance. Based on fluorescent microscope test, the compatibility of the binder with the 12.5% QRA content is regarded as superior, then specimens 4, 5', and 6' are subjected to DSR test, and the results are depicted in **Figure 7**.

As anticipated, complex modulus $G^*$ before and after aging decreases with the rising temperature, phase angle δ before and after aging increases with the rising temperature. At the same temperature, the larger $G^*$ of the binder with modifier #2 appears than that of binder without modifier #2, indicating that binder with modifier #2 has better deformation resistance, but the $G^*$ of binder with 3% modifier #2 before aging has not much difference with that of binder without modifier #2 before aging. And the δ of modified binder is less than that of unmodified binder, the δ increases as the temperature increases for all samples. With the increasing dosage of modifier #2, the δ decreases at the same temperature, which indicates that the ratio of the elastic component in asphalt increases, the elastic recovery performance of asphalt has been improved. According to Superpave$^{TM}$, rutting factor $G^*/\sin\delta$ is limited to no less than

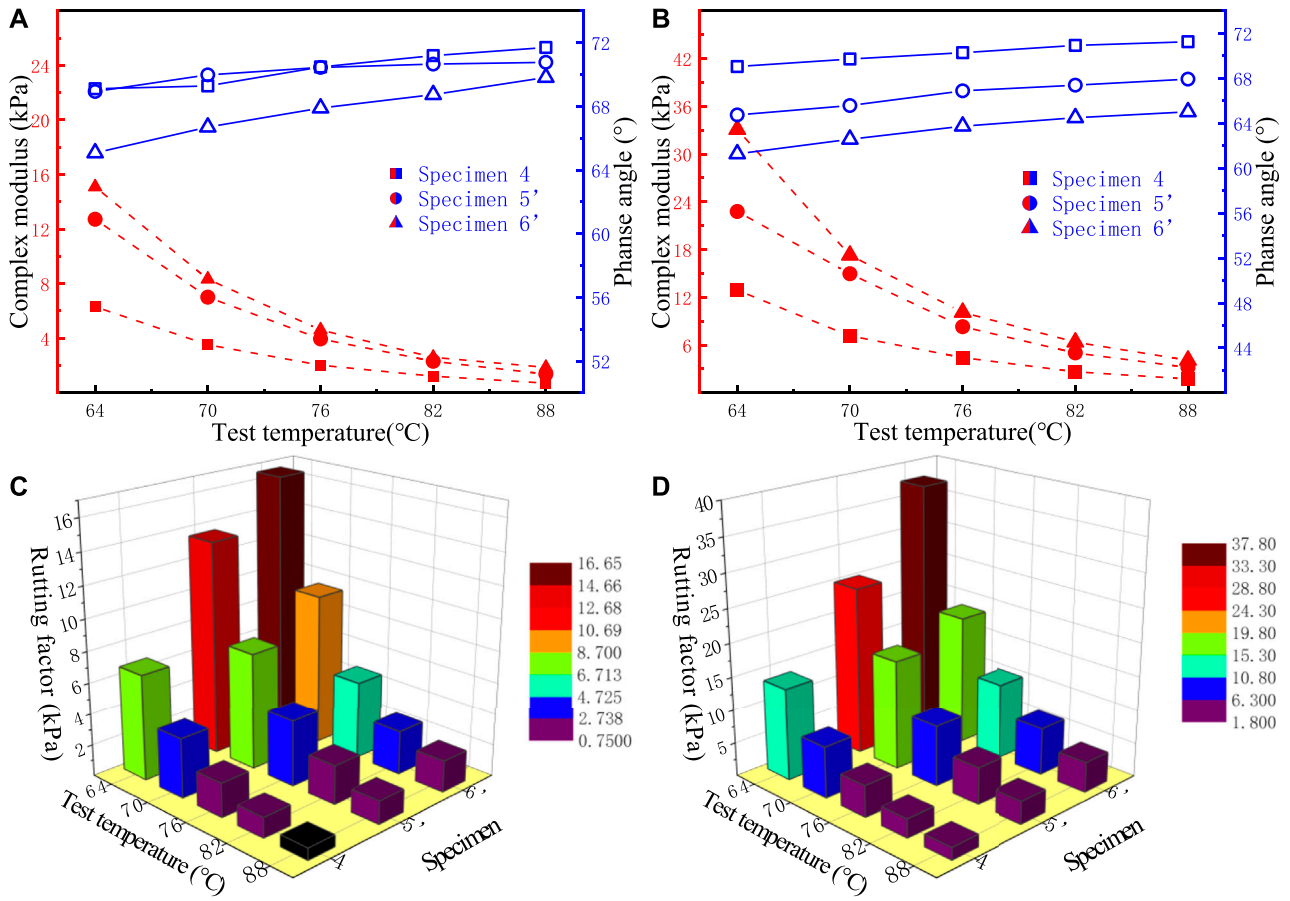


**FIGURE 7 |** Complex modules $G^*$ and phase angle δ **(A)** before RTFO-aged and **(B)** after RTFO-aged, rutting factor $G^*/\sin\delta$ **(C)** before RTFO-aged and **(D)** after RTFO-aged.

1.0 kPa for unaged binders or 2.2 kPa for RTFO-aged binders (Jamshidi et al., 2012; Fazaeli et al., 2016; Kim et al., 2017b). As shown in **Figures 7C,D**, specimen 4 at 88°C before and after aging doesn't meet the requirements. Specimen 6', which has the largest $G^*/\sin\delta$ value, has a superior high-temperature performance. The incorporation of the modifier changes the colloid structure of the asphalt, increasing the asphaltene content, which could harden the asphalt binder. Harder asphalt shows less conversion from elasticity to viscosity at high temperatures, enhancing the resistance to shear deformation at high temperatures. The composition of natural asphalt is similar to that of petroleum asphalt, but the content of hard components (resin and asphaltene) is higher in natural asphalt. Almost every large molecule of asphaltene contains the polar functional groups of carbon, hydrogen, oxygen, nitrogen, and sulfur, which can produce a strong adsorption force on the surface and improve the high-temperature performance of the asphalt. The performance grade (PG) at high or intermediate temperatures is increased by one level. From the above analysis, it can be seen that the high-temperature performance of the binder with 5% modifier #2 is better.

### 3.3.2 Low-Temperature Performance

Cracking not only destroys the continuity of pavement and reduces the driving quality, but also poses a water-induced distress concern, leading to the deterioration of the pavement bearing capacity and pavement damage. The low-temperature cracking resistance of asphalt pavement mainly depends on the tensile properties of the binder at low temperatures. In contrast to the high-temperature anti-rutting ability, the shrinkage cracking of asphalt pavement is usually caused by continuous aging, an increase in the stiffness modulus, and the gradual transformation of the low-temperature compliance into brittleness of the binder during its service life (You et al., 2011; Yao et al., 2012, Hui Yao et al., 2013). For comparison with the unadjusted modified binder, modifier #2 is used to make specimens 5' and 6' according to the collocation of specimens 5 and 6 with modifier #1, and the test results are shown in **Figure 8**.

Reflecting the release rate of the shrinkage stress caused by the viscoelastic flow of the asphalt, a larger creep rate *m*-value indicates a better stress dissipation capacity for the asphalt and its crack resistance. Asphalt with a small creep stiffness (S) has less internal stress, better low-temperature compliance,

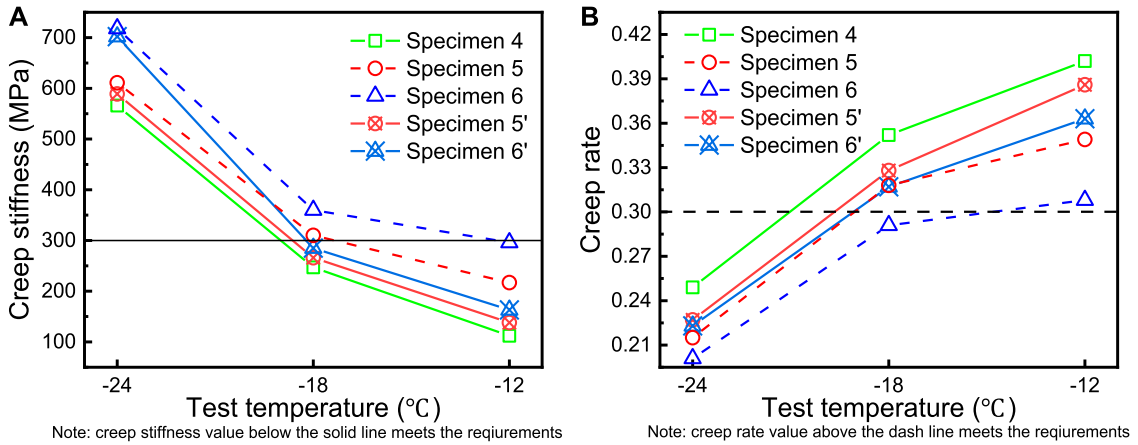


**FIGURE 8 | (A)** Creep stiffness *S* and **(B)** creep rate *m*-value of different binder.

**TABLE 5 |** PG of binder before and after aging.

| Specimen | PG of original specimen (°C) | PG of RFO-aged specimen (°C) | PG of PAV-aged specimen (°C) | Low-temperature PG (°C) | PG results (°C) |
|---|---|---|---|---|---|
| 4 | 82 | 82 | 25 | −18 | 82–18 |
| 5' | 88 | 88 | 25 | −18 | 88–18 |
| 6' | 88 | 88 | 25 | −18 | 88–18 |

and less chance of cracking at low temperatures. As shown in **Figure 8**, with the same QRA content, the S value of the binder-added modifier is larger than that of the binder with no modifier, whereas the *m*-value of the binder with the modifier is smaller than that of the binder without the modifier. With an increase in the modifier content, S increases, and the *m*-value decreases. It can be seen from this phenomenon that the binder will be hardened and the stress relief capacity will be reduced after the modifier is added, which will reduce the low-temperature performance of the binder to a certain extent. At the same time, note that the S value of the binder with modifier #2 is smaller and the *m*-value is larger than that of the binder with the same content of modifier #1. The PG at low temperature is also improved by one level. Modifier #2 plays a role in enhancing the low-temperature performance of the binder, strongly proving that the adjusted modifier composition works effectively.

### 3.3.3 Temperature Susceptibility

Based on American Association of State Highway and Transportation Officials (2010) and American Association of State Highway and Transportation Officials (2007), the results of the PG determination of asphalt binder are summarized in **Table 5**.

**Table 5** shows that the addition of modifier #2 improved the PG at high or intermediate temperatures, and the influence of modifier #2 on the PG at low-temperature is stable. Reflecting the sensitivity of the asphalt binder to temperature changes (Rasmussen et al., 2002; Al-Hadidy and Tan, 2009; Walters et al., 2014), the temperature susceptibility (TS) has an important influence on the pavement performance. One of technical indicators of the TS is the penetration.

The penetration index (PI) proposed by Pfeiffer (Pfeiffer and Doormaal, 1936) is calculated by the linear regression of the penetration test results in a temperature range of 15–30°C. Obviously, the PI only reflects the TS at a normal temperature. It is meaningless for high or intermediate temperatures and low temperatures, which significantly affect the rheological properties of the binder. The G*/sinδ value with a change in temperature exactly indicates the TS of the asphalt at high or intermediate temperature ranges, and the S value with a change in temperature exactly reflects the TS value of the asphalt in the low-temperature range. With temperature T as the independent variable, lg (G*/sin) and lgS are considered as dependent variables, and can be defined as follows:

$$lg\left(G^{*}/\sin\delta\right) = -A_1T + K_1,$$
$$lgS = -A_2T + K_2,$$

where $A_1$ and $A_2$ are susceptibility factors, and $K_1$ and $K_2$ are regression constants.

Regression fitting was performed on the data of the three specimens, and the results are listed in **Table 6**.

As shown in **Table 6**, the fitting degree, $R^2$, values of all the equations were greater than 0.98, indicating that both G*/sinδ and *S* were highly correlated with temperature T. By covering

**TABLE 6 |** Linear equation regression analysis.

| Specimen | TS of high or intermediate temperatures | | TS of low temperature | |
|---|---|---|---|---|
| | Regression equation | $R^2$ | Regression equation | $R^2$ |
| 4 | lg ($G^*/sin\delta$) = –0.0396T + 3.3552 | 0.9993 | lgS = 0.3518*T* + 1.6946 | 0.9998 |
| 5' | lg ($G^*/sin\delta$) = –0.2430T + 1.3650 | 0.9991 | lgS = 0.3151*T* + 1.8147 | 0.9970 |
| 6' | lg ($G^*/sin\delta$) = –0.2356T + 1.4308 | 0.9905 | lgS = 0.3308*T* + 1.8336 | 0.9889 |

the evaluated temperature, it is feasible for the binder to form an evaluation system for the TS. Generally speaking, a smaller absolute value for the susceptibility factor indicates a better resistance to TS. Among the three specimens, the TS at high or intermediate temperatures for specimen 4 is the best, while that at a low temperature is the worst. The TS at high or intermediate temperatures for specimen 5' is the worst, while that at a low temperature is the best. Combining the above factors, the collocation of specimen 6' could be identified as a better collocation with a superior comprehensive TS.

## 4 CONCLUSION

This study evaluated the compatibility of components at the microscale, as well as the thermal properties and rheological properties at the macroscale, of the CNAMGA binder. The following conclusions are drawn based on the results and discussion.

1) Variance analysis indicates the modifier #1 has no significant impact on the improvement of ductility. Fluorescent microscope test implies that the compatibility of the binder with 12.5% QRA and 5% modifier #2 is superior.
2) The incorporation of the modifier obviously improves the high-temperature performance and reduces the low-temperature performance of the binder to a certain extent. Whereas the low-temperature PG of the binder with modifier #2 is superior compared with that of binder with modifier #1.
3) The collocation of 12.5% QRA and 5% modifier #2 could be identified as an optimal collocation with a superior high-temperature performance and comprehensive TS; it has a better performance in terms of the general and rheological properties. The performance of the mix prepared using the CNAMGA binder remains to be verified through relevant tests.

## DATA AVAILABILITY STATEMENT

The original contributions presented in the study are included in the article/Supplementary Material, further inquiries can be directed to the corresponding authors.

## AUTHOR CONTRIBUTIONS

Conceptualization, TL and QJ; methodology, TL and PJ; software, YD; writing—original draft preparation, QJ and PJ; writing—review and editing, QJ and HS; visualization, ZY; supervision, QJ; project administration, NS; funding acquisition, HS and YD. All authors have read and agreed to the published version of the manuscript.

## FUNDING

This research was funded by the China Postdoctoral Science Foundation (Grant Nos 2019M662442), the National Natural Science Foundation of China (No. 51803109), and the Young Talent of Lifting engineering for Science and Technology in Shandong (SDAST 2021qt01).

## ACKNOWLEDGMENTS

The authors wish to express their sincere gratitude for the kind assistance of Shandong province key laboratory of Shandong Jiaotong University and Shandong University.

## REFERENCES

Al-Hadidy, A. I., and Yi-qiu, T. (2009). Mechanistic Approach for Polypropylene-Modified Flexible Pavements. *Mater. Des.* 30, 1133–1140. doi:10.1016/j.matdes.2008.06.021

Ali, S. I. A., Ismail, A., Karim, M. R., Yusoff, N. I. M., Al-Mansob, R. A., and Aburkaba, E. (2017). Performance Evaluation of Al2O3 Nanoparticle-Modified Asphalt Binder. *Road Mater. Pavement Des.* 18, 1251–1268. doi:10.1080/14680629.2016.1208621

Al-Khateeb, G. G., and Al-Akhras, N. M. (2011). Properties of Portland Cement-Modified Asphalt Binder Using Superpave Tests. *Constr. Build. Mater.* 25, 926–932. doi:10.1016/j.conbuildmat.2010.06.091

American Association of State Highway and Transportation Officials (2010). *AASHTO M 320, Standard Specification for Performance-Graded Asphalt Binder*. Washington DC.

American Association of State Highway and Transportation Officials (2007). *AASHTO PP 42, Standard Practice for Determination of Low-Temperature Performance Grade (PG) of Asphalt Binders*. Washington DC.

American Association of State Highway and Transportation Officials (2016). *AASHTO T 313, Standard Method of Test for Determining the Flexural Creep Stiffnessof Asphalt Binder Using the Bending BeamRheometer*. Washington DC: BBR.

American Association of State Highway and Transportation Officials (2012). *AASHTO T 315, Standard Method of Test for Determining the Rheological Propertiesof Asphalt Binder Using a Dynamic ShearRheometer*. Washington DC: DSR.

Artamendi, I., Allen, B., Allpress, C., Phillips, P., and Wingrove, C. (2017). "Resurfacing of the Queen Elizabeth II Bridge: Binder Selection and evaluation," in Railways and Airfields (BCRRA 2017), Athens, Greece, 28-30 June, 2017. doi:10.1201/9781315100333-325

Bai, T., Hu, Z.-a., Hu, X., Liu, Y., Fuentes, L., and Walubita, L. F. (2020). Rejuvenation of Short-Term Aged Asphalt-Binder Using Waste Engine Oil. *Can. J. Civ. Eng.* 47, 822–832. doi:10.1139/cjce-2019-0268

Cavalli, M. C., Griffa, M., Bressi, S., Partl, M. N., Tebaldi, G., and Poulikakos, L. D. (2016). Multiscale Imaging and Characterization of the Effect of Mixing Temperature on Asphalt concrete Containing Recycled Components. *J. Microsc.* 264, 22–33. doi:10.1111/jmi.12412

Chen, J. S., Liao, M. C., and Huang, C. C. (2011a). "Evaluation of Guss Asphalt Applied to Steel Deck Surfacing," in 1st Congress of the Transportation and Development Institute of ASCE, Chicago, IL, 13–16 March, 2011. doi:10.1061/41167(398)45

Chen, J. S., Liao, M.-C., Huang, C.-C., and Wang, C.-H. (2011b). Fundamental Characterization of Engineering Properties of Gussasphalt Mixtures. *J. Mater. Civ. Eng.* 23, 1719–1726. doi:10.1061/(ASCE)MT.1943-5533.0000339

Chen, Q., Wang, C., Sun, X., Cao, Y., Guo, T., and Chen, J. (2019). Evaluation and Prediction for Effect of Conductive Gussasphalt Mixture on Corrosion of Steel Bridge Deck. *Constr. Build. Mater.* 228, 116837. doi:10.1016/j.conbuildmat.2019.116837

Code of China (2011). *JTG E20-2011, Standard Test Methods of Bitumen and Bituminous Mixtures for Highway Engineering*. Beijing: China Communications Press.

Das, P. K., Baaj, H., Tighe, S., and Kringos, N. (2016). Atomic Force Microscopy to Investigate Asphalt Binders: a State-Of-The-Art Review. *Road Mater. Pavement Des.* 17, 693–718. doi:10.1080/14680629.2015.1114012

Du, S. (2014). Interaction Mechanism of Cement and Asphalt Emulsion in Asphalt Emulsion Mixtures. *Mater. Struct.* 47, 1149–1159. doi:10.1617/s11527-013-0118-1

Fazaeli, H., Amini, A. A., Moghadas Nejad, F., and Behbahani, H. (2016). Rheological Properties of Bitumen Modified with a Combination of Ft Paraffin Wax (Sasobit) and Other Additives. *J. Civil Eng. Manage.* 22, 135–145. doi:10.3846/13923730.2014.897977

Gao, B., Wang, M., and Hao, Z. H. (2015). Bending Behavior of Glass Fiber Grid Reinforced Gussasphalt. *Appl. Mech. Mater.* 744-746, 754–757. doi:10.4028/www.scientific.net/amm.744-746.754

Grover Allen, R. G., Little, D. N., Bhasin, A., and Glover, C. J. (2014). The Effects of Chemical Composition on Asphalt Microstructure and Their Association to Pavement Performance. *Int. J. Pavement Eng.* 15, 9–22. doi:10.1080/10298436.2013.836192

Huang, W., Sun, M., and Qin, Y. (2019). The Influence of the Warm-Mixed Agent on the Performance of Gussasphalt after Superheated Aging, *IOP Conf. Ser. Earth Environ. Sci.* 304, 052128. doi:10.1088/1755-1315/304/5/052128

Jamshidi, A., Hamzah, M. O., and Aman, M. Y. (2012). Effects of Sasobit Content on the Rheological Characteristics of Unaged and Aged Asphalt Binders at High and Intermediate Temperatures. *Mat. Res.* 15, 628–638. doi:10.1590/S1516-14392012005000083

Jia, X., Huang, B., Chen, S., and Shi, D. (2016). Comparative Investigation into Field Performance of Steel Bridge Deck Asphalt Overlay Systems. *KSCE J. Civ Eng.* 20, 2755–2764. doi:10.1007/s12205-016-0259-1

Jin, L., Qian, Z., and Zheng, Y. (2014). High Temperature Performance and Evaluation index of Gussasphalt Mortar Based on DMA Method. *Dongnan Daxue Xuebao (Ziran Kexue Ban)/J. Southeast Univ. (Nat. Sci. Ed.)* 44, 1062–1067. doi:10.3969/j.issn.1001-0505.2014.05.033

Ke, Z., Mingzhi, S., and Yunjie, Q. (2019). Study on the Rheological Properties of Gussasphalt after Superheat Aging, *IOP Conf. Ser. Earth Environ. Sci.* 233, 032002. doi:10.1088/1755-1315/233/3/032002

Kim, H. H., Lee, M. S., Lee, M. S., and Lee, S. J. (2016). Identification of the Microstructural Components of Crumb Rubber Modified Asphalt Binder (CRMA) and the Feasibility of Using Environmental Scanning Electron Microscopy (ESEM) Coupled with Energy Dispersive X-Ray Spectroscopy (EDX). *Int. J. Highw. Eng.* 18, 41–50. doi:10.7855/ijhe.2016.18.6.041

Kim, H. H., Mazumder, M., and Lee, S. J. (2017a). Micromorphology and Rheology of Warm Binders Depending on Aging. *J. Mater. Civil Eng.* 29, 04017226. doi:10.1061/(ASCE)MT.1943-5533.0002082

Kim, H. H., Mazumder, M., Torres, A., Lee, S.-J., and Lee, M.-S. (2017b). Characterization of CRM Binders with Wax Additives Using an Atomic Force Microscopy (AFM) and an Optical Microscopy. *Adv. Civ. Eng. Matls.* 6, 20160071. doi:10.1520/acem20160071

Liu, X., Zou, X., Yang, X., and Zhang, Z. (2018). Effect of Material Composition on Antistripping Performance of SBS Modified Asphalt Mixture under Dry and Wet Conditions. *J. Adhes. Sci. Technol.* 32, 1503–1516. doi:10.1080/01694243.2018.1426973

Liu, K. (2019). Research on Construction Fluidity of Gussasphalt Mixture. *Wuhan Ligong Daxue Xuebao (Jiaotong Kexue Yu Gongcheng Ban)/J. Wuhan Univ. Technol. (Transport. Sci. Eng.)* 43, 341–345. doi:10.3963/j.issn.2095-3844.2019.02.032

Lu, Z., He, Z., Yu, Q., and Gang, H. (2009). Influence of Rock Asphalt Modified Asphalt on Asphalt Rheological Property. *Chongqing Jiaotong Univ. (Nat. Sci. Version)* 28, 543–547. doi:10.3969/j.issn.1674-0696.2009.03.18

Luo, R., Shi, C., Fan, X., and Feng, G. (2018a). Research on Permanent Deformation of Gussasphalt Mixture under Dynamic Penetration. *Huazhong Keji Daxue Xuebao (Ziran Kexue Ban)/J. Huazhong Univ. Sci. Technol. (Nat. Sci. Ed.)* 46, 13–16. doi:10.13245/j.hust.180703

Luo, S., Qian, Z., Yang, X., and Lu, Q. (2018). Laboratory Evaluation of Double-Layered Pavement Structures for Long-Span Steel Bridge Decks. *J. Mater. Civil Eng.* 30, 04018111. doi:10.1061/(ASCE)MT.1943-5533.0002291

Mazumder, M., Ahmed, R., Wajahat Ali, A., and Lee, S.-J. (2018). SEM and ESEM Techniques Used for Analysis of Asphalt Binder and Mixture: A State of the Art Review. *Construction Building Mater.* 186, 313–329. doi:10.1016/j.conbuildmat.2018.07.126

Pfeiffer, J. P., and Doormaal, P. M. (1936). The Rheological Properties of Asphaltic Bitumens. *J. Inst. Pet.* 22, 414–440.

Pouget, S., Sauzéat, C., Di Benedetto, H., and Olard, F. (2010). Numerical Simulation of the Five-point Bending Test Designed to Study Bituminous Wearing Courses on Orthotropic Steel Bridge. *Mater. Struct.* 43, 319–330. doi:10.1617/s11527-009-9491-1

Qian, J., Wang, Q., Wu, W., and Zhang, H. (2013). Fatigue Performance of Gussasphalt concrete Made from Modified AH-70# Asphalt. *Mater. Des. (1980-2015)* 52, 686–692. doi:10.1016/j.matdes.2013.06.009

Qiu, Y., An, S., Rahman, A., and Ai, C. (2019). Evaluation and Optimization of Bridge Deck waterproof Bonding System Using Multi-Objective Grey Target Decision Method. *Road Mater. Pavement Des.* 21, 1844–1858. doi:10.1080/14680629.2019.1568288

Rasmussen, R. O., Lytton, R. L., and Chang, G. K. (2002). Method to Predict Temperature Susceptibility of an Asphalt Binder. *J. Mater. Civil Eng.* 14, 246–252. doi:10.1061/(asce)0899-1561(2002)14:3(246)

Shadkam, H. R., Dadsetan, S., Tadayon, M., Sanchez, L. F. M., and Zakeri, J. A. (2017). An Investigation of the Effects of limestone Powder and Viscosity Modifying Agent in Durability Related Parameters of Self-Consolidating concrete (SCC). *Constr. Build. Mater.* 156, 152–160. doi:10.1016/j.conbuildmat.2017.08.165

Singh, D., and Sawant, D. (2016). Understanding Effects of RAP on Rheological Performance and Chemical Composition of SBS Modified Binder Using Series of Laboratory Tests. *Int. J. Pavement Res. Technol.* 9, 178–189. doi:10.1016/j.ijprt.2016.06.002

Walters, R. C., Fini, E. H., and Abu-Lebdeh, T. (2014). Enhancing Asphalt Rheological Behavior and Aging Susceptibility Using Bio-Char and Nano-clay. *Am. J. Eng. Appl. Sci.* 7, 66–76. doi:10.3844/ajeassp.2014.66.76

Wang, H., and Li, G. (2015). Study of Factors Influencing Gussasphalt Mixture Performance. *Constr. Build. Mater.* 101, 193–200. doi:10.1016/j.conbuildmat.2015.10.082

Wang, M., Zhang, H., Zhu, M., Hao, Z., and Xue, X. (2011). "Research on Structure and Properties of Embedded Gussasphalt," in Proceedings of the GeoHunan International Conference, Hunan, China, 9–11 June, 2011.

Wang, C., Chen, Q., Fu, H., and Chen, J. (2018a). Heat Conduction Effect of Steel Bridge Deck with Conductive Gussasphalt concrete Pavement. *Constr. Build. Mater.* 172, 422–432. doi:10.1016/j.conbuildmat.2018.03.161

Wang, C., Yang, X., Li, Q., Guo, T., and Jiang, T. (2018b). Preparation and Performance of Conductive Gussasphalt concrete. *Transportmetrica A: Transport Sci.* 15, 55–70. doi:10.1080/23249935.2018.1449913

Wang, M., Fang, M. S., Zhang, G. J., Li, J., and Wen, F. (2019). Design of Asphalt Pavement Structure on Steel Deck of Hong Kong-Zhuhai-Macao Bridge. *Bridge Constr.* 49, 69–74. doi:10.3969/j.issn.1003-4722.2019.04.013

Wu, W. J., He, Z. Y., Hao, Z. H., and Wang, M. (2013). "Differences in Fatigue Behavior Among the Gussasphalt, SMA and AC," in *Advanced Materials Research*. doi:10.4028/www.scientific.net/amr.723.276

Xie, F., Zhang, D., Zhou, A., Ji, B., and Chen, L. (2017). On the Viscoelastic Parameters of Gussasphalt Mixture Based on Modified Burgers Model: Deviation and Experimental Verification. *Adv. Mater. Sci. Eng.* 2017, 1–11. doi:10.1155/2017/4324765

Xin, C., Lu, Q., Ai, C., Rahman, A., and Qiu, Y. (2017). Optimization of Hard Modified Asphalt Formula for Gussasphalt Based on Uniform Experimental Design. *Constr. Build. Mater.* 136, 556–564. doi:10.1016/j.conbuildmat.2017.01.068

Yang, J., Zhu, X., Yuan, Y., and Li, L. (2020). Effects of Aging on Micromechanical Properties of Asphalt Binder Using AFM. *J. Mater. Civil Eng.* 32, 04020081. doi:10.1061/(ASCE)MT.1943-5533.0003030

Yao, H., You, Z., Li, L., Lee, C. H., Wingard, D., Yap, Y. K., et al. (2013). Rheological Properties and Chemical Bonding of Asphalt Modified with Nanosilica. *J. Mater. Civil Eng.* 25, 1619–1630. doi:10.1061/(ASCE)MT.1943-5533.0000690

Yao, B., Cheng, G., Wang, X., and Cheng, C. (2013). Characterization of the Stiffness of Asphalt Surfacing Materials on Orthotropic Steel Bridge Decks Using Dynamic Modulus Test and Flexural Beam Test. *Construction Building Mater.* 44, 200–206. doi:10.1016/j.conbuildmat.2013.03.037

Yao, H., and You, Z. (2016). Effectiveness of Micro- and Nanomaterials in Asphalt Mixtures through Dynamic Modulus and Rutting Tests. *J. Nanomater.* 2016, 1–14. doi:10.1155/2016/2645250

Yao, H., You, Z., Li, L., Shi, X., Goh, S. W., Mills-Beale, J., et al. (2012). Performance of Asphalt Binder Blended with Non-modified and Polymer-Modified Nanoclay. *Construction Building Mater.* 35, 159–170. doi:10.1016/j.conbuildmat.2012.02.056

You, Z., Mills-Beale, J., Fini, E., Goh, S. W., and Colbert, B. (2011). Evaluation of Low-Temperature Binder Properties of Warm-Mix Asphalt, Extracted and Recovered Rap and Ras, and Bioasphalt. *J. Mater. Civil Eng.* 23, 1569–1574. doi:10.1061/(ASCE)MT.1943-5533.0000295

Yu, X., Burnham, N. A., and Tao, M. (2015). Surface Microstructure of Bitumen Characterized by Atomic Force Microscopy. *Adv. Colloid Interf. Sci.* 218, 17–33. doi:10.1016/j.cis.2015.01.003

Zhang, H., Qian, J. S., Wu, W. J., Zhang, F., and Hao, Z. H. (2010). Fatigue Life Analysis of Gussasphalt concrete Based on Energy Method. *Tumu Jianzhu Yu Huanjing Gongcheng/Journal Civil, Architectural Environ. Eng.* 32, 135–140.

Zhang, H., Zhang, G., Han, F., Zhang, Z., and Lv, W. (2018). A Lab Study to Develop a Bridge Deck Pavement Using Bisphenol A Unsaturated Polyester Resin Modified Asphalt Mixture. *Construction Building Mater.* 159, 83–98. doi:10.1016/j.conbuildmat.2017.10.126

Zhao, Y., Ni, F., Zhou, L., and Jiang, J. (2020). Performance Evaluation of Long-Span Suspension Bridge Pavement Based on Long-Term Maintenance Data. *J. Mater. Civil Eng.* 32, 04019363. doi:10.1061/(ASCE)MT.1943-5533.0003019

Zou, G., Xu, X., Li, J., Yu, H., Wang, C., and Sun, J. (2020). The Effects of Bituminous Binder on the Performance of Gussasphalt Concrete for Bridge Deck Pavement. *Materials* 13, 364. doi:10.3390/ma13020364

**Conflict of Interest:** TL, ZY, and NS were employed by Shandong Hi-speed Construction Management Group Co., Ltd.

The remaining authors declare that the research was conducted in the absence of any commercial or financial relationships that could be construed as a potential conflict of interest.

**Publisher's Note:** All claims expressed in this article are solely those of the authors and do not necessarily represent those of their affiliated organizations, or those of the publisher, the editors and the reviewers. Any product that may be evaluated in this article, or claim that may be made by its manufacturer, is not guaranteed or endorsed by the publisher.

frontiers | Frontiers in Materials

REVIEW
published: 14 April 2022
doi: 10.3389/fmats.2022.879245

# Literature Review on the Discrete Element Method in Asphalt Mixtures

*Hui Yao*[1]*, *Mei Xu*[1], *Junfu Liu*[1], *Yu Liu*[2], *Jie Ji*[3] and *Zhanping You*[4]

[1]Beijing Key Laboratory of Traffic Engineering, College of Metropolitan Transportation, Faculty of Architecture, Civil, and Transportation Engineering, Beijing University of Technology, Beijing, China, [2]Professor, School of Highway, South Erhuan Middle Section, Chang'an University, Xi'an, China, [3]Professor, School of Civil Engineering and Transportation, Beijing University of Civil Engineering and Architecture, Beijing, China, [4]Professor, Department of Civil and Environmental Engineering, Michigan Technological University, Houghton, MI, United States

Asphalt mixtures are commonly used in pavement engineering, especially for highway construction. The mechanism exploration and analysis of pavement distress are the main challenges for researchers and industry managers. Thereby, it is important to understand their properties and interaction mechanisms in asphalt mixtures. It is difficult to conduct some sophisticated or microscale tests in the laboratory, and numerical simulation and virtual tests can be solutions for these cases with low costs. The Discrete Element Method (DEM) is a promising tool for researchers to undertake these tasks. This paper mainly summarized and analyzed the research progress and development prospect of DEMs in asphalt mixtures from a series of technical sections. The laboratory test results were often used to calibrate the DEM simulations as well as Two-dimensional (2D) and Three-dimensional (3D) modeling. Several modeling methods were developed to generate digital samples, like user-defined, image-based, random-modeling. In addition, the conclusions can be referenced by researchers for the development of numerical simulations.

**Keywords: pavement engineering, asphalt, asphalt mixtures, discrete element, modeling**

OPEN ACCESS

***Edited by:***
*Antonio Caggiano, Darmstadt University of Technology, Germany*

***Reviewed by:***
*Tao Ma, Southeast University, China*
*Tuo Huang, Changsha University of Science and Technology, China*
*Augusto Cannone Falchetto, Aalto University, Finland*

***Correspondence:**
*Hui Yao*
*huiyao@mtu.edu*

***Specialty section:***
*This article was submitted to Structural Materials, a section of the journal Frontiers in Materials*

***Received:*** *19 February 2022*
***Accepted:*** *25 March 2022*
***Published:*** *14 April 2022*

***Citation:***
*Yao H, Xu M, Liu J, Liu Y, Ji J and You Z (2022) Literature Review on the Discrete Element Method in Asphalt Mixtures. Front. Mater. 9:879245. doi: 10.3389/fmats.2022.879245*

## 1 INTRODUCTION

Generally, the behaviors of materials can be evaluated from the performance of asphalt mixtures, such as high-temperature stability, low-temperature crack resistance, durability, workability, etc., The laboratory test method is a good way to understand the properties of asphalt mixtures. Also, another analysis way is the numerical simulation method to get the fundamental views and insights. Different numerical simulation methods are gradually emerged to study the properties of asphalt mixtures, such as the Finite Element Method (FEM), Discrete Element Method (DEM), Molecular Dynamics (MD) method, etc., Three numerical methods focus on the different scales. The time scale is from femtosecond to second, and the length scale is from meter to Angstrom. The time scale and length scale of the DEM is microsecond and micrometer, respectively. The DEM is a suitable numerical simulation method to analyze the interactions in asphalt mixtures at the microscale. Many tests cannot deal with the interaction between materials at the microscale, but the DEM is a good way to explore mechanisms at the microscale. Therefore, many scholars used the DEM to research the properties of asphalt mixtures in recent years. The following discussions relate to applications of the DEM in asphalt mixtures.

Generally speaking, the research on the performance of asphalt mixture mainly starts from the macroscopic and microscopic aspects. Firstly, from the macroscopic perspective, the experimental

method is a more traditional method to study the performance of asphalt mixtures, and it is also the most widely used method. It is controlled by humans in the laboratory, and its advantage is strong intuitiveness. 1) Although some errors cannot be avoided during the test process, the test results are still generally more reliable from realistically thinking. However, the costs of some tests are high and the operation process is also complicated and time-consuming. 2) During data collection in the tests, indirect and direct measures can be collected, like stress and strain data. However, the stress and strain values of each point in the entire material cannot be obtained directly and the route of the force transfer cannot be directly demonstrated. It indicates that the mechanisms or operation ways are not visible for the researchers during laboratory tests. Therefore, different numerical methods are invented and developed for different purposes.

Compared with the experimental method, the advantages of numerical simulations are 1) the cost is low and most cases in the tests can be simulated using the computer resource; 2) any type or amount of loading can be applied without worrying about the actual loss caused by the excessive load; 3) some extreme situations cannot be achieved and done by the experimental method and they can also be applied in the numerical methods. On the other hand, the numerical simulation method can analyze the stress of each area and measuring point of the test materials, and get the change of stress and strain, as well as the force and displacement distributions. The test results can be obtained quickly through certain operation settings, but the numerical simulation method is not perfect, and there are some shortcomings, such as abstraction, intuition, credibility, etc., The accuracy of the simulation can make certain predictions about the experiment results. The numerical simulation method mainly refers to the finite element method and DEM, which are the most commonly used. The DEM is used to solve the problems of discontinuous media by analyzing the interlocking contacts of discrete elements. The constitutive relation of the contact is found out and the physical and mechanical model of contact is established. Then the discontinuous and discrete elements are simulated according to Newton's second law of motion. The DEM can better explain the stress or loading types, deformation mechanism, and failure processing of the asphalt mixtures from the meso and micro perspectives. It can also be used to predict rutting initiations, fatigue mechanisms, and engineering evaluation indexes for asphalt mixtures. However, the finite element method is not good for large and discontinuous deformations and is more suitable for the study of continuum problems. Therefore, the researchers tend to use the DEM to simulate the stress-strain relationships, damage situations, and fracture processing of the asphalt mixtures. The examples of specific studies on discrete elements are discussed as follows:

The parameters of the generalized Burgers model fitted by Mao (2018) were used to simulate the uniaxial test of asphalt mortars with a three-dimensional (3D) DEM. Although the results had deviations from the tests, this simulation provided a good attempt to understand the asphalt mortars and their behaviors. The scholars used the 3D DEM to simulate the porosity changes of asphalt mixtures under the dynamic loading and summarize the changing laws Zhang and Li

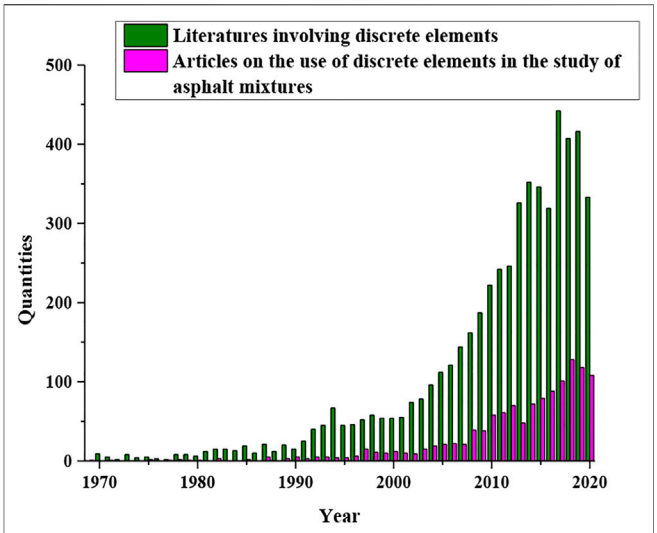


**FIGURE 1 |** Trends for the discrete element method (DEM) in the literature review.

(2017). The results showed that the DEM was an effective way to simulate elastic-plastic properties of the asphalt mixtures, and simulation results were also of great help to improve the durability and drainage performance of the asphalt pavement. Hou et al. (2015) established discrete element specimens for asphalt mastic macadam mixtures, SMA-13, and applied vehicle loads to study its meso-mechanical response under loading. Huang et al. (2008) carried out a series of biaxial compression tests on sand granular materials under different densities and confining pressures, and further analyzed their mechanical properties through the response of sand characteristics from simulation tests. Compared with laboratory test methods, the DEM simulation can provide the details of meso-structural changes in the loading process. The researchers simulated the Compaction Flow Test (CFT) of asphalt mixtures based on the 3D DEM (Roozbahany et al. (2019) and analyzed several factors, including the fluidity of asphalt mixture particles, mold size, loading strip geometry and loading rate, etc., Kusumawardani and Wong (2020) carried out the DEM simulation and laboratory tests on the mechanical properties of Porous Asphalt Mixtures (PAM) with three aggregates shapes, and also analyzed the influence of the aggregate shape on the accumulation of mixtures. Other studies tried to simulate the rutting test of asphalt mixtures with 3D DEM and analyze the influence of internal structural characteristics of the mixtures on the rutting behavior (Zhang et al., 2018). The three-stage simulations (gravity drop, static, and rotary compaction) were performed on three different asphalt mixtures to analyze the internal consistency of the mixtures (Zhou et al., 2020). The randomly generated algorithm was used to establish a model to simulate the aggregate penetration test and the uniaxial creep test. Compared with the experimental tests, it was proved that the established microstructure models were correct and simulation results are feasible (Ma et al., 2016b). The static indirect tensile test of the asphalt mixture was simulated, and the laboratory

experiment was carried out to verify the model. The crack propagation mechanism of asphalt mixtures was explained through simulation and test results (Dan et al., 2018). There are many scholars to publish more manuscripts related to the DEM and they are trying to solve many kinds of engineering problems through numerical simulations. According to the currently statistical survey and literature review (main databases), research on the application of the DEM showed an increasing trend, and also the topic of the literature mainly focused on asphalt mixtures. This trend can be seen from **Figure 1**.

This paper briefly introduced the historical status and development of the DEM, and demonstration of its advantages and disadvantages, as well as differences between the laboratory test method and DEM in performance analysis of asphalt mixtures. The key point was to summarize characteristics of the DEM and learn from others. The DEM applications and shortcomings were also mentioned, as well as prospects of its future development in civil engineering.

# 2 HISTORICAL OVERVIEW AND DISCRETE ELEMENT METHOD

## 2.1 Basic Overview of Discrete Element Method

The numerical simulation is a more advanced analysis method based on computer resources and it is different from the traditional laboratory test method. The numerical simulation mainly included the finite element method and boundary element method before the invention of the DEM (Wang and Li, 2005). As a new numerical simulation method, the DEM was applied to various studies by researchers. Compared with the former two methods, the DEM focused on solutions of discontinuous media based on Newton's second law of motion (F = ma) (Wang et al., 2019). The DEM software PFC (Particle Flow Code) was more suitable and widely used (Liu et al., 2020). The PFC was divided into two-dimensional (2D) and three-dimensional (3D) PFC programs. The PFC was based on the theories of Newton's second laws and relationship between force and displacement, when simulating the related model of asphalt materials (You and Liu, 2010).

## 2.2 Historical Overview

The DEM was originally proposed by Prof. Cundall (1971) as a method for the analysis of granular discrete materials. It was originally used to analyze geotechnical problems. He also realized the purpose of interactive simulations after inputting and outputting geometric data on the computer (Cundall, 1974), and developed a 2D plane "Ball" program to simulate the behavior of granular media (Cundall, 1978). Cundall and Strack (1979) carried out the numerical simulation in 1979 and compared them with the real experimental data. The use of the DEM can carry out more realistic simulations of specimens. However, due to the immaturity of the technology and the limitations of the conditions at that time, the research was carried out based on the 2D plane. The 3D program was not developed because of the complexity and advanced computer technology. After the development of the computer algorithms, the DEM was gradually accepted to solve the problem of discontinuous media. One of DEM companies is called "ITASCA," and it developed many discrete element programs including the 2D discrete element program—UDEC (Universal Distinct Element Code), and 3D discrete element program—3DEC (3D Distinct Element Code). These programs aimed to solve problems from rock mechanics and mining engineering.

Wang (1986a) introduced the basic principle and application cases of DEMs to the field of rock mechanics and engineering in China at the first National Symposium. The DEM can also be generalized for other research areas (Wang, 1986b), like mining or other engineering fields (Wang and Xing, 1986; Wang et al., 1987; Xing and Wang, 1988; Wang and Xing, 1991; Wang and Xing1993a; Wang and Xing1993b). The DEM progress was summarized from application examples (Wang and Xing, 1989; Wang, 1990). The 2D and 3D DEMs were also promoted for the simulation of civil engineering materials (Wang and Xing, 1990; Xing and Wang, 1990). One of the discrete element programs was called "MatDEM" based on MATLAB and it was developed by Liu et al. (2020) for 3D DEM. This program can build the virtual particles of asphalt mixtures with 2D and 3D models. Another discrete element simulation software "StreamDEM" was developed and it improved the simulation speed and efficiency based on the GPU operation. It met the calculation requirement of the large-scale and large number of particles (million levels), and can be commonly used in the engineering fields (Zhang and Zhang, 2016; Zhang et al., 2017).

# 3 RESEARCH METHODS FOR ASPHALT MIXTURES

## 3.1 Analysis of the Laboratory Test Method

The traditional tests were employed to evaluate the properties of the asphalt binders and mixtures with different modifiers at different conditions based on the Marshall and Superpave systems. The recycled materials are the hotspot for the development of asphalt mixtures. Recently, Li et al. (2021) recycled SMA-13 asphalt mixtures for the pavement reconstruction project. Song (2021) utilized waste materials to reduce emissions and increase waste consumption, as well as the polypropylene fibers and glass. Yao et al. (2021) used comparative experiments to analyze performance with other waste materials, such as red mud. It was mixed into asphalt mixtures by the replacement of the mineral powder. Based on the test results, it is a good way to use the waste resources in the pavement engineering. In addition, different modifiers were used for performance improvement of asphalt mixtures. The polyester fibers can also effectively improve performance of asphalt mixtures with the Reclaimed Asphalt Pavement (RAP) (Zhong and Zhang, 2021). The comparative tests were also used to

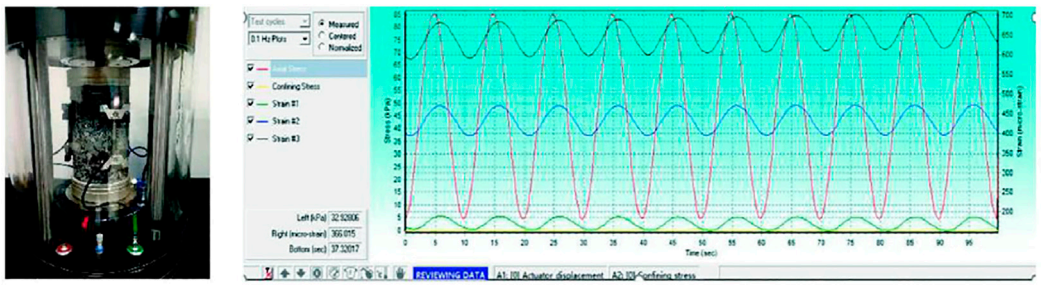

A the dynamic modulus test samples (Jia et al., 2021); B changes in the stress and strain with loading frequencies (Jia et al., 2021);

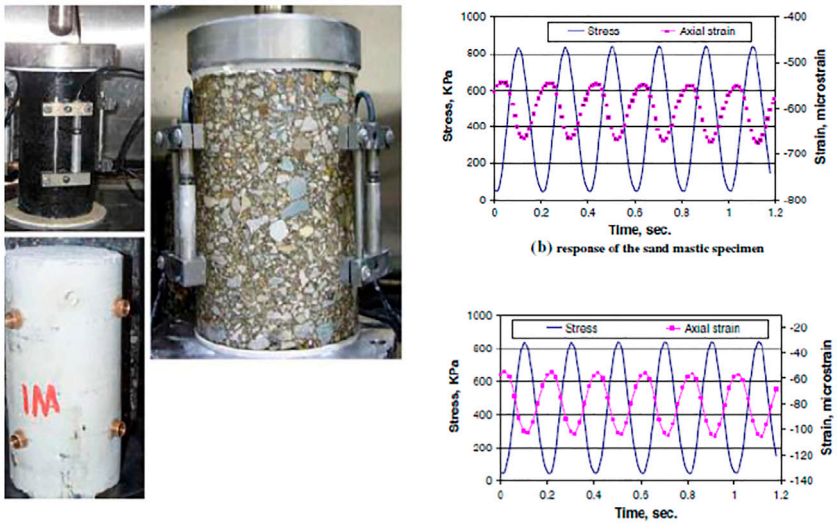


C the dynamic modulus tests with the sand mastic and asphalt mixtures (You et al., 2009;Adhikari and You, 2010); D stress and Strain response during the tests (You et al., 2009;Adhikari and You, 2010);

**FIGURE 2 |** Laboratory tests and processing for the dynamic modulus of the asphalt mixtures (Jia et al., 2021; You et al., 2009; Adhikari and You, 2010). **(A)** the dynamic modulus test samples (Jia et al., 2021); **(B)** changes in the stress and strain with loading frequencies (Jia et al., 2021); **(C)** the dynamic modulus tests with the sand mastic and asphalt mixtures (You et al., 2009; Adhikari and You, 2010); **(D)** stress and Strain response during the tests(You et al., 2009; Adhikari and You, 2010).

determine the optimum content of these modifiers, like the Freeze-Thaw Test, Four-Point Bending Beam, Dynamic Shear Rheometer (DSR) and Bending Beam Rheometer (BBR) test (Gao, 2021). Meng et al. (2021) studied the effect of the snow melting agent on the adhesion of asphalt mixtures. The use of the snow melting agent (chloride) did not affect the adhesion between asphalt mixtures, but the negative effect on performance of asphalt mixtures may occur by the increase of the agent content. The Styrene-butadiene-styrene (SBS) modified asphalt binders were used for the preparation of the composite modified asphalt binders to enhance the low-temperature performance (Xia et al., 2021). **Figures 2A,B** show the dynamic modulus test samples and curve of stress and strain changes with time in asphalt mixtures (Jia et al., 2021).

The dynamic modulus test is conducted under the haversine or sinusoid loading conditions. The output parameters (the dynamic modulus and phase angle) are measured at different temperatures and frequencies. Before testing, the samples are mixed by asphalt binders and aggregates with the certain gradation. The mixtures are compacted by the Superpave Gyratory Compactor (SGC) with a targeted air void. The samples are compacted and cut with the specified dimension (100 mm in diameter and 150 mm in height); The detailed procedure can be found from the specification AASHTO T378. The indirect tensile test is measured by the Universal Testing Machine (UTM), and this test is destructive and used to evaluate the moisture susceptibility. This test results can also be used to predict the performance of anti-stripping and fracture toughness. The range of the air void in the asphalt mixture is around 6%–8%. The dimension of the sample is 100 mm in height and 63.5 mm in diameter. One group of the samples is cured with different conditions and another group is stored in the dry environment. The procedure

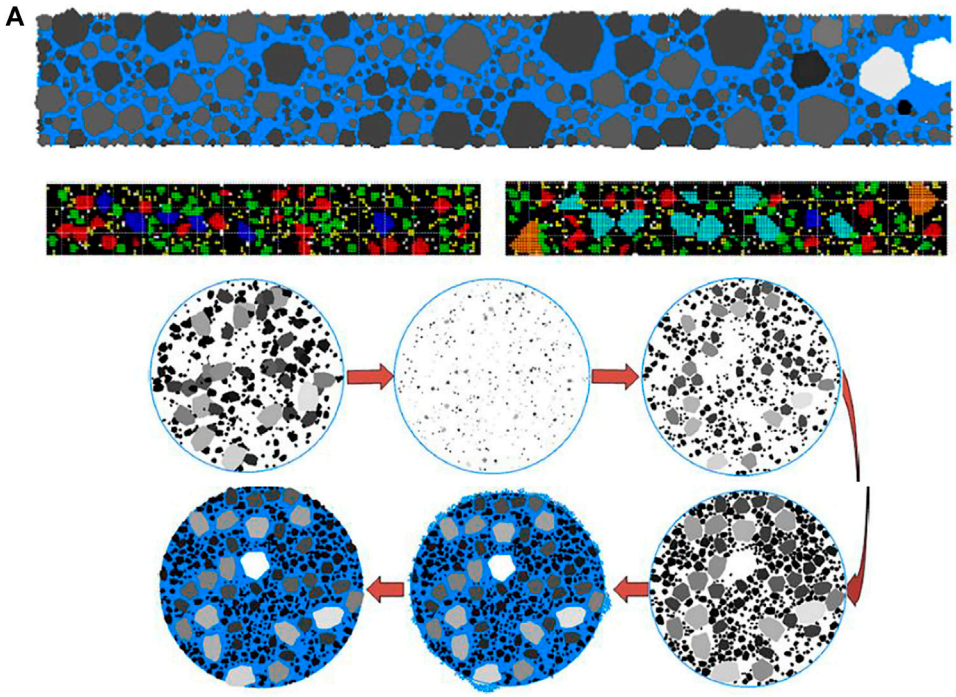

2D discrete element samples of the asphalt mixtures with different sizes (Nian et al., 2021) (Zhang et al., 2018)

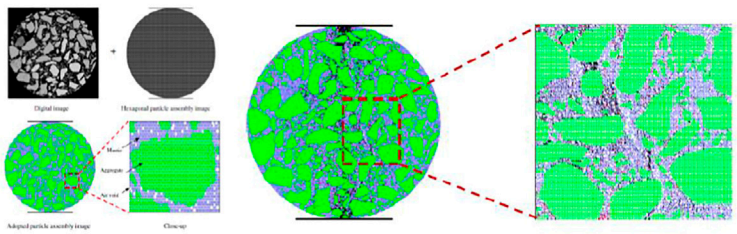

2D DEM model generation for the AC13 asphalt mixture (Peng and Sun, 2015a)

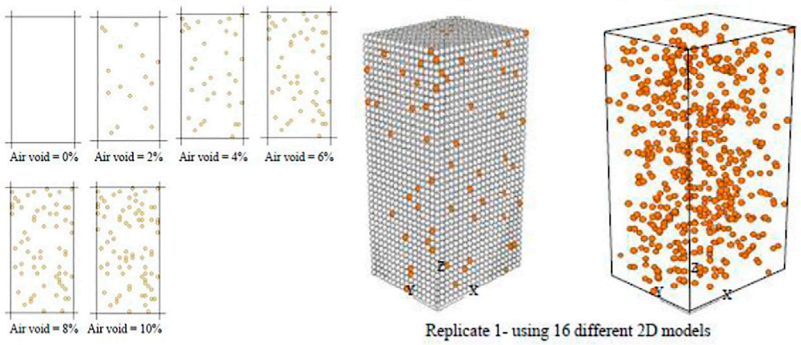


Air void distribution in the 2D DEM models and 3D DEM models from 16 slices of 2D models (You et al., 2010)

**FIGURE 3 |** 2D DEM samples with different gradation and air void distributions (Nian et al., 2021; Zhang et al., 2018; Peng and Sun, 2015a; You et al., 2010). **(A)** 2Ddiscrete element samplesof the asphalt mixtureswith different sizes (Nian et al., 2021; Zhang et al., 2018). **(B)** 2D DEM model generation for the AC13 asphalt mixture (Peng and Sun, 2015a). **(C)** Air void distribution in the 2D DEM models and 3D DEM models from 16 slices of 2D models (You et al., 2010).

of this test can be found from the specification AASHTO T283. These are the details for the dynamic modulus and indirect tensile test.

## 3.2 Discrete Element Analysis

### 3.2.1 Two-Dimensional Discrete Element Method

In many early studies of the discrete element modeling method, the 2D model was commonly used and the advantage of the 2D model is high calculation speed for the complex system. Sometimes, although simulation results of some relatively complex experiments are not consistent with the actual measured data, the 2D model program is still advantageous for the experiments with the simple internal structure of the mixture and the analysis of the general trend without requiring accurate results. The asphalt mixtures with a 2D discrete element program as an example (Nian et al., 2021; Peng and Sun 2015a) are shown in **Figure 3**.

Liu et al. (2009) established a 2D discrete element model to focus on the viscoelastic properties of asphalt mixtures with the burger model. Through the DEM simulation of the asphalt mixtures, the dynamic modulus and phase angle of the asphalt mixtures were predicted under the sinusoidal loading, and the viscoelastic models were verified by the measured results. There is only a little research on the influence of aggregate uniformity on the splitting strength test of asphalt mixtures. The simulation results showed that whether the aggregates are uniform or not has little effect on the average splitting strength. However, it was closely related to the variability of splitting strength, which showed that the coefficient of variation of the splitting strength decreases with a better aggregate uniformity (Peng Y. and Sun L., 2015a). The variation relationship of the splitting strength under different loading rates was that the higher the loading rate was, the higher the splitting strength was with a logarithmic growth (Pei et al., 2010). The cracking and failure properties of asphalt mixtures with three different gradations were analyzed and compared under the splitting test simulations using the 2D DEM. The simulation results demonstrated that the large nominal maximum particle size and huge porosities of aggregates with low asphalt contents caused low splitting strength in asphalt mixtures. The crack resistance of the OLSM-25 (Open-graded Large Stone Asphalt Mixes) asphalt mixture was better than that of AC-16 and AC-25 (Asphalt Concrete) (Guo and Chen, 2014; Guo and Chen, 2015). The splitting test process of four different aggregates was simulated by the 2D DEM and the influence of aggregate properties on splitting strength was also analyzed with laboratory tests. It was concluded that the high stiffness and strength of aggregates lead to a strong bearing capacity of the asphalt mixture models (Xiong, 2013). The indirect tensile test of the asphalt mixture was simulated by 2D DEM to analyze the influence of the bond strength ratio and loading rate on the splitting strength of the asphalt mixture. The results showed that the splitting strength decreased with the increase of the bond strength; the splitting strength increases with the increase of loading rate, and it is proved that the performance of asphalt mixtures plays the most important role in enhancing the crack resistance of asphalt mixture (Chang et al., 2011). Four kinds of aggregates with different properties and gradations were selected (Yu, 2015) for laboratory tests and simulations of the splitting test with the 2D DEM. The feasibility of discrete element simulation was studied and the influence of aggregates with different properties on the cracking of asphalt mixtures was analyzed. The results demonstrated that the DEM simulation may provide more intuitive and effective details compared to the laboratory test processing, like loading changes, displacements, and cracking propagations during testing. However, this study also revealed the limitations of the 2D DEM, such as the lack of geometric information. **Figure 4** shows the loading-displacement relationship of the AC-16 gradation section at different temperatures when simulating the splitting test of the asphalt mixture by a 2D DEM (Peng and Sun 2015b). In addition, the 2D DEM can be also used in many other studies, like other Marshall system tests of asphalt mixtures.

### 3.2.2 Three-Dimensional Discrete Element Method

From the morphology perspective, the effect of the 3D model is close to the real experiment compared to the 2D one and the 3D model has more complex structures and interactions. During the generation and optimization of 3D models, the calculation time is longer than that of the 2D model and the time depends on the element number in the simulation system. Sometimes, the computing time can be greatly reduced using the temperature-frequency superposition method, but the computation time is still relatively long compared to the 2D model. The temperature-frequency superposition method specifically is to amplify or adjust the normal loading frequency from the available test results and convert Burger's model parameters under the normal frequency into parameters under the virtual frequency. The model can be established with the magnified virtual frequency and is matched by the modified Burger's model parameters. The comparative test results of the dynamic modulus of asphalt mixtures at different temperatures and frequencies showed that the simulation results were close to measured results under the temperature-frequency superposition method. However, the calculation time was greatly reduced. When the computation time took months or even years in the traditional method, it can be reduced to only hours, and the calculation speed increased rapidly (Liu and You, 2011a). It has been used most by scholars in recent years.

Due to the limitation of the computer technology in the early stage, the research with the 3D DEM is far less than the 2D one. Dr. You's research team members conducted much research on the 3D DEM, like a 3D DEM model to predict the dynamic modulus and phase angle of asphalt mixtures, and the relative errors between the laboratory and simulation results were within an acceptable range (You and Liu, 2010). Another 3D DEM model was established to simulate the creep test of the asphalt mixture to study the creep stiffness and response (You et al., 2011), and also, it was used to analyze whether the element size affected the performance of the asphalt mixtures (especially in mechanics) (Liu et al., 2012). The dynamic modulus of the asphalt mixture was predicted and the influence of the aggregate size was analyzed by comparing the predicted results with the measured data (Adhikari and You, 2011). The fitting curves of the dynamic

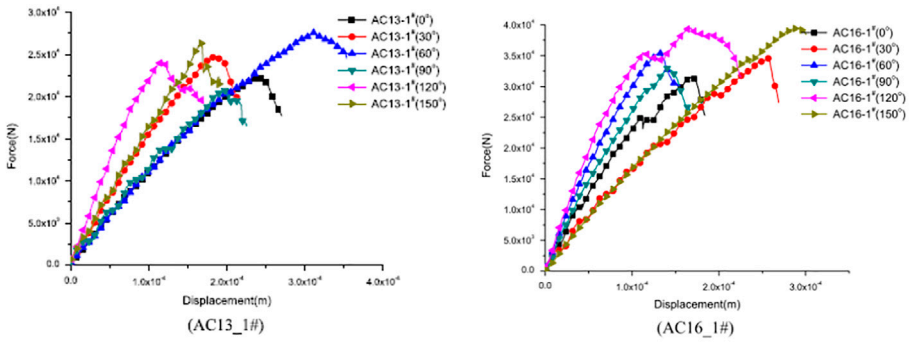


(i) force-displacement distributions in the DEM models, AC13 and AC16

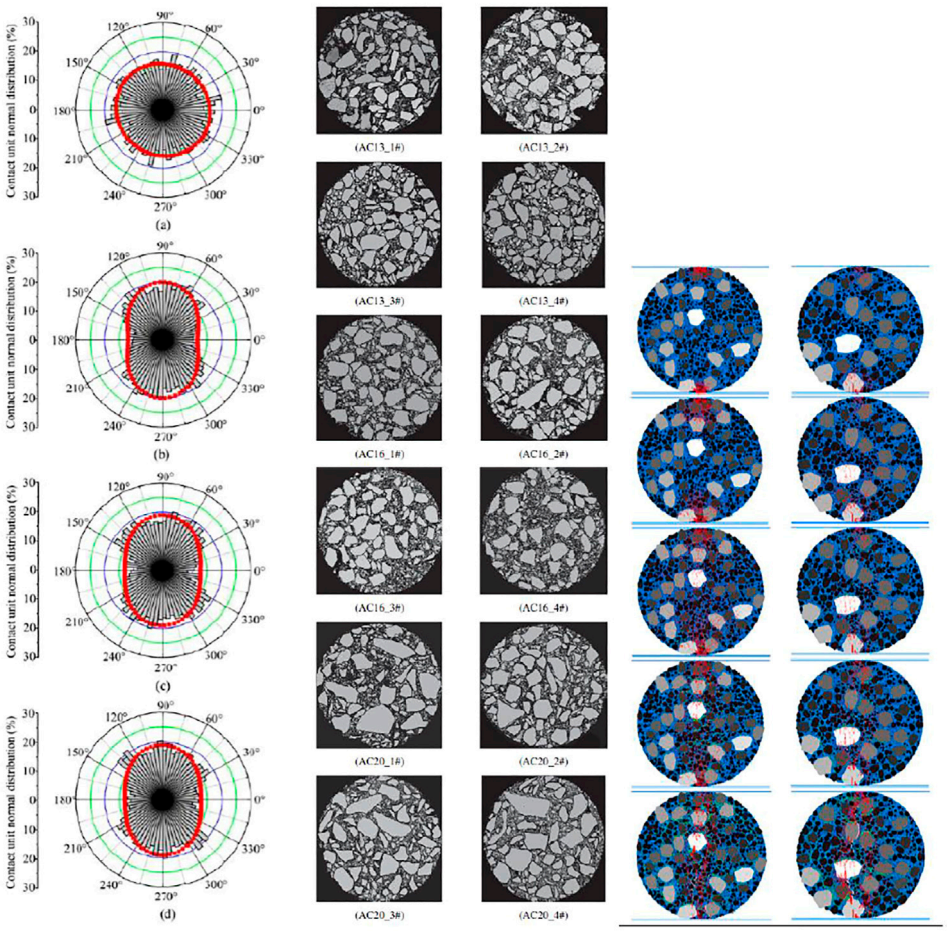


(ii) Distributions of contacts with different shearing statuses (a) 0; (b) 10%; (c) 20%; (d) 40% (Huang et al. (2008); (iii) Scanning 2D samples of the asphalt mixtures (Peng and Sun, 2015b); (iv) the contact responses under the loading (Nian et al., 2021)

**FIGURE 4 |** Load-displacement curves of the splitting test (indirect tensile test) and contact distributions (Peng and Sun, 2015b; Huang et al., 2008; Nian et al., 2021). **(i)** force-displacement distributions in the DEM models, AC13 and AC16. **(ii)** Distributions of contacts with different shearing statuses (A) 0; (B) 10%; (C) 20%; (D) 40% (Huang et al., 2008); **(iii)**Scanning 2D samples of the asphalt mixtures(Peng and Sun, 2015b); **(iv)** the contact responses under the loading (Nian et al., 2021).

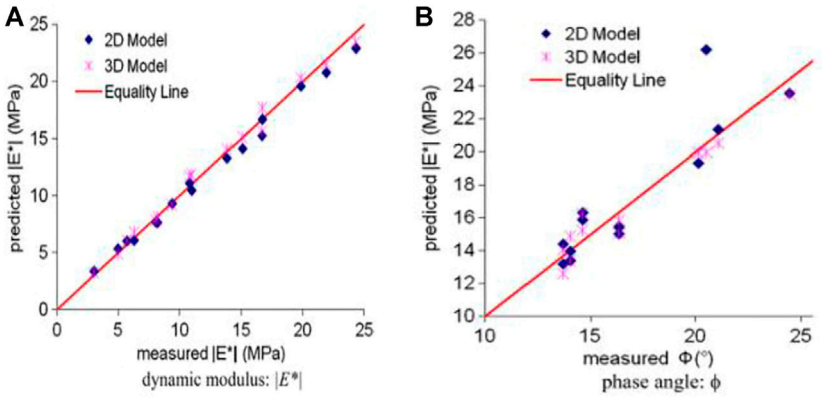


**FIGURE 5 |** Fitting curves between the simulation data and measured values in the laboratory with the 2D and 3D DEMs, **(A)** the dynamic modulus; **(B)** the phase angle (Liu and You, 2011b).

modulus and phase angle of asphalt mixtures are shown in **Figure 5**, and the relationship between the 2D and 3D DEM simulation values and laboratory-measured values was demonstrated (Liu and You, 2011b). Both 2D and 3D DEM coincide with the test results. Zhang et al. (2015) modeled rubber particles and aggregates, respectively, to simulate the splitting test of the asphalt mixture by the 3D DEM. The simulation results were in good agreement with the test results. It can be seen that it was successful to use the DEM to simulate the test processing from the initial loading and cracking to the failure of the asphalt mixture. In addition, the contact model in the DEM is composed of three built-in parts: "stiffness model, slip model and bonding model." These models constitute other complicate models. The slip model in the DEM means the frictional properties between contact points. The bonding model represents shear and normal strength between contact points. The stiffness model addresses the relationship between the contact forces and displacements of elements. The viscoelastic models or properties of asphalt mixtures can be expressed by the Burger's model and this model can be constituted from three parts (stiffness model for asphalt mastics and aggregates or within asphalt mastics; slip model for all contacts; bonding model for all contacts except between aggregates). Thereby, different viscoelastic models can be further formed from three contact parts in the DEM (Liu et al., 2012).

The Digital Image Processing Technology and Computerized Tomography (CT) Scanning Technology were also employed and assisted for the DEM simulation to explore the interaction mechanisms in the asphalt mixtures. Different factors were analyzed through the splitting test of the asphalt mixture with the 3D DEM by Wan (2016), including the aggregate gradation, asphalt contents, temperatures, and loading rates. The research results were consistent with the previous analysis results. A possible reason for the error between simulation and measured results is the selection of parameters in the DEM models. It can be concluded and referred that 3D DEM simulation is more stable and reliable than the 2D one through the comparison between microstructures of the 2D and 3D DEM models (Peng et al., 2016). The accuracy of the simulation model was also improved from the 2D model to the 3D model (Peng and Bao, 2018). The influence of the aggregate gradation and temperature on the splitting strength of asphalt mixtures was also analyzed with the 3D DEM by Peng et al. (2019). The DEM simulation data trend of the asphalt mixtures was consistent with the laboratory test results. However, minor errors can be found in the simulation data. Further studies were needed for the improvement method and fundamental interactions. **Figure 6** shows the 3D asphalt mixture DEM model (Shan et al., 2019; Liu and You, 2011b; Ma et al., 2016b; You et al., 2008; Zhou et al., 2020; Liu et al., 2012).

The aggregate uniformity of asphalt mixtures was also investigated with the 3D DEM through the low-temperature splitting strength, and the Cohesive Zone Model (CZM) was also used in the DEM model to explore the relationship between the aggregate uniformity and splitting strength of asphalt mixtures. In the study of Liu et al. (2018), the same conclusion was obtained as the previous study (Yu, 2015) did. In recent years, the 3D DEM and the cohesive zone model were also used by many scholars to study the splitting strength of asphalt mixtures. The asphalt and aggregate models were reconstructed by Liang et al. (2019) to simulate the splitting test with the 3D DEM and MATLAB, and the cohesive model in this model was applied. The cohesive model was also combined with the finite element analysis in six kinds of asphalt mixtures. The results showed that the splitting strength trends of the asphalt mixtures were the same as the experimental results roughly. The DEM simulation was feasible for the asphalt mixtures and provided a reference for the fundamental research. The applicability of the contact bond and parallel bond models was explored by Shan et al. (2019) and Sheng et al. (2018) through the 2D model and 3D DEM models with different parameters. The results showed that it was reasonable to adapt the parallel bond model when simulating the mechanical properties of asphalt mixtures with the load-displacement behavior. The splitting test is commonly used for the evaluation of water susceptibility and permanent deformation resistance of asphalt

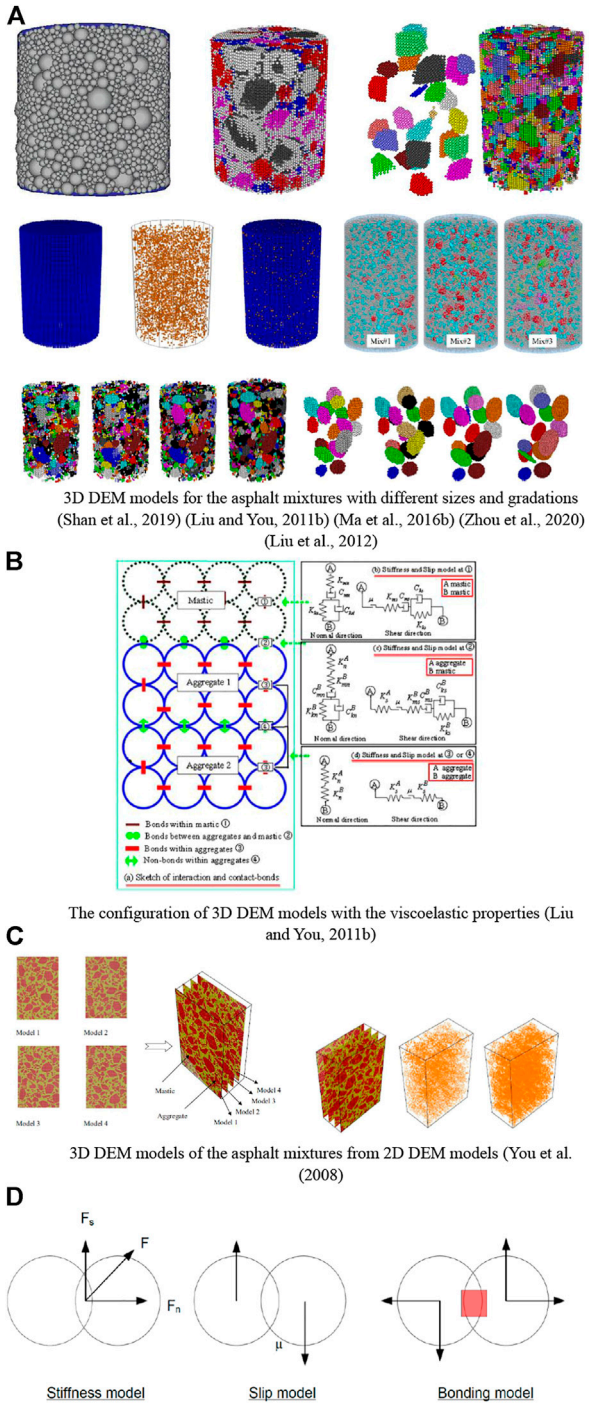


**FIGURE 6 |** Three-dimensional discrete element model and DEM viscoelastic configurations of the asphalt mixtures (Shan et al., 2019; Liu and You, 2011b; Ma et al., 2016b; Zhou et al., 2020; You et al., 2008; Liu et al., 2012). **(A)** 3D DEM models for the asphalt mixtures with different sizes and gradations (Shan et al., 2019; Liu and You, 2011b; Ma et al., 2016b; Zhou et al., 2020; You et al., 2008; Liu et al., 2012). **(B)** The configuration of 3D DEM models with the viscoelastic properties (Liu and You, 2011b). **(C)** 3D DEM models of the asphalt mixtures from 2D DEM models(You et al., 2008). **(D)** Three basic contact models in the DEM.

mixtures. The dynamic modulus test of the asphalt mixture is also used for the evaluation of the high- and low-temperature performance. The 3D DEM is a promising way to understand the microscopic behavior of the asphalt mixtures, as well as the splitting test and dynamic modulus test of asphalt mixtures. More fundamental understanding between the materials may be revealed and induced from the DEM simulations in the near future.

# 4 DISCRETE ELEMENT MODELING METHOD AND SIMULATION PROCESS

## 4.1 Modeling Method

Generally speaking, there are three modeling methods to construct the microstructure of asphalt mixtures with DEM, including the idealized model, randomly generated irregular shape model and image-based model. The idealized model cannot represent the geometric properties of aggregates and mixtures, and does not have authenticity; the image-based model can truly simulate the characteristic structures of asphalt mixtures with the help of computer scanning technology. However, it is dependent on the laboratory conditions. The scanning equipment is expensive and the cost is relatively high. The testing process is long and complex; the randomly generated irregular shape model is independent of the laboratory, which is more convenient and faster than the former two modeling methods and consumes less manpower and material resources. The above has been emphatically mentioned in many kinds of literature. The idealized model is idealized, which is not consistent with the real experimental results, the latter two models are mostly used in general research. Therefore, only the latter two modeling methods are introduced in this article.

### 4.1.1 Based on Scanning and Image Processing Technology

A 3D viscoelastic model of the asphalt mixture was established by You et al. (2008) based on X-ray image scanning technology to simulate and restore the creep flexibility test. A time-temperature superposition principle was developed to improve the calculation time. The microstructure reconstruction of asphalt mixtures with the 3D DEM was completed by You and Liu (2010) based on images from the X-ray computed tomography. The frequency-temperature superposition principle was used to shorten the simulation time. The advantage of this image processing technology is that it can truly show most of the structural characteristics of asphalt mixtures. The dynamic modulus and phase angle of the asphalt mixtures were predicted and compared with the laboratory test results. The results showed that most of the predicted values were close to the measured values. The 3D discrete element model of the asphalt mixture was reconstructed through the scanned 2D model of the aggregates and the related research was carried out to analyze the influence factors of the modulus (You et al., 2011). Also, the 3D structured light scanning technology

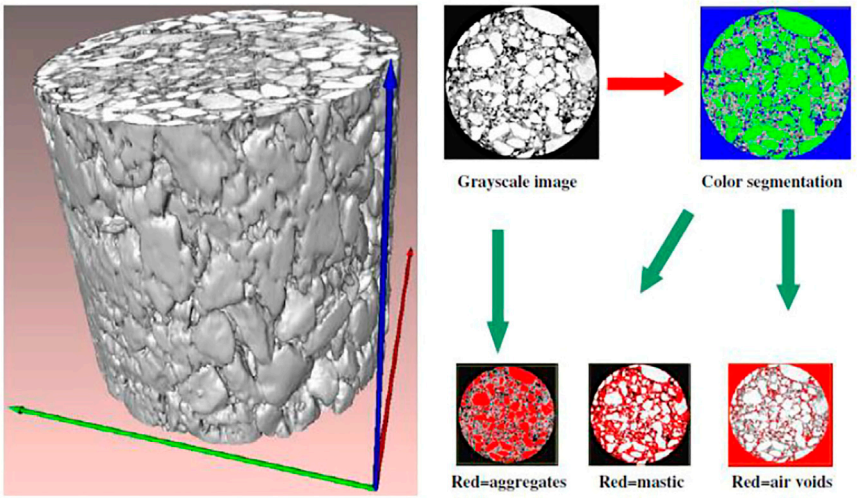


(a) 3D virtual samples from X-ray computed images (You et al., 2009;Adhikari and You, 2010); (b) aggregates, mastic, and air void distributions in the 2D models (You et al., 2009;Adhikari and You, 2010)

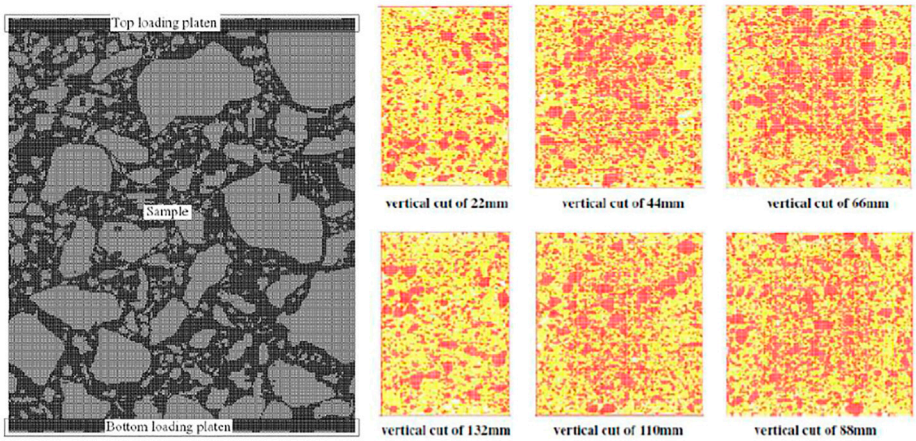


(e) 2D DEM samples with loading platen (Liu, 2011); (d) 2D samples with different vertical cuts (You et al., 2009;Adhikari and You, 2010)

**FIGURE 7 |** Virtual samples of the asphalt mixtures (Liu, 2011; You et al., 2009; Adhikari and You, 2010). **(A)** 3D virtual samples from X-ray computedimages (You et al., 2009; Adhikari and You, 2010); **(B)** aggregates, mastic,and air void distributions in the 2D models (You et al., 2009; Adhikari and You, 2010). **(C)** 2D DEM samples with loading platen(Liu, 2011); **(D)** 2D samples with different vertical cuts(You et al., 2009; Adhikari and You, 2010).

was used to scan the aggregate particles and the aggregate information was compiled with the help of the MATLAB program. The 3D model of asphalt mixtures was established based on the aggregated information in PFC5.0 to study the multiscale influence factors of volume characteristics (Li et al., 2020). X-ray CT technology was used to scan aggregates for the microstructure of aggregates. The MATLAB program and PFC3D were employed to establish a 3D model of the asphalt mixture to simulate the uniaxial penetration test to explore how aggregate affected the shear performance (Wu et al., 2021). The scanned internal images of aggregates were processed by Guo (2020) and Peng et al. (2021)with image information acquisition software with the help of CT scanning. The aggregate characteristics were imported into PFC3D to generate a 3D discrete element model of the asphalt mixture to study the effect of the gap distribution on the shear fatigue life. the relevant information of aggregate particles was obtained by Shi (2020) from the laser scanning and established a PFC3D model of the asphalt mixture. The model was verified with the help of the laboratory experimental data and it was used to analyze the aggregate characteristics. The particle images of aggregates were intercepted by Lu (2020) with CT scanning technology and processed them with the MATLAB program to establish a 3D model of the asphalt mixture in PFC3D. The

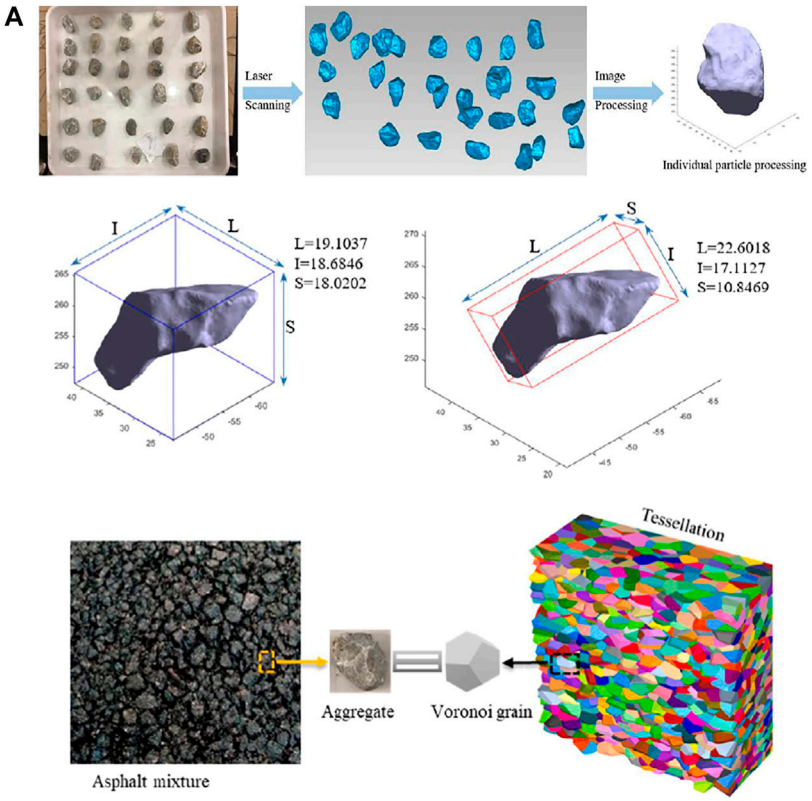


3D scanning processing and model generation of the asphalt mixtures (Ge et al., 2021)

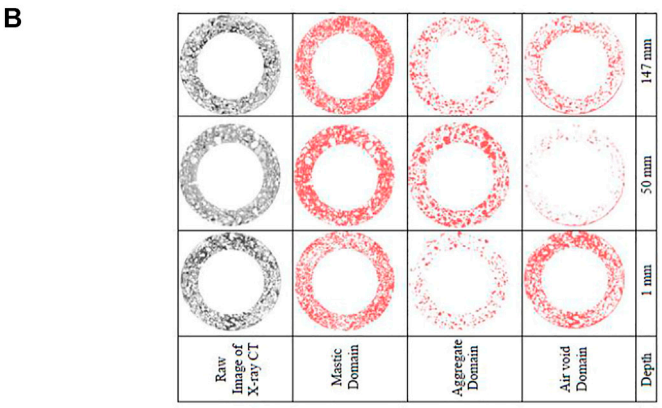


X-ray CT images, Mastic, aggregate, and air void samples (Adhikari and You, 2010)

**FIGURE 8 |** 3D DEM scanning samples and digital generation specimens (Ge et al., 2021; Adhikari and You, 2010). **(A)** 3D scanning processingand model generation of the asphalt mixtures (Ge et al., 2021). **(B)** X-ray CT images, Mastic, aggregate, andair void samples (Adhikari and You, 2010).

virtual splitting test (indirect tensile test) and uniaxial penetration test of the asphalt mixtures were carried out and verified with real experimental data for further research. The 2D mixture image and the scanning process of 3D specimens obtained with the help of scanning technology are shown in **Figure 7** (Liu, 2011) You et al., 2009; Adhikari

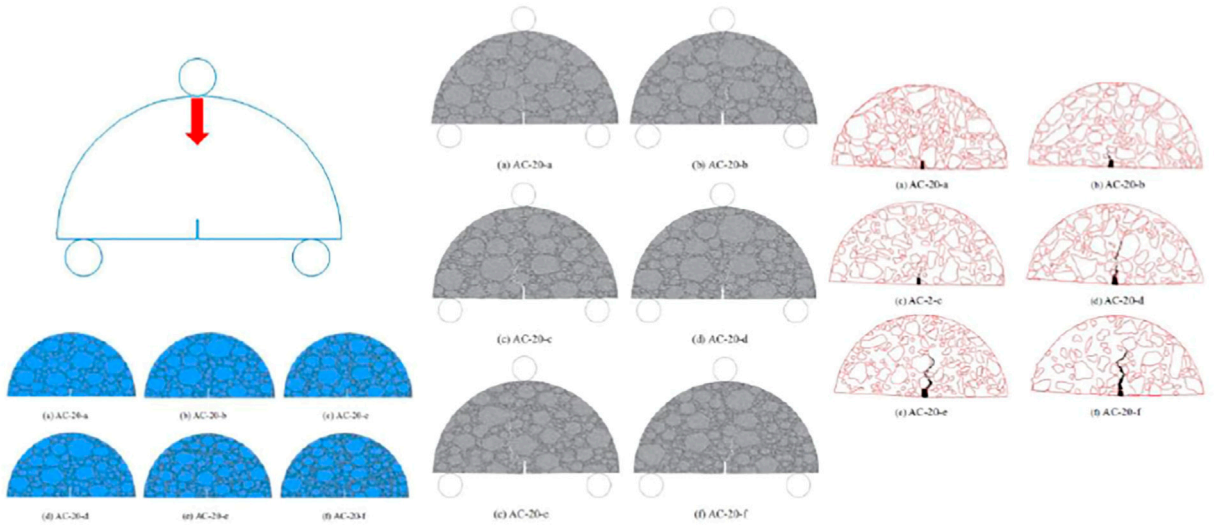

**FIGURE 9 |** SCB digital samples, loading setting and deformations of the asphalt mixtures (Liang et al., 2021; Nian et al., 2021).

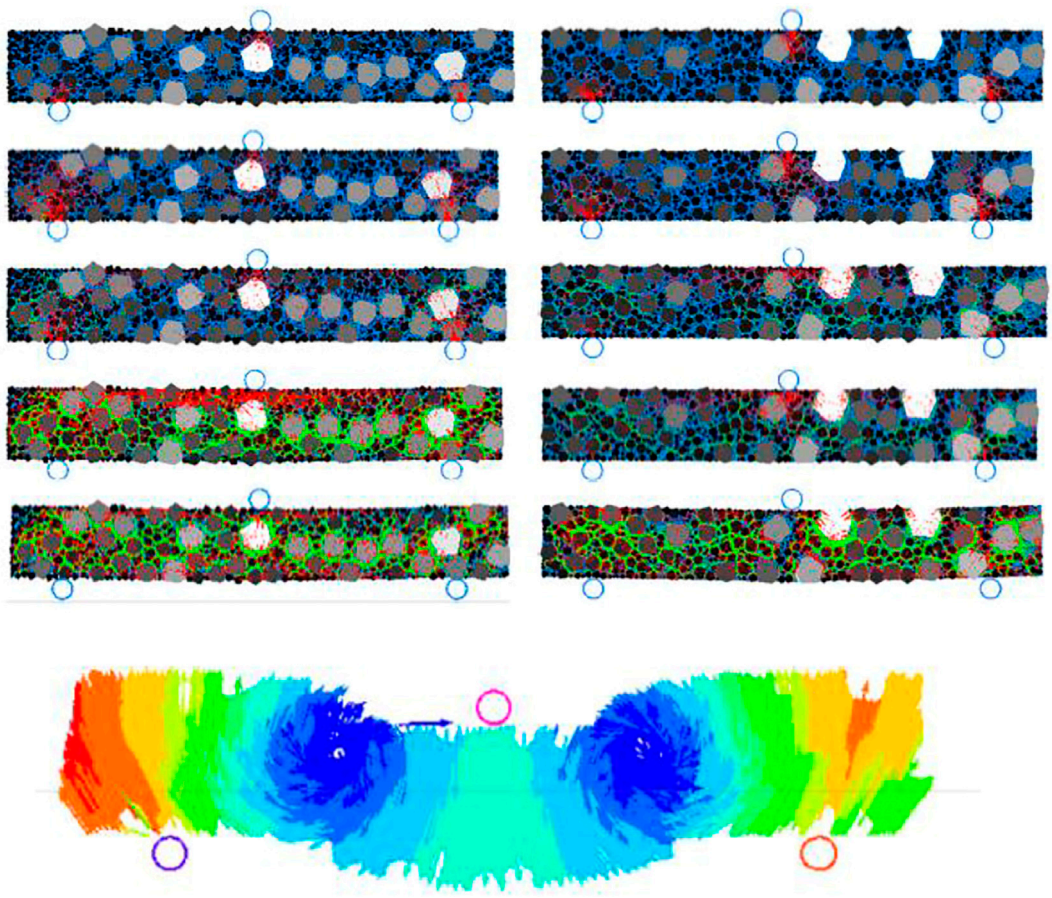

**FIGURE 10 |** Splitting test (indirect tensile test) and three-point bending test samples of the asphalt mixtures with the DEM models (Nian et al., 2021).

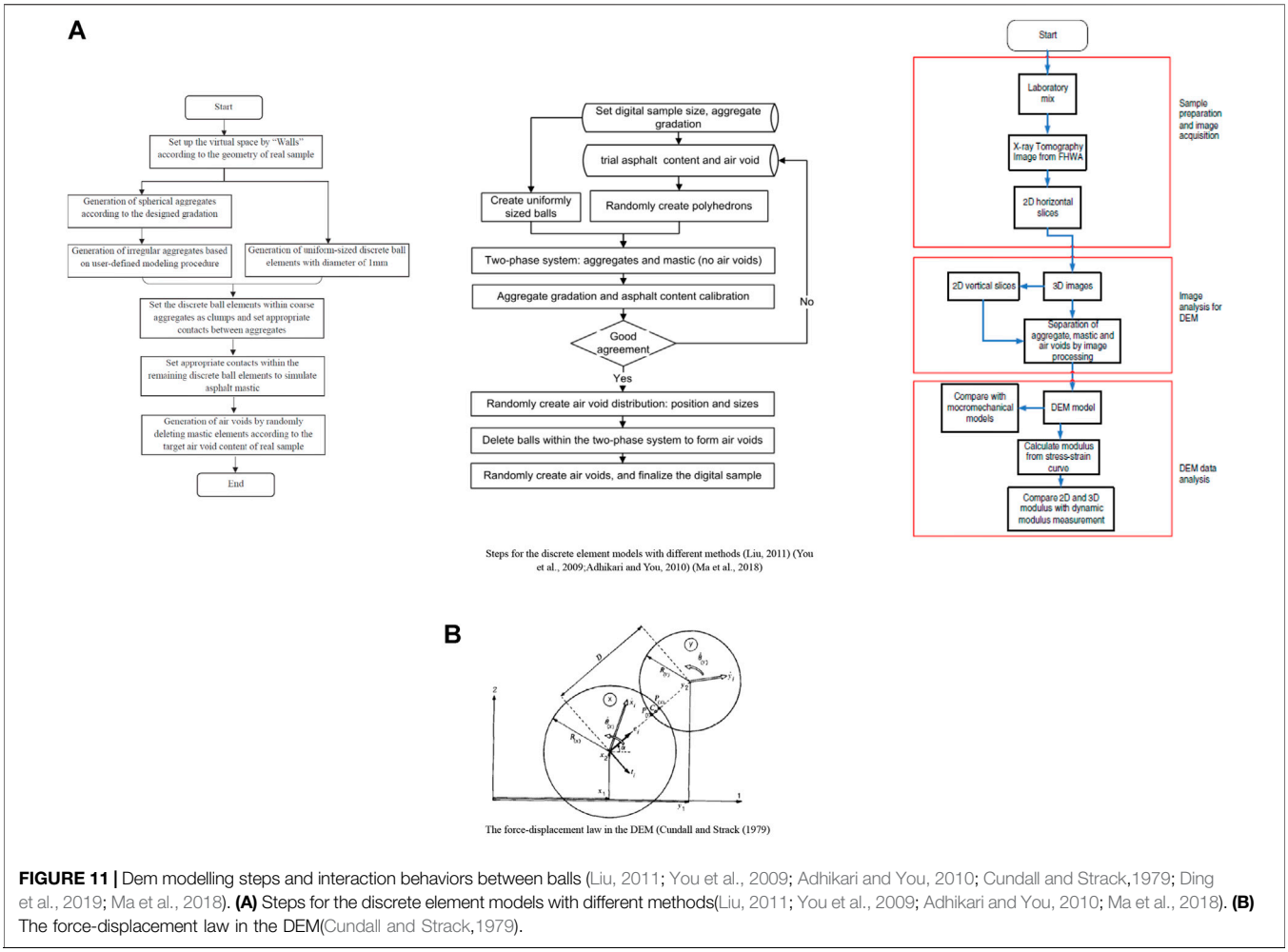


**FIGURE 11 |** Dem modelling steps and interaction behaviors between balls (Liu, 2011; You et al., 2009; Adhikari and You, 2010; Cundall and Strack,1979; Ding et al., 2019; Ma et al., 2018). **(A)** Steps for the discrete element models with different methods(Liu, 2011; You et al., 2009; Adhikari and You, 2010; Ma et al., 2018). **(B)** The force-displacement law in the DEM(Cundall and Strack,1979).

and You, 2010) and **Figure 8** (Ge et al., 2021) (Adhikari and You, 2010).

### 4.1.2 User-Defined Method

The randomly generated irregular shape model refers to the aggregates of the asphalt mixtures represented by irregular polygonal particles in the discrete element model established by a random polygon algorithm (Liu and You, 2008). A self-defined discrete element model was established by Chen et al. (2012) and the cyclic loading uniaxial compression tests of asphalt mixtures were carried out. The model was verified to predict the dynamic modulus and phase angle of asphalt mixtures and analyze factors for the viscoelastic characteristics of asphalt mixtures. four kinds of typical aggregate gradations were selected by Zhou (2016) to carry out the dynamic modulus test and generate the numerical model to analyze the DEM feasibility for the virtually mechanical test of asphalt mortars and mixtures. The classically viscoelastic model (Burger's self-defined constitutive contact model) was adopted in the discrete element model. The digital cylinder specimen was composed of multiple discrete elements with different sizes and the discrete element model was used for the dynamic modulus test. The randomly generated PFC3D models of asphalt mixtures were used to simulate the creep experiments to study the influence of void-related factors at different temperatures (Ma et al., 2016a). A 3D user-defined model was established by Du et al. (2021) to simulate the indirect tensile test to analyze the gradation effect on the crack propagation at low temperatures, as well as the virtual performance test of different gradation asphalt mixtures. Different mixture gradations were adapted for the performance analysis and improvement measurements (Ling et al., 2020). the user-defined method was used by Wang et al. (2021) to establish PFC2D and PFC3D models of asphalt mixtures and simulated the dynamic creep and rutting tests. Other tests were modeled with the PFC2D program to study the factors of asphalt mixtures for the low-temperature performance, such as the Semicircular Bending Test (SCB) (**Figure 9**), Splitting Test (indirect tensile test), and Three-point Bending Test (**Figure 10**) (Liang et al., 2021; Nian et al., 2021).

## 4.2 Simulation Process

### 4.2.1 Modeling

The basic steps of the discrete metamodels (Randomly Generated Models) for asphalt mixtures in PFC3D were roughly divided into the following steps (Liu, 2011) (You et al., 2009; Adhikari and You, 2010). 1) the digital size and aggregate gradations were

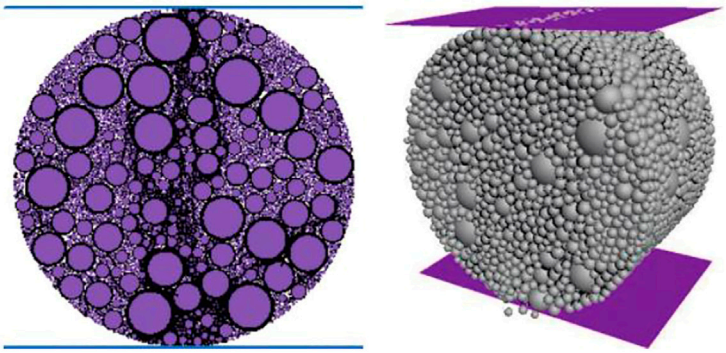

(a) 2D DEM model with simple ball systems (Shan et al., 2019); (b) 3D DEM model with simple ball systems (Shan et al., 2019)

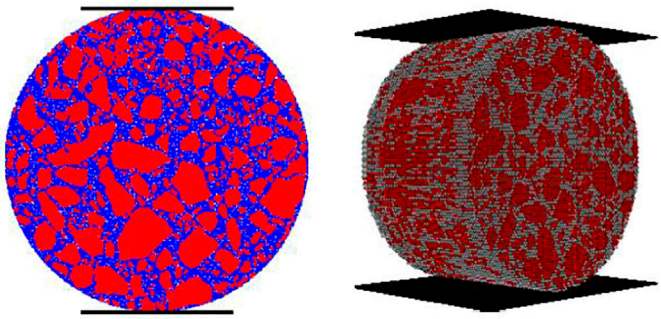

(c) 2D DEM model with different shapes of aggregates (Peng and Bao, 2018); (d) 3D DEM model with different shapes of aggregates (Peng and Bao, 2018)

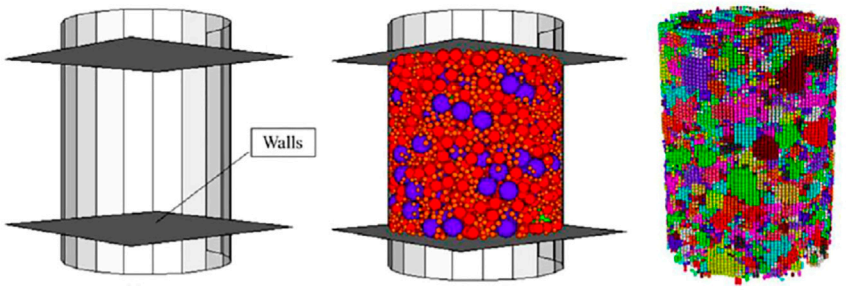


(e) the coarse aggregates in the 3D DEM models (Ma et al., 2016b)

**FIGURE 12 |** 2D and 3D DEM simulations for the splitting test (indirect tensile test) of the asphalt mixtures (Shan et al., 2019; Peng and Bao, 2018; Ma et al., 2016b). **(A)** 2D DEM model with simple ball systems (Shan et al., 2019); **(B)** 3D DEM model with simple ball systems (Shan et al., 2019). **(C)** 2D DEM model with different shapes of aggregates(Peng and Bao, 2018); **(D)** 3D DEM model with different shapes of aggregates(Peng and Bao, 2018). **(E)** the coarse aggregates in the 3D DEM models (Ma et al., 2016b).

defined, and the asphalt content and air voids were set based on the volume characteristics of asphalt mixtures; 2) balls with the same size were created and a polyhedron was randomly created; 3) A two-phase system of the aggregate and mortar was generated; 4) the volume characteristics of the two-phase system were verified. The air voids were randomly generated by deleting the balls in the two-phase system. Finally, a digital PFC sample of the asphalt mixture was generated with the air void by the random method. The Aggregate Imaging Measurement System (AIMS) was used to measure the aggregate particles to get the image characteristics. Three methods were adopted to form the virtual aggregate samples, including the Radius Expansion (RE), Interior Filling (IF), and Contour Filling (CF) Methods (Ding et al., 2019). The relationship between the contact points was also demonstrated and defined in the literature (Ding et al., 2019) (Cundall and Strack (1979). Three parts (asphalt mastic, aggregates and air voids) was combined to generate the asphalt mixture samples in PFC3D with the user-defined procedure. The

asphalt mixture samples were made for the wheel tracking test (Ma et al., 2018). The complex processes and interaction behaviors of these methods are shown in **Figure 11** (Liu, 2011; You et al., 2009; Adhikari and You, 2010; Cundall and Strack,1979; Ding et al., 2019; Ma et al., 2018).

### 4.2.2 Loading Model

The shapes and sizes of the asphalt mixture models were relatively different from the test samples. The dynamic modulus test models of asphalt mixtures were cylindrical; the splitting strength test models of asphalt mixtures were cylindrical with the same size as the actual Marshall specimen, and the four-point bending beam test model is rectangularly trabecular. It is necessary to apply the load in the model with "force" after the generation of the mixture model. The specific operation was summarized as follows: setting several different gradations; writing the servo control program in the Fish language; and achieving the function of applying load to the top and bottom of the model specimen. It is worth noting that the force on the "wall" cannot be directly controlled in the program. Instead, it is necessary to control the speed of the "wall" through commands. The "wall" at the bottom of the specimen is not moving and a downward speed is applied to the "wall" at the top of the specimen to realize the loading of the model, and the control of the speed of the "wall" is realized using the servo control program to apply the periodic load to the model specimen. The PFC2D and PFC3D models of the asphalt mixtures are generated as shown in **Figure 12** (Shan et al., 2019; Peng and Bao, 2018; Ma et al., 2016b).

## 5 DISCUSSIONS

(1) The DEM was designed for the analysis of rock problems and it was extended to solve the pavement problems later, as well as to explore the mechanical behaviors of asphalt mixtures or cement. The difference between the continuum-based method and DEM is the system topology and construction manner, as well as the solution strategies and material behaviors. During the development of discrete elements, the DEM algorithms were invented and developed for different scenarios of materials at the micro scales, such as the boundary types, contact-point constitutions, force transfers, and calculation, sample generation, particle shape and types, fluid flow mechanics, geomaterial micromechanics, etc. Many algorithm blocks and methods were investigated to fully satisfy different research proposes and objectives, such as the discrete fracture network, the Navier-Stokes equation, deformation analysis, stiffness matrix, heat conduction, stress wave propagation, various moduli, tensile test, etc. There are many advantages and disadvantages for the laboratory test method and the discrete element numerical simulation method to evaluate the performance and analyze the interaction between elements. The virtual laboratory test plan is the main reason for us to use the simulation to conduct the test; Another reason is that the simulation can solve the problems and it is hard to deal with or figure out them through the laboratory test. Most importantly, the simulations can avoid most laboratory risks during real testing in the laboratory, and it is safe that the hazardous materials are also processed with the simulations. Thereby, more scholars tried to use different simulations to solve the problems with different scales. In addition, the required simulation time is shorter than that used in the laboratory. Some tests in the laboratory may take as long as several years, like the creep test for concretes. For instance, during the dynamic modulus simulations of asphalt mixtures, the calculation time in the DEM simulation can be shortened to several days or even hours using the temperature-frequency superposition method (Liu and You, 2011a). It can be found that most DEM simulations are verified by real experimental data from different studies. The computational and numerical simulations may be the promising way to understand the behavior of materials based on the fast development of computer technologies. Some advantages are highlighted compared to laboratory testing, like the fast calculation, low cost, less labor, less risk, no damage to human health, and so on. Most importantly, the numerical simulation can explore the interactions between materials, which cannot easily realize by the experiments, such as the interaction at the nano- and micro-scale between materials compositions. In addition, experimental data is still needed in the DEM simulations of asphalt mixtures to ensure the relative accuracy of the results.

(2) Generally speaking, there are two ways to simulate different tests or models of asphalt mixtures with discrete element programs, PFC2D for 2D mixture models and PFC3D for 3D mixture models. It also means that two aspects and perspectives are available to explore the digital materials. The PFC3D program is developed and extended from the PFC2D. It is difficult to reflect the simulation authenticity with the PFC2D under different conditions and research proposals. Thereby, the PFC3D programs are produced and introduced with more accurate simulation results, and the programs restore the actual actions between materials. The 2D and 3D discrete element models of asphalt mixtures are established, respectively, and the two-type models are compared from these aspects, such as the calculation speed and simulation effect compared with the laboratory-measured data. Some example models can be described as follows: Prediction for the dynamic modulus of the asphalt mixture with DEMs (You et al., 2009; Adhikari and You, 2010); Influence of voids and its distribution laws in asphalt mixtures with DEMs (You et al., 2010). After comparison, the effect of 3D model simulation is better than that of the 2D model in most cases. It is relatively close to the laboratory results.

(3) The generation methods or algorithms of DEM samples were discussed here, like the image-based, user-defined, idealized and random models. Three methods had their advantages and the application scenarios depend on the research purposes. Integrating the current simulation databases and computer resources, the image-based method seemed to be

more likely to be real samples. However, the image-based model was restricted by the image capturing technology and image numbers or databases. More images of samples needed to be captured and processed under different conditions and these are not transferable. Compared to the idealized models, the other two methods (image-based and user-defined models) are commonly used in 2D or 3D discrete element programs. Through the study of the literature (Yang et al., 2016), the image-based DEM models are inseparable from the scanning equipment and image processing technology, and these are needed to be completed in the laboratory with the high cost and long time-consuming processing. The advantage of this method is that the simulation effect is close to the real status for materials, which can accurately present the shape, position, and distribution of aggregates, and also reflect the real structures of the asphalt mixtures. In contrast, the user-defined model method is used to build the model according to the basic data of the simulation test in the discrete element program with the help of the "Fish" language in the program. It is not expensive and also not time-consuming, as well as the independence of the laboratory restriction. However, sometimes, the accuracy of the simulation data is less than that of the image-based model method. It is difficult to fully show the internal structures of the aggregates in the asphalt mixtures.

## 6 CONCLUSION

After the above discussions, we can understand that:

(1) The application of DEMs in pavement engineering, especially in asphalt mixtures, was also studied from the function realization to the mechanism discussion. Many contact/connectivity patterns and behaviors were generated and developed for the interaction discovery of asphalt and aggregates. Many tests of asphalt mixtures were simulated to explain and investigate the performance by the DEM, like the splitting test (indirect tensile test), dynamic modulus test, three-point, and four-point beam test, compressive test, etc., Those were demonstrated partially in this manuscript. There are still more questions and mechanisms needed to be discovered and explored in the DEM simulation, for instance, 1) interaction between the water and mixtures under different conditions, 2) damage patterns of different shapes and forces under different conditions in the pavement, 3) contribution rates of different aggregates and asphalt in asphalt mixtures under different conditions, 4) void distributions in asphalt mixtures and formation laws, 5) water propagations in asphalt mixtures, etc., Sometimes, these questions may be divided into different pieces and can be solved from different views and sights. In addition, it is common that the DEM simulation explores from 2D to 3D for the reality demonstration and links the microscale to macro scale. Also, there are some different advantages in the 2D and 3D simulations and researchers need to integrate your aims and thoughts to make decisions.

(2) The user-defined and random models also have more potential to be developed for virtual laboratory tests, 1) The difficulty of the methods is the useful and universal databases for the virtual sample generation; 2) The shape and texture properties of aggregates can be precisely described and added in the virtual samples, as well as other properties in the models; 3) The interaction between materials, like asphalt and aggregates in asphalt mixtures, can be accurately expressed in the models; 4) The physical and chemical reactions can be strictly presented in the models; 5) The DEM calculation speed and element numbers also affect the simulation effect and generalization. 6) the contact model between the elements may be updated for the constitutive models in DEM model, and this update may provide an option for the solution of the plastic deformation problems in the DEM simulation. It helps to understand behaviors of visco-elastic plastic materials. These points are needed to be considered for us to generate good models, as well as other possible factors.

Therefore, the DEM is a promising tool for us to explore the micro behaviors of asphalt mixtures. It is also affordable for researchers to conduct the tests in the virtual laboratory. It can achieve different test simulations at different dimensions and explore mechanisms under extreme conditions. These operations can not be easily realized in the laboratory or fields. The researchers benefit from these advantages and program the simulation with their purposes. The research results can directly guide the industry application and production, and also, accelerate the research development for the engineering field.

## AUTHOR CONTRIBUTIONS

HY and MX wrote the manuscript; JL and YL helped revise the manuscript; JJ and ZY provided the technical support for the manuscript.

## FUNDING

The authors appreciate the financial support of the Hunan Department of Transportation (No. 202152) and Hunan Expressway Group Co. Ltd. The authors also appreciate the funding support from the National Natural Science Foundation of China (No. 51778038), Beijing Key Laboratory of Traffic Engineering (No. 2018BJUT-JTJD007), and Beijing Municipal Commission of Transportation (Grant Number: 2018-kjc-01-213). Any opinion, finding, and conclusion expressed in this paper are those of the authors and do not necessarily represent the view of any organization. The funder was not involved in the study design, collection, analysis, interpretation of data, the writing of this article or the decision to submit it for publication. All authors declare no other competing interests.

## REFERENCES


Adhikari, S., and You, Z. (2010). 3D Discrete Element Models of the Hollow Cylindrical Asphalt concrete Specimens Subject to the Internal Pressure. *Int. J. Pavement Eng.* 11. doi:10.1080/10298436.2010.489114

Adhikari, S., and You, Z. (2011). Investigating the Sensitivity of Aggregate Size within Sand Mastic by Modeling the Microstructure of an Asphalt Mixture. *J. Mater. Civil Eng.* 23. doi:10.1061/(asce)mt.1943-5533.0000212

Chang, M., Pei, J., and Zhang, J. (2011). "Influences of Mesoscopic Parameters on Crack Resistance of Asphalt Mixture," in *ICCTP 2011: Towards Sustainable Transportation Systems*, 3324–3332. doi:10.1061/41186(421)329

Chen, J., Pan, T., Chen, J., Huang, X., and Lu, Y. (2012). Predicting the Dynamic Behavior of Asphalt concrete Using Three-Dimensional Discrete Element Method. *J. Wuhan Univ. Technol. Mater. Sci. Edition* 27. doi:10.1007/s11595-012-0470-y

Cundall, P. (1974). *A Computer Model for Rock Mass Behavior Using Interactive Graphics for the Input and Output of Geometrical Data. A Report Prepared under Contract Number DACW 45-74-C-006*. Washington, D.C.: The National Academies of Sciences, Engineering, and Medicine.

Cundall, P. A. (1971). "A Computer Model for Simulating Progressive, Large-Scale Movement in Blocky Rock System," in *Symposium of the International Society for Rock Mechanics*.

Cundall, P. A. (1978). *BALL–A Program to Model Granular media Using the Distinct Element Method*. London, United Kingdom: Dames & Moore. Advanced Technology Group". Technical Note No. TN-LN.

Cundall, P. A., and Strack, O. D. L. (1979). A Discrete Numerical Model for Granular Assemblies. *Géotechnique* 29, 47–65. doi:10.1680/geot.1979.29.1.47

Dan, H.-C., Zhang, Z., Chen, J.-Q., and Wang, H. (2018). Numerical Simulation of an Indirect Tensile Test for Asphalt Mixtures Using Discrete Element Method Software. *J. Mater. Civ. Eng.* 30, 04018067. doi:10.1061/(asce)mt.1943-5533.0002252

Ding, X., Ma, T., and Huang, X. (2019). Discrete-Element Contour-Filling Modeling Method for Micromechanical and Macromechanical Analysis of Aggregate Skeleton of Asphalt Mixture. *J. Transp. Eng. Part. B: Pavements* 145, 04018056. doi:10.1061/jpeodx.0000083

Du, J., Ren, D., Ai, C., and Qiu, Y. (2021). Study on Low Temperature Crack Propagation and Evolution of Asphalt Mixture[J/OL]. *J. Building Mater.*, 1–10.

Gao, Y. (2021). Experimental Study on Rheological Properties of Sulfur SBS Modified Asphalt and Pavement Performance of its Mixture[J]. *Synth. Mater. Aging Appl.* 50, 67–69+22.

Ge, H., Quezada, J. C., Houerou, V. L., and Chazallon, C. (2021). Three-dimensional Simulation of Asphalt Mixture Incorporating Aggregate Size and Morphology Distribution Based on Contact Dynamics Method. *Construction Building Mater.* 302, 124124. doi:10.1016/j.conbuildmat.2021.124124

Ghafoori Roozbahany, E., Partl, M. N., and Jelagin, D. (2019). Modelling the Flow of Asphalt under Simulated Compaction Using Discrete Element. *Construction Building Mater.* 227, 116432. doi:10.1016/j.conbuildmat.2019.07.158

Guo, H., and Chen, S. (2014). Discrete Element Numerical Analysis of Splitting Test of Open-Graded Large-Size Asphalt Macadam Mixture[J]. *J. Highw. Transportation Res. Dev.* 31, 22–26+40.

Guo, H., and Chen, S. (2015). Numerical Analysis on the Splitting Test of Open-Graded Large Stone Asphalt Mixture Based on Discrete Element Method. *J. Highw. Transportation Res. Dev.* 9. doi:10.1061/jhtrcq.0000434

Guo, Z. (2020). Influence of Void Distribution Based on Discrete Element Method on Shear Fatigue Life of Asphalt Mixture[J]. *Low Temperature Architecture Tech.* 42, 11–14.

Hou, S., Zhang, D., Huang, X., and Zhao, Y. (2015). Investigation of Micro-mechanical Response of Asphalt Mixtures by a Three-Dimensional Discrete Element Model. *J. Wuhan Univ. Technol.-Mat. Sci. Edit.* 30, 338–343. doi:10.1007/s11595-015-1150-5

Huang, Z.-y., Yang, Z.-x., and Wang, Z.-y. (2008). Discrete Element Modeling of Sand Behavior in a Biaxial Shear Test. *J. Zhejiang Univ. Sci. A.* 9, 1176–1183. doi:10.1631/jzus.a0720059

Jia, H., Sheng, Y., Lv, H., Kim, Y. R., Zhao, X., Meng, J., et al. (2021). Effects of Bamboo Fiber on the Mechanical Properties of Asphalt Mixtures[J]. *Construction Building Mater.* 289. doi:10.1016/j.conbuildmat.2021.123196

Kusumawardani, D. M., and Wong, Y. D. (2020). The Influence of Aggregate Shape Properties on Aggregate Packing in Porous Asphalt Mixture (PAM). *Construction Building Mater.* 255, 119379. doi:10.1016/j.conbuildmat.2020.119379

Li, Q., Wu, C., Fang, Y., Zhong, M., Huang, H., and Han, Q. (2021). Performance Research and Application of SMA-13 Asphalt Mixture with Plant Mixed Hot Recycling[J/OL]. *Highw. Eng.*, 1–12.

Li, Z., Jing, H., and Wang, Z. (2020). Multi-factor Interaction of Asphalt Mixture Volume Characteristics Based on Discrete Element Method[J]. *J. Guangxi Univ. (Natural Sci. Edition)* 45, 1301–1314.

Liang, H., Shi, L., Wang, D., Xiao, X., and Deng, K. (2021). Influence of Graded Coarse Aggregate Content and Specific Surface Area on the Fracture Properties of Asphalt Mixtures Based on Discrete Element Simulations and Indoor Tests. *Construction Building Mater.* 299, 123942. doi:10.1016/j.conbuildmat.2021.123942

Liang, H., Wang, D., Deng, Z., Liang, X., and Xu, C. (2019). Application of Cohesive Zone Model in Discrete Element Simulation of Foamed Asphalt Mixture[J]. *J. Hunan Univ. (Natural Sciences)* 46, 115–123.

Ling, T., Yang, Y., Zhao, C., Zhu, L., and Chen, Q. (2020). Design of Asphalt Mixture with Low Voidage Based on PFC3D[J]. *J. Chongqing Jiaotong Univ. (Natural Science)* 39, 73–80.

Liu, C., Le, T., Shi, B., and Zhu, Y. (2020). Discussion on Three Major Problems of Engineering Application of the Particle Discrete Element Method. *Chin. J. Rock Mech. Eng.* 39, 1142–1152.

Liu, G., Dai, J., Liu, Y., Gao, H., and Peng, Y. (2018). Numerical Simulation of Aggregate Uniformity Influence on Low Temperature Splitting Strength of Asphalt Mixtures[J]. *Low Temperature Architecture Tech.* 40, 12–16.

Liu, Y., Dai, Q., and You, Z. (2009). Viscoelastic Model for Discrete Element Simulation of Asphalt Mixtures. *J. Eng. Mech.* 135. doi:10.1061/(asce)0733-9399(2009)135:4(324)

Liu, Y. (2011). *Discrete Element Methods for Asphalt concrete: Development and Application of User-Defined Microstructural Models and a Viscoelastic Micromechanical Model*. Houghton, MI: Michigan Technological University.

Liu, Y., and You, Z. (2011a). Accelerated Discrete-Element Modeling of Asphalt-Based Materials with the Frequency-Temperature Superposition Principle. *J. Eng. Mech.* 137, 355–365.

Liu, Y., and You, Z. (2011b). Accelerated Discrete-Element Modeling of Asphalt-Based Materials with the Frequency-Temperature Superposition Principle. *J. Eng. Mech.* 137, 355–365. doi:10.1061/(asce)em.1943-7889.0000234

Liu, Y., and You, Z. (2008). "Simulation of Cyclic Loading Tests for Asphalt Mixtures Using User Defined Models within Discrete Element Method," in *GeoCongress 2008: Characterization, Monitoring, and Modeling of Geosystems*, 742–749.

Liu, Y., You, Z., and Zhao, Y. (2012). Three-dimensional Discrete Element Modeling of Asphalt concrete: Size Effects of Elements. *Construction Building Mater.* 37, 775–782. doi:10.1016/j.conbuildmat.2012.08.007

Lu, J. (2020). *Study on Numerical Simulation of Asphalt Mixture Based on CT Technology and Three-Dimensional Discrete Element Method[D]. Master*. Guangzhou, China: South China University of Technology.

Ma, T., Zhang, D.-y., Zhang, Y., Zhao, Y.-l., and Huang, X.-m. (2016b). Microstructure Modeling and Virtual Test of Asphalt Mixture Based on Three-Dimensional Discrete Element Method. *J. Cent. South. Univ.* 23, 1525–1534. doi:10.1007/s11771-016-3204-z

Ma, T., Zhang, D., Zhang, Y., Wang, S., and Huang, X. (2018). Simulation of Wheel Tracking Test for Asphalt Mixture Using Discrete Element Modelling. *Road Mater. Pavement Des.* 19, 367–384. doi:10.1080/14680629.2016.1261725

Ma, T., Zhang, D., Zhang, Y., Zhao, Y., and Huang, X. (2016a). Effect of Air Voids on the High-Temperature Creep Behavior of Asphalt Mixture Based on Three-Dimensional Discrete Element Modeling. *Mater. Des.* 89, 304–313. doi:10.1016/j.matdes.2015.10.005

Mao, Z. (2018). The Research on Creep of Asphalt Mortar Based on Three-Dimensional Discrete Element[J]. *Low Temperature Architecture Tech.* 40, 4–6+13.

Meng, L., Zhang, W., and Wang, X. (2021). Research on the Effect of Chlorine Salt Snow-Melting Agent on Asphalt concrete Performance[J]. *J. Qingdao Univ. Tech.* 42, 45–51.

Nian, T., Ge, J., Li, P., Wang, M., and Mao, Y. (2021). Improved Discrete Element Numerical Simulation and experiment on Low-Temperature Anti-cracking

Performance of Asphalt Mixture Based on PFC2D. *Construction Building Mater.* 283, 122792. doi:10.1016/j.conbuildmat.2021.122792

Pei, J., Chang, M., Chen, S., and Wang, B. (2010). Numerical Simulation of Indirect Tensile Test for Asphalt Mixture[J]. *J. Chang'an Univ. (Natural Sci. Edition)* 30, 6–10.

Peng, Y., and Bao, J. (2018). Comparative Study of 2D and 3D Micromechanical Discrete Element Modeling of Indirect Tensile Tests for Asphalt Mixtures. *Int. J. Geomechanics* 18. doi:10.1061/(asce)gm.1943-5622.0001155

Peng, Y., Bao, J., and Wang, Z. (2016). A Comparison of Two-Dimensional and Three-Dimensional Micromechanical Discrete Element Modeling of the Splitting Tests for Asphalt Mixtures. *DEStech Trans. Eng. Tech. Res.*

Peng, Y., Gao, H., Wan, L., and Liu, G. (2019). Numerical Simulation of Influence Factors of Splitting Strength of Asphalt Mixtures[J]). *J. Jilin Univ. (Engineering Tech. Edition)* 49, 1521–1530.

Peng, Y., and Sun, L. (2015a). Aggregate Distribution Influence on the Indirect Tensile Test of Asphalt Mixtures Using the Discrete Element Method. *Int. J. Pavement Eng.* 18. doi:10.1080/10298436.2015.1121778

Peng, Y., and Sun, L. J. (2015b). Aggregate Distribution Influence on the Indirect Tensile Test of Asphalt Mixtures Using the Discrete Element Method [J]. *Int. J. Pavement Eng.* 18, 1–14. doi:10.1080/10298436.2015.1121778

Peng, Y., Yang, H., Lu, X., and Li, Y. (2021). Effect of Void Characteristics on Virtual Shear Fatigue Life of Asphalt Mixtures Using Discrete Element Method [J]. *J. Jilin Univ. (Engineering Tech. Edition)* 51, 956–964.

Shan, J., Du, Y., Fan, D., Guo, L., and Yang, X. (20192019). Determination of Parameters of the Discrete Element Bond Model for Asphalt Mixture Based on Splitting Test. *Adv. Civil Eng.* doi:10.1155/2019/5047214

Sheng, F., Hou, L., Wang, Y., Li, Z., and Shan, J. (2018). Studying on the Parameters of Bond-Model in DEM for Asphalt Mixture. *IOP Conf. Ser. Mater. Sci. Eng.* 392. doi:10.1088/1757-899x/392/2/022004

Shi, Y. (2020). *Simulation Study on Split Test of Asphalt Mixture with Flat-Elongated Particles Using Discrete Element Method[D]. Master*. Harbin, China: Harbin Engineering University.

Song, W. (2021). Influence of Polymer Fiber and Glass on the Mechanical Properties of Asphalt Mixture[J/OL]. *Highway* 66, 29–33.

Wan, L. (2016). *Study on Asphalt Mixture Splitting Test Using Cohesive Zone Model and Three-Dimensional Discrete Element Method[D]. Master*. Zhejiang, China: Zhejiang University.

Wang, H., Huang, W., Cheng, J., and Ye, G. (2021). Mesoscopic Creep Mechanism of Asphalt Mixture Based on Discrete Element Method. *Construction Building Mater.* 272, 121932. doi:10.1016/j.conbuildmat.2020.121932

Wang, W., and Li, X. (2005). *A Review on Fundamentals of Distinct Element Method and its Applications in Geotechnical Engineering[J]*. Beijing, China: Geotechnical Engineering Technique, 177–181.

Wang, X., Zheng, D., and Yu, C. (2019). Application of Discrete Element in the Teaching of "Asphalt and Asphalt Mixture. *Education Modernization* 6, 218–220.

Wang, Y. (1990). "Development of Discrete Element Method and its Application in Geotechnical Engineering[A]," in *Engineering Application of Numerical Methods in Rock and Soil Mechanics——Proceedings of the Second National Symposium on Numerical Calculation and Model Experiments in Rock Mechanics*, 44–54.

Wang, Y. (1986b). *Discrete Element Method and its Application in Rock mechanics [J]*. Shenyang, China: Metal Mine, 13–17+15.

Wang, Y. (1986a). Discrete Element Method—A Numerical Method Suitable for Analysis in Jointed Rocks. *Proc. first Natl. Symp. Numer. calculation Model Test Rock Mech.* 6.

Wang, Y., Liu, G., and Xing, J. (1987). *Research on Applications of Discrete Element Method in Ore Drawing for Caving system[J]*. Beijing, China: Non-ferrous metal, 20–26.

Wang, Y., and Xing, J. (1993a). Discrete Element Method and its Application in Coal Mining (Lecture 1)[J]. *Coal Mining Tech.*, 55–58.

Wang, Y., and Xing, J. (1993b). Discrete Element Method and its Application in Coal Mining (Lecture 2)[J]. *Coal Mining Tech.*, 56–58.

Wang, Y., and Xing, J. (1986). *Discrete Element Method and its Applications in Mine Pressure research[J]*. Fuxin, China: Journal of Fuxin Institute of Mining Technology, 1–12.

Wang, Y., and Xing, J. (1990). "Fully Deformed Discrete Element Method and its Application in Mining[A]," in *Rock Mechanics Issues in Hydropower and Mining Engineering——Proceedings of the Academic Conference on Rock Mechanics and Engineering Applications in North China*, 502–508.()

Wang, Y., and Xing, J. (1989). "Improvement and Application of Discrete Element Method[A]," in *Engineering Application of Numerical Methods in Rock and Soil Mechanics——Proceedings of the Second National Symposium on Numerical Calculation and Model Experiments in Rock Mechanics*, 254–259.

Wang, Y., and Xing, J. (1991). "New Progress of Numerical Methods and Their Engineering Applications[A]," in *New Progress in Rock Mechanics*, 168–192.()

Wu, W., Si, L., and Lu, J. (2021). Influence of Aggregate on Study on Shear Performance of Asphalt Mixture Based on Virtual Uniaxial Penetration Test[J]. *J. Highw. Transportation Res. Dev.* 38, 1–8.

Xia, Q., Gao, J., Zhang, Q., Li, Z., Yang, F., and Luo, H. (2021). *Low-temperature Performance of Composite Modified Hard Asphalt Used in High Modulus Asphalt concrete[J/OL]*. Changchun, China: Journal of Jilin University Engineering and Technology Edition, 1–9.

Xing, J., and Wang, Y. (1988). *Discrete Element Simulation of Ore Drawing by Caving Method in Mining[J]*. Shenyang, China: Journal of Northeast University of Technology, 148–153.

Xing, J., and Wang, Y. (1990). Improvement of Discrete Element Method and its Applications in Granular Media[J]. *Chin. J. Geotechnical Eng.*, 51–57.

Xiong, Y. (2013). Analysis of the Influence of Aggregate Properties on Splitting Test of Asphalt Concrete Based on Discrete Element Method[J]. *J. China Foreign Highw.* 33, 318–322.

Yang, X., You, Z., Wang, Z., and Dai, Q. (2016). Review on Heterogeneous Model Reconstruction of Stone-Based Composites in Numerical Simulation. *Construction Building Mater.* 117, 229–243. doi:10.1016/j.conbuildmat.2016.04.135

Yao, L., Gao, W., Tao, F., and Wang, H. (2021). Effects of Bayer Red Mud as Filler on Properties of Asphalt Mixture[J/OL]. *Highway* 66, 61–68.

You, Z., Adhikari, S., and Dai, Q. (2010). Air Void Effect on an Idealised Asphalt Mixture Using Two-Dimensional and Three-Dimensional Discrete Element Modelling Approach. *Int. J. Pavement Eng.* 11. doi:10.1080/10298436.2010.488737

You, Z., Adhikari, S., and Dai, Q. (2008). Three-Dimensional Discrete Element Models for Asphalt Mixtures. *J. Eng. Mech.* 134. doi:10.1061/(asce)0733-9399(2008)134:12(1053)

You, Z., Adhikari, S., and Kutay, M. E. (2009). Dynamic Modulus Simulation of the Asphalt concrete Using the X-ray Computed Tomography Images. *Mater. Structures* 42. doi:10.1617/s11527-008-9408-4

You, Z., Liu, Y., and Dai, Q. (2011). Three-Dimensional Microstructural-Based Discrete Element Viscoelastic Modeling of Creep Compliance Tests for Asphalt Mixtures. *J. Mater. Civil Eng.* 23. doi:10.1061/(asce)mt.1943-5533.0000038

You, Z., and Liu, Y. (2010). Three-Dimensional Discrete Element Simulation of Asphalt Concrete Subjected to Haversine. Loading an Application of the Frequency-Temperature Superposition Technique. *Road Mater. Pavement Des.* 11, 273–290. doi:10.3166/rmpd.11.273-290

Yu, D. (2015). Splitting Test Modeling of Asphalt Mixture Using Particle Flow Code[J]. *Mod. Transportation Tech.* 12, 1–4.

Zhang, D., and Li, Y. (2017). Numerical Simulation of Asphalt Concrete's Porosity Variation under Dynamic Loading[J]. *J. Xuzhou Inst. Tech. (Natural Sci. Edition)* 32, 73–76.

Zhang, H., Lian, H., and Yang, D. (2015). Split Test and Numerical Simulation of Crumb Rubber-Modified Asphalt Mixture[J]. *Mater. Rep.* 29, 145–148.

Zhang, Y., Ma, T., Ding, X., Chen, T., Huang, X., and Xu, G. (2018). Impacts of Air-Void Structures on the Rutting Tests of Asphalt concrete Based on Discretized Emulation. *Construction Building Mater.* 166, 334–344. doi:10.1016/j.conbuildmat.2018.01.141

Zhang, Y., and Zhang, B. (2016). "Blast Furnace for Bell Distribution Chute Research Based on StreamDEM[A]," in *Proceedings of the 12th China CAE Engineering Analysis Technology Annual Conference*, 141–143.

Zhang, Y., Zhong, X., Zhong, Y., and Zhang, B. (2017). "Study on the First Layer of Blast Furnace Fabric Based on StreamDEM[A]," in *Proceedings of the 11th China Iron and Steel Annual Conference-S01* (Beijing, China: Ironmaking and Raw Materials), 830–834.

Zhong, X., and Zhang, Y. (2021). Influence of Fiber Type on Road Performance of High RAP Content Asphalt Mixture[J]. *Highways & Transportation in Inner Mongolia*, 29–33.

Zhou, J. (2016). Laboratory Test and Numerical Simulation for Dynamic Modulus of Asphalt Mortar[J]. *Mod. Transportation Tech.* 13, 1–5.

Zhou, X., Chen, S., Ge, D., Jin, D., and You, Z. (2020). Investigation of Asphalt Mixture Internal Structure Consistency in Accelerated Discrete Element Models. *Construction Building Mater.* 244, 118272. doi:10.1016/j.conbuildmat.2020.118272

**Conflict of Interest:** The authors declare that the research was conducted in the absence of any commercial or financial relationships that could be construed as a potential conflict of interest.

**Publisher's Note:** All claims expressed in this article are solely those of the authors and do not necessarily represent those of their affiliated organizations, or those of the publisher, the editors and the reviewers. Any product that may be evaluated in this article, or claim that may be made by its manufacturer, is not guaranteed or endorsed by the publisher.

frontiers | Frontiers in Materials

ORIGINAL RESEARCH
published: 29 April 2022
doi: 10.3389/fmats.2022.845718

# The Effects of Activation Treatments for Crumb Rubber on the Compatibility and Mechanical Performance of Modified Asphalt Binder and Mixture by the Dry Method

*Ming Liang[1†], Zhengmei Qiu[1†], Xuehao Luan[1], Cong Qi[2], Ning Guo[3], Zhaoxin Liu[4], Linping Su[1], Zhanyong Yao[1] and Jizhe Zhang[1*]*

[1]School of Qilu Transportation, Shandong University, Jinan, China, [2]Shandong Chambroad Petrochemicals Co., Ltd., Binzhou, China, [3]State Key Laboratory of Heavy Oil Processing, China University of Petroleum, Qingdao, China, [4]Shandong Hi-Speed Infrastructure Construction Co., Ltd., Jinan, China

Compatibility and mechanical performance of crumb rubber (CR)-modified asphalt and mixtures prepared by the dry method are poor at present, which limits the application of dry-mixed asphalt rubber in paving engineering. To solve this problem, various activated treatments for CR were performed, and the modified asphalt binder was prepared by the dry process in this study, aiming to activate the CR as the modifier and improve the compatibility of CR-asphalt blends. The effects of pre-treating methods of high temperature, pre-swelling, and microwave treatment on rutting resistance and compatibility of the asphalt binder and asphalt mixture were evaluated. Furthermore, the dynamic shear rheometer (DSR) of temperature sweep, Brookfield rotary viscosity, physical properties, rutting resistance, and microstructure of modified asphalt were measured. The results indicated that the three treatments have a pronounced effect on the high temperature performance of the crumb rubber-modified asphalt (CRMA) binder in the dry process and modified asphalt storage stability improvement. The high-temperature and microwave pre-treatment for CR lead to the largest complex modulus, viscosity, and rutting factor. Moreover, high-temperature, pre-swelling, and microwave treatment for CR significantly increases the dynamic stability of dry-mixed asphalt mixtures, which indicates the enhanced resistance to permanent deformation. In microscopy, homogeneous and compatible states were obtained for asphalt modified by high temperature-treated CR and pre-swelled CR, in which the strong interaction occurs among rubber molecules and the asphalt component. The microstructure of dry CR-asphalt blends sheds light on the mechanical performance. Consequently, activated CR modification for the asphalt binder by the dry process in this study is a promising technology, and other properties need to be verified in the future.

**Keywords: crumb rubber, modified asphalt, dry process, rutting resistance, pre-treating methods**

OPEN ACCESS

***Edited by:***
*Han-Cheng Dan,*
*Central South University, China*

***Reviewed by:***
*Tao Ma,*
*Southeast University, China*
*Peiwen Hao,*
*Chang'an University, China*
*Xianyong Ma,*
*Harbin Institute of Technology, China*
*Jian Ouyang,*
*Dalian University of Technology, China*

****Correspondence:***
*Jizhe Zhang*
*jizhe.zhang@sdu.edu.cn*

*†These authors have contributed equally to this work*

***Specialty section:***
*This article was submitted to Structural Materials, a section of the journal Frontiers in Materials*

***Received:*** *30 December 2021*
***Accepted:*** *23 February 2022*
***Published:*** *29 April 2022*

***Citation:***
*Liang M, Qiu Z, Luan X, Qi C, Guo N, Liu Z, Su L, Yao Z and Zhang J (2022) The Effects of Activation Treatments for Crumb Rubber on the Compatibility and Mechanical Performance of Modified Asphalt Binder and Mixture by the Dry Method. Front. Mater. 9:845718. doi: 10.3389/fmats.2022.845718*

# 1 INTRODUCTION

Asphalt is widely used as a binder in high-grade road pavement. Approximately 92% of four million kilometers of road were surfaced with asphalt in the United States (Wang et al., 2018), and more than 90% of 5.2 million kilometers of highways were estimated to be surfaced with asphalt materials as of 2020 in China. The axle load in highways reached 13.6 million tons at the end of 2019, which has brought a great challenge for asphalt pavement.

In recent years, asphalt pavement has suffered from various damages (rutting, cracking, and water damage) because of the adverse climate and enormous traffic volume (Qin et al., 20092009; Lu et al., 2013; Behnood and ModiriGharehveran, 2019; Du et al., 2020). Therefore, rutting, load-induced permanent deformation, is one of the most serious distresses in asphalt pavement (Witczak et al., 1997). Rutting is divided into three types, wearing, shear, and configuration rutting (Li, 2020). Shear rutting is the main type in recent research because of the insufficient performance of asphalt mixtures at high temperature. A large number of strategies have been proposed for improving the rutting resistance performance of asphalt pavement at high temperature. At present, reducing the heat absorption of asphalt pavement (Ameri et al., 2018; Shanbara et al., 2020), optimizing the asphalt pavement structure combination (Jiang et al., 2020), and improving the high-temperature performance of asphalt binders (Al-Hadidy and Tan, 2010; Geng et al., 2013; Dong et al., 2014; Hajikarimi et al., 2015) and mixtures (Wu et al., 2007; Nazirizad et al., 2015) have been used to improve the rutting resistance of asphalt mixtures. Using modified asphalt is one of the most popular methods. Additives such as styrene-butadiene-styrene (SBS) and anti-rutting additives are the most popular modifiers. However, these additives are expensive and lead to big performance variation in rutting resistance.

With the development of the economy, millions of industrial tires were generated. About 1.4 billion tires are sold worldwide each year, which fall into the end of life after several years (Lo Presti, 2013). These waste tires are generally disposed of by burning, landfill, or stacking, which may cause a potential threat to human health in some cases. To improve the utilization of waste tires, many researchers attempted to focus on the production and application of crumb rubber for asphalt pavement to reduce its environmental burden (Bahia and Davies, 1994; Jang et al., 1998; Navarro et al., 2002). The crumb rubber (CR) modifier could improve the mechanical and rheological properties of asphalt binders (Xiao et al., 2007a; Ameri et al., 2020; Yazdipanah et al., 2021). It has been confirmed that CR can improve the rutting resistance properties of asphalt mixtures (Cao, 2007; Lee et al., 2008; Bessa et al., 2019). The main two productive process for producing crumb rubber-modified asphalt mixtures are the wet process and dry process. Nearly all these reports adopted the "wet process" to prepare the CR-modified asphalt mixture. In wet processes, crumb rubber is added to the paving asphalt before it is blended with aggregates and delivered to the drum mixer. Light fractions in asphalt are absorbed by rubber particles during this process (Xiao et al., 2007b; Cheng et al., 2011; Li et al., 2018). However, the wet process has poor storage stability and higher construction temperature (Xiang and Huang, 2014; Liang et al., 2015; Chavez et al., 2019). In dry processes, crumb rubber is added to the aggregate in a plant as the fine aggregate before adding the asphalt binder (Cheng et al., 2011). The compatibility of CR and asphalt binders in the dry process is expected to be worse than the wet process, but the dry process is economically and environmentally better due to the short reaction time (Shook and Inc, 1990; Lawrence et al., 1991; Buncher, 1995; Moreno et al., 2011). It was agreed that using fine rubber and high asphalt binder content can obtain the stronger rubber-asphalt interaction (Picado-Santos et al., 2020). Several methods, such as optimizing aggregates gradation (Xie and Shen, 2013), utilizing additives (Zhu and Jiang, 2013), and chemical treating for CR (Yin et al., 2020), have been applied to improve the properties of CR-asphalt mixtures in the dry process. However, the blends' compatibility depends on the interaction among rubber molecules and the asphalt component (Li et al., 2021). If rubber particles are subjected to deep treatment, the inert surface could be activated. In this situation, the compatibility of CR-asphalt blends can be enhanced and a good performance that is equivalent to the wet process can be achieved by the dry process. In addition, the researchers believed that the dry process had more prospects because of its sampling process and economic value, etc. (Rodríguez-Fernández et al., 2020). In recent years, crumb rubber asphalt produced by other methods has also been widely used, such as warm mix asphalt mixtures (Hu et al., 2022) and stable crumb rubber asphalt (SCRA) (Ding et al., 2019). SCRA was obtained by a special manufacturing technique to make the rubber particles sufficiently dissolve in the asphalt, which was different from the traditional wet process (Ding et al., 2019). Thus, the effective treatment for CR needs to be promoted. Even though some literature reported other activating methods for CR to improve the properties of asphalt and mixtures in the dry process, these methods are insufficient for the demands of easy processing, low-cost, and effective treatment for CR.

In this study, various treating methods, including microwave, pre-swelling, and high-temperature treatment, were used to activate the crumb rubber, with the aim of improving the compatibility of crumb rubber and the asphalt binder in the dry process. The influence of high-temperature treatment, pre-swelling, and the two combinations, as well as microwave treatment for CR on the physical performance, viscosity, rheology, and rutting performance of the modified asphalt and mixture were studied through the dry process. The compatibility of activated CR-modified asphalt was evaluated by fluorescence microscopy and the relationship of compatibility, microstructure, and mechanical performance was discussed.

# 2 MATERIALS AND EXPERIMENTAL METHOD

## 2.1 Aggregate and Asphalt Matrix

In this study, Qilu AH-70 asphalt provided by Shandong Hi-speed Huarui Road Materials Technologies Co. Ltd. was used as the asphalt matrix. **Table 1** summarizes the basic properties of the selected asphalt matrix.

The aggregates used in this research were obtained from the limestone quarry in Wenzu Town, Jinan, China. The aggregates gradation of the final blend, based on the limitation of the JTG E20-2011 (JTGE20-2011, 2011) specification for dense-graded aggregates, is shown in **Figure 1**.

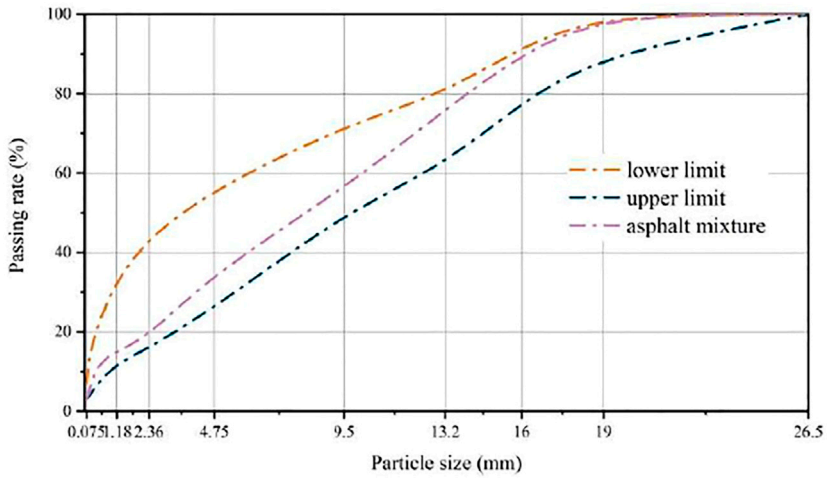


**FIGURE 1 |** The gradation of AC-20 dense-graded aggregates.

**TABLE 1 |** Specifications of the asphalt matrix.

| Physical property | Reference value in the standard (Wu et al., 2007) | Results |
|---|---|---|
| Penetration (25°C, 100 g, 5 s)/0.1 mm | 60 ~ 80 | 71.6 |
| Softening point (R&B)/°C | ≥46 | 48.6 |
| Ductility (15°C, 5 cm/min)/cm | >100 | 102 |

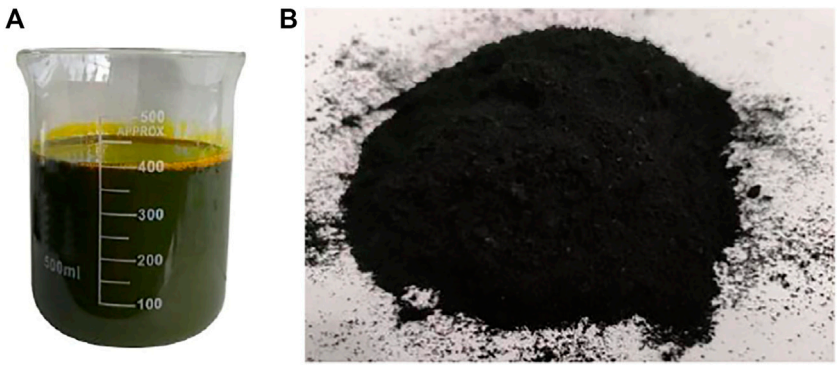


**FIGURE 2 |** The appearance of aromatic oil **(A)** and crumb rubber **(B)**.

## 2.2 Treatment of Crumb Rubber

Crumb rubber (40 mesh) was provided by Shandong An-zhitai Environmental Protection Technology Co. Ltd. Several treatment methods were adopted to activate the raw crumb rubber, including high-temperature processing, pre-swelling, microwave irradiation, and their combinations. In high-temperature treatment, the scrap tires were heated at 300°C for 6 h after adding the resin tackifier and antioxidant. After that, the waste fiber was filtered and finally, the tires were grinded. During pre-swelling treatment, 0.5 g of aromatic oil was first sprayed on 100 g of CR and then the blends were heated to 200°C for 1.5 h (as shown in **Figure 2A**). As for the microwave irradiation, 50 g of crumb rubber was irradiated for 5 min each time in a microwave oven at 700 W (as shown in **Figure 2B**). The microwave frequency was 2,450 MHz. The abbreviations of CR treated by various methods are summarized in **Table 2**.

## 2.3 Preparation of CRMA and Mixture

The modified asphalt was prepared using a motor stirrer in the laboratory. The base asphalt was heated in a cylindrical container until it became fluid. Then the activated CR (18% by weight of the asphalt matrix) was added into the container, after that, the CR/asphalt was blended at 170°C for 10 min. It is worth mentioning

**TABLE 2 |** The abbreviations of various activation methods of crumb rubber.

| Activation methods | The activated CR | Crumb rubber-modified asphalt |
|---|---|---|
| Raw CR without processing | R-CR | R-CRMA |
| High-temperature treatment | H-CR | H-CRMA |
| Pre-swelling | S-CR | S-CRMA |
| Microwave irradiation | M-CR | M-CRMA |
| High temperature and pre-swelling | HS-CR | HS-CRMA |

that the CR/asphalt mixture was only stirred for 10 min to evaluate the compatibility of activated CR and asphalt, to distinguish it from the traditional wet process with high-speed shear for CR/asphalt blends for a long time.

The dry method was applied to prepare the activated CR-modified asphalt mixture, which mixes activated CR with mineral aggregates before incorporating asphalt. AC-20 dense asphalt mixtures were designed in the study. The preparation of the CR asphalt mixture was conducted as follows. The mixing machine was preheated until the temperature reached 175°C; then the aggregates were put into the pot and blended for 90 s. After that, the rubberized asphalt was added into the pot and blended for 90 s; finally, the mineral powder was added into the pot for 90 s.

## 2.4 Measurements

### 2.4.1 The Test of Basic Physical Properties

The basic physical properties tests were carried out for asphalt with various activated CR mixtures, including penetration (25°C) (T0604-2011), softening point (T0606-2011), and ductility (10°C) (T0605-2011) according to the Chinese specification JTG E20-2011 (JTGE20-2011, 2011). Three virgin samples were used and averaged for three parallel sample data. Three replicates were measured and the average of measured data was achieved.

### 2.4.2 Brookfield Rotary Viscosity Test

A Brookfield viscometer was employed to characterize the viscosity-temperature properties of the activated asphalt based on the Chinese specification JTG E20-2011 of T0625-2011 (JTGE20-2011, 2011). The 27th rotor was selected and the test temperature rose from 120 to 180°C with a temperature interval of 10°C.

### 2.4.3 Oscillatory Shear Test

The rheological properties of asphalt modified with activated CR were evaluated by oscillatory shear tests using a dynamic shear rheometer (CV0100, Malvern, United Kingdom). A temperature sweep test was conducted from 30 to 80°C at the 10 Hz frequency based on the AASHTO T315 test protocol (AASHTO, 2013). A parallel plate with a diameter of 25 mm and a gap of 2 mm was selected.

### 2.4.4 Fluorescence Microscopy

The dispersion state in microscopy of the CR particles in asphalt was evaluated by fluorescence microscopy in this study, which can further reflect the interaction between CR particles and the asphalt component. The two glass slides sandwiched with a drop of CR-modified asphalt were manufactured previously and the surface of the glass was kept clean. The glass slides with the sample were observed with fluorescence microscopy under blue light irradiation with a magnification ratio of 200 at 25°C. The photographs of swelled CR particles were recorded by a high definition camera.

### 2.4.5 Wheel-Tracking Test

It is important to evaluate the influence of different CR activation methods on rutting resistance of crumb rubber-modified asphalt mixtures. A laboratory wheel-tracking test was conducted to assess the high-temperature rutting resistance of CRMA mixtures in accordance with Chinese standard JTG E20-2011 (JTGE20-2011, 2011). The asphalt mixture slab with the dimensions of 300 × 300 × 50 mm was compacted by a roller compactor. After that, they were placed in an oven at 60°C for at least 6 h to ensure a homogeneous temperature. In the test, the contact tire pressure of 0.7 MPa was set between the slab surface and rubber tire wheel. The standard rubber wheel was reciprocated on the surface of the slab with a speed of 42 rpm and a traveling distance of 230 mm. The rutting depth (RD) was recorded automatically by a Linear Variable Differential Transformer (LVDT) sensor. Dynamic stability was defined as the ratio of 15*42 and the difference between rutting depth at 60 min and 45 min. The higher value of dynamic stability corresponds to the better rutting stability at high temperatures.

### 2.4.6 Marshall Stability Test

It is important to design the mix ratio of the asphalt mixture and examine the quality of asphalt pavement by a Marshall stability test according to the Chinese standard JTG E20-2011 (JTGE20-2011, 2011). This test aims to evaluate the maximum load sustained by the bituminous material at a constant loading rate of 50 mm/min ±5 mm/min. The diameter and height of the Marshall specimen was 101.6 ± 0.2 mm, 63.5 ± 1.3 mm, respectively. Then the sample was placed in the thermostatic water bath at 60°C for 30–40 min. Four parallel samples were used and averaged for parallel sample data.

# 3 RESULTS AND DISCUSSION

## 3.1 Conventional Properties

The penetration, softening point, and ductility of CRMA modified with different activated CR mixtures are shown in **Figure 3**. Compared with R-CRMA (23.3), the penetration of H-CRMA, S-CRMA, M-CRMA, and HS-CRMA increased by nearly 29.6%, 72.1%, −8.6%, and 67%, respectively, which

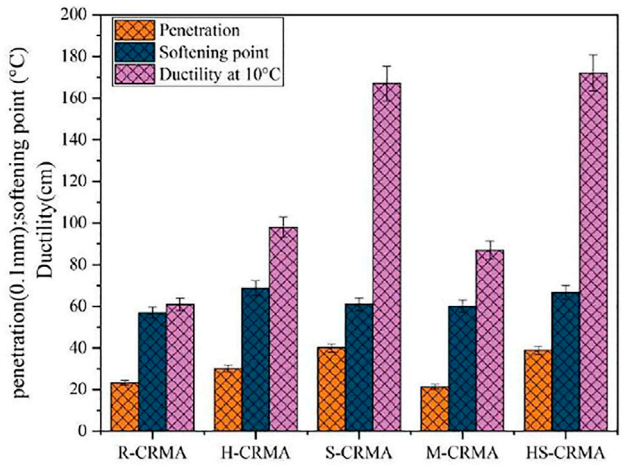


**FIGURE 3 |** The basic physical properties of asphalt with various activated CR mixtures.

suggests that the consistency performance of the modified asphalt has been improved compared with raw asphalt. The penetration of microwave-activated CR-modified asphalt was lower than that the asphalt modified by raw CR, indicating the hardness effect of the resulting asphalt by microwave treatment. The softening point of activated CR-modified asphalt increased more than 3.1°C, and the largest softening point of CRMA was 68.7°C of H-CRMA, compared with that of raw CR. Therefore, the high-temperature treatment for CR was most effective to enhance the softening point of CRMA, followed by pre-swelling with high temperature. It is indicated that high-temperature treatment for CR improved the high-temperature stability of modified asphalt. The ductility of modified asphalt with different activated CR mixtures showed a similar increasing tendency, indicating improved flexibility and tensile performance at low temperature. Particularly, pre-swelling and high-temperature/pre-swelling methods can significantly improve the low temperature ductility of modified asphalt. Therefore, high-temperature, pre-swelling, and both combinations, as well as microwave treatment for CR benefitted the physical properties of modified asphalt. These treatment methods in this study are related to the desulfurization of CR (de Sousa et al., 2017; Dong et al., 2017; Dong et al., 2019a), meanwhile, the fracture of the three-dimensional network structure of rubber molecules promotes the low-temperature performance.

## 3.2 Viscosity-Temperature Property

The viscosity-temperature property of CR-modified asphalt needs to be confirmed in order to obtain good workability, since the incorporation of rubber particles generally results in the evident increase of viscosity. As shown in **Figure 4**, the viscosity of the modified asphalt decreased with temperature increasing, but the decrease rate was different for asphalt with various activated CR mixtures. Compared with R-CRMA, modified asphalt with CR treated by high-temperature and microwave treatment showed higher viscosity, while pre-swelling and high-temperature/pre-swelling for CR led to the lower viscosity of asphalt. The viscosity changes caused by incorporation of different CR were weakened with increasing temperature.

The variation of viscosity as a function of temperature was described by the Arrhenius equation in this study, as shown in **Eq. 1** (Jiang et al., 2019). The fitting results are listed in **Table 3**.

$$\eta = A \cdot e^{E_\eta / RT} \tag{1}$$

Where the $\eta$ is the viscosity, Pa s; A is the regression coefficient; $E_\eta$ is the viscous activation energy, J/mol; R is the universal gas constant, 8.314 J mol-1 $K^{-1}$; and T is the absolute temperature, K. As displayed in **Figure 4B**, there was a good linear relationship between ln $\eta$ and 1/T and the correlation coefficient was more than 0.98. The dependence of viscosity on temperature of CR-modified asphalt in the study was well described by the Arrhenius equation. $E_\eta$ was related to the energy of asphalt flow deformation and the larger $E_\eta$ implied the better property of resistance deformation of asphalt. Sensitivity of viscosity to temperature change can be evaluated from the slope of linear fitting results as shown in **Figure 4B**. According to, M-CRMA had the lowest value of 6,834.4 J/mol of $E_\eta$ while HS-CRMA showed the highest $E_\eta$: 8,211.0 J/mol. The lower absolute value of the slope corresponded to the lower sensitivity of viscosity to temperature change. **Figure 4B** clearly shows that the slope value of S-CRMA and HS-CRMA were lower than the R-CRMA, which indicated that pre-swelling and pre-swelling/high-temperature treatment decreased the viscosity of asphalt compared to the untreated CR-modified asphalt. It is noteworthy that the incorporation of aromatic oil during pre-swelling for CR contributed to the lower viscosity. The M-CRMA and H-CRMA presented higher viscosity compared to R-CRMA at the same temperature, indicating more interactions among rubber molecules and the asphalt component.

## 3.3 Rheological Properties: Temperature Dependence

As a temperature-sensitive material, asphalt shows different temperature-dependent rheological behaviors, which is crucial for the service performance of asphalt pavement (Yang et al., 2021). The parameters of complex modulus G* and G*/sin $\delta$ were obtained from the temperature sweep test. G* is the stress-strain ratio of viscoelastic materials subjected to sinusoidal loads. G*/sin $\delta$ is the rutting factor. The larger the rutting factor, the stronger the resistance of asphalt to permanent deformation. The influence of temperature on the viscoelastic properties of various CR-modified asphalt mixtures with a constant frequency of 10 rad/s is shown in **Figure 5**.

As shown in **Figure 5**, the dynamic viscoelastic parameters of various crumb rubber-modified asphalt mixtures had a similar change curve with temperature in the logarithmic coordinate. S-CRMA and HS-CRMA had a sharp drop at high temperatures, while asphalt modified by high-temperature and microwave treatment showed a gentle reduction in the range of high temperature. Within the test temperatures ranging from

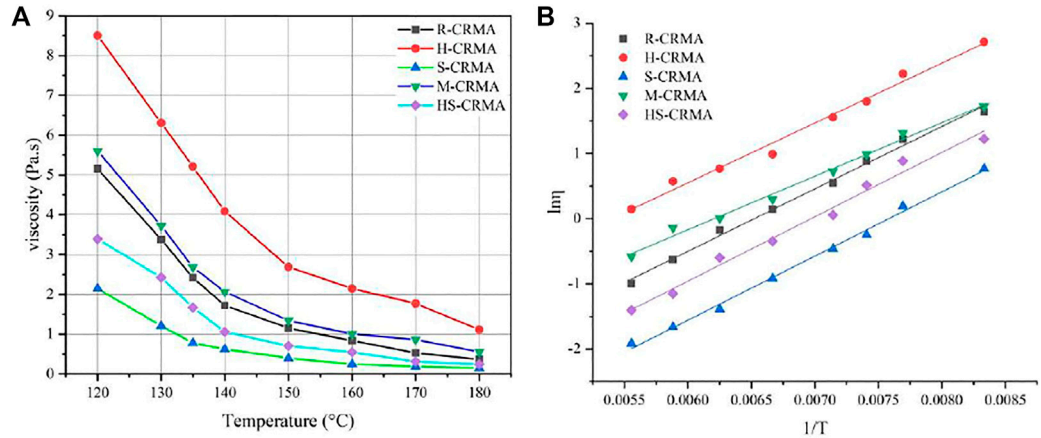


**FIGURE 4 |** The viscosity-temperature curve **(A)** from 120 to 180°C and **(B)** the fitting results.

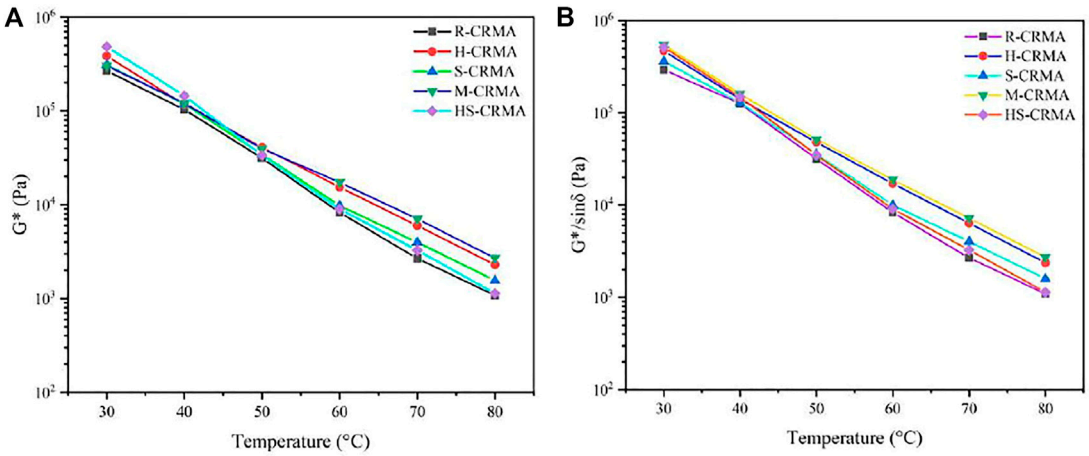


**FIGURE 5 |** The temperature sweep results of DSR at 10 Hz. **(A)** The complex modulus G*; **(B)** the rutting factor G*/Sin *δ*.

**TABLE 3 |** The fitting results for viscosity as a function of temperature.

| | ln A | Eη(J/mol) | $R^2$ |
|---|---|---|---|
| R-CRMA | −6.2462 | 7,961.2 | 0.99312 |
| H-CRMA | −4.9655 | 7,617.5 | 0.98564 |
| S-CRMA | −7.4639 | 8,183.2 | 0.99493 |
| M-CRMA | −5.1031 | 6,834.4 | 0.99013 |
| HS-CRMA | −6.8843 | 8,211.0 | 0.98389 |

30–60°C, the complex modulus G* and rutting factor G*/sin *δ* distinctly decreased, respectively, with the temperature increasing, which shows that temperature had a great influence on the complex modulus and rutting resistance. The G*/sin *δ* change rate (binder thermal sensitivity) decreased for all the modified binders compared to the base binder, which means an increase in the rutting resistance at high temperatures.

The complex modulus G* and rutting factor G*/sin *δ* of activated CR-modified asphalt were higher than that of raw CR-modified asphalt. This indicates that the activated CR had a great advantage on improving the high-temperature performance of asphalt, meanwhile activated CR had significant environmental benefits. Such increments in G* and G*/sin *δ* of activated CR-modified asphalt were pronounced in the interval of 50–80°C, which demonstrated that activated CR significantly improved the mechanical properties of the asphalt matrix and its resistance to deformation. The range of modified asphalt value |G*|/sin *δ* was 545.9 KPa–1.14 KPa which was greater than 1 KPa. The value of |G*|/sin *δ*≥ 1 KPa was considered to be sufficient to resist rutting and the failure temperature can be calculated at the critical point. The G* and G*/sin *δ* corresponding to the microwave activation method were the largest and the changing rate of G*/sin *δ* was the lowest. This indicated that the microwave activation method can significantly

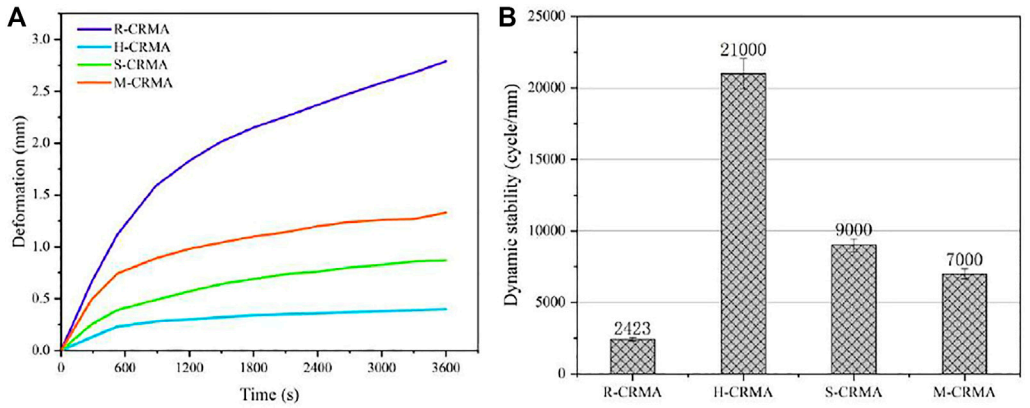


**FIGURE 6 |** The wheel-tracking test results: **(A)** the deformation against loading time; **(B)** the dynamic stability of various asphalt mixtures.

decrease the deformation and improve the elastic recovery performance in the medium temperature, because the microwave activation broke the cross-linked chemical bonds of rubber molecules and enhanced the chemical activity of rubber particles and the elasticity of the rubber asphalt (de Sousa et al., 2017; Rodríguez-Fernández et al., 2020). Whereas, the HS-CRMA had the smallest complex modulus G* and G*/sin $\delta$ and the largest changing rate. The pre-swelling and high-temperature treatment promoted the degree of desulfurization and degradation of rubber molecules at high temperature, which improved the compatibility of crumb rubber and the asphalt binder. **Figure 5B** shows the decreasing trend of G*/sin $\delta$ with the increasing temperature. Treated CR-modified asphalt had the higher value of G*/sin $\delta$, which denoted improved rutting resistance. Microwave and high-temperature treatment had the most benefits on the high-temperature rheological property of CR-modified asphalt.

## 3.4 Rutting Resistance

The influence of activated CR on the rutting resistance of asphalt mixture was evaluated by the wheel-tracking test, as shown in **Figure 6**. As shown, R-CRMA had the highest permanent deformation (2.8 mm), and the curve of deformation versus loading time had an obvious constant increasing trend. After treating CR, the deformation of the asphalt mixture track showed a dramatic decrease, meanwhile, the rutting depth curves gradually increased. The H-CRMA samples showed the minimum deformation, followed by S-CRMA and M-CRMA. Specifically, compared with R-CRMA, the H-CRMA rutting depth reduced by 598%, followed by S-CRMA and M-CRMA with a reduction of 221 and 110%, respectively.

Based on the curve of rutting depth against loading time, dynamic stability was obtained by calculating the proportion of 15*42 with the difference between rutting depth at 60 and 45 min, as displayed in **Figure 6A**. It can be seen from **Figure 6B** that for AC20, the dynamic stability of different activated CR-modified asphalt mixtures was 2,423, 21,000, 9,000, and 7,000 cycle/mm. Among these studied samples,

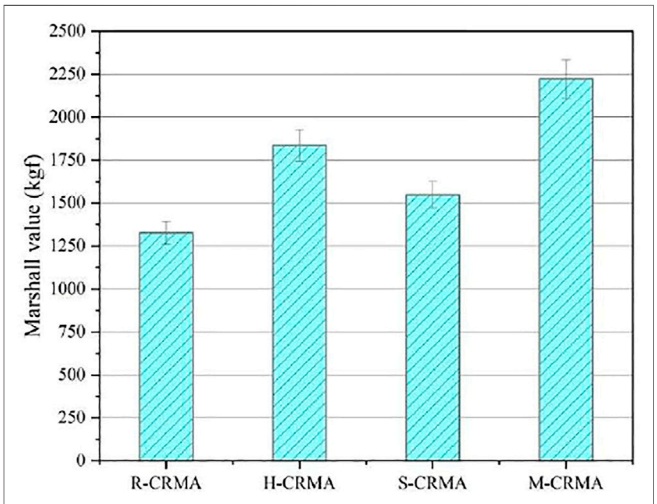


**FIGURE 7 |** Marshall stability of crumb rubber-modified asphalt.

the high-temperature treatment for CR led to significantly increased dynamic stability, which indicated the obviously enhanced resistance to permanent deformation of the asphalt mixture. In the stirring process, the aromatic components were reduced, and the resins and asphaltenes increased. As a result, the CRMA mixture became harder and the dynamic stability increased. The dynamic stability results were well in line with the temperature sweeping results for H-CRMA. The viscoelastic properties of H-CRMA changed and the elasticity increased at high temperature, which means improved recoverable deformation ability under the load and the reduced rutting depth. Besides, high viscosity of H-CRMA means the strong adhesion among asphalt and aggregates, which benefits the anti-rutting ability.

## 3.5 Marshall Stability

The results of Marshall stability are shown in **Figure 7**. As can be seen, the activated crumb rubber presented an increasing effect on the strength performance of the asphalt mixture. Among these

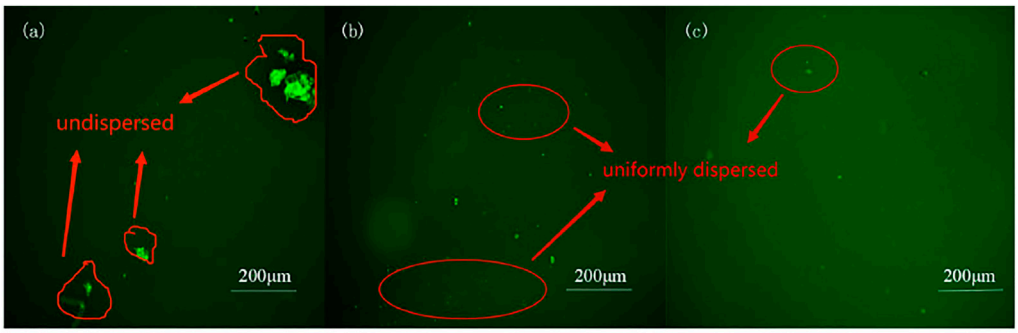


**FIGURE 8 |** Fluorescence microscopy of **(A)** R-CRMA; **(B)** H-CRMA; and **(C)** S-CRMA.

samples, the crumb rubber activated by microwave ameliorated the strength up to 2,223.6 kgf which was 1.5 times more than the untreated CRMA. And the Marshall values of the crumb rubber-modified asphalt mixture by high-temperature treatment and pre-swelling were both higher than the untreated CRMA mixture, which could help to determine the improving effect of crumb rubber activation methods. These can be attributed to the elastic behavior of crumb rubber (Saberi.K et al., 2017), because microwave irradiation can only break the C-S and S-S bonds, not C-C bonds. The process of high-temperature treatment includes shallow cracking that can greatly maintain the elastic property of crumb rubber. As for the pre-swelling activation method, the viscosity of S-CRMA was lower than R-CRMA which is the reason for the low Marshall value of S-CRMA. The viscosity of the asphalt mixture was lower, therefore the strength was worse.

## 3.6 Fluorescence Microscopy

To figure out the above results, fluorescence observation was conducted to shed light on the microstructure of various CR-modified asphalt mixtures. The fluorescence microstructures of R-CRMA, H-CRMA, and S-CRMA are presented in **Figure 8**. As shown, the dark green area is the asphalt phase and the light green spot is the rubber phase. For R-CRMA, the rubber particles were large and assembled with each other, which indicates the inhomogeneity and incompatibility. This indicated that the mechanical behavior of rubber cannot be delivered to the asphalt matrix due to the poorly dispersed raw rubber particles. Moreover, the chemical inert surface of raw CR with activation led to fewer interactions between rubber molecules and the asphalt component (Adhikari et al., 2000), which accounts for the poor rheological properties and rutting resistance. Contrary to this, homogeneous and compatible states were obtained for asphalt modified by high temperature-treated CR and pre-swelled CR. In **Figure 8**, it can be seen that the uniformly dispersed rubber particles are nearly round and the dimensions of dispersed particles are much smaller than that of untreated CR. For H-CRMA, the blends had few large rubber particles and the compatibility evidently improved. This is related to the desulfurization effect of CR when subjected to high-temperature treatment and rubber particle surface activation effect. Thus, the strong interaction among rubber molecules and the asphalt component results in the continuous and homogeneous asphalt phase formed with a few light green spots. For S-CRMA, the addition of aromatic oil accelerated the swelling of CR in the asphalt binder, so the dispersive and homogenous composite asphalt phase was formed. Consequently, the blends became more compatible systems after activation treatment for CR. The microstructure of asphalt blends explains their mechanical performance.

# 4 CONCLUSION

In this study, the effects of activating treatment for CR on rutting resistance of modified asphalt were evaluated. The correlation of fluorescence microscopy with mechanical behavior was discussed, the following findings can be given:

1) The activated CR increased the high temperature performance of the CRMA binder. The microwave and high-temperature pre-treating methods had the largest of complex modulus G* and rutting factor G*/sin $\delta$. While, pre-swelling and pre-swelling/high-temperature treatment for CR decreased the viscosity of asphalt compared to raw CR-modified asphalt. Microwave and high-temperature treatment benefitted the high-temperature rheological property of CR-modified asphalt.
2) The high temperature pre-treating method significantly improved the rutting resistance of the CR asphalt mixture, followed by the pre-swelling and microwave treatment. Homogeneous and compatible states were obtained for asphalt modified by high temperature-treated CR and pre-swelled CR.
3) The microstructure of asphalt blends explains their mechanical performance. Further investigations are needed to complement the findings of this study, such as fatigue behavior and the low temperature properties. Lastly, high-temperature, pre-swelling, and microwave treatment on CR are highly recommended for asphalt modification in paving engineering.

## DATA AVAILABILITY STATEMENT

The raw data supporting the conclusions of this article will be made available by the authors, without undue reservation.

## AUTHOR CONTRIBUTIONS

ML: Data curation, Writing - original draft, Writing - review & editing. ZQ: Data curation,Writing – original draft, Writing - review & editing, Funding acquisition. XL: Investigation. CQ: Methodology. NG: Project administration, Supervision. ZL: Drafting and review. LS: Investigation. Zhanyong Yao: Methodology. JZ: Project administration. All authors have read and agreed to the published version of the manuscript. We confirm that the order of authors listed in the manuscript has been approved by all named authors.

## FUNDING

The authors acknowledge the financial support of the National Natural Science Foundation of China (No. 51908330), the Qilu Young Scholars Program of Shandong University (No. 202099000060), the Fundamental Research Funds of Shandong University (No. 2020GN059), and State Key Laboratory of Heavy Oil Processing.

## REFERENCES

Aashto (2013). *T315 Determining the Rheological Properties of Asphalt Binder Using a Dynamic Shear Rheometer (DSR)*. American Association of State Highway and Transportation Officials.

Adhikari, B., De, D., and Maiti, S. (2000). Reclamation and Recycling of Waste Rubber. *Progr. Polym. Sci.* 25, 909–948. doi:10.1016/s0079-6700(00)00020-4

Al-Hadidy, A. I., and Tan, Y. Q. (2010). Effect of Styrene-Butadiene-Styrene on the Properties of Asphalt and Stone-Matrix-Asphalt Mixture. *J. Mater. Civil Eng.* 23 (4), 504–510.

Ameri, M., Afshin, A., Ebrahimzadeh, M., and Yazdipanah, F. (2020). Effect of Wax-Based Warm Mix Additives on Fatigue and Rutting Performance of Crumb Rubber Modified Asphalt. *Construction Building Mater.* 262. doi:10.1016/j.conbuildmat.2020.120882

Ameri, M., Mirzaiyan, D., and Amini, A. (2018). Rutting Resistance and Fatigue Behavior of Gilsonite-Modified Asphalt Binders. *J. Mater. Civil Eng.* 30 (11), 1–9. doi:10.1061/(asce)mt.1943-5533.0002468

Bahia, H. U., and Davies, R. (1994). Effect of Crumb Rubber Modifiers (CRM) on Performance-Related Properties of Asphalt Binders. *Asphalt Paving Technol.* 63, 414–449.

Behnood, A., and Modiri Gharehveran, M. (2019). Morphology, Rheology, and Physical Properties of Polymer-Modified Asphalt Binders. *Eur. Polym. J.* 112, 766–791. doi:10.1016/j.eurpolymj.2018.10.049

Bessa, I. S., Vasconcelos, K. L., Castelo Branco, V. T. F., and Bernucci, L. L. B. (2019). Fatigue Resistance of Asphalt Binders and the Correlation with Asphalt Mixture Behaviour. *Road Mater. Pavement Des.* 20, S695–S709. doi:10.1080/14680629.2019.1633741

Buncher, M. S. (1995). *Evaluating the Effects of the Wet and Dry Processes for Including Crumb Rubber Modifier in Hot Mix Asphalt*.

Cao, W. (2007). Study on Properties of Recycled Tire Rubber Modified Asphalt Mixtures Using Dry Process. *Construction Building Mater.* 21 (5), 1011–1015. doi:10.1016/j.conbuildmat.2006.02.004

Chavez, F., Marcobal, J., and Gallego, J. (2019). Laboratory Evaluation of the Mechanical Properties of Asphalt Mixtures with Rubber Incorporated by the Wet, Dry, and Semi-wet Process. *Construction Building Mater.* 205 (APR.30), 164–174. doi:10.1016/j.conbuildmat.2019.01.159

Cheng, G., Shen, B., and Zhang, J. (2011). A Study on the Performance and Storage Stability of Crumb Rubber Modified Asphalts. *Pet. Sci. Technology* 29. doi:10.1080/10916460903070421

de Sousa, F. D. B., Scuracchio, C. H., Hu, G.-H., and Hoppe, S. (2017). Devulcanization of Waste Tire Rubber by Microwaves. *Polym. Degrad. Stab.* 138 (APR), 169–181. doi:10.1016/j.polymdegradstab.2017.03.008

Ding, X., Chen, L., Ma, T., Ma, H., Gu, L., Chen, T., et al. (2019). Laboratory Investigation of the Recycled Asphalt concrete with Stable Crumb Rubber Asphalt Binder. *Construction Building Mater.* 203, 552–557. doi:10.1016/j.conbuildmat.2019.01.114

Dong, R., Liang, W., Tang, N., and Zhao, M. (2019a). Composition and Viscoelasticity of Asphalt Modified with Crumb Rubber Pre-desulfurized by Waste Cooking Oil. *China J. Highw. Transp.* 32, 226–234.

Dong, R., Qi, C., and Zheng, K. (2017). Test on Low- Temperature Performance for High 3temperature Pyrolytic Rubber Modified Asphalt. *China J. Highway Transp.* 30, 32–38. doi:10.19721/j.cnki.1001-7372.2017.10.005

Dong, Z. J., Xiao, G. Q., and Gong, X. B. (2014). Analysis on Impact of Gradation and Anti-rutting Additive on Rutting Resistance of Asphalt Mixture. *J. Highw. Transportation Res. Development*.

Du, C., Sun, Y., Chen, J., Gong, H., Wei, X., and Zhang, Z. (2020). Analysis of Cohesive and Adhesive Damage Initiations of Asphalt Pavement Using a Microstructure-Based Finite Element Model. *Construction Building Mater.* 261 (1), 119973. doi:10.1016/j.conbuildmat.2020.119973

Geng, H., Clopotel, C. S., and Bahia, H. U. (2013). Effects of High Modulus Asphalt Binders on Performance of Typical Asphalt Pavement Structures. *Construction Building Mater.* 44 (jul), 207–213. doi:10.1016/j.conbuildmat.2013.03.035

Hajikarimi, P., Rahi, M., and Nejad, F. M. (2015). Comparing Different Rutting Specification Parameters Using High Temperature Characteristics of Rubber-Modified Asphalt Binders. *Road Mater. Pavement Des.* 16 (4), 1–16. doi:10.1080/14680629.2015.1063533

Hu, J., Ma*, T., Yin, T., and Zhou, Y. (2022). Foamed Warm Mix Asphalt Mixture Containing Crumb Rubber: Foaming Optimization and Performance Evaluation. *J. Clean. Prod.*. doi:10.1016/j.jclepro.2021.130085

Jang, J. W., Yoo, T. S., Oh, J. H., and Iwasaki, I. (1998). Discarded Tire Recycling Practices in the united states, japan and Korea. *Resour. Conservation Recycling* 22 (1-2), 1–14. doi:10.1016/s0921-3449(97)00041-4

Jiang, X., Li, P., Ding, Z., Yang, L., and Zhao, J. (2019). Investigations on Viscosity and Flow Behavior of Polyphosphoric Acid (PPA) Modified Asphalt at High Temperatures. *Construction Building Mater.* 228, 116610. doi:10.1016/j.conbuildmat.2019.07.336

Jiang, Y., Zhang, Y., Deng, C., Yi, Y., Tian, T., and Yuan, K. (2020). High-temperature Rutting Resistance of Inverted Asphalt Pavement Structure. *Adv. Civil Eng.* 2020 (2), 1–10. doi:10.1155/2020/1937508

Jtg E20-2011. (2011). *Standard Test Methods of Bitumen and Bituminous Mixtures for Highway Engineering JTG E20-2011*. Beijing: Chinese Communications Press.

Lawrence, C., Killackey, B., and Lynch, D. (1991). *Experimental Hot Mix Pavement with Scrap Tire Rubber at Thamesville*. Ontario.

Lee, S.-J., Akisetty, C. K., and Amirkhanian, S. N. (2008). The Effect of Crumb Rubber Modifier (CRM) on the Performance Properties of Rubberized Binders in HMA Pavements. *Construction Building Mater.* 22 (7), 1368–1376. doi:10.1016/j.conbuildmat.2007.04.010

Li, C. M. (2020). "Application of Ground Penetrating Radar in the Analyzing of Rut Type of Asphalt Pavement," in 5th International Symposium on Test and Measurement.

Li, J., Chen, Z., Xiao, F., and Amirkhanian, S. N. (2021). Surface Activation of Scrap Tire Crumb Rubber to Improve Compatibility of Rubberized Asphalt. *Resour. Conservation Recycling* 169, 105518. doi:10.1016/j.resconrec.2021.105518

Li, R., Guo, Q., Shi, Z., and Pei, J. (2018). Effects of Conductive Carbon Black on PZT/PVDF Composites. *Ferroelectrics* 526 (1), 176e186. doi:10.1080/00150193.2018.1456308

Liang, M., Xin, X., Fan, W., Sun, H., Yao, Y., and Xing, B. (2015). Viscous Properties, Storage Stability and Their Relationships with Microstructure of Tire Scrap Rubber Modified Asphalt. *Construction Building Mater.* 74 (jan.15), 124–131. doi:10.1016/j.conbuildmat.2014.10.015

Lo Presti, D. (2013). Recycled Tyre Rubber Modified Bitumens for Road Asphalt Mixtures: A Literature Review. *Construction Building Mater.* 49 (6), 863–881. doi:10.1016/j.conbuildmat.2013.09.007

Lu, W., Sascha, K., and Frohmut, W. (2013). Impact of Surface Temperature on Fatigue Damage in Asphalt Pavement[J]. *J. Highw. Transportation Res. Development* 7 (3), 1–6.

Moreno, F., Rubio, M. C., and Martinez-Echevarria, M. J. (2011). Analysis of Digestion Time and the Crumb Rubber Percentage in Dry-Process Crumb Rubber Modified Hot Bituminous Mixes. *Construction Building Mater.* 25 (5), 2323–2334. doi:10.1016/j.conbuildmat.2010.11.029

Navarro, F. J., Partal, P., Martnez-Boza, F., Valencia, C., and Gallegos, C. (2002). Rheological Characteristics of Ground Tire Rubber-Modified Bitumens. *Chem. Eng. J.* 89 (1-3), 53–61. doi:10.1016/s1385-8947(02)00023-2

Nazirizad, M., Kavussi, A., and Abdi, A. (2015). Evaluation of the Effects of Anti-stripping Agents on the Performance of Asphalt Mixtures. *Construction Building Mater.* 84, 348–353. doi:10.1016/j.conbuildmat.2015.03.024

Picado-Santos, L. G., Capito, S. D., and Neves, J. (2020). Crumb Rubber Asphalt Mixtures: A Literature Review. *Construction Building Mater.* 247, 118577. doi:10.1016/j.conbuildmat.2020.118577

Qin, R., Li, Y., and Li, Z. (20092009). Analyzing the Cause of Asphalt Pavement Rut Damage of Heng-Zao Freeway. *GeoHunan Int. Conf.*. doi:10.1061/41047(354)7

Rodríguez-Fernández, I., Cavalli, M. C., and Poulikakos, L. D. (2020). Long-Term Aging Behaviour of Asphalt Mixtures Modified with Crumb Rubber Using the Dry Process. *Int. Symp. Asphalt Pavement Environ.*. 48. doi:10.1007/978-3-030-29779-4_22

Saberi.K, F., Fakhri, M., and Azami, A. (2017). Evaluation of Warm Mix Asphalt Mixtures Containing Reclaimed Asphalt Pavement and Crumb Rubber. *J. Clean. Prod.* 165 (nov1), 1125–1132. doi:10.1016/j.jclepro.2017.07.079

Shanbara, H. K., Shubbar, A., Ruddock, F., and Atherton, W. (2020). Characterizing the Rutting Behaviour of Reinforced Cold Mix Asphalt with Natural and Synthetic Fibres Using Finite Element Analysis. *Adv. Struct. Eng. Rehabil.* 38. doi:10.1007/978-981-13-7615-3_20

Shook, James., and Inc, A. (1990). *Experimental Construction of Rubber-Modified Asphalt Pavements in new york State - Final Report*.

Wang, T., Xiao, F., Zhu, X., Huang, B., Wang, J., and Amirkhanian, S. (2018). Energy Consumption and Environmental Impact of Rubberized Asphalt Pavement. *J. Clean. Prod.* 180 (APR.10), 139–158. doi:10.1016/j.jclepro.2018.01.086

Witczak, M. W., Quintas, H. V., and Schwartz, C. W. (1997). Superpave Support and Performance Models Management: Evaluation of the SHRP Performance Models System. *Proc. Eighth Int. Conf. Asphalt Pavements* III, 175–195.

Wu, S., Xue, Y., Ye, Q., and Chen, Y. (2007). Utilization of Steel Slag as Aggregates for Stone mastic Asphalt (SMA) Mixtures. *Building Environ.* 42 (7), 2580–2585. doi:10.1016/j.buildenv.2006.06.008

Xiang, S., and Huang, B. (2014). Recycling of Waste Tire Rubber in Asphalt and portland Cement concrete: an Overview. *Construction Building Mater.* 67 (B), 217–224.

Xiao, F., Amirkhanian, S., and Juang, C. H. (2007). Rutting Resistance of Rubberized Asphalt concrete Pavements Containing Reclaimed Asphalt Pavement Mixtures. *J. Mater. Civ. Eng.* 19 (6), 475e483. doi:10.1061/(asce)0899-1561(2007)19:6(475)

Xiao, F., Amirkhanian, S., and Juang, C. H. (2007). Rutting Resistance of Rubberized Asphalt concrete Pavements Containing Reclaimed Asphalt Pavement Mixtures. *J. Mater. Civ. Eng.* 19 (6), 475–483. doi:10.1061/(asce)0899-1561(2007)19:6(475)

Xie, Z., and Shen, J. (2013). "Long-term Performance of SMA Mixtures Added with Crumb Rubbers in Dry Process," in *Airfield and Highway Pavement* (American Society of Civil Engineers), 1145–1155. doi:10.1061/9780784413005.096

Yang, Q., Qian, Y., Fan, Z., Lin, J., Wang, D., Zhong, J., et al. (2021). Exploiting the Synergetic Effects of Graphene and Carbon Nanotubes on the Mechanical Properties of Bitumen Composites. *Carbon* 172, 402–413. doi:10.1016/j.carbon.2020.10.020

Yazdipanah, F., Ameri, M., Shahri, M., Hasheminejad, N., and Haghshenas, H. F. (2021). Laboratory Investigation and Statistical Analysis of the Rutting and Fatigue Resistance of Asphalt Mixtures Containing Crumb-Rubber and Wax-Based Warm Mix Asphalt Additive. *Construction Building Mater.* 309, 0950–0618. doi:10.1016/j.conbuildmat.2021.125165

Yin, L., Yang, X., Shen, A., and Bo, L. (2020). Mechanical Properties and Reaction Mechanism of Microwave-Activated Crumb Rubber-Modified Asphalt before and after thermal Aging. *Construction Building Mater.* 267, 120773. doi:10.1016/j.conbuildmat.2020.120773

Zhu, X. L., and Jiang, D. (2013). Mix Design of Sup-13 Mixed with TOR and Crumb Rubber Using Dry Process. *Amm* 368-370 (III), 764–770. doi:10.4028/www.scientific.net/amm.368-370.764

**Conflict of Interest:** Author CQ was employed by the company Shandong Chambroad Petrochemicals Co., Ltd. Author ZL was employed by the company Shandong Hi-Speed Infrastructure Construction Co. Ltd.

The remaining authors declare that the research was conducted in the absence of any commercial or financial relationships that could be construed as a potential conflict of interest.

**Publisher's Note:** All claims expressed in this article are solely those of the authors and do not necessarily represent those of their affiliated organizations, or those of the publisher, the editors and the reviewers. Any product that may be evaluated in this article, or claim that may be made by its manufacturer, is not guaranteed or endorsed by the publisher.

frontiers | Frontiers in Materials

ORIGINAL RESEARCH
published: 22 July 2022
doi: 10.3389/fmats.2022.956742

# Stochastic Model Generation of Porous Rocks and Study on 2D Pore Morphology Influencing Rock Strength and Stiffness

*Lianheng Zhao[1,2], Min Deng[1], Xiang Wang[1]*, Dongliang Huang[1] and Shi Zuo[1]*

*[1]School of Civil Engineering, Central South University, Changsha, China, [2]Key Laboratory of Heavy-Haul Railway Engineering Structure, Ministry of Education, Changsha, China*

With the increasing usage of porous rocks in engineering construction, their well-performed properties (e.g., permeability and heat insulation) have attracted increasing attention from researchers in engineering geology. In nature, the vesicles in porous rocks always exhibit irregularity in morphology. This article proposes a workflow combining photogrammetry and Fourier transform to accurately acquire, characterize, and regenerate the natural pore morphology of porous rocks, including four steps: 1) initially, several 3D digital models of volcanic porous rock surfaces are reconstructed through a photogrammetry system, and the hollow pores in the surface are split into assemblies; 2) then, the 3D pore assembly is projected to a 2D reference plane with each pore being recognized and extracted; 3) the contours of a single pore are processed based on discrete Fourier transform (DFT), and a series of Fourier descriptors (mainly consist of $D_2$, $D_3$, and $D_8$) are then statistically analyzed; 4) an inverse discrete Fourier transform (IDFT) is then conducted to quantitatively reconstruct the pores. Based on the earlier processes, the pores are distributed in a numerical model (rock failure and process analysis code, RFPA$^{2D}$), and uniaxial compression simulations are performed to further investigate the influences of porosity and pore morphology on rock strength and stiffness. Herein, we introduce significant Fourier descriptors (i.e., $D_2$, $D_3$, and $D_8$) as representations of three levels of pore morphology. Thus, 12 groups of numerical simulations considering the impact of porosity, pore orientation, $D_2$, $D_3$, and $D_8$ are conducted. Results show that the porosity exerts a first-order control on the mechanical properties of rocks, while the effect of pore orientation is related to $D_2$. All of them closely match those typically observed in previous studies. Furthermore, these simulations also highlight the influence of detailed pore morphology, such as convex hulls and subtle zigzags characterized by $D_3$ and $D_8$, respectively, on the rock failure process, marking that a more complicated morphology (e.g., with more convex hulls) may result in a reduction in rock strength and Young's modulus. The proposed study provides a novel perspective on natural pore morphology together with its influence on rock strength and stiffness.

**Keywords: porous rock, photogrammetry, Fourier transform, pore morphology, RFPA, rock strength**

OPEN ACCESS

***Edited by:***
*Weina Meng,*
*Stevens Institute of Technology, United States*

***Reviewed by:***
*Tongming Qu,*
*Swansea University, United Kingdom*
*Teguh Prayitno,*
*Jakarta State University, Indonesia*
*Yingbin Zhang,*
*Southwest Jiaotong University, China*

****Correspondence:***
*Xiang Wang*
*wangxiang_csu@126.com*

***Specialty section:***
*This article was submitted to Structural Materials, a section of the journal Frontiers in Materials*

***Received:*** *30 May 2022*
***Accepted:*** *21 June 2022*
***Published:*** *22 July 2022*

***Citation:***
*Zhao L, Deng M, Wang X, Huang D and Zuo S (2022) Stochastic Model Generation of Porous Rocks and Study on 2D Pore Morphology Influencing Rock Strength and Stiffness. Front. Mater. 9:956742. doi: 10.3389/fmats.2022.956742*

## INTRODUCTION

Porous rocks, e.g., vesicular basalt, carbonates, sandstones, and tuff, are widely used in engineering constructions, mainly due to their superior quality in noise reduction and thermal insulation. However, pores always impose an adverse effect on the mechanical behavior of rocks, viz., compressive strength, elastic modulus, and Poisson's ratio. In the early stages of research studies on the relationship between porosity and mechanical properties, researchers proposed empirical relations between porosity and compressive strength or Young's modulus for several types of rocks, such as quartz arenites (Dunn et al., 1973), siliciclastic rocks (Vernik et al., 1993), sandstones (Ju et al., 2013), and carbonates (Farquhar et al., 1994; Chang et al., 2006). On the other hand, porosity also affects the inelastic and failure behavior of rock, such as compaction localization (Olsson and Holcomb, 2000), shear-enhanced compaction, and strain hardening (Vajdova et al., 2004; Gao and Kang, 2017; Zhao H. et al., 2018). Regarding the failure mode of porous rock, Sammis and Ashby (1986) first proposed a pore-based crack model that some researchers, Wong et al. (2006) and Lin et al. (2015), have modified and combined with more general conditions to study the influence of other pore indices, such as size, on the brittle failure of porous rocks. In early laboratory testing, Peng and Podnieks (1972) conducted a series of uniaxial tests to study the time-dependent behavior of porous tuff, interpreting various phenomena of rock fracture due to changes in strain rate. Baud et al. (2004) further studied the damage evolution and acoustic emission activity on strain localization of porous sandstones through triaxial compression tests.

Actually, the vesicles on porous rocks play a crucial role in mechanical behavior. Heap et al. (2014) and Griffiths et al. (2017) have investigated the influences of basic pore geometry on the compressive strength and stiffness of porous rocks containing circular and elliptical pores, respectively. However, the shapes of pores or vesicles in rocks show obvious irregularities in profile. With the development of X-ray microcomputed tomography (μXCT) and image processing technology, it is possible for researchers to acquire the natural pores. A large number of research studies verify the shape irregularity and spatial distribution variation of pores in on-site rock samples such as basalt, carbonates, and limestones (Cilona et al., 2014; Jeong et al., 2014; Rozenbaum and Du Roscoat, 2014; Ji et al., 2015). Based on their CT results, Bubeck et al. (2017) further studied the influences of porosity and pore orientation relating to the coring direction of samples on the rock strength, only considering the samples cored normal to bedding and parallel to bedding of a lava.

In previous studies, they either focused on the influence of basic pore morphology, such as basic shape (e.g., circular, elliptical), pore orientation, and pore aspect ratio (Heap et al., 2014; Griffiths et al., 2017; Gui et al., 2017), or performed several laboratory tests on rock samples through analyzing their pore structure (Bubeck et al., 2017). However, they seldom characterize the irregularity of comprehensive pore morphology and study the influence of detailed pore morphology such as convex hulls or corners on the rock strength and stiffness.

Based on photogrammetry, a more efficient and convenient way to visualize external contour features of objects compared to μXCT (Paixão et al., 2018; Zhao et al., 2020a; Zhao et al., 2020b; Lianheng et al., 2020), it is easier to acquire digital models of rock samples. In order to characterize and analyze the morphology of pores, herein, we introduce a workflow to extract each pore. Further processes applying discrete Fourier transform (DFT) and inverse discrete Fourier transform (IDFT) are performed in the extracted pore contour, obtaining a series of Fourier descriptors (mainly including $D_2$, $D_3$, and $D_8$, as seen in similar cases for rock particles) (Mollon and Zhao, 2013; Lianheng et al., 2017) to characterize rock pore morphology and regenerate a large number of shape-controlled pores. Later, uniaxial compressive simulations using rock failure processing analysis (RFPA, Chun'an Tang, 1997) are conducted to investigate the influence of pore morphology on rock strength and Young's modulus. Initially, several groups of numerical simulations considering the influence of porosity and pore orientation are performed and compared with previous studies (Heap et al., 2014; Bubeck et al., 2017; Griffiths et al., 2017) for verification. To demonstrate that significant Fourier descriptors (i.e., $D_2$, $D_3$, and $D_8$) could be representations of pore morphology, we compared the results of $D_2$ with data of aspect ratio from Griffiths et al. (2017), which shows a high agreement. In this case, three significant Fourier descriptors $D_2$, $D_3$, and $D_8$ relating to the pore elongation, convexity, and roughness, respectively (as similarly seen in Lianheng et al., 2017), are regarded as different levels of pore morphology and their influence on rock strength and stiffness are studied.

## WORKFLOW OF ROCK PORE EXTRACTION

Unlike solid objects, porous rock includes empty pores with solid rock boundaries. The pore part is a little darker than the solid rock part in the natural light, showing an inconspicuous color difference. Moreover, the color difference is actually sensitive to the numerous micropore-induced noises and the shadow darkness, causing the grayscale close and indistinguishable from their neighbor surface. With the usage of photogrammetry in geomaterials, 2D pore geometries can be obtained through 3D porous rock models with higher precision and less noise.

In this article, a workflow for acquiring the 2D pore geometry of natural volcanic rocks is proposed based on photogrammetry, mesh processing, and image recognition techniques. The main steps are as follows:

(1) taking pictures along a shooting path; (2) defining the local coordinate system and aligning photos for sparse point cloud establishment; (3) reconstructing the dense point cloud and tilt correction; (4) meshing and splitting the hollow pores and rock surface; (5) projecting the 3D mesh model of the pore assembly to the 2D plane; and (6) recognizing and extracting each pore for the subsequent Fourier analysis.

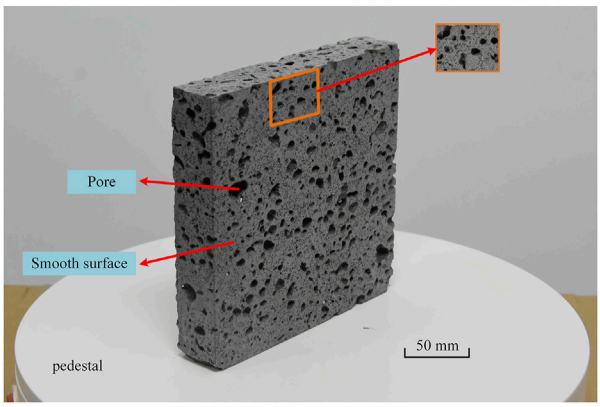


**FIGURE 1 |** Diagram of volcanic rock specimens.

## Materials and Equipment

A typical porous rock, namely, volcanic rock, is studied in this section. There are various particle shapes in volcanic rocks, for instance, slick-surfaced volcanic rock blocks and spherical volcanic rock particles. To simply obtain 2D surface pore geometries, the selected specimens of volcanic rock (**Figure 1**) are several smooth rock blocks from Tengchong, Yunnan Province, China. The density and coefficient of water absorption are 3.52 g/cm$^3$ and 11.7%, respectively. All of these specimens are cuboids with uniform dimensions of 150 mm*150 mm*30 mm. For convenience, we set surfaces with dimensions of 150 mm*150 mm as the major principal surfaces and surfaces with dimensions of 150 mm*30 mm as the minor principal surfaces. In this way, there are six surfaces with approximately 70 external pores in total for a single specimen. Additionally, the pore size is mainly within the range of 2–20 mm.

A Nikon D7200 digital camera with an AF-S DX NIKKOR 18–200 mm f/3.5–5.6G ED VR II camera lens is used to photograph the volcanic rock specimens. Moreover, a calibration board of the same size as the rock specimens is selected to define a local coordinate system. It contains a number of orderly distributed white dots surrounded by a black background (**Figure 2C**).

## Photogrammetry Framework

Therefore, a systematic photogrammetry framework is established, as **Figure 2B** shows, mainly including the pedestal, camera, calibration board, and some fixed supports behind. The rock specimen is placed on the center of the pedestal so that its major principal surface can be photographed by the camera. The distance between the camera and the rock specimen is approximately 0.5 m, ensuring that both the rock surface and hollow pores are in focus.

During the process of image collection, the calibration board is placed on the right of the rock specimen. A shooting route is designed to traverse all of the points of the rock surface and calibration board. There are necessary overlaps between the adjacent images both horizontally and vertically, as **Figure 2A** shows, to ensure that the same points are sufficient for the subsequent reconstruction (Zhu et al., 2016). In detail, the one-third grid lines in the camera are activated, and the image is divided into nine parts of equal area. Therefore, the overlaps between the horizontally adjacent images are the right (or left) 1/3 part, while between the vertically adjacent images are the bottom (or top) 1/3 part. In this way, there is at least a 55% overlap for each image.

The calibration board contributes to the establishment of a local coordinate system (**Figure 2C**). Its front surface along with the smooth part on the front major surface of the rock specimen is approximately in the same plane. The four white dots in the corners are selected as the major reference points. Point 1 is set as the coordinate origin, point 2 defines the positive direction of the *x*-axis, and point 4 defines the *z*-axis. Additionally, point 3 serves as a control point for error reduction.

## Reconstruction of 3D Dense Point Cloud and Tilt Correction

A series of images along the shooting path is then processed through the structure from the motion (SfM) technique (Longuet-Higgins, 1981; Spetsakis and Aloimonost, 1991;

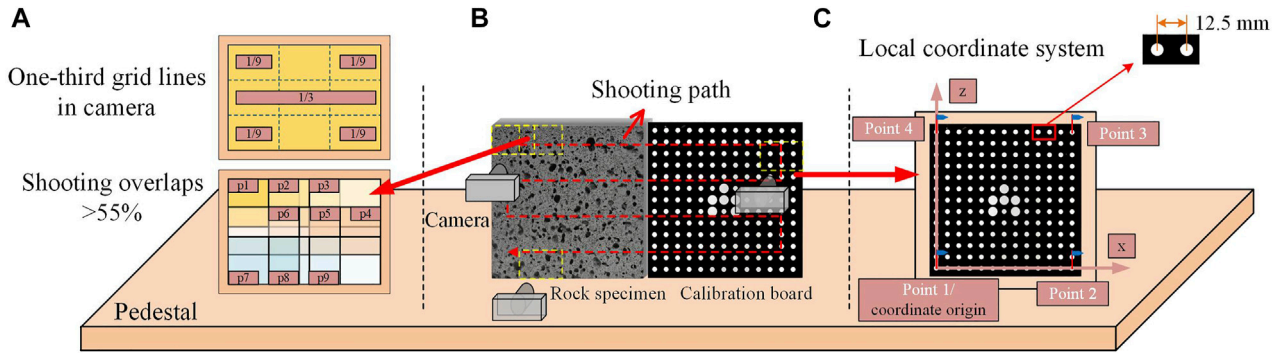


**FIGURE 2 |** Schematic diagram of the photogrammetry framework: **(A)** necessary overlaps between the adjacent images both horizontally and vertically; **(B)** the shooting route and subjects; **(C)** the calibration board and establishment of local coordinate system.

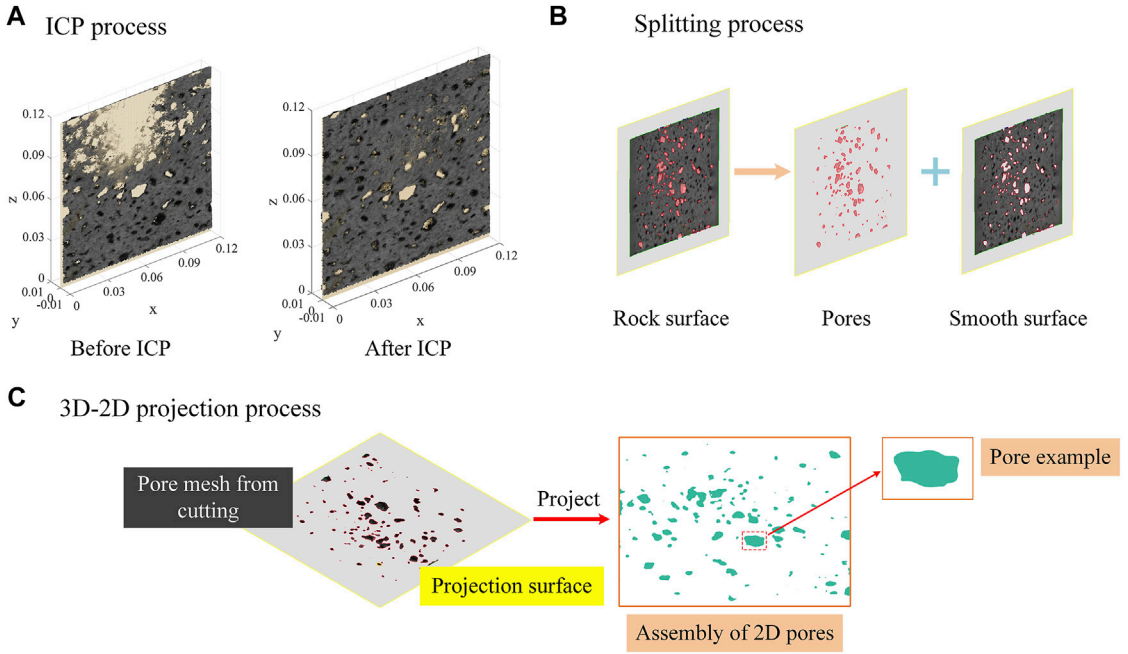


**FIGURE 3 |** Schematic diagram of processes for rock pore extraction after obtaining the 3D model: **(A)** tilt correction based on ICP algorithm; **(B)** process of splitting the pores and smooth surface; **(C)** 3D-to-2D projection process of rock pores.

Pollefeys et al., 2004; Carrivick et al., 2016), in which the camera position and pose relative to objects can be estimated. For this purpose, the 3D modeling and mapping software Agisoft Metashape (version 1.8.1, commercial, www.agisoft.com) is employed. In the Agisoft Metashape workflow, the digital images are first aligned, and a sparse point cloud is built. However, the object is originally in the global coordinate system. To shift to the local coordinate system built from the calibration board, reference points 1–4 are marked accurately in every image containing the calibration board, and the images are aligned once again. The sparse point cloud in the local coordinate system is further used for generating a dense point cloud by multi-view stereo (MVS) algorithms (Furukawa and Ponce, 2009), which are also applied in the software.

Although the local coordinate system built from the calibration board is sufficient to characterize the surface of the rock specimen, it may be slightly shifted off of the smooth surface of the rock specimen, which affects the practicality of the subsequent splitting process. For this reason, a secondary correction of the dense point cloud is conducted based on the iterative closest point (ICP) algorithm that was first proposed by Besl and McKay (1992) and applied to point cloud registration. In this article, a raster reference plane coinciding with the *xOz* plane is introduced. The boundary of the reference plane is approximately the same as that of the rock specimen. **Figure 3A** shows the dense point cloud before and after ICP algorithm processing.

## Meshing and Splitting the Rock Surface

Reconstructing the triangle mesh is then conducted based on the screened Poisson algorithm, a watertight surface reconstruction algorithm, proposed and modified by Kazhdan et al. (2006) and Kazhdan and Hoppe (2013). Notably, since the rock surface investigated was not sealed, some extra mesh around the real surface was reconstructed and should be deleted during the process of screened Poisson surface reconstruction. MeshLab software (www.meshlab.net), which is free for research, was applied to implement all of these processes, and a watertight mesh of the rock surface was established.

Splitting the resulting smooth surface part and hollow pore part is easy to execute along a simple plane parallel to the *xOz* plane. The smooth surface part is deleted, and the hollow pore part is reserved, so a number of bumps protruding from the cutting plane can be saved. These bumps consist of the 3D digital model of the volcanic pore assembly. **Figure 3B** shows the diagram of the splitting process.

## Acquisition of 2D Projection of Rock Pores

To obtain the 2D pores from the 3D mesh model of the rock pores, projection is a convenient method. Owing to the watertight surface reconstruction algorithm, all of the pore bumps protruding from the cutting plane are semi-closed, making the 3D model easier to project. On the other hand, the 3D pores are transformed during the tilt correction of the whole dense point cloud, where the raster reference plane coincides with the *xOz* plane. Consequently, all of the 3D pores can be directly projected to the *xOz* plane and outputted to one image, in which the highest resolution was set. **Figure 3C** shows the process of rock pore projection from 3D bumps to 2D faces. The 3D pores split from the rock surface were projected onto a plane, and a series of 2D pores were obtained.

## Recognition and Extraction of 2D Pore Contours

Combining the previous steps, all of the 2D projected pores are distributed in one region, and each single pore should be recognized and extracted for analysis. Whereas the recognition and classification of each pore during the previously described photogrammetry process are impractical, the open-source library OpenCV (version 3.4.1) embedded in MATLAB is employed to recognize and extract the 2D contours of each pore. OpenCV is a computer vision and machine learning software library that was built to provide a common infrastructure for computer vision applications and to accelerate the use of machine perception (www.OpenCV.org).

To recognize the pores, the background is set as white, and the faces are set as green in the projection process (**Figure 3C**). A high-resolution image is then imported to MATLAB through the "cv.imread" function, where the prefix "cv." means that the function belongs to the OpenCV library. Therefore, the processes of graying and binarization are conducted *via* the functions "cv.cvtColor" and "cv.threshold," respectively. A gray threshold of 10 is chosen for binarization. Notably, the gray threshold is flexible if only the object and background must be distinguished.

As a result, images of rock surfaces with black rock and white pores are built. The function "cv.findContours" is then applied to the binary image to identify the contours via the binary codes of 0 and 1, and then the contours are exported as coordinate points in the pixel coordinate system. Each contour, described as a series of coordinate points ($[x_i, y_i]$), is saved in a single cell. In the subsequent analysis, only contours with more than 30 coordinate points are regarded as real pores and selected for regeneration. Note that if the coordinate points for a contour are too low, these points may not form a certain contour. In this case, the threshold of 30 coordinate points was selected by experience. In total, 387 pore contours are extracted from the four rock specimens. The pore sizes are approximately in the range of [4 $mm^2$, 100 $mm^2$], while the equivalent circle diameters are mainly in the range of [2 mm, 10 mm].

# CHARACTERIZATION AND REGENERATION OF ROCK PORES

DFT and IDFT are the two inverse mathematical processes for mutual conversion between the time domain and frequency domain. The DFT can transform the irregular time-domain (or space domain) signal into regular and periodic sine (or cosine) waves in the frequency domain with a continuous spectrum from low frequency to high frequency, where the sine (or cosine) waves depend on only the amplitude and phase angle. In contrast, IDFT can integrate those sine (or cosine) waves and transform them back into a new time-domain signal. Actually, these two methods are widely used in the problems relating to signals, whether they are periodic or non-periodic. For instance, Lianheng et al. (2017) conducted a series of studies on the reconstruction of non-periodic 2D contours of granular ballast based on IDFT. This article combined the DFT and IDFT techniques to characterize and regenerate rock pores with a similar application.

## Fourier Descriptors of Real Pore Contours

The whole DFT procedure is executed in MATLAB, and the Fourier descriptors $D_1$–$D_{64}$ are calculated. **Figure 4A** shows a sample of 2D natural volcanic pore contours extracted and the frequency spectrum (i.e., Fourier descriptors $D_0$–$D_{64}$, where $D_0$ and $D_1$ are set as constants 1 and 0, respectively) after the DFT process.

Several studies (Mollon and Zhao, 2012; Lianheng et al., 2017; Zhao L. et al., 2018; Zhao et al., 2021) have shown that Fourier descriptors are related to the shape characteristics of 2D particle contours or cavity contours, especially the significant Fourier descriptors $D_2$, $D_3$, and $D_8$, which represent the corresponding series of Fourier descriptors: $D_2$, $D_3$–$D_7$, and $D_8$–$D_{64}$. These three types of Fourier descriptors can be related to three different levels of shape features. Specifically, $D_2$ relates to elongation, $D_3$–$D_7$ relates to convexity, and $D_8$–$D_{64}$ relates to roughness. In this case, we statistically analyze the distribution of $D_2$, $D_3$, and $D_8$. **Figures 4B–D** show the statistical histogram of significant Fourier descriptors $D_2$, $D_3$, and $D_8$ from 387 real pore contours. All three descriptors have mainly lognormal distributions. On the other hand, the ranges of $D_2$, $D_3$, and $D_8$ were also calculated. Instead of selecting the whole range of data, we set a confidence level of 95% and regard the left side of the confidence interval as the acceptable range for reducing extreme points. The final ranges of $D_2$, $D_3$, and $D_8$ are listed in **Table 1**.

During the IDFT, the two series of Fourier descriptors $D_3$–$D_7$ and $D_8$–$D_{64}$ are generally calculated through empirical formulas that are controlled by $D_3$ and $D_8$ (Mollon and Zhao, 2012):

$$\begin{cases} D_n = 2^{\alpha \cdot \log_2\left(\frac{n}{3}\right)+\log_2(D_3)}, 3 < n < 8 \\ D_n = 2^{\beta \cdot \log_2\left(\frac{n}{8}\right)+\log_2(D_8)}, n > 8 \end{cases}. \quad (1)$$

Based on the numerous Fourier descriptors $D_1$–$D_{64}$ acquired earlier, the mean values of $D_3$–$D_{64}$ are calculated and divided into two categories, namely, those of $D_3$–$D_7$ and those of $D_8$–$D_{64}$, for fitting the parameters $\alpha$ and $\beta$. In this case, the fitting values of $\alpha$ and $\beta$ are -1.246 and -1.731 with the goodness of fit $R^2$ values of 0.724 and 0.907, respectively.

## Reconstruction of 2D Pores Based on Inverse Discrete Fourier Transform

After obtaining the actual range of the significant Fourier descriptors $D_2$, $D_3$, and $D_8$ for the pore contours of the real volcanic rock, we further reconstruct the 2D pores through IDFT based on reasonable Fourier descriptors, which are more similar to the real volcanic rock pore geometries than the regular pore geometries such as circles, ellipses, and squares. According to the theory of IDFT, the number of harmonics ($N$) is a factor that cannot be ignored (Su and Xiang, 2020). **Figures 5A–G** show the

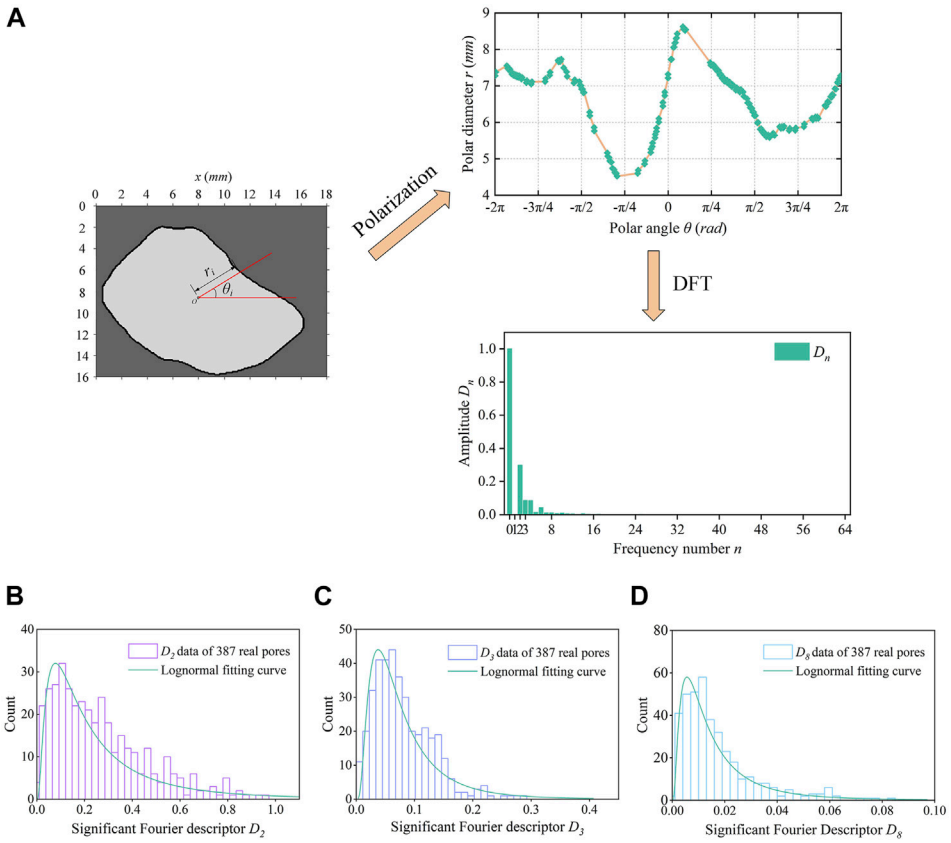


**FIGURE 4 |** Analysis for extracted natural pores: **(A)** process of polarization and DFT for a natural pore example; **(B)**–**(D)** the statistical results of Fourier descriptors $D_2$, $D_3$, and $D_8$, respectively, from 387 extracted pores.

**TABLE 1 |** The ranges of significant Fourier descriptors for pore contours.

| | $D_2$ | $D_3$ | $D_8$ |
|---|---|---|---|
| Range | [0.00, 0.60] | [0.00, 0.16] | [0.00, 0.05] |

reconstruction results of the pore contours for $N$ = 1, 2, 4, 8, 16, 32, and 64, and **Figure 5H** shows the result of the original contours. With increasing harmonic number $N$, the difference between the reconstructed pore contours and original pore contours decreases. Furthermore, the difference can be ignored when $N$ = 64, which also verifies the practicality of this method. Therefore, we set 64 as the harmonic number for the IDFT process.

# RESULTS

## Numerical Modeling Based on the RFPA Method

RFPA is a numerical solution based on the linear finite element method and allows the simulation of the progressive failure leading to rock collapse. A numerical model can become more realistic by considering the heterogeneity of the material and assigning different parameter values to different elements. The parameter value of each element in the same material statistically obeys a Weibull distribution and is controlled by the homogeneity coefficient (Tang, 1997).

The numerical models in this section are a series of 2D rectangular rock models with dimensions of 150 mm*100 mm. They are established by inputting the digital bitmap images into the RFPA code (version 2D-DIP). The number of finite elements is equal to the number of pixels. Also, the image sizes are uniformly set as 360 × 240 pixels, within the limit of the total number of elements (100,000) allowed for computational efficiency; hence, the numerical model resolution is 2.4 pixels/mm. In addition, the plane strain model has been adopted in the numerical experiments of the uniaxial compressive loading process.

Several pores reconstructed are randomly or certainly distributed that depend on the research factors in the rock range without contact based on overlapping detection algorithms, both global and local (Wang et al., 2019). However, the pores are allowed to contact the rock boundary to more closely reflect reality. The average diameter of pores is approximately 7 mm, and the number of pores contained in the numerical model is controlled by the index porosity ($p$). The pore direction angle ($\omega$) is first defined as the angle between the major

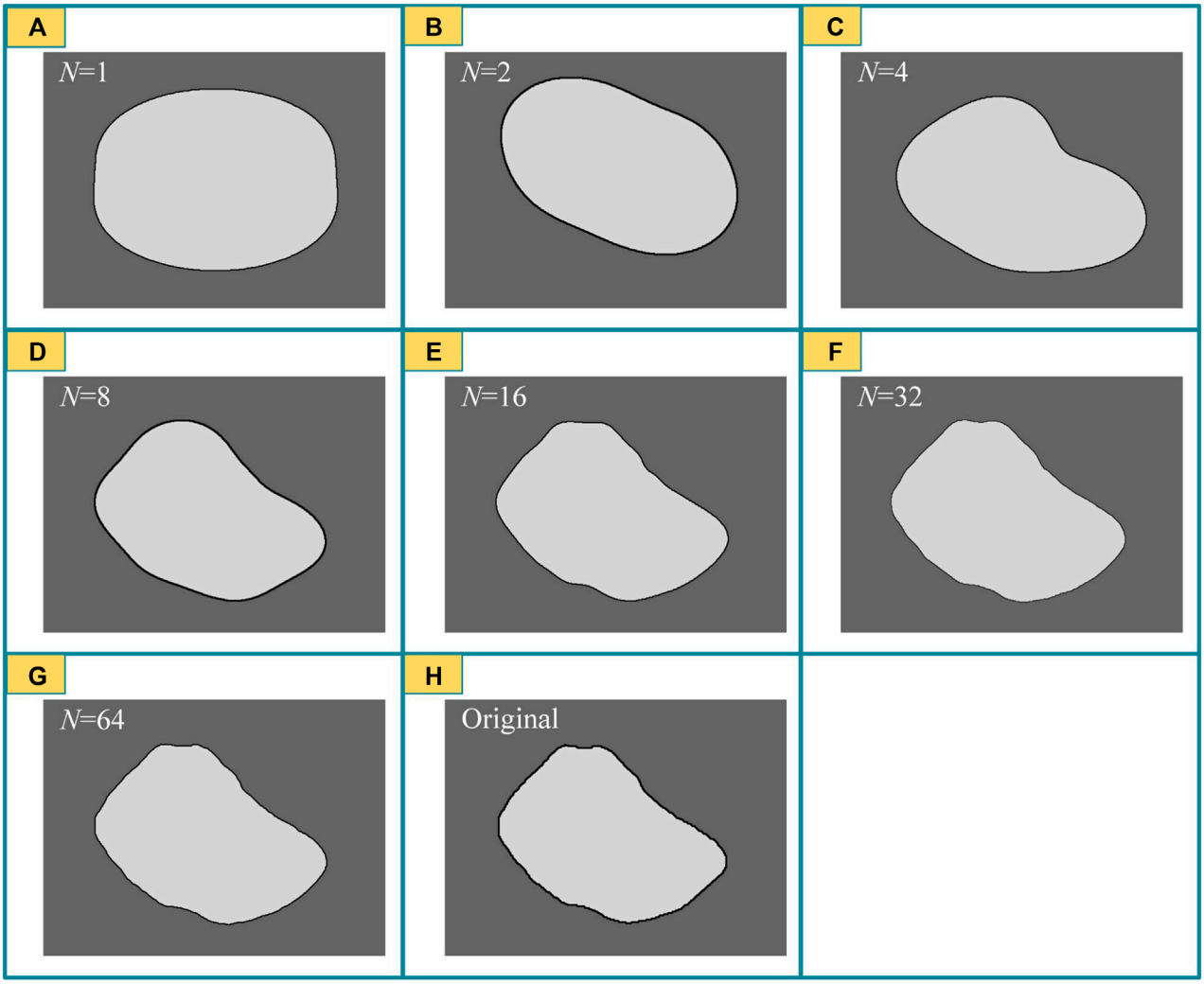


**FIGURE 5 |** Comparison between reconstructed pores based on IDFT with different numbers of harmonics $N$ = **(A)** 1; **(B)** 2; **(C)** 4; **(D)** 8; **(E)** 16; **(F)** 32; **(G)** 64; and **(H)** natural extracted (original) pores.

axis of the pore and the vertical direction (parallel to the direction of loading stress). **Figure 6** shows some examples of porous rock images with different porosities, pore direction angles, and significant Fourier descriptors. The images are two-phase images, with the discrete white areas representing pores and the continuous gray part representing rock. All of the images are generated in MATLAB by combining the IDFT and an overlapping detection algorithm.

After inputting the images into the RFPA$^{2D}$ code, each element is assigned material properties, mainly including Young's modulus, the uniaxial compressive strength, and Poisson's ratio, all of which follow Weibull distributions. The detailed mesoscopic values are listed in **Table 2**, where the parameters of rock mass are the same as those used in recent studies (Griffiths et al., 2017). In terms of the mechanical parameters of pores, Sammis and Ashby (1986) proposed a pore-emanating crack model, which idealizes pores as equant spheres within an elastic medium and is widely applied (Heap et al., 2014). So, in this study, the mechanical parameters of pores are set small enough instead of regarding as voids. Notably, the homogeneity index is the same as the shape parameter of the Weibull distribution. During the uniaxial compression numerical tests, the bottom boundary is set as a fixed boundary, while the other boundaries (i.e., top, left, and right boundary) are set as free boundaries.

To investigate the influence of pores on the failure of porous rock and verify the feasibility of the porous rock regeneration method proposed earlier, three indices, i.e., the porosity ($p$), pore direction angle ($\omega$), and significant Fourier descriptors $D_2$, $D_3$, and $D_8$ of the pores ($D_2$, $D_3$, and $D_8$), were introduced. The significant Fourier descriptors $D_2$, $D_3$, and $D_8$ reflect the different levels of two-dimensional object morphology, mainly the aspect ratio, angularity, and roughness, respectively (Lianheng et al., 2017). Correspondingly, the

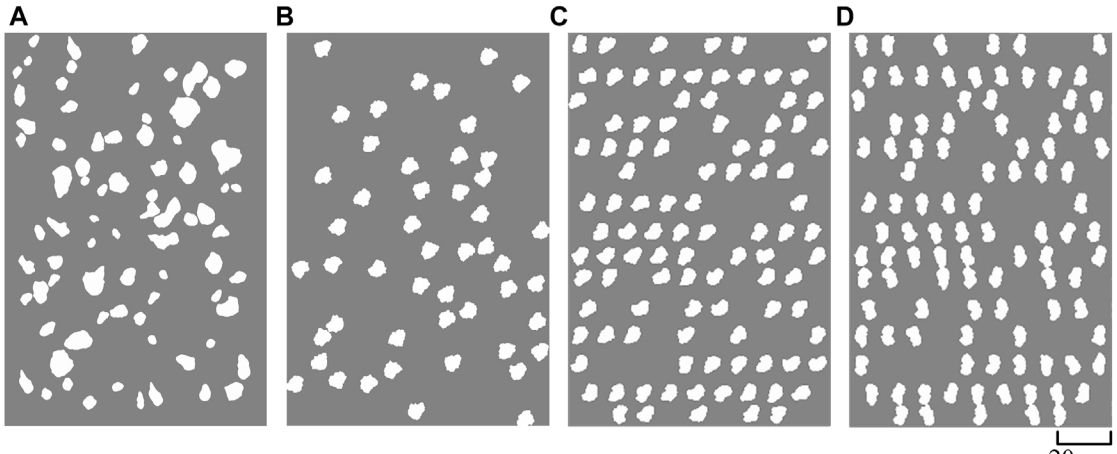


**FIGURE 6 |** Examples of generated porous rock samples with parameters porosity of **(A,B)** 15.8%; **(C,D)** 20.0%; pore direction angle of **(A)** random in the range of [0°, 90°]; **(B)** 0°; **(C)** 45°; **(D)** 90°; Fourier descriptors $D_2$, $D_3$, and $D_8$ of **(A)** random in the range in **Table 1**; **(B–D)** 0.1, 0.1, and 0.03, respectively.

**TABLE 2 |** The physical and mechanical properties of the numerical models utilized in RFPA$^{2D}$.

| Properties | Rock mass | Pores |
|---|---|---|
| Homogeneity index | 3 | 10 |
| Mean uniaxial compressive strength (MPa) | 2300 | 0.0023 |
| Mean Young's modulus (GPa) | 100 | $1.0 \times 10^{-8}$ |
| Poisson's ratio | 0.25 | 0.25 |
| Frictional angle (°) | 30 | 0.3 |
| Ratio of compressive to tensile strength | 10 | 10 |

numerical models are then established, and the results are analyzed in the following sections. Notably, to control the influence of pore distribution, the pores are only randomly placed in models studying the factor porosity, while in models studying other factors (i.e., pore direction angle and significant Fourier descriptors $D_2$, $D_3$, and $D_8$ of the pores), the pores in each group are under the same distribution. In addition, three models were performed at least for each sample configuration in groups studying the factor porosity to further minish the influence of pore distribution.

All the numerical models are divided into five parts with regard to those five factors, as listed in **Table 3**. A total of 12 groups of numerical experiments are conducted.

Porosity is one of the main factors impacting the failure mechanism of porous rocks (Chang et al., 2006; Heap et al., 2014). To study this influence, three groups of numerical experiments (i.e., P-A-1, P-A-2, and P-A-3) with different porosities are performed, in which the significant Fourier descriptors $D_2$, $D_3$, and $D_8$ are set as constants 0.1, 0.1, and 0.03. The pore direction angles $\omega = 0^{\circ}$, $45^{\circ}$, and $90^{\circ}$ are assigned to those three groups, respectively, and the porosity changes from 4.91% to 30.07% at an approximately 5% interval. After establishing the numerical model, a displacement control method was employed to load the rock model parallel to its long axis, and the increments were set as 0.02 mm.

**Figure 7** illustrates the compressive peak strength and corresponding Young's modulus in the three tested groups. The value of a data point is the mean value of at least three numerical models to eliminate the influence of random pore distribution. The results show that both the compressive peak strength and Young's modulus decrease with increasing porosity. Additionally, the results of group P-A-3 are mainly smaller than those of group P-A-1 with the same porosity, while the results of group P-A-2 fall between those of P-A-1 and P-A-3. **Figure 8** shows the stress-strain curves of the three groups. In all three groups, with increasing porosity, the porous rock may reach failure earlier with a smaller strain. The failure strain is no more than 0.6% for models that are the most difficult to fail and no less than 0.3% for those models that are the easiest to fail.

## The Influence of Pore Direction Angle

The orientation of pores in porous rock is another key factor influencing the mechanical behavior of the porous rock (Bubeck et al., 2017; Griffiths et al., 2017). In this article, the pore direction

**TABLE 3 |** The uniaxial compressive simulation projects.

| No. | Simulation code | Porosity | Pore direction angle | Fourier descriptor $D_2$ | Fourier descriptor $D_3$ | Fourier descriptor $D_8$ |
|---|---|---|---|---|---|---|
| 1 | P-A-1 | 4.9%–30.1% | 0° | 0.1 | 0.1 | 0.03 |
| 2 | P-A-2 | 4.9%–30.1% | 45° | 0.1 | 0.1 | 0.03 |
| 3 | P-A-3 | 4.9%–30.1% | 90° | 0.1 | 0.1 | 0.03 |
| 4 | A-D2-1 | 20.04% | 0–90 | 0.1 | 0.1 | 0.03 |
| 5 | A-D2-2 | 20.04% | 0–90 | 0.2 | 0.1 | 0.03 |
| 6 | A-D2-3 | 20.04% | 0–90 | 0.3 | 0.1 | 0.03 |
| 7 | D2-A | 20.04% | 0–90° | 0, 0.1–0.3 | 0.1 | 0.03 |
| 8 | D2-P-1 | 10.02% | 45° | 0.1–0.3 | 0.1 | 0.03 |
| 9 | D2-P-2 | 20.04% | 45° | 0.1–0.3 | 0.1 | 0.03 |
| 10 | D2-P-3 | 30.07% | 45° | 0.1–0.3 | 0.1 | 0.03 |
| 11 | D3-D2 | 20.04% | 45° | 0.1 | 0.02–0.16 | 0.03 |
| 12 | D8-D2 | 20.04% | 45° | 0.1 | 0.1 | 0.01–0.05 |

*Note: The values 4.91%–30.07% including 4.91%, 10.02%, 15.13%, 20.04%, 24.95%, and 30.07%; the values 0–90° including 0°, 10°, 20°, 30°, 40°, 50°, 60°, 70°, 80°, and 90°; the values 0.1–0.3 including 0.1, 0.15, 0.2, 0.25, and 0.3; the values 0.02–0.16 including 0.02, 0.04, 0.06, 0.08, 0.10, 0.12, 0.14, and 0.16; and the values 0.01–0.05 including 0.01, 0.015, 0.02, 0.025, 0.03, 0.035, 0.04, 0.045, and 0.05.*

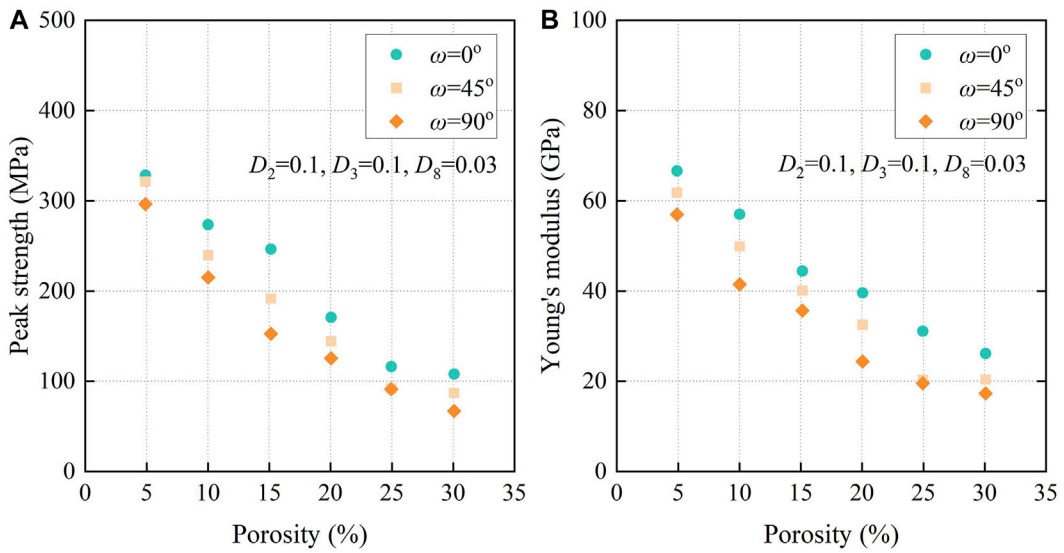


**FIGURE 7 |** Results of **(A)** compressive peak strength; and **(B)** corresponding Young's modulus for groups P-A-1, P-A-2, and P-A-3.

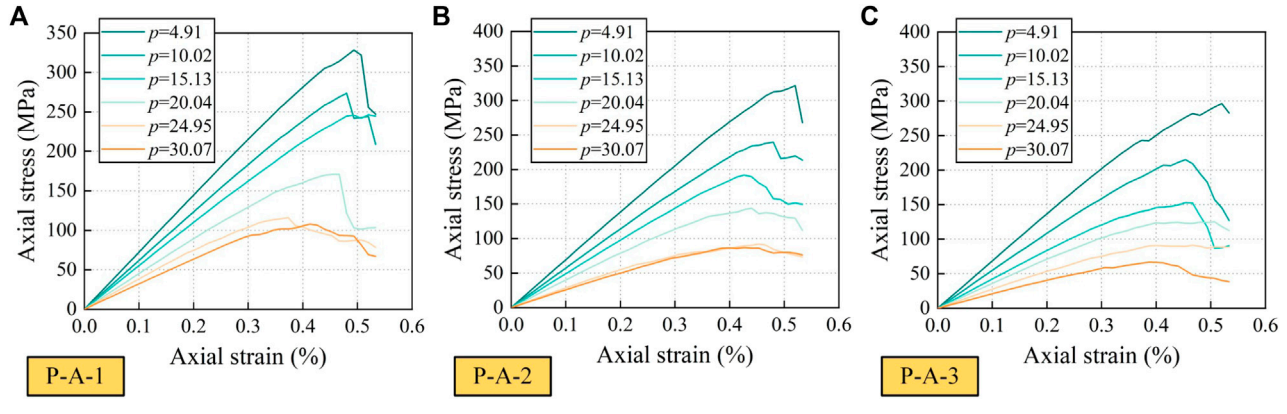


**FIGURE 8 |** Uniaxial stress-strain curves of groups **(A)** P-A-1; **(B)** P-A-2; and **(C)** P-A-3.

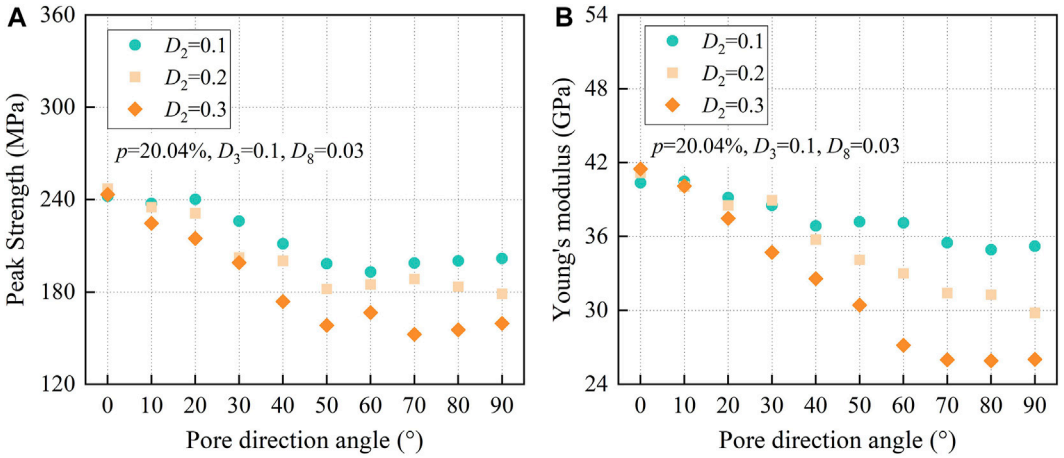


**FIGURE 9 |** Results of **(A)** compressive peak strength; and **(B)** corresponding Young's modulus for groups A-D2-1, A-D2-2, and A-D2-3.

angle is defined as the angle between the major axis of the pore and the vertical direction, which is also parallel to the loading direction. Therefore, another three groups of numerical simulations (i.e., A-D2-1, A-D2-2, and A-D2-3) with the same porosity $p$ = 20.04% and significant Fourier descriptors $D_3$ = 0.1 and $D_8$ = 0.03 are conducted. The $D_2$ values of these three groups are 0.1, 0.2, and 0.3, while the pore direction angle changed from 0° to 90° at an interval of 10°.

**Figure 9** shows the compressive peak strength and corresponding Young's modulus data of the three groups. Overall, the results show that both the compressive peak strength and Young's modulus decrease with increasing pore direction angle for these groups. On the other hand, with an increasing value of $D_2$, the growth becomes more significant. For example, for a $D_2$ value of 0.1, the Young's modulus decreases from 40 to 35 GPa, while for a $D_2$ value of 0.3, the Young's modulus drops from 41 to 26 GPa. In addition, when the pore direction angle exceeds 70° (i.e., 70°, 80°, and 90°), in other words, the major axis of the pore is further away from the loading direction, the changes in compressive peak strength and Young's modulus turn into steady.

## The Influence of the Significant Fourier Descriptors $D_2$, $D_3$, and $D_8$

The three significant Fourier descriptors $D_2$, $D_3$, and $D_8$ control the morphology of two-dimensional object contours at three different levels, elongation, convexity, and roughness, gradually becoming more detailed (Lianheng et al., 2017). Recent studies have investigated the influence of the aspect ratio on the failure behavior of porous rocks with regular pores (Griffiths et al., 2017). Therefore, considering the relationship between $D_2$ and the elongation of pores, another series of numerical models were established and performed.

In order to underline the combined effect of $D_2$ and pore direction angle, several simulations with $D_2$ = 0, $D_2$ = 0.15, and $D_2$ = 0.25 were implemented into groups A-D2-1, A-D2-2, and A-D2-3 and set the $D_2$ as $x$-axis, forming the group D2-A. **Figure 10** compares the compressive strength and Young's modulus in the group D2-A. Results show that for low angles (0–10°), both strength and Young's modulus show little growth or fluctuation as $D_2$ increases. For higher angles (20°–90°), an increasing $D_2$ would result in reductions in strength and Young's modulus. In addition, the pore direction angle also relates to the range of strength and Young's modulus. As the pore direction angle grows, the magnitude of decline becomes larger. For example, for a pore direction angle of 40°, the Young's modulus decreases from 39 to 32 GPa, while for a pore direction angle of 90°, the Young's modulus drops from 39 to 26 GPa. It is worth mentioning that when $D_2$ is close to 0, the aspect ratio of the corresponding pores is close to 1, i.e., the major axis and minor axis are almost the same, where the pores have no specific direction. Hence, the results of the strength and Young's modulus for $D_2$ = 0 in **Figure 10** share the same value.

To study the impact of $D_2$ further, groups D2-P-1, D2-P-2, and D2-P-3 were conducted to investigate the influence of $D_2$ through different porosities, where $D_3$ and $D_8$ were set as constants 0.1 and 0.03. **Figure 11** shows the compressive peak strength and Young's modulus data of groups D2-P-1, D2-P-2, and D2-P-3 with the same pore direction angle of $\omega$ = 45°, while $D_2$ changes from 0.1 to 0.3 at an interval of 0.05. As for different $D_2$ values with the same porosity, both the results of strength and Young's modulus are nearly constant. This mainly means that the influence of $D_2$ is insignificant compared with the influence of porosity on the strength and Young's modulus.

Compared with $D_2$, another two significant Fourier descriptors $D_3$ and $D_8$ reflect more detailed morphology of pores, i.e., convexity and roughness, respectively. To further study the effects of pore morphology on the mechanical properties of porous rocks, groups D3-D2 and D8-D2 were conducted. **Figures 12A and B** show results of compressive peak strength and Young's modulus for group D3-D2, where the porosity, pore direction angle, and $D_8$ were set as 20.04%, 45°, and 0.01, respectively. As we can see, an increasing value of $D_3$ leads to a decrease in strength and Young's modulus. Also,

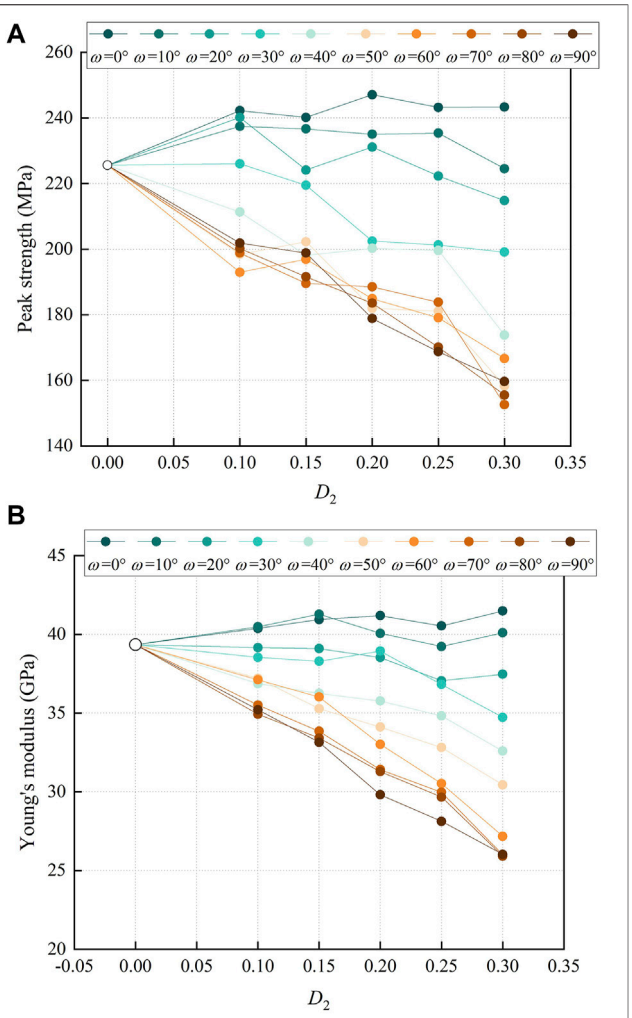


**FIGURE 10 |** Results of **(A)** compressive peak strength; and **(B)** corresponding Young's modulus for group D2-A.

for different values of $D_2$, the magnitude of the difference is almost similar. **Figures 12C and D** show results of compressive peak strength and Young's modulus for group D8-D2, where the porosity, pore direction angle, and $D_3$ were set as 20.04%, 45°, and 0.1, respectively. Unlike the regular trends during investigating factors $D_2$ and $D_3$, the results for group D8-D2 reveal more fluctuation, which has no obvious pattern.

## DISCUSSION

We have shown that the porosity, pore direction angle, and Fourier significant descriptors $D_2$, $D_3$, and $D_8$ as controls on porous rocks affected the mechanical behavior under uniaxial compression loading through RPFA$^{2D}$ simulations. In the following section, we conduct a comparison with existing experimental and numerical data to verify our simulations and further give explanations and discussion about the influences of natural pore morphology on the mechanical properties of porous rocks.

## Comparison With Previous Studies

X-ray computed tomography (X-ray CT) is a more complicated and accurate method of acquiring the realistic morphology of objects, which is, however, also expensive and time-consuming. The CT volume analysis of porous basalts conducted by Bubeck et al. (2017) reveals that the individual pores in their studied region are not spherical, which range from sub-spherical to elongated and flat ellipsoids. In this study, we introduce the significant Fourier descriptor $D_2$ as a representation of aspect ratio, which is actually inversely proportional to aspect ratio. **Table 4** compares the aspect ratio obtained by Bubeck et al. (2017) (defined as c/a for pores with semi-axes a = b >> c) in three field zones and calculated from pores controlled by index $D_2$, which is acquired from the workflow of rock pore extraction or applied in RFPA$^{2D}$ simulations. It can be seen that the range of aspect ratio obtained from our porous rock specimens (0.50–1.00, converted by $D_2$) is a little larger than that acquired by Bubeck et al. (2017) from the top and core zones of a lava in the field (0.60–1.00). In this case, the range of aspect ratio utilized in our simulations (0.65–1.00, converted by $D_2$) is set in the range obtained by Bubeck et al. (2017) from the top and core zones of a lava in the field.

To further investigate the influence of pore geometry on rock strength, Bubeck et al. (2017) carried out several uniaxial compressive tests on porous lava samples. All of their samples are classified into two types relative to the measured pore shape: (1) horizontal, oriented normal to bedding, with the pore direction angle almost 0° and (2) vertical, oriented parallel to bedding, with the pore direction angle almost 90°. Herein, we compare the results of Bubeck et al. (2017) from top and core zones on strength and Young's moduli with our simulations. As shown in **Figure 13**, the porosity of samples from top zones is nearly centered between 20% and 30%, while that from core zones is centered between 10% and 15%. Compared to the results on a similar porosity, we can see that in top zones, both the strength and Young's moduli from Bubeck's experiments are close to that in our simulations, especially for those from the upper top zones with horizontal orientation. However, in the core zone, the experimental results are considerably lower than our simulations. The main reason for this consequence, we guess, is the discrepancy between pore distribution and pore diameter. For a lower porosity, the diversity of pore distribution on different samples is larger, causing a more discrepant influence on the strength and Young's modulus. On the other hand, the average pore diameter in the core zone is lower than that in the top zone in Bubeck's study, where the latter one is similar to it in our simulations. Notably, Bubeck et al. (2017) also draw the same conclusion as our study that rock samples are weaker in cases where the compression is applied parallel to the pore short axis, i.e., the pore direction angle is 90°.

Griffiths et al. (2017) also performed a series of simulations on porous rocks considering the influence of porosity, pore aspect ratio, and pore orientation through RFPA$^{2D}$ and compared results with several experimental data on different types of

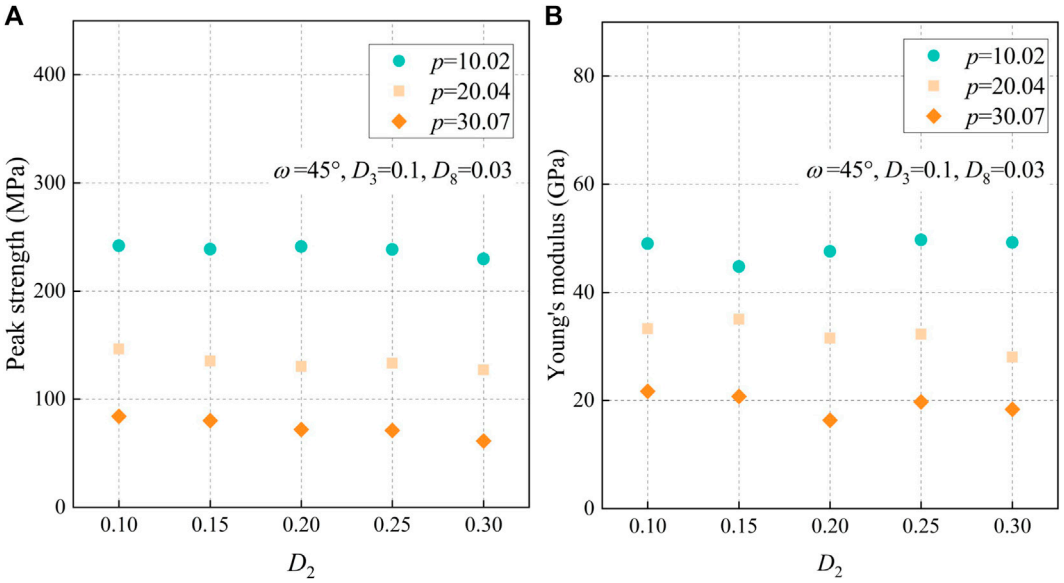


**FIGURE 11 |** Results of **(A)** compressive peak strength; and **(B)** corresponding Young's modulus for groups D2-P-1, D2-P-2, and D2-P-3.

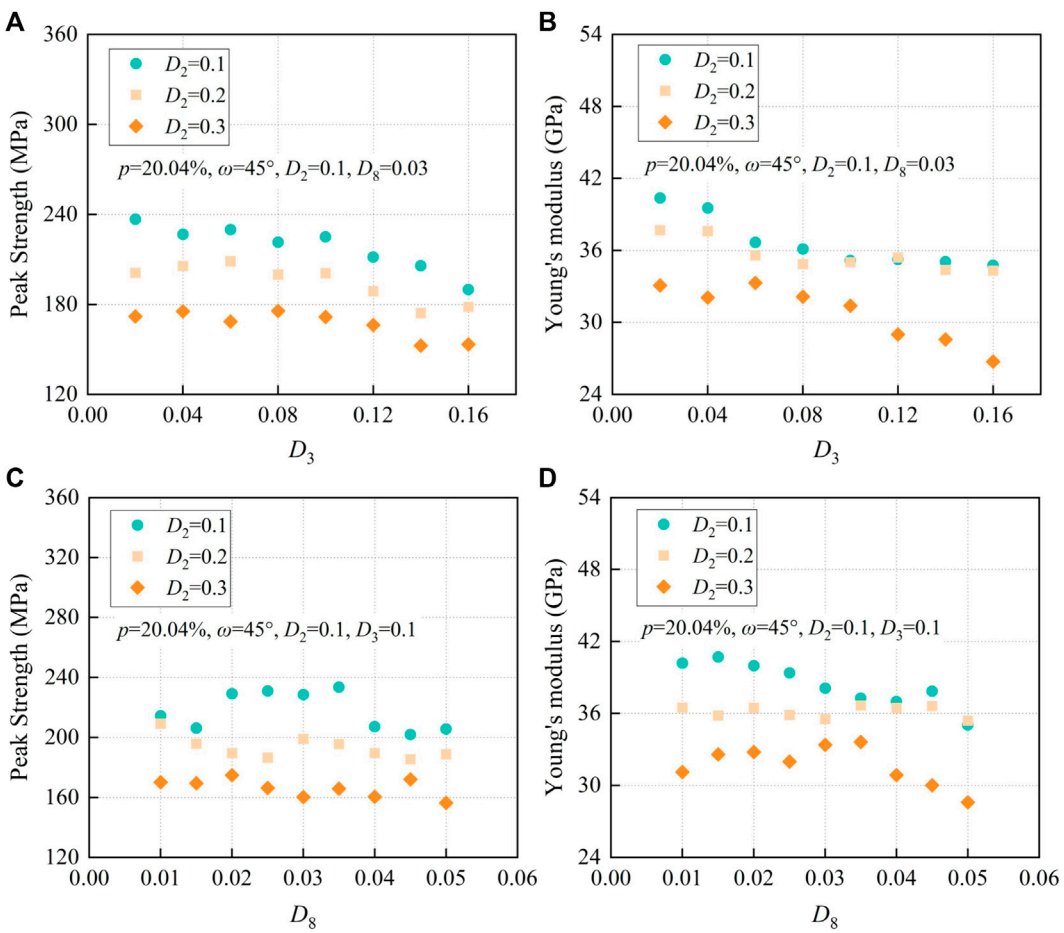


**FIGURE 12 |** Results of **(A)** compressive peak strength for group D3-D2; **(B)** corresponding Young's modulus for group D3-D2; **(C)** compressive peak strength for group D8-D2; and **(D)** corresponding Young's modulus for group D8-D2.

**TABLE 4 |** Comparison between pore aspect ratio obtained by Bucket et al. (2017) and converted by $D_2$ in this study.

| | Source/application | Fourier descriptor $D_2$ | Aspect ratio |
|---|---|---|---|
| Workflow of rock pore extraction, this study | Porous rock blocks | 0–0.6 | 0.50–1.00 |
| RFPA$^{2D}$ simulation, this study | For simulation | 0–0.3 | 0.65–1.00 |
| CT volume analysis, Bubeck et al. (2017) | Top and core zones of a lava in the field | — | 0.60–1.00 |
| | Basal zone of a lava in the field | — | 0.10–0.80 |

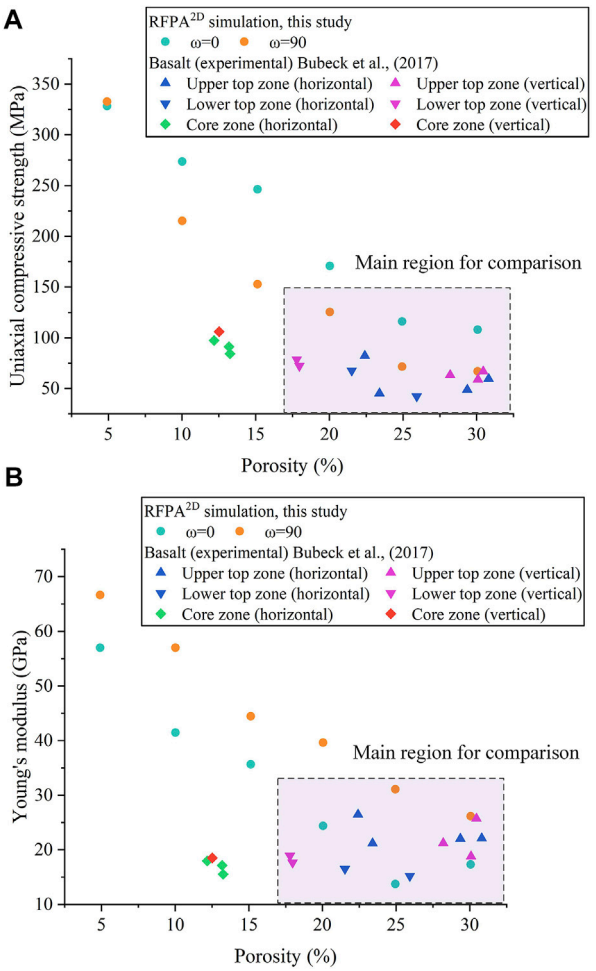


**FIGURE 13 |** Comparison between RFPA$^{2D}$ simulation results with experimental data from Bubeck et al. (2017) of **(A)** strength and **(B)** Young's modulus. The purple box highlights the main region for comparison.

rocks. Although they simplified the pore shape as an ellipse, which could not represent the real pores well, the results are still helpful to verify our simulations. Using the same definition of pore aspect ratio (the ratio of the minor to major semi-axis) as Bubeck et al. (2017) and Griffiths et al. (2017) studied this factor in the range from 0.2 to 1.0, which has little overlap with our simulations (0.6–1.0, as mentioned earlier). In this case, we mainly compare the results considering the influence of porosity and pore orientation. As shown in Griffith's study, with an increasing value of porosity or a growing angle between the loading direction and the major axis of a pore, the strength and Young's modulus are dropped, which shows a high degree of agreement with our simulations. At the same time, the results considering the influence of pore aspect ratio relating to pore orientation also show a similar trend to the data presented in Griffiths et al. (2017): (1) at low angles (0°–10°), an increase in aspect ratio (decrease in $D_2$) reduces the strength and Young's modulus; (2) at higher angles (40°–90°), an increase in aspect ratio (decrease in $D_2$) results in an increase in the strength and Young's modulus, and as the angle grows, the change is more significant; (3) at intermediate angles (20°–30°), there is a little discrepancy with that in Griffith's research, and strength and Young's modulus first increase and then decrease as pore aspect ratio approaches unity ($D_2$ approaches 0). While in our study, there is a small reduction as $D_2$ increases (pore aspect ratio decreases).

## The Major Influences of Porosity, Pore Direction Angle, and $D_2$

Numerical models studying the effects of porosity, pore direction angle, and significant Fourier descriptor $D_2$ in **Figure 7** and **Figures 9–11** show that pore geometry controls the strength and Young's modulus of porous rock samples in different aspects.

In terms of porosity, results in our simulations show that strength and Young's modulus are inversely proportional to the porosity, which is observed in several kinds of rocks such as basalts, sandstones, and limestones (Al-Harthi et al., 1999; Sabatakakis et al., 2008). For higher porosity (20%–30%), our results are in agreement with Bubeck's experimental data (**Figure 13**, in the purple main region). However, for lower porosity (10%–15%), the results show a high discrepancy (**Figure 13**, out of the purple main region). Actually, the porosity in some of the basaltic rocks is far low (1%–4%, e.g., Mt. Etna volcano, Heap et al., 2009; Heap et al., 2010), representing the strongest part of the lava. In such cases, the rock mass strength and stiffness are principally influenced by intact rock and pore distribution. It is therefore essential to study the impact of pore distribution on low porosity rock samples through numerical modeling and be verified by experimental results.

The field lava sample observations always show that oblate vesicles are aligned and relate to bedding orientation, e.g., aligned sub-horizontally, parallel to bedding, in the basal zones of Kilauea pahoehoe lava (Bubeck et al., 2017). The results considering the different angles between the loading stress and major axis of pores (i.e., pore direction angle in this study) in our simulations demonstrated the influence on strength and Young's modulus. It is weaker for a vertical load than a horizontal load if the pores'

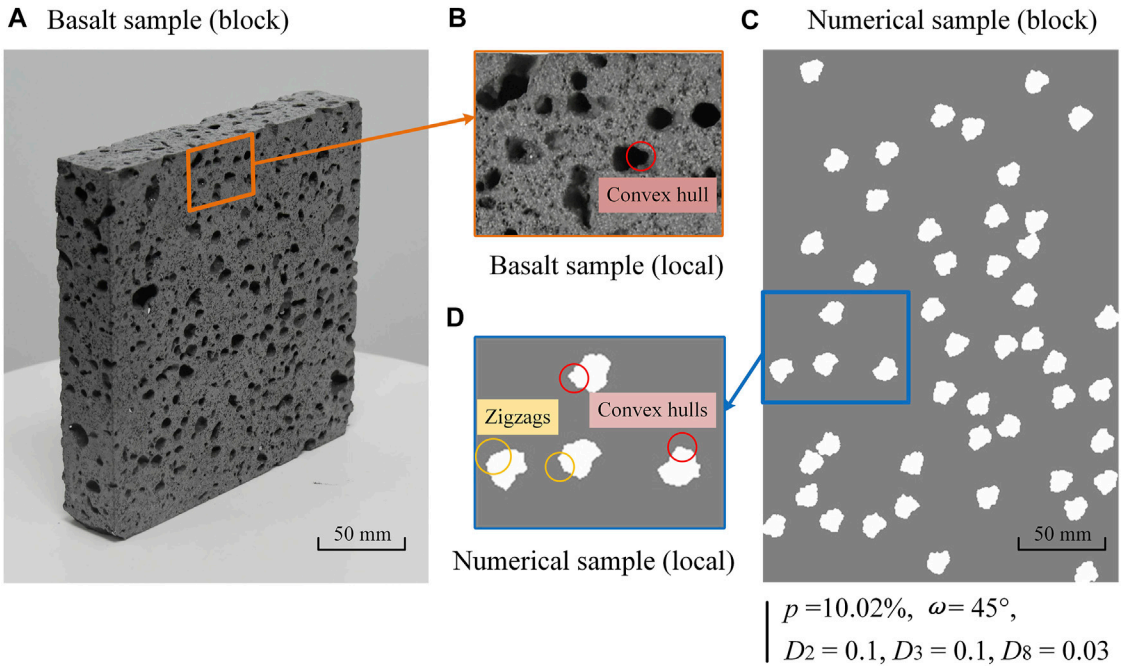


**FIGURE 14 |** Convex hulls and zigzags of pores in natural basalts and regenerated numerical porous sample: **(A)** basalt sample; **(B)** local basalt sample; **(C)** numerical sample with porosity of 10.02%, pore direction angle of 45°, and Fourier descriptors $D_2$ = 0.1, $D_3$ = 0.1, and $D_8$ = 0.03; and **(D)** local numerical samples.

major axis is oriented parallel to bedding in lavas. Also, for a tilt load, as the orientation is closer to the horizontal direction, the rocks are stronger.

The pore shape also shows a large diversity on lava samples from oblate to spherical pores with the pore aspect ratio ranging from 0.1 to 1.0, which exhibits a regional relevance. For instance, from the south flank of Kilauea volcano, Hawaii (Bubeck et al., 2017), individual pores in the top and core zones typically have aspect ratios between 0.60 and 1.00, while in the basal zone, there is a mixture of large oblate geometries with aspect ratios between 0.10 and 0.40 and smaller pores with lower aspect ratios in the range of 0.41–0.80. Herein, we introduce the significant Fourier descriptor $D_2$ as a new representation of pore shape, which is inversely proportional to the aspect ratio. Compared with porosity, the effects of $D_2$ on strength and Young's modulus are subtle (**Figure 11**). However, considering pore direction angle, mechanical results are impacted by $D_2$ in two types: for low angles (0°–10°), they are positively related, while for higher angles (20°–90°), there is a negative correlation. Also, in Griffith's research, there are three types of angles ranging from 0 to 90°. Overall, these rough results show an associated influence between pore direction angle and $D_2$ (or aspect ratio) on rock strength and stiffness, which is meaningful to further investigate in follow-up studies.

## Different Levels of Pore Morphology Affect Differently

Three significant Fourier descriptors (i.e., $D_2$, $D_3$, and $D_8$) control the contour of a two-dimensional closed area at different levels. Several researchers applied this signal processing method (i.e., discrete Fourier transform) to characterize the 2D morphology of rock materials such as railway ballast, sand particles, coral reefs, etc. (Mollon and Zhao, 2013; Davis and Chojnacki, 2017; Lianheng et al., 2017), and verified the quantitative relation between significant Fourier descriptors and shape indices such as elongation, convexity, and roughness. If we sort out the 2D morphology into three levels: 1) basic level, which describes basic shapes such as circular, elliptical, and oblate; 2) local level, such as some large convex hulls or apparent corners; 3) global detailed level, such as some subtle zigzag and wave, the significant Fourier descriptors $D_2$, $D_3$, and $D_8$ could represent them, respectively. Researchers studying the effect of detailed pore morphology on rock strength and Young's modulus have mainly focused on the pore aspect ratio (i.e., the basic level) (Bubeck et al., 2017; Griffiths et al., 2017) and seldom considered the influence of obvious convex hulls or subtle zigzags. Results in our simulations show that $D_2$, $D_3$, and $D_8$ affect the strength and Young's modulus at distinct levels, showing a decreasing trend in terms of the influence significance (**Figure 12**). As mentioned earlier, $D_2$ that relates to aspect ratio has an obvious impact on rock strength and Young's modulus, whereas $D_3$ exhibits a relatively small impact. In the range of 0.02–0.16, although there is a little fluctuation in some parts, for instance, the strength first decreases, then increases, and decreases again for $D_3$ from 0.02 to 0.08 when $D_2$ = 0.1, the overall trend is that the strength and Young's modulus decrease as $D_3$ increasing (**Figures 12A, B**). It means that $D_3$ has the same but smaller impact on rock mechanical properties versus $D_2$. As discussed in Heap et al. (2014), the vesicle clustering, and the stress field overlap and interaction may be more likely to occur as

porosity increases. In this case, with more and more convex hulls or obvious corners (**Figure 14**), the possibilities of vesicle clustering and stress field overlap are larger, resulting in the reduction of strength and Young's modulus. However, as for $D_8$, the results are more unpredictable, and there is a discrepancy between different $D_2$ values or even between strength and Young's modulus. This mainly implies that $D_8$ has little effect on the rock's mechanical properties. Therefore, we should not only focus on the influence of obvious pore shapes such as circular or elliptical but also consider the impact of local pore features such as convex hulls or apparent corners, which although has a smaller effect when studying the rock strength and stiffness.

## CONCLUSION

This article proposes a novel perspective on natural pore morphology, together with its influence on rock strength and stiffness. Initially, a workflow based on photogrammetry is established to digitize rock pores. The following processes consist of dense point cloud reconstruction, meshing, splitting, projection, and extraction are then conducted to acquire a two-dimensional single pore. Adapting to discrete Fourier transform (DFT) and inverse discrete Fourier transform (IDFT), all of the pores are statistically analyzed and Fourier descriptors (mainly including $D_2$, $D_3$, and $D_8$) are introduced to represent pore morphology and regenerate a series of shape-controlled pores. Next, uniaxial compressive simulations utilizing rock failure process analysis (RFPA) are then performed, considering the influence of porosity, pore orientation, and pore morphology on rock strength and stiffness. Results are eventually compared with previous experimental and numerical data. The main conclusion is as follows:

(1) Photogrammetry and OpenCV along with DFT and IDFT theory provide effective means for acquiring, characterizing, and regenerating volcanic porous rocks with irregular pores, which are more realistic. The significant Fourier descriptors $D_2$, $D_3$, and $D_8$ can be used to represent different levels of shape features in rock pores.
(2) The numerical simulation results show that porosity exerts a crucial control on the rock strength and stiffness, while there is an associated influence between pore orientation and $D_2$ value of pores (inversely proportional to pore aspect ratio), all of which are in agreement with previous studies.
(3) The detailed pore morphology, such as convex hulls or obvious corners, represented by significant Fourier descriptor $D_3$, performs a small but cannot be ignored impact on rock strength and stiffness, that as $D_3$ increasing (i.e., detailed morphology is more complicated), the rock strength and stiffness are dropped. This is mainly due to the fact that the vesicle clustering and stress field overlap are larger. However, the more detailed pore morphology, such as subtle zigzags and waves, represented by significant Fourier descriptor $D_8$, has fewer effects that can be neglected.

## DATA AVAILABILITY STATEMENT

The original contributions presented in the study are included in the article/Supplementary Material; further inquiries can be directed to the corresponding author.

## AUTHOR CONTRIBUTIONS

LZ: conceptualization, supervision, project administration, and funding acquisition; MD: methodology, investigation, and writing-original draft; XW: conceptualization, methodology, writing-review, and editing; DH: methodology and resources; SZ: investigation. All authors have read and agreed to the published version of the manuscript. We confirm that the order of authors listed in the manuscript has been approved by all named authors.

## FUNDING

This study was financially supported by the National Natural Science Foundation of China (grant number 51878668) and the Science and Technology Progress and Innovation Project of the Department of Transportation of Hunan Province (grant numbers 202017, 202008, and 202115).

## REFERENCES

Al-Harthi, A. A., Al-Amri, R. M., and Shehata, W. M. (1999). The Porosity and Engineering Properties of Vesicular Basalt in Saudi Arabia. *Eng. Geol.* 54, 313–320. doi:10.1016/s0013-7952(99)00050-2

Baud, P., Klein, E., and Wong, T.-f. (2004). Compaction Localization in Porous Sandstones: Spatial Evolution of Damage and Acoustic Emission Activity. *J. Struct. Geol.* 26, 603–624. doi:10.1016/j.jsg.2003.09.002

Besl, P. J., and McKay, N. D. (1992). A Method for Registration of 3-D Shapes. *IEEE Trans. Pattern Anal. Mach. Intell.* 14, 239–256. doi:10.1109/34.121791

Bubeck, A., Walker, R. J., Healy, D., Dobbs, M., and Holwell, D. A. (2017). Pore Geometry as a Control on Rock Strength. *Earth Planet. Sci. Lett.* 457, 38–48. doi:10.1016/j.epsl.2016.09.050

Carrivick, J. L., Smith, M. W., and Quincey, D. J. (2016). *Structure from Motion in the Geosciences*. Chicester: John Wiley & Sons. doi:10.1002/9781118895818

Chang, C., Zoback, M. D., and Khaksar, A. (2006). Empirical Relations between Rock Strength and Physical Properties in Sedimentary Rocks. *J. Petroleum Sci. Eng.* 51, 223–237. doi:10.1016/j.petrol.2006.01.003

Cilona, A., Faulkner, D. R., Tondi, E., Agosta, F., Mancini, L., Rustichelli, A., et al. (2014). The Effects of Rock Heterogeneity on Compaction Localization in Porous Carbonates. *J. Struct. Geol.* 67, 75–93. doi:10.1016/j.jsg.2014.07.008

Davis, J. D., and Chojnacki, J. D. (2017). Two-dimensional Discrete Fourier Transform Analysis of Karst and Coral Reef Morphologies. *Trans. GIS* 21 (3), 521–545. doi:10.1111/tgis.12277

Dunn, D. E., LaFountain, L. J., and Jackson, R. E. (1973). Porosity Dependence and Mechanism of Brittle Fracture in Sandstones. *J. Geophys. Res.* 78, 2403–2417. doi:10.1029/jb078i014p02403

Farquhar, R. A., Somerville, J. M., and Smart, B. G. D. (1994). "Porosity as a Geomechanical Indicator: An Application of Core and Log Data and Rock Mechanics," in European Petroleum Conference - Proceedings (London: Society of Petroleum Engineers). doi:10.2118/28853-ms

Furukawa, Y., and Ponce, J. (2009). Accurate Camera Calibration from Multi-View Stereo and Bundle Adjustment. *Int. J. Comput. Vis.* 84, 257–268. doi:10.1007/s11263-009-0232-2

Gao, F., and Kang, H. (2017). Grain-Based Discrete-Element Modeling Study on the Effects of Cementation on the Mechanical Behavior of Low-Porosity Brittle Rocks. *Int. J. Geomechanics* 17, 04017061. doi:10.1061/(asce)gm.1943-5622.0000957

Griffiths, L., Heap, M. J., Xu, T., Chen, C.-f., and Baud, P. (2017). The Influence of Pore Geometry and Orientation on the Strength and Stiffness of Porous Rock. *J. Struct. Geol.* 96, 149–160. doi:10.1016/j.jsg.2017.02.006

Gui, Y. L., Zhao, Z. Y., Zhang, C., and Ma, S. Q. (2017). Numerical Investigation of the Opening Effect on the Mechanical Behaviours in Rocks Under Uniaxial Loading Using Hybrid Continuum-Discrete Element Method. *Comput. Geotech* 90, 55–72. doi:10.1016/j.compgeo.2017.05.021

Heap, M. J., Faulkner, D. R., Meredith, P. G., and Vinciguerra, S. (2010). Elastic Moduli Evolution and Accompanying Stress Changes with Increasing Crack Damage: Implications for Stress Changes Around Fault Zones and Volcanoes during Deformation. *Geophys. J. Int.* 183 (1), 225–236. doi:10.1111/j.1365-246X.2010.04726.x

Heap, M. J., Vinciguerra, S., and Meredith, P. G. (2009). The Evolution of Elastic Moduli with Increasing Crack Damage during Cyclic Stressing of a Basalt from Mt. Etna Volcano. *Tectonophysics* 471 (1–2), 153–160. doi:10.1016/j.tecto.2008.10.004

Heap, M. J., Xu, T., and Chen, C.-F. (2014). The Influence of Porosity and Vesicle Size on the Brittle Strength of Volcanic Rocks and Magma. *Bull. Volcanol.* 76, 856. doi:10.1007/s00445-014-0856-0

Jeong, Y. J., Kang, D. H., Kim, K. Y., and Yun, T. S. (2014). "Morphology-Based Characterization of 3D Anisotropy in Porous Rock: Pore Orientation," in Geo-Congress 2014: Geo-characterization and Modeling for Sustainability (Atlanta: American Society of Civil Engineers). doi:10.1061/9780784413272.056

Ji, Y., Hall, S. A., Baud, P., and Wong, T.-f. (2015). Characterization of Pore Structure and Strain Localization in Majella Limestone by X-Ray Computed Tomography and Digital Image Correlation. *Geophys. J. Int.* 200, 701–719. doi:10.1093/gji/ggu414

Ju, Y., Yang, Y., Peng, R., and Mao, L. (2013). Effects of Pore Structures on Static Mechanical Properties of Sandstone. *J. Geotechnical Geoenvironmental Eng* 139 (10), 1745–1755. doi:10.1061/(asce)gt.1943-5606.0000893

Kazhdan, M., Bolitho, M., and Hoppe, H. (2006). "Poisson Surface Reconstruction," in *Eurographics Symposium on Geometry Processing* (Goslar: The Eurographics Association). doi:10.5555/1281957.1281965

Kazhdan, M., and Hoppe, H. (2013). Screened Poisson Surface Reconstruction. *ACM Trans. Graph.* 32, 1–13. doi:10.1145/2487228.2487237

Lianheng, Z., Dongliang, H., Han-Cheng, D., Shuaihao, Z., and Dejian, L. (2017). Reconstruction of Granular Railway Ballast Based on Inverse Discrete Fourier Transform Method. *Granul. Matter* 19, 74. doi:10.1007/s10035-017-0761-2

Lianheng, Z., Dongliang, H., Jingyu, C., Xiang, W., Wei, L., Zhiheng, Z., et al. (2020). A Practical Photogrammetric Workflow in the Field for the Construction of a 3D Rock Joint Surface Database. *Eng. Geol.* 279, 105878. doi:10.1016/j.enggeo.2020.105878

Lin, P., Wong, R. H. C., and Tang, C. A. (2015). Experimental Study of Coalescence Mechanisms and Failure under Uniaxial Compression of Granite Containing Multiple Holes. *Int. J. Rock Mech. Min. Sci.* 77, 313–327. doi:10.1016/j.ijrmms.2015.04.017

Longuet-Higgins, H. C. (1981). A Computer Algorithm for Reconstructing a Scene from Two Projections. *Nature* 293, 133–135. doi:10.1038/293133a0

Mollon, G., and Zhao, J. (2012). Fourier-Voronoi-based Generation of Realistic Samples for Discrete Modelling of Granular Materials. *Granul. Matter* 14, 621–638. doi:10.1007/s10035-012-0356-x

Mollon, G., and Zhao, J. (2013). Generating Realistic 3D Sand Particles Using Fourier Descriptors. *Granul. Matter* 15, 95–108. doi:10.1007/s10035-012-0380-x

Olsson, W. A., and Holcomb, D. J. (2000). Compaction Localization in Porous Rock. *Geophys. Res. Lett.* 27, 3537–3540. doi:10.1029/2000GL011723

Paixão, A., Resende, R., and Fortunato, E. (2018). Photogrammetry for Digital Reconstruction of Railway Ballast Particles - A Cost-Efficient Method. *Constr. Build. Mater.* 191, 963–976. doi:10.1016/j.conbuildmat.2018.10.048

Peng, S., and Podnieks, E. R. (1972). Relaxation and the Behavior of Failed Rock. *Int. J. Rock Mech. Min. Sci. Geomech. Abstr.* 9 (6), 699–700. doi:10.1016/0148-9062(72)90031-9

Pollefeys, M., van Gool, L., Vergauwen, M., Verbiest, F., Cornelis, K., Tops, J., et al. (2004). Visual Modeling with a Hand-Held Camera. *Int. J. Comput. Vis.* 59 (3), 207–232. doi:10.1023/B:VISI.0000025798.50602.3a

Rozenbaum, O., and Du Roscoat, S. R. (2014). Representative Elementary Volume Assessment of Three-Dimensional X-Ray Microtomography Images of Heterogeneous Materials: Application to Limestones. *Phys. Rev. E* 89, 053304. doi:10.1103/PhysRevE.89.053304

Sabatakakis, N., Koukis, G., Tsiambaos, G., and Papanakli, S. (2008). Index Properties and Strength Variation Controlled by Microstructure for Sedimentary Rocks. *Eng. Geol.* 97 (1–2), 80–90. doi:10.1016/j.enggeo.2007.12.004

Sammis, C. G., and Ashby, M. F. (1986). The Failure of Brittle Porous Solids under Compressive Stress States. *Acta Metall.* 34 (3), 511–526. doi:10.1016/0001-6160(86)90087-8

Spetsakis, M., and Aloimonost, J. (1991). A Multi-Frame Approach to Visual Motion Perception. *Int. J. Comput. Vis.* 6, 245–255. doi:10.1007/bf00115698

Su, D., and Xiang, W. (2020). Characterization and Regeneration of 2D General-Shape Particles by a Fourier Series-Based Approach. *Constr. Build. Mater.* 250, 118806. doi:10.1016/j.conbuildmat.2020.118806

Tang, C. (1997). Numerical Simulation of Progressive Rock Failure and Associated Seismicity. *Int. J. Rock Mech. Min. Sci. Geomechanics Abstr.* 34, 249–261. doi:10.1016/S0148-9062(96)00039-3

Vajdova, V., Baud, P., and Wong, T.-F. (2004). Compaction, Dilatancy, and Failure in Porous Carbonate Rocks. *J. Geophys. Res.* 109, B05204. doi:10.1029/2003JB002508

Vernik, L., Bruno, M., and Bovberg, C. (1993). Empirical Relations between Compressive Strength and Porosity of Siliciclastic Rocks. *Int. J. Rock Mech. Min. Sci. Geomech. Abstr.* 30 (7), 677–680. doi:10.1016/0148-9062(93)90004-W

Wang, X., Liang, Z., Nie, Z., and Gong, J. (2019). Stochastic Numerical Model of Stone-Based Materials with Realistic Stone-Inclusion Features. *Constr. Build. Mater.* 197, 830–848. doi:10.1016/j.conbuildmat.2018.10.062

Wong, R. H. C., Lin, P., and Tang, C. A. (2006). Experimental and Numerical Study on Splitting Failure of Brittle Solids Containing Single Pore under Uniaxial Compression. *Mech. Mater.* 38, 142–159. doi:10.1016/j.mechmat.2005.05.017

Zhao, H., Zhou, S., Zhao, M., and Shi, C. (2018). Statistical Micromechanics-Based Modeling for Low-Porosity Rocks under Conventional Triaxial Compression. *Int. J. Geomechanics* 18 (5), 04018019. doi:10.1061/(asce)gm.1943-5622.0001121

Zhao, L., Huang, S., Zhang, R., and Zuo, S. (2018). Stability Analysis of Irregular Cavities Using Upper Bound Finite Element Limit Analysis Method. *Comput. Geotechnics* 103, 1–12. doi:10.1016/j.compgeo.2018.06.018

Zhao, L., Zhang, S., Deng, M., and Wang, X. (2021). Statistical Analysis and Comparative Study of Multi-Scale 2D and 3D Shape Features for Unbound Granular Geomaterials. *Transp. Geotech.* 26, 100377. doi:10.1016/j.trgeo.2020.100377

Zhao, L., Zhang, S., Huang, D., and Wang, X. (2020a). A Digitalized 2D Particle Database for Statistical Shape Analysis and Discrete Modeling of Rock Aggregate. *Constr. Build. Mater.* 247, 117906. doi:10.1016/j.conbuildmat.2019.117906

Zhao, L., Zhang, S., Huang, D., Wang, X., and Zhang, Y. (2020b). 3D Shape Quantification and Random Packing Simulation of Rock Aggregates Using Photogrammetry-Based Reconstruction and Discrete Element Method. *Constr. Build. Mater.* 262, 119986. doi:10.1016/j.conbuildmat.2020.119986

Zhu, Z.-H., Fu, J.-Y., Yang, J.-S., and Zhang, X.-M. (2016). Panoramic Image Stitching for Arbitrarily Shaped Tunnel Lining Inspection. *Computer-Aided Civ. Infrastructure Eng.* 31, 936–953. doi:10.1111/mice.12230

**Conflict of Interest:** The authors declare that the research was conducted in the absence of any commercial or financial relationships that could be construed as a potential conflict of interest.

**Publisher's Note:** All claims expressed in this article are solely those of the authors and do not necessarily represent those of their affiliated organizations, or those of the publisher, the editors, and the reviewers. Any product that may be evaluated in this article, or claim that may be made by its manufacturer, is not guaranteed or endorsed by the publisher.

frontiers | Frontiers in Materials

TYPE Original Research
PUBLISHED 31 August 2022
DOI 10.3389/fmats.2022.939579



OPEN ACCESS

EDITED BY
Hugo M. R. D. Silva,
University of Minho, Portugal

REVIEWED BY
Bin Hong,
Harbin Institute of Technology, China
Songtao Lv,
Changsha University of Science and Technology, China

*CORRESPONDENCE
Han-Cheng Dan,
danhancheng@csu.edu.cn
Zhiheng Zhu,
zzh8207@163.com

SPECIALTY SECTION
This article was submitted to Structural Materials,
a section of the journal
Frontiers in Materials

RECEIVED 09 May 2022
ACCEPTED 08 July 2022
PUBLISHED 31 August 2022

CITATION
Dan H-C, Ling C, Zhu Z, Gao L and Zeng X (2022), A data fusion approach for estimating traffic distribution characteristics of expressway: A case study of guangdong province, china. *Front. Mater.* 9:939579.
doi: 10.3389/fmats.2022.939579



# A data fusion approach for estimating traffic distribution characteristics of expressway: A case study of guangdong province, china

Han-Cheng Dan[1,2]*, Chongyu Ling[1], Zhiheng Zhu[1]*, Liansheng Gao[1] and Xiaojun Zeng[3]

[1]School of Civil Engineering, Central South University, Changsha, Hunan, China, [2]Rail Data Research and Application Key Laboratory of Hunan Province, Changsha, Hunan, China, [3]Guangdong Hualu Transportation Technology Co., Ltd., Guangzhou, China

Currently, people pay more and more attention to road maintenance, and the traffic characteristics of vehicles play an important role in road quality evolution and maintenance decision, which commonly depends on the collection and analysis of traffic data. Nevertheless, the rationality of traffic data analysis and the scientificity of maintenance decision are deficient. This study carries out a research on the data fusion of multisource traffic data including toll data and video surveillance data. First, the information of vehicle type and axle load is acquired from the toll data, and the lane, speed and temporal information are obtained from the video surveillance data. A Bayesian method is used to train toll data and video surveillance data to recover missing data. The vehicle type distribution probabilities of traffic volume during different periods and speeds in different lanes are investigated. Next, the number of equivalent standard axle load (ESAL) at different lanes, time periods, and speeds are estimated based on the axle load conversion relationship between different vehicle types. Then the axle load spectrum and distribution characteristics of traffic in different sections, lanes, speeds, and time periods are analyzed. Finally, the comparison of rutting depth from the multisource data fusion and specification is carried out, and it shows an apparent difference (e.g., beyond 20%) when the lateral distribution in lanes is taken into account. Although the difference is less than 10% by considering vehicle speed and time periods, the time to reach the same value of rutting depth maybe more than 1 year. Therefore, it greatly affects accurate determination of preventive maintenance timing. As a whole, this study provides beneficial information for accurately understanding the preventive maintenance opportunities and making reasonable maintenance decisions.

KEYWORDS

**traffic distribution, asphalt pavement, multisource traffic data, data fusion, video surveillance**

# 1 Introduction

## 1.1 Background

At present, the concept of preventive maintenance is gradually recommended by maintenance managers, which means good pavement maintenance can prolong the service life of the pavement and it can reduce the impact of maintenance wastes on the environment (Shi et al., 2019; Dan et al., 2022a; Liu et al., 2022). However, the reasonable decision of preventive maintenance closely depends on the accurate understanding of the traffic volume and the accurate grasp of deterioration law of pavement performance (Tarefder and Rodriguez-Ruiz, 2013; Cirilovic et al., 2015; Dhatrak et al., 2020; Dan et al., 2022b). Traffic volume and axle load data are important basic parameters in pavement maintenance planning and design (Song et al., 2019). Meanwhile, it is well known that traffic loading is an important factor for road performance degradation and pavement damage (Dan et al., 2019; Perez-Acebo et al., 2019). Under the same conditions, the larger the equivalent standard axle load (ESAL) is, the faster the road condition deteriorates. Therefore, the analysis of highway traffic load is one of the most important references for pavement performance prediction and maintenance (Amorim et al., 2015; Dos et al., 2019).

Generally speaking, the traffic designers used the axle load spectrum (i.e., the percentage of different axle loads) to describe traffic loading, which is the main data source of traffic parameters in pavement design methods in developed countries (Ali et al., 2018; Dinegdae and Birgisson, 2018). To analyze the variation in traffic load and traffic volume, both the United States and Germany adopted the method of combining long-term observation with short-term observation to investigate the highway traffic volume and load distribution. It is mainly based on long-term observations and is supplemented by short-term sampling observations (Tang et al., 2019; Wang S. L et al., 2019). As for the influence of traffic loading on the pavement, researchers always attached great importance to the distribution of the actual axle load on the road. The designers often adapted an established wheel load as the standard design load in flexible pavement design methods in various countries (Heymsfield and Tingle, 2019). In the 1950s, the conversion coefficient was obtained for converting the mixed load into a single load by carrying out large full-scale road tests in the United States (Yin, 2015). In 2004, the mechanistic–empirical (M-E) design method was introduced by replacing the equivalent number of axle loading times with the axle load spectrum to characterize traffic loading for the pavement structure design in the United States, and a new road mechanics empirical design method based on the axle load spectrum was developed (AASHTO, 2020). The mixed traffic bearing capacity of the road was converted into the equivalent standard axle loads (ESALs) in current pavement structure design method in China (Wang et al., 2007; Wang and Zhang, 2016; Gao et al., 2019).

For some studies, the axle load spectrum and the traffic flow information were obtained by artificial statistics, which is difficult to calculate and restricted with poor accuracy (Haider et al., 2010; Mai et al., 2014). Certainly, they did not take some factors such as the distribution of traffic flow in different road sections, lanes, time periods (day and nights), and vehicle speed into consideration at the same time. Nevertheless, with the development of radio frequency identification technology, dynamic weighing technology, and high-definition image recognition technology, network tolling systems, weight-calculating charge systems, and high-definition video surveillance systems have been widely used in highway operation management faced with increasing traffic volume (Abbas et al., 2014; Ren et al., 2019; Feng et al., 2020). Massive traffic data are being collected on every expressway

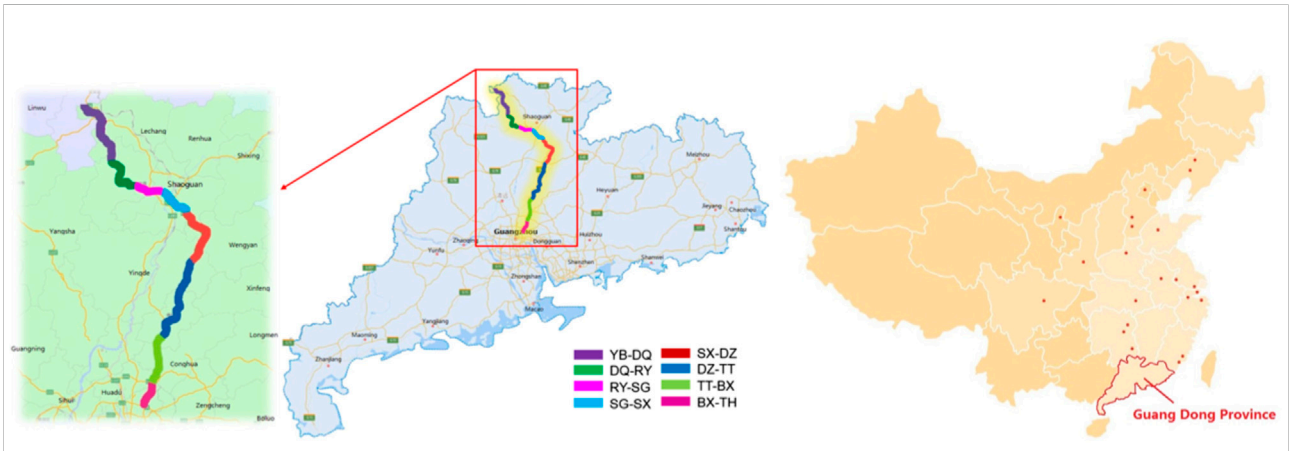


FIGURE 1
Location of expressway sections in Guangdong province, China (the legends represent the section names between toll stations).

TABLE 1 Data for analysis.

| Data type | Data component | Data period | Data volume |
|---|---|---|---|
| Toll data | Toll flow data of export | 01 July 2014–30 June 2017 | About 135 million records, and 68.8 Gb |
| | Coded data of a road section | 01 July 2014–30 June 2017 | About 156 million records, and 22.9 Gb |
| | Coded data of a toll station | Static data | — |
| | Toll station coding data | Static data | — |
| Video surveillance data | Flow data of the high-definition camera | 01 July 2014–30 June 2017 | About 33.64 million records, and 4.56 Gb |
| | Coded data of the high-definition camera | Static data | — |

every day. The daily raw data generated by expressway tolling systems and video surveillance systems have the features of large quantity, various types, high speed of generation, and strong real-time performance, which are the characteristics of typical big data. If the traffic flow information of different sections, different lanes, different time periods, different speeds, and different vehicle types can be extracted from the massive tolling data and video surveillance data, the problem of difficulty in obtaining and analyzing traffic load information in pavement performance prediction can be effectively solved (Mai et al., 2013; Tarefder and Hasan, 2016). Furthermore, according to the Chinese standard (specification for design of highway asphalt pavement JTG D50-2017), the lane coefficient is determined by counting the number of vehicles including passenger cars and trucks on different lanes in the design direction according to the traffic volume observation data. Similarly, for the American standard (AASHTO 2020), the lane coefficient is the percent of trucks in the design direction that are expected to travel in the design lane. This percentage is used to calculate the total number of trucks in the design lane. It is unfortunate that the lane factor does not truly and completely reflect the traffic flow distribution of different lanes. As a matter of fact, due to the influence of channelized traffic, the distribution of vehicles and the speed on different lanes is extremely varied, which makes the degradation of pavement performance different. Especially, there are many heavy-duty vehicles on the expressway, and the existing axle load spectrum cannot truly reflect the complex traffic axle load characteristics as well.

Therefore, a large number of traffic data through the traffic information acquisition system, the data fusion analysis can be carried out to provide a better way to accurately understand the characteristics of traffic volume and axle load distribution.

## 1.2 Objective and scope

The main objective of the study is to integrate toll data and video surveillance data to analyze, and the traffic distribution characteristics will be refined and understood through data integration analysis, disassembling, and processing the data in terms of road section, vehicle type, axle type, axle load, lane, speed, and time. Furthermore, the significance of the traffic data fusion analysis will be highlighted through the application of the presented method, and it also provides crucial information and approach for management department of expressway to rationally take use of traffic data.

# 2 Methodology

## 2.1 Data source and description

The main data used in this study were derived from toll, video surveillance, maintenance service, and meteorological data from the transportation department of Guangdong province in China. The traffic axle load data were collected from a section of expressway (about 289.7 km) in Guangdong province, which is shown in Figure 1, and the data information are listed in Table 1. It is pointed out that the abbreviations in Figure 1 are the names of toll stations. The distance between toll stations is the expressway section and the full name is listed as follows:

YB-DQ: Yuebei–Daqiao, DQ-RY: Daqiao–Ruyuan, RY-SG: Ruyuan–Shaoguan, SG-SX: Shaoguan–Shaxi, SX-DZ: Shaxi–Dazhen, DZ-TT: Dazhen–Tangtang, TT-BX: Tangtang–Beixing, and BX-TH: Beixing–Taihe.

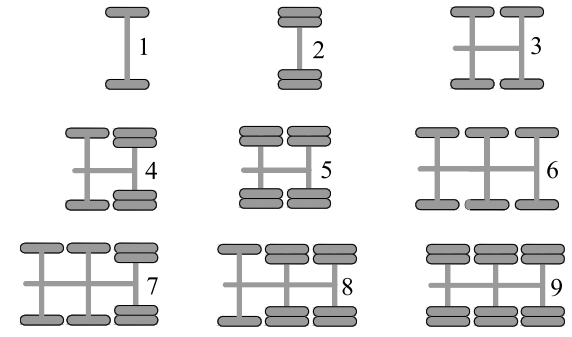


FIGURE 2
Schematic diagram of axle type of vehicles.

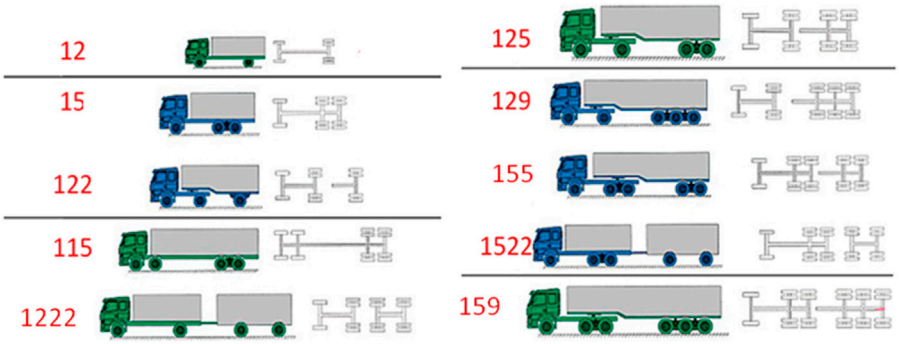


FIGURE 3
Schematic diagram of model type of vehicles.

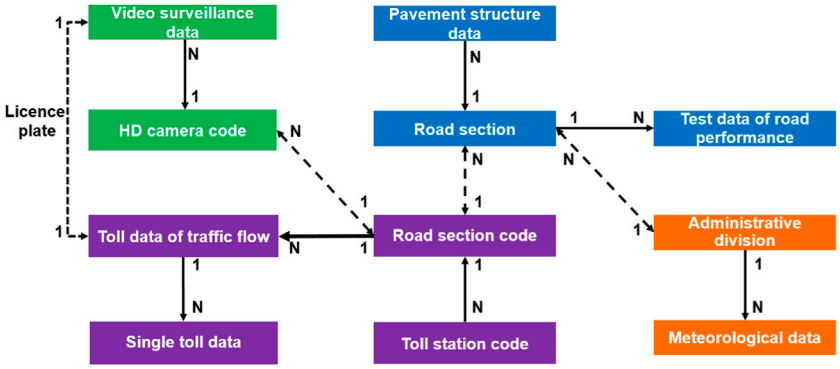


FIGURE 4
Data model of road section coding.

The traffic data mainly include toll data and video surveillance data.

(1) The toll data include toll flow data of export, coded data of a road section, and the coded data of a toll station. The main axle types and model type of vehicles are shown in Figures 2, 3, respectively.

It should be pointed out that the maintenance and meteorological data are not listed and analyzed in this study because the mechanics and performance analysis of pavement is beyond the scope of this study.

## 2.2 Data disassembly of data from different sources

As a matter of fact, the video surveillance data, toll data, meteorological data, and maintenance data have different data formats. It is difficult to directly extract the traffic information of a certain road section. To establish the connection between different types of data, the road section code is used to unify different types of data in the road network model (Figure 3), and the specific link information of each type of data is shown in Figure 4. The specific process is as follows.

First, the video surveillance data are imported and the high-definition camera code is extracted by programming with MATLAB and *R* language. Then the HD camera code is converted into the corresponding road section code in the road network. Furthermore, the detailed toll data are imported and disassembled to acquire the corresponding number and name of each toll station through programming. Basically, every single data contain the license plate information of vehicle, and it can be linked to the video surveillance data. That is the vehicle flow in the road section can be clarified. Finally, the toll station code is also linked to the corresponding road section code in the road network. Likewise, the meteorological data collected in the region of administration division, pavement

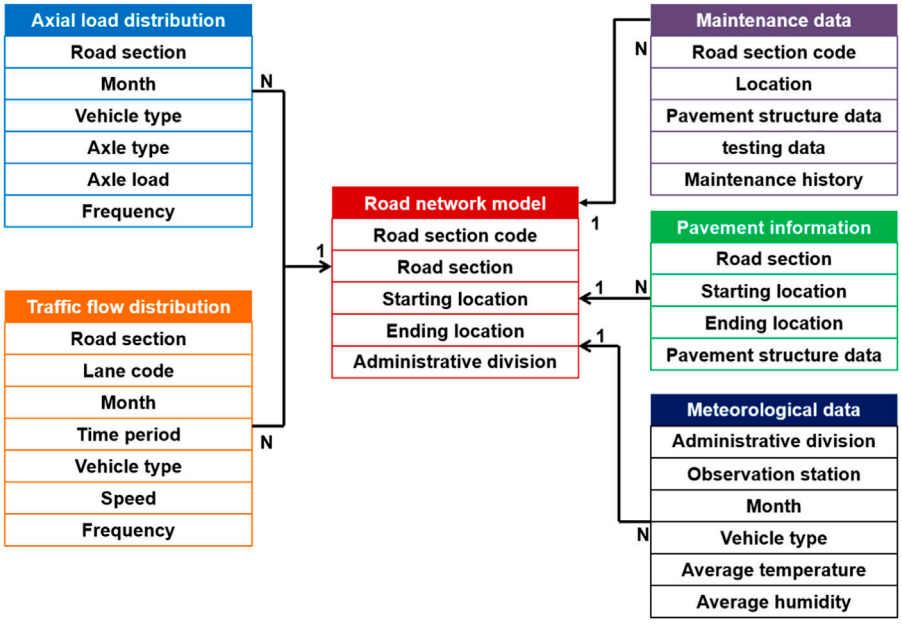


FIGURE 5
Schematic diagram data disassembly model.

structure data, and the testing data of road performance can be easily referred to the road section and road section code. Therefore, all the provided data can be unified by the road section code and then can be disassembled into the target data, which is shown in Figure 5. The following process can be specified as below.

First, the toll data is disassembled to acquire the axle type, vehicle type, and the traffic flow distribution. Second, the video surveillance data is similarly disassembled to obtain the vehicle speed, passing time, and lane information of each vehicle. Finally, the traffic flow distribution can be obtained by taking in consideration the vehicle speed, passing time, and lane information of all vehicles.

## 2.3 Refined computing method of multisource traffic data

In general, the distribution of axle weight and total weight in each road section (between toll stations) can be calculated through toll data, and the vehicle speed, passing time, and traffic flow in different lanes can be calculated using the video surveillance data. However, as a matter of fact, the volume of video surveillance data is smaller than that of toll data to some extent due to the absence of video surveillance data by HD camera. Therefore, accurate traffic information cannot be linked just by using the existing video surveillance data and toll data. To solve this problem, the traffic flow distribution of different vehicle in different lanes are obtained using the Bayesian decision method (Tang and Huang, 2019; Wen et al., 2019; Fleischhacke et al., 2020) by training partial toll and video surveillance data.

Several studies have previously employed the Bayesian method in the analysis of traffic to express certain relationships between the different factors (Chen, et al., 2019; Febres et al., 2019; Wang F. Y et al., 2019). Therefore, the toll and video surveillance data are trained to obtain the posterior probability of the data (i.e., the probability of traffic distribution of different lanes of vehicles in different sections, time periods, and speeds; and the probability of different vehicle types). According to the probability, the vehicle flow distribution and the number of axle load in each road section are restored. Then the vehicle flow distribution characteristics of different road sections, and lanes, vehicle types are obtained at different speeds and in time periods. Specifically, the process is as follows.

Referring to the road network model, the toll data is disassembled to acquire the axle and vehicle type as well as the vehicle flow distribution of different vehicle types (see Figure 6). Then the video surveillance data is disassembled to obtain the vehicle speed, driving time and lane information of each vehicle.

First, *a priori* distribution probability of the axle load spectrum is defined, and then the likelihood function of the axle load spectrum is determined. Then the toll data and video surveillance data are trained to obtain the posterior probability, including the different vehicles in different

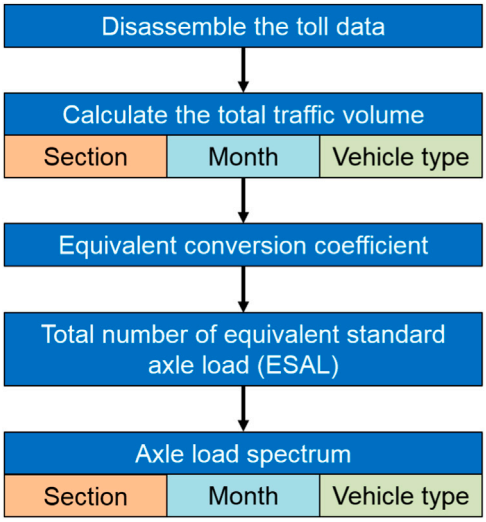


FIGURE 6
Acquisition process of vehicle flow distribution for different vehicle types.

sections, time periods, and vehicle speeds. Furthermore, the probability of vehicle flow distribution of lane as well as the vehicle types is obtained to calculate the loss function and prior probability, of which the expected value of the loss function is the largest. Finally, according to the probability, the vehicle flow distribution and the number of axle load of each road section can be restored. Accordingly, the axle load spectrum can be obtained including the statistics on the speed, driving time, and lane information of all vehicles (see Figure 7).

# 3 Results and discussion

## 3.1 Distribution characteristics of traffic in different sections

The traffic data are refined according to the steps in Section 2.3. The ESALs (equivalent standard axle loads) of the eight sections of an expressway in Guangdong province are obtained by converting the obtained data, as shown in Figure 8 and Figure 9 as below.

It can be seen in Figure 8 that the traffic volume decreases as road sections sorted from top to bottom. In addition, the traffic volume decreases substantially after September 2014 because another double-track expressway was opened to traffic, which causes a very significant diversion to an expressway in Guangdong province at the end of September 2014. The diversion volume is approximately 80%. The only unaffected part is the southbound lane of the BX-TH section, which has a stable traffic flow and little change. The traffic flow of the whole line is basically stable after October 2014. The annual traffic flow has a small trough in the Spring

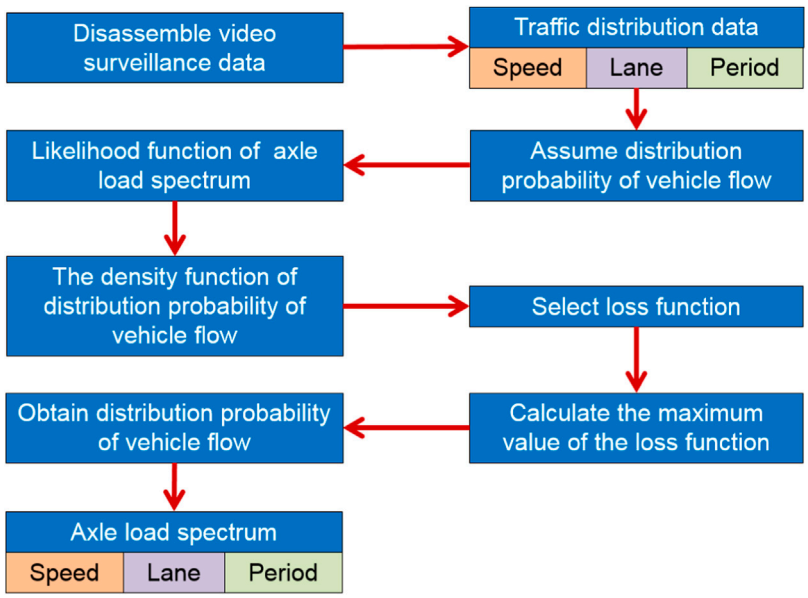


FIGURE 7
Acquisition process of vehicle flow distribution for different lanes.

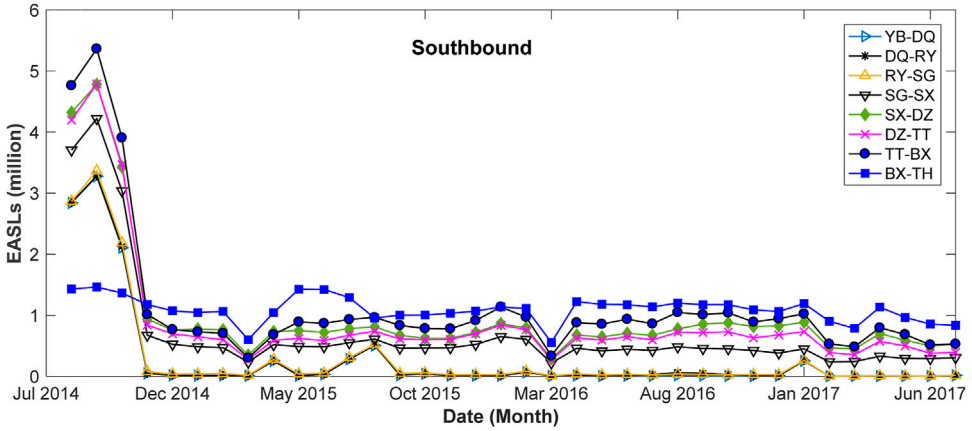


FIGURE 8
Statistics of accumulative ESAL of eight southbound sections of an expressway in Guangdong province from July 2014 to June 2017.

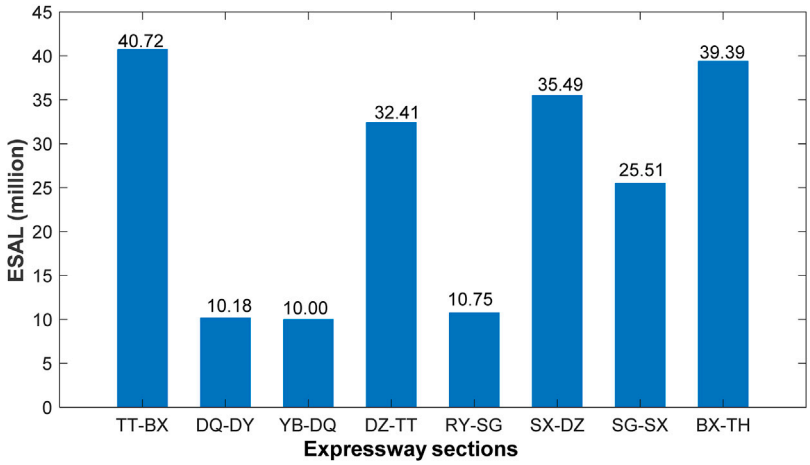


FIGURE 9
Cumulative ESAL of eight southbound sections from July 2014 to June 2017.

Festival of China, and the traffic flow is basically stable in the rest of the year.

As shown in Figure 9, the cumulative ESAL times of eight sections in 3 years change greatly, and the maximum difference is 4.07 times, indicating that the traffic flow varies greatly between different sections. Due to the different traffic flow of sections, the pavement performance attenuation rate of is not the same, and the timing for preventive maintenance of each section is also out of step (Mohammed et al., 2018). Therefore, it is necessary to refine the traffic flow in different sections, and accurate traffic volume information is obtained as the input of the pavement performance prediction model of each section, which can scientifically guide the maintenance department to carry out preventive maintenance in a timely manner.

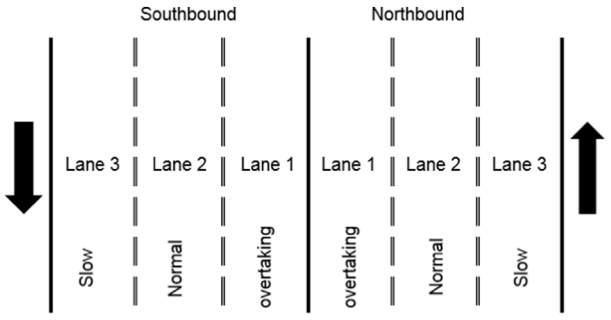


FIGURE 10
Schematic diagram of lanes for an expressway in Guangdong province, China.

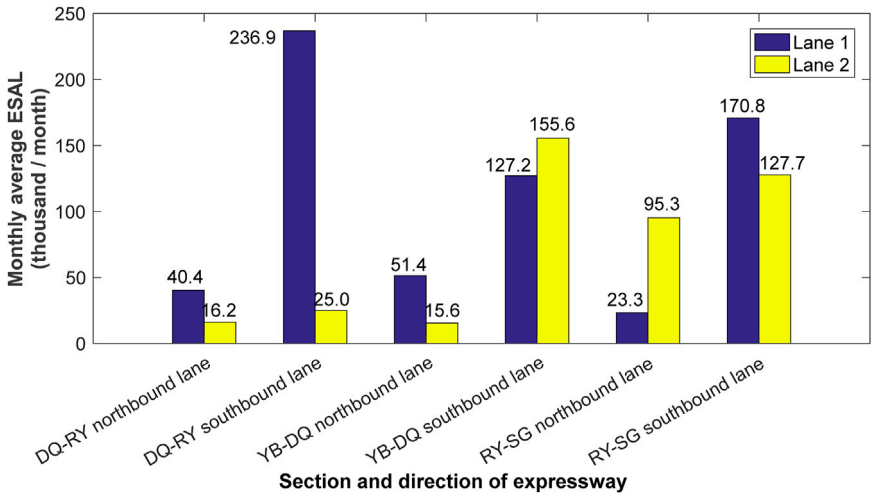


FIGURE 11
Monthly average ESAL times of each lane for sections of four bidirectional lanes.

## 3.2 Distribution characteristics of traffic in different lanes

Most sections of expressways in Guangdong province are bidirectional six lanes (e.g., SG-SX, SX-DZ, DE-TT, TT-BX, and BX-TH sections), and a few sections are bidirectional four lanes (e.g., YB-DQ, DQ-RY, and RY-SG sections). Taking bidirectional six lanes as an example, the form of lanes is shown in Figure 10.

The axle type and number of vehicles in each lane are obtained by separating the vehicle information data, which are acquired by a high-definition camera and toll stations. Traffic flow information at different lanes in the eight sections of expressway can be obtained through load conversion, and then the monthly average ESAL times of each lane are obtained and shown in Figures 11, 12 for the southbound and northbound lanes in 3 years.

Figures 11, 12 show that the monthly average ESAL times on different sections and lanes changes greatly. The percentage of ESAL in each lane and lane coefficient of expressway are counted and shown in Figures 13, 14, respectively.

It can be seen from Figure 11 that the distribution of EASL in lane 1 and lane 2 of two-way four-lane sections is not very

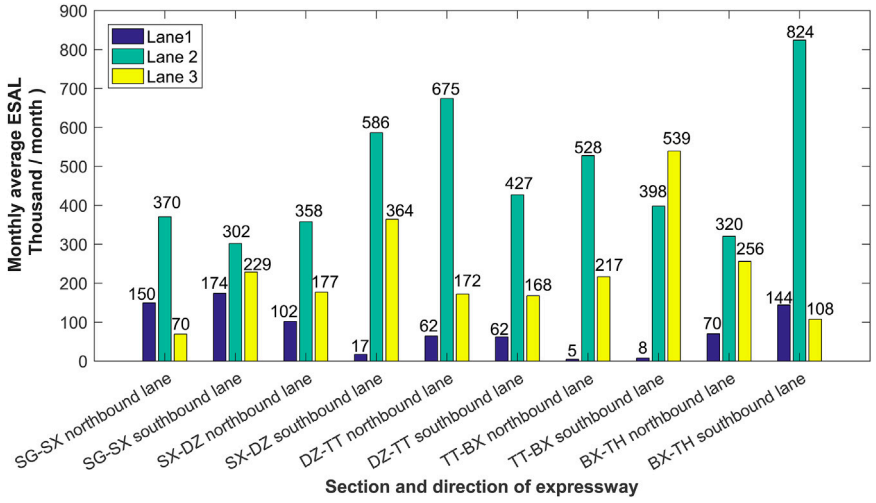


FIGURE 12
Monthly average ESAL times of each lane for sections of six bidirectional lanes.

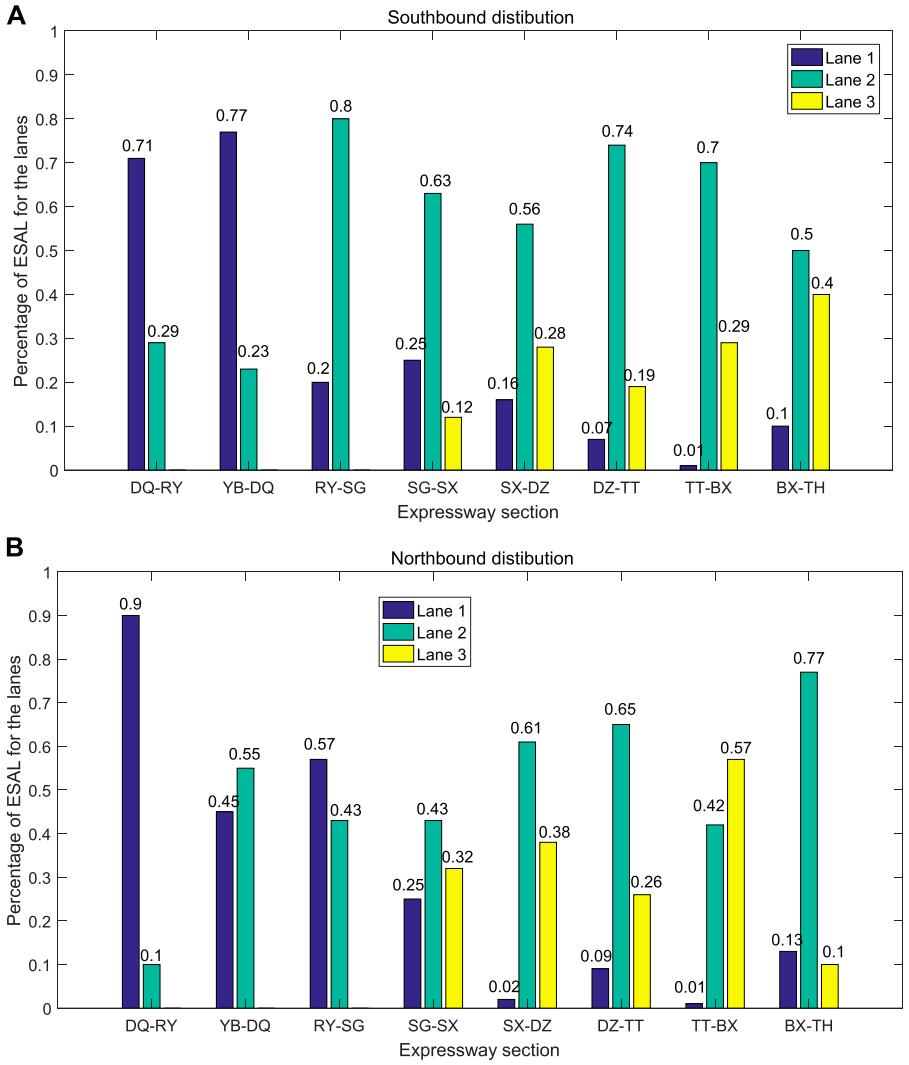


FIGURE 13
**(A)** Percentage of ESAL for the lanes in southbound distribution. **(B)** Percentage of ESAL for the lanes in northbound distribution.

regular. In some sections, EASL in lane 1 is significantly larger than that in lane 2 (e.g., DQ-RY southbound), while in others, it is opposite. However, for the section of six bidirectional lanes, a distinguishing feature is that, the EASL in lane two is significantly larger than that in the other lanes (see Figure 12). For instance, the number of EASL in lane two is 105.6 times that in lane 1 for the TT-BX northbound lane. On the whole, the ratio relationship between the lane two and the smallest ESAL of other lanes is within a range of 1.74–105.6. Obviously, there are three sections with very large ratios in Figure 12 (SX-DZ southbound, TT-BX northbound, and TT-BX southbound). According to the investigation of the highway management department, there are two reasons. The first is that the quality of the three sections of the pavement is poor and has not been timely maintained. The vehicles especially the trucks selectively avoid driving on the lane one. The second is that the subsequently temporary maintenance activities affect traffic flow to some extent.

It can be seen from Figures 13A,B that there is a significant difference in the ESAL for different lanes in the same section. In general, the percentage of EASL on Lane 1 is relatively large for four bidirectional lanes, while the percentage of EASL on the Lane 2 is relatively large for six bidirectional lanes. The change in range of the percentage of EASL for the four bidirectional lanes is 0.55–0.9 and that of the six bidirectional lanes is 0.43–0.77.

It can be seen that the lane coefficients of most sections are consistent with those of the design specification (Ministry of Transport of the People's Republic of China, 2017), but the lane coefficients of nearly quarter of the sections are not within the

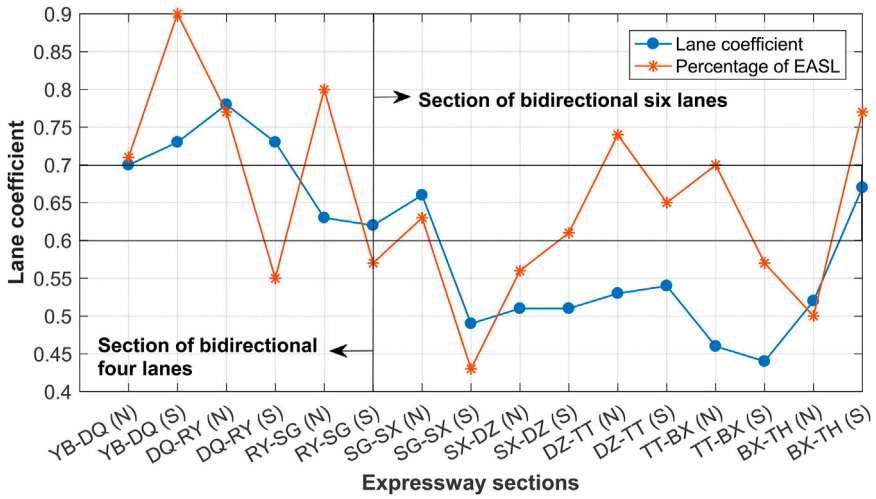


FIGURE 14
Comparison between the lane coefficient and percentage of ESAL on lanes.

range of the design specification. For the four bidirectional lanes, the lane coefficient of YB-DQ northbound and RY-SG northbound and southbound are, respectively, 0.07 and 0.06 lower than the lower limit of the lane coefficient in the specification (i.e., 0.7). For six bidirectional lanes, the lane coefficients of SG-SX northbound and BX-TH southbound are 0.06 and 0.07 higher, respectively, than the upper limit of the lane coefficient in the specification (i.e., 0.6).

Nevertheless, maintenance needs to make a maintenance plan according to the actual pavement quality which largely depends on the action of traffic loading. It can be seen from Figure 14 that the percentage of ESAL on different lanes varies sharply. For instance, in the eight sections from YB-DQ to BX-TH, the percentage of ESAL is extremely fluctuant, which indicates the degree of pavement subjected to traffic load changes greatly. Therefore, it will lead to a result that the pavement performance of lanes deteriorate rapidly are not maintained in time and that of lanes declines slowly in some sections are maintained in advance.

Likewise, due to the difference of the traffic flow in different lanes, the performance of each lane of the expressway declines unevenly, and the time for each lane to enter into the pre-maintenance is not the same. Therefore, it is necessary to analyze the traffic flow distribution of different lanes in spatial and temporal for decision making of pre-maintenance.

## 3.3 Distribution characteristics of traffic at different vehicle speeds

Different vehicle speed will cause different effects on the road surface and contribute to the occurrence and evolution of distress such as rutting, cracking, and water damage to some extent (Peng et al., 2019; Dan et al., 2020). In order to investigate the change law of speed distribution, the traffic flow of eight sections of the expressway from July 2014 to June 2017 is counted, and the statistical results are shown in Figure 15.

Figure 15 shows that the proportions of vehicle speed in range of 40–60 km/h, 60–80 km/h, 80–100 km/h, 100–120 km/h, and above 120 km/h are 4.68%, 19.96%, 35.41%, 29.08%, and 6.45%, respectively. Without taking the vehicle types into account, more than 90% in total of the vehicles in these sections of expressway drive with speed ranging from 60 km/h to 120 km/h. Furthermore, the loading times of different vehicle types are converted into the ESAL times based on the equal failure principle according to the Chinese specification (Ministry of Transport of the People's Republic of China, 2017), and the statistical results are shown in Figure 16.

It can be seen from Figure 16 that the proportions of the ESAL times in the range of 40–60 km/h, 60–80 km/h, 80–100 km/h, 100–120 km/h, and above 120 km/h are 14.49%, 39.19%, 33.4%, 8.24%, and 1.04%, respectively. More than 95% of the ESAL times range from 40 km/h to 100 km/h. Compared with Figure 15, the speed distribution range after axle load conversion (40–100 km/h) is 20 km/h lower than that before axle load conversion (60–120 km/h). The main reason is that a large number of heavy-duty vehicles traveling on the expressway with speeds ranging from 50 km/h to 80 km/h. A heavy-duty vehicle can be converted into a ESAL several hundred times, even thousands of times, while a small bus with a full load of vehicle type 11 can be converted into a ESAL only approximately 0.004 times. Most of the vehicles on the expressway at high speed are vehicle type 11. Although the number is large, the influence on the

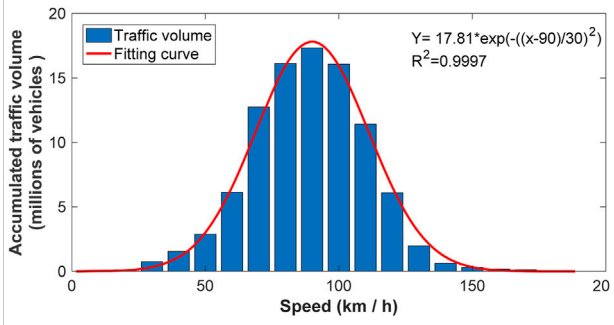


FIGURE 15
Histogram of traffic volume corresponding to different speeds.

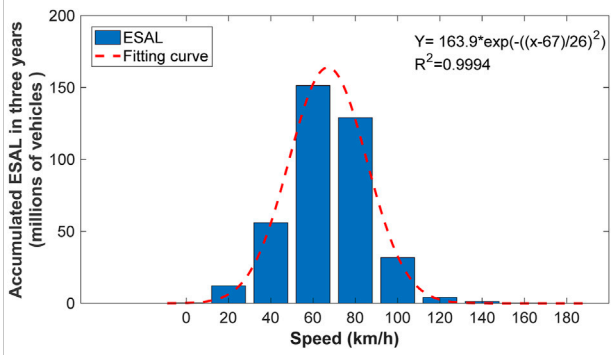


FIGURE 16
Histogram of ESAL times for different vehicle speeds.

performance of the road is not as good as that of heavy vehicles due to the small axle weight. The proportion of the low-speed vehicle increases significantly after the axle load is converted, and the decrease in the speed of the vehicle increases the loading time and accelerates the occurrence of road surface distress. Therefore, it is significant that differentiating the speed distribution can help accurately predict the attenuation law of pavement performance (especially rutting).

Although the highway engineering technical standard recommends that the design speed of the expressway is 80–120 km/h which mainly considers the traffic capacity of expressways (Ministry of Transport of the People's Republic of China, 2014), it does not consider the influence of the speed and vehicle type on the performance of the road. Therefore, it is not reasonable to apply this standard directly to road maintenance, and it is necessary to consider the speed of vehicle to refine traffic volume and obtain more accurate traffic characteristic data.

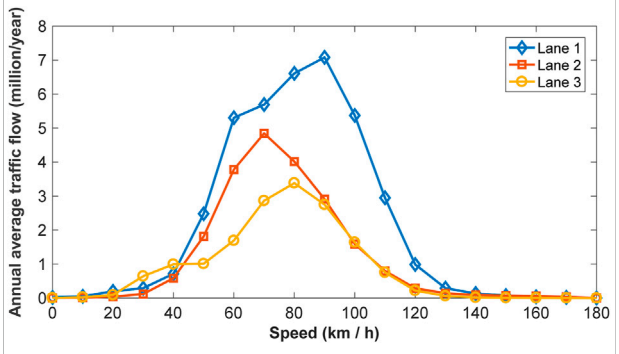


FIGURE 17
Statistics of vehicle speed in different lanes.

In addition, the vehicles distributed in different lanes are also investigated in this study. The following is a statistical distribution of the speed at different lanes based on the traffic volume in 2016 which are shown in Figure 17.

It can be seen from Figure 17 that most of vehicles are traveling at 90 km/h in Lane 1, with vehicle speeds ranging from 70 km/h to 110 km/h in Lane 1. Most of vehicles are traveling at 70 km/h in Lane 2, with vehicle speeds ranging from 60 km/h to 100 km/h in Lane 2. Most of vehicles are traveling at 80 km/h in Lane 3, with vehicle speeds ranging from 60 km/h to 100 km/h in Lane 3. It can be seen from the above analysis that vehicle speed varies greatly in different lanes, therefore, it is necessary to consider the influence of speed of different lanes on road performance when analyzing road performance degradation in different lanes.

## 3.4 Distribution characteristics of traffic at different time periods

As we known that the traffic distribution is not only different in space, but also unevenly distributed in time (Turochy et al., 2005), accordingly, the traffic volume corresponding to different times of a 24 h day is calculated based on the traffic volume in 2016, and the statistical results are shown in Figure 18.

Obviously, Figure 18 shows the bimodal distribution. That's to say, the traffic volume gradually increases from 6 a.m., and the maximum traffic flow is between 11:00 and 17:00 for vehicle type 11. Other type vehicles contribute to the largest traffic flow between 10:00 and 18:00, and the traffic flow of all type vehicles starts to decrease gradually after 18:00, and the traffic volume during the day accounts for more than 70% of the total traffic flow. The corresponding temperature varies at different times of the day, and traffic flow is not evenly distributed throughout the day. Likewise, the influence of the same traffic flow on pavement

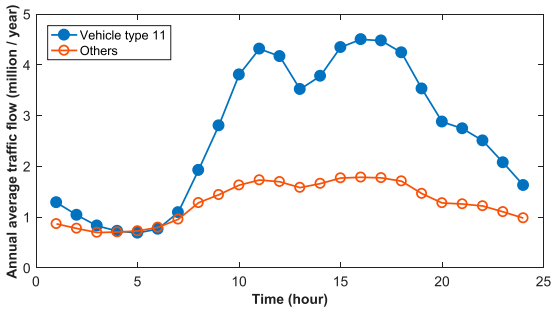


FIGURE 18
Statistics of traffic flow corresponding to different times of a 24 h day.

performance at different times of the day is also different. Therefore, the attenuation law of road performance can be predicted more accurately by comparing the traffic flow in each time period with the temperature field of road structure in the time period.

Furthermore, considering the large temperature changes in different months, the traffic volume of different months is also counted based on the traffic volume from July 2014 to June 2016. The statistical results are shown in Figure 19.

It can be seen from Figure 18 that the traffic volume in July is the largest, while that in October is the smallest. The traffic volume in July is 1.6 times higher than that in October. The traffic volume varies greatly in different months. The temperature in Guangdong province is higher in summer, and the high temperature adversely affects the performance of asphalt pavement. In other words, the temperature varies from month to month in Guangdong province, and the damage degree of the same traffic flow to asphalt pavement varies from month to month as well. Therefore, for instance, it is significant to evaluate the rutting of the asphalt pavement caused by the traffic flow monthly so that the predicted rutting depth of the pavement can be more representative of the attenuation law of asphalt pavement.

## 3.5 Impact of traffic distribution on pavement performance

In order to investigate the impact of the non-uniformity of traffic load distribution in time and in space on pavement performance, we adopt the rutting depth of pavement as the comparison index, and four sections of expressway are selected for comparison of rutting depth. The pavement structure and materials are listed in Table 2.

The computing method rutting depth can refer to the study by Gao et al. (2017), which proposed a model on predicting the rutting of asphalt pavement based on a simplified Burgers creep model. According to Gao's model, the Burgers model parameters of asphalt mixture are obtained by laboratory test (Table 3).

The lane coefficients are respectively based on the data analysis results in this study and the Specification for Design of Highway Asphalt Pavement (0.3 is used as standard value for calculation) (Ministry of Transport of the People's Republic of China, 2017). The vehicle speed is selected to be 100 km/h. The traffic flow in each period is considered (every 2 h is a period, and 1 day is divided into 12 periods) and the traffic flow without considering the period is substituted into the established rutting prediction model (Dan et al., 2015; Gao et al., 2017). Accordingly, the rutting depth can be calculated for pavement of each road section, which is shown in Figures 20–22, respectively.

As can be seen from the comparison results in Figure 20, the maximum difference of rutting depth between the lane

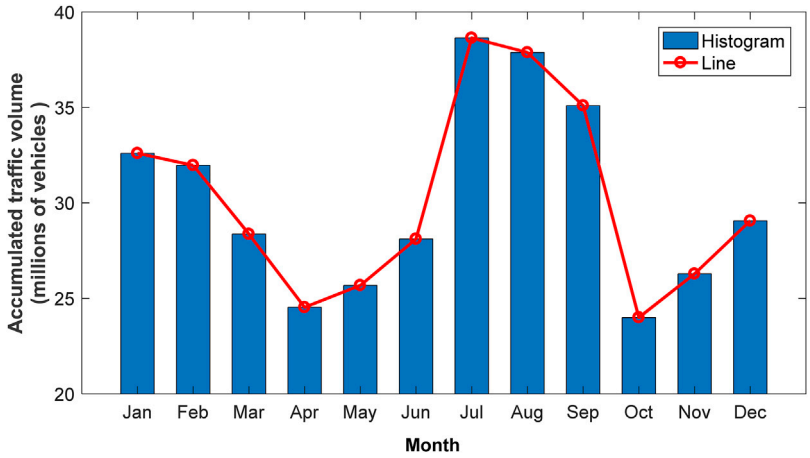


FIGURE 19
Statistical traffic flow in different months from July 2014 to June 2016.

TABLE 2 Pavement structure of the case study.

| Structure layer | | Materials | Thickness (cm) |
|---|---|---|---|
| Surface course | top | SMA-16 | 4.5 |
| | middle | AC-20 | 5.5 |
| | bottom | AC-25 | 6.0 |
| Base course | | Cement stabilized macadam (cement content 6%) | 36 |
| | | Cement stabilized macadam (cement content 4%) | 20 |

TABLE 3 Burgers model parameters.

| Materials | Creep parameters | 15°C | 30°C | 40°C | 50°C | 60°C |
|---|---|---|---|---|---|---|
| SMA-16 | $E_1$(MPa) | 270.31 | 210.32 | 46.85 | 31.05 | 20.57 |
| | $E_2$(MPa) | 95.34 | 57.56 | 25.89 | 24.65 | 18.82 |
| | $\eta_1$(MPa·s) | 1980 | 1,096 | 390 | 230 | 186 |
| | $\eta_2$(MPa·s) | 240 | 102 | 70.3 | 50.4 | 41.1 |
| AC-20 | $E_1$(MPa) | 240.2 | 186.5 | 37.99 | 25.36 | 15.53 |
| | $E_2$(MPa) | 87.4 | 51.32 | 22.33 | 20.49 | 11.43 |
| | $\eta_1$(MPa·s) | 1761 | 945 | 346 | 187 | 91.3 |
| | $\eta_2$(MPa·s) | 187 | 80 | 34.5 | 30.7 | 23.4 |
| AC-25 | $E_1$(MPa) | 220.1 | 176.59 | 36.21 | 24.51 | 14.65 |
| | $E_2$(MPa) | 75.32 | 46.87 | 19.54 | 18.64 | 12.35 |
| | $\eta_1$(MPa·s) | 1,594 | 874 | 316 | 137 | 80.5 |
| | $\eta_2$(MPa·s) | 175 | 60.4 | 40.5 | 30.4 | 26.4 |

coefficient calculated by the standard value and the presented value in this study is 24% (only the lane with the maximum rutting depth is calculated), because the lane coefficient specified in the standard does not reasonably reflect the characteristics of channelized traffic on the expressway. As a matter of fact, due to the influence of lane division, traffic organization and management and channelized traffic of expressway, the distribution of different vehicle types on different lanes is extremely varied, and the vehicle types on the same lane are also complex (Jasim et al., 2019). Therefore, it is necessary to divide the expressway traffic flow into lanes to obtain the actual lane coefficient, obtain the accurate traffic flow of each lane, and accurately detect the pavement performance of the expressway, so as to guide the maintenance decision and construction.

Secondly, it can be seen from Figure 21 that the maximum difference between the fixed speed (100 km/h) and the actual speed is about 6.9%. Inevitably, there are vehicles traveling at low speed (less than 60 km/h) on expressways, and the influence of driving speed on the anti-rut performance of asphalt pavement is mainly reflected in the duration of loading. The vehicle traveling at low speed is equivalent to increasing the duration of loading, thus leading to the rapid increase of rutting depth. Although speed has less influence on rut performance than load and temperature, low speed is often associated with heavy load, which will aggravate rutting damage. Therefore, it is necessary to consider speed to carry out refined treatment on traffic flow.

In addition, Figure 22 shows that the maximum difference of calculated rutting depth is about 8.8% between distinguish and not distinguish different periods of traffic flow. The diurnal cycle and seasonal cycle of temperature are often ignored in the traditional analysis, however, the asphalt mixture is a temperature sensitive material, and its pavement performance is closely related to its temperature sensitivity. Furthermore, the traffic volume is not uniformly distributed in different time periods of each day, and the pavement structure temperature field is not the same in different time periods. Thus, the same traffic volume has different influence on the pavement rut in different time periods. That's to say, a one-to-one correspondence between the traffic volume in a certain period and the temperature field of the pavement structure in that period can be used to calculate rutting depth more accurately. Therefore, the fusion and calculation of multisource data is an important means to improve the study of pavement rutting development.

Currently, traffic analysis in the MEPDG (e.g., Level 2 and Level 3) (MEPDG Documentation, 2010; Hasan, et al., 2020) is different

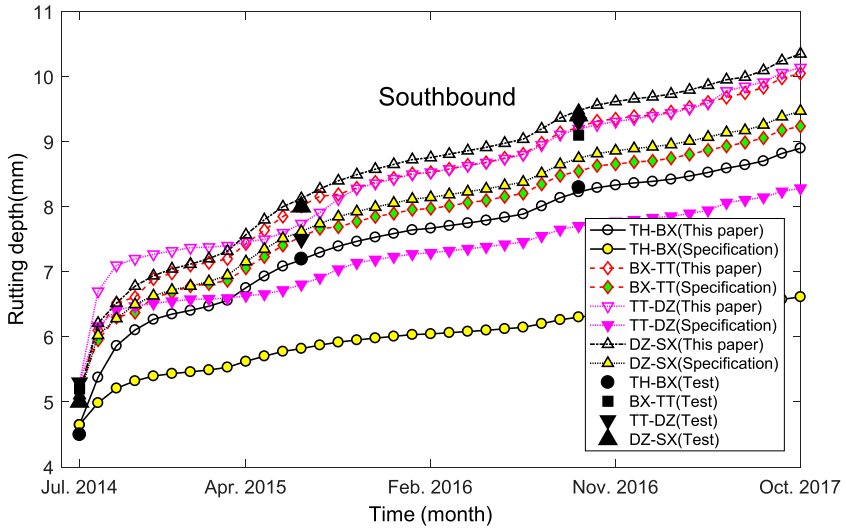


FIGURE 20
Comparison of rutting depth between the lane coefficient calculated by the standard value and the presented value in this study.

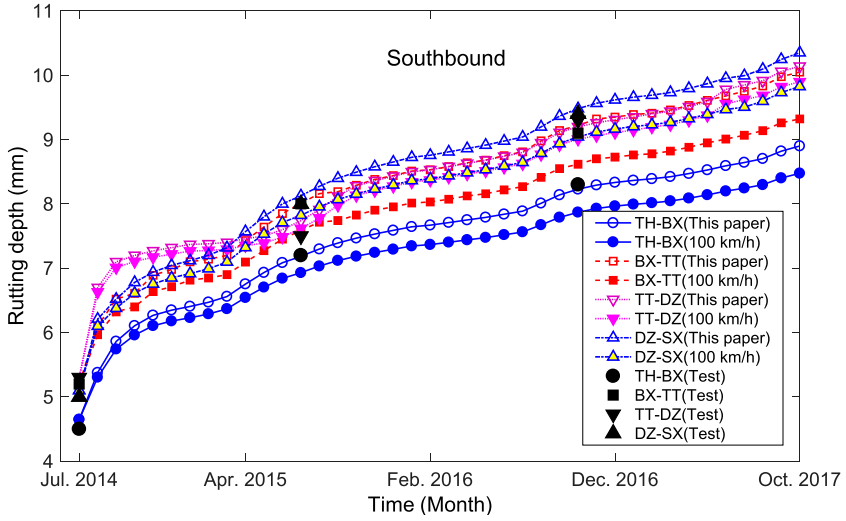


FIGURE 21
Comparison of calculated rutting depth between distinguish and not distinguish different speeds of traffic flow.

from the actual situation (Level 1) to some extent, and various factors (lane distribution characteristics of traffic load, difference in speed and time period) also have different influences on the pavement performance analysis, and such differences become more and more significant with the passage of time (See Figures 20–22). More importantly, these differences may lead to misjudgment in the decision of preventive maintenance of road surface, which to some extent affects the determination of maintenance timing, the accuracy and scientificity of preventive maintenance decision. For instance, from the perspective of rutting depth development, there is an apparent difference (e.g., beyond 20%) when the lateral distribution in lanes is taken into account. Although the difference is less than 10% by considering vehicle speed and time periods, the time to reach the same value of rutting depth maybe more than 1 year because the rut depth increases slowly. This may greatly affect the accurate determination of preventive maintenance

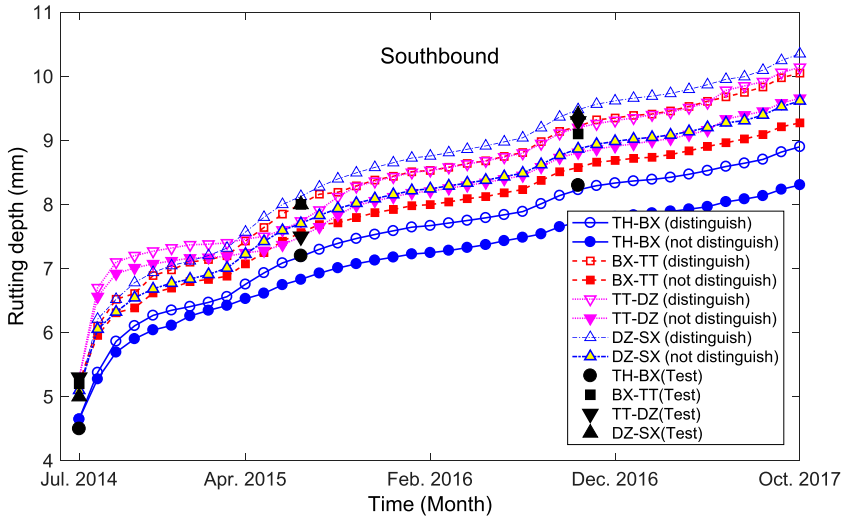


FIGURE 22
Comparison of calculated rutting depth between distinguish and not distinguish different periods of traffic flow.

timing. Therefore, it is very important to carry out traffic multi-data fusion analysis, which is the basis for the research on pavement performance decay and preventive maintenance decision.

## 4 Concluding remarks

The findings of this study are summarized in brief as follows.

(1) The maximum traffic volume of eight sections of an expressway in Guangdong province is 9.76 times the minimum traffic volume, and the traffic flow of different sections is quite different.
(2) Compared with the lane coefficient in the specification, a considerable amount of road sections of which the lane coefficient is higher and lower than the limit of the lane coefficient in the Chinese specification. The percentage of ESAL is extremely fluctuant, which indicates the degree of pavement subjected to traffic load changes greatly.
(3) The speed of vehicles in different lanes is quite different, and the average speed of vehicles on the Lane 1, Lane 2, and Lane 3 is 90 km/h, 70 km/h, and 80 km/h, respectively. It is proposed that the traffic flow should be refined according to the lane and the speed of the vehicle, and it helps more specifically to guide the maintenance department to accurately maintain the road lanes.
(4) The distribution of the traffic flow in different months and different time periods are uneven, which leads to the rutting of asphalt pavement varying from month to month accordingly. It is significant to evaluate the rutting of the asphalt pavement caused by the traffic flow monthly due to more representative of the attenuation law of asphalt pavement in Guangdong province.
(5) From the perspective of rutting depth development, it may greatly affect the accurate determination of preventive maintenance timing by considering the vehicle speed and time periods or not.

In practical application of preventive maintenance, it needs to determine the pavement condition in time and the maintenance timing, and reasonable preventive maintenance measures can be applied. Therefore, from the perspective of application, it is suggested to combine the pavement management system (PMS) with the method presented in this study to analyze the traffic volume and axle load data in detail. Then it is more reasonable to combine the data analysis results with the attenuation model of pavement quality to predict the variation of performance indexes of pavement (e.g., skid resistance performance, rutting resistance performance, etc.) by considering the influence of lane, vehicle speed and time period, and finally comprehensively determine the timing of pavement preventive maintenance.

Generally speaking, the traffic data can be put into use of predicting pavement condition in the future study, for instance, the rutting, fatigue, skid resistance performance can be investigated through the integration analysis and refinement processing. As mentioned in Section 2.1, a large amount of maintenance data can be also utilized to validate the deterioration law and condition of pavement.

## Data availability statement

The original contributions presented in the study are included in the article/Supplementary Material; further inquiries can be directed to the corresponding authors.

## Author contributions

H-CD: conceptualization, methodology, funding, and writing—original draft preparation; CL: methodology and writing—original draft preparation; ZZ: methodology, programming, and writing—reviewing and editing; LG: writing—original draft preparation; XZ: data resources.

## Funding

This research was supported by the Natural Science Foundation of Hunan Province (Grant No. 2020JJ4702), Guizhou Transportation Science and Technology Foundation of China (Grant No. 2019-122-006), and Jiangxi Transportation Science and Technology Foundation of China (Grant No. 2020H0028).

## Acknowledgments

Special acknowledgement to the Guangdong Hualu Transportation Technology Co., Ltd. for providing the traffic multi-source data.

## Conflict of interest

XZ was employed by Guangdong Hualu Transportation Technology Co., Ltd.

The remaining authors declare that the research was conducted in the absence of any commercial or financial relationships that could be construed as a potential conflict of interest.

## Publisher's note



## References

AASHTO (2020). *Mechanistic empirical pavement design guide: a manual of practice*. 3rd Edition. Washington, DC, USA: American Association of State Highway and Transportation Officials.

Abbas, A. R., Frankhouser, A., and Papagiannakis, A. T. (2014). Effect of traffic load input level on mechanistic-empirical pavement design. *Transp. Res. Rec.* 2443, 63–77. doi:10.3141/2443-08

Ali, Y., Irfan, M., Zeeshan, M., Hafeez, I., and Ahmed, S. (2018). Revisiting the relationship of dynamic and resilient modulus test for asphaltic concrete mixtures. *Constr. Build. Mater.* 170, 698–707. doi:10.1016/j.conbuildmat.2018.03.098

Amorim, S. I. R., Pais, J. C., Vale, A. C., and Minhoto, J. C. (2015). A model for equivalent axle load factors. *Int. J. Pavement Eng.* 16 (10), 881–893. doi:10.1080/10298436.2014.968570

Chen, X., Dong, Q., Gu, X., and Mao, Q. (2019). Bayesian analysis of pavement maintenance failure probability with Markov chain Monte Carlo simulation. *J. Transp. Eng. Part B Pavements* 145 (2), 04019001. doi:10.1061/jpeodx.0000107

Cirilovic, J., Mladenovic, G., and Queiroz, C. (2015). Implementation of preventive maintenance in network-level optimization case study of the Serbian low-volume road network. *Transp. Res. Rec.* 2473, 49–55. doi:10.3141/2473-06

Dan, H. C., Bai, G. W., Zhu, Z. H., Liu, X., and Cao, W. (2022b). An improved computation method for asphalt pavement texture depth based on multiocular vision 3D reconstruction technology. *Constr. Build. Mater.* 321, 126427. doi:10.1016/j.conbuildmat.2022.126427

Dan, H. C., He, L. H., Zhao, L. H., and Chen, J. Q. (2015). Coupled hydro-mechanical response of saturated asphalt pavement under moving traffic load. *Int. J. pavement Eng.* 16 (2), 125–143. doi:10.1080/10298436.2014.937712

Dan, H. C., He, L. H., and Zhao, L. H. (2020). Experimental investigation on the resilient response of unbound graded aggregate materials by using large-scale dynamic triaxial tests. *Road Mater. Pavement Des.* 21 (2), 434–451. doi:10.1080/14680629.2018.1500300

Dan, H. C., Zeng, H. F., Zhu, Z. H., Bai, G. W., and Cao, W. (2022a). Methodology for interactive labeling of patched asphalt pavement images based on U-net convolutional neural network. *Sustainability* 14, 861. doi:10.3390/su14020861

Dan, H. C., Zhou, Z. M., Chen, J. Q., and Peng, A. P. (2019). DEM-aided method for predicting the hydraulic properties with particle-size distribution of porous media. *Eng. Comput. Swans.* 36 (5), 1716–1743. doi:10.1108/ec-09-2018-0398

Dhatrak, O., Vemuri, V., and Gao, L. (2020). Considering deterioration propagation in transportation infrastructure maintenance planning. *J. Traffic Transp. Eng. Engl. Ed.* 7 (4), 520–528. doi:10.1016/j.jtte.2019.04.001

Dinegdae, Y. H., and Birgisson, B. (2018). Effects of truck traffic on top-down fatigue cracking performance of flexible pavements using a new mechanics-based analysis framework. *Road Mater. Pavement Des.* 19 (1), 182–200. doi:10.1080/14680629.2016.1251958

Dos, S., Thais, A., Prado, D. S. J., Carlos, A., and Fontenele, H. B. (2019). The effect of axle load spectra from AASHTO method on flexible pavement performance. *Acta Sci. Technol.* 41, 35117. doi:10.4025/actascitechnol.v41i1.35117

Febres, J. D., Mohamadi, F., Mariscal, M. A., Herrera, S., and Garcia-Herrero, S. (2019). The role of journey purpose in road traffic injuries: a bayesian network approach. *J. Adv. Transp.* 2019, 1–10. doi:10.1155/2019/6031482

Feng, M. Q., Leung, R. Y., and Eckersley, C. M. (2020). Non-contact vehicle weigh-in-motion using computer vision. *Measurement* 153, 107415. doi:10.1016/j.measurement.2019.107415

Fleischhacke, A., Ghonima, O., and Schumacher, T. (2020). Bayesian survival analysis for US concrete highway bridge decks. *J. Infrastruct. Syst.* 26 (1), 04020001. doi:10.1061/(asce)is.1943-555x.0000511

Gao, L. S., Dan, H. C., and Chen, J. Q. (2017). Research on predicting the rutting of asphalt pavement based on a simplified burgers creep model. *Math. Problems Eng.* 2017, 1–14. doi:10.1155/2017/3459704

Gao, L. S., Dan, H. C., and Li, L. (2019). Response analysis of asphalt pavement under dynamic loadings: loading equivalence. *Math. Problems Eng.* 2019, 1–15. doi:10.1155/2019/7020298

Haider, S. W., Harichandran, R. S., and Dwaikat, M. B. (2010). Effect of axle load measurement errors on pavement performance and design reliability. *Transp. Res. Rec.* 2160, 107–117. doi:10.3141/2160-12

Hasan, M. M., Asifur Rahman, A. S. M., and Tarefder, R. A. (2020). Investigation of accuracy of pavement mechanistic empirical prediction performance by

incorporating Level 1 inputs. *J. Traffic Transp. Eng. Engl. Ed.* 7 (2), 259–268. doi:10.1016/j.jtte.2018.06.006

Heymsfield, E., and Tingle, J. S. (2019). State of the practice in pavement structural design/analysis codes relevant to airfield pavement design. *Eng. Fail. Anal.* 105, 12–24. doi:10.1016/j.engfailanal.2019.06.029

Jasim, A. F., Wang, H., and Bennert, T. (2019). Evaluation of clustered traffic inputs for mechanistic-empirical pavement design: case study in New Jersey. *Transp. Res. Rec.* 2673 (11), 332–348. doi:10.1177/0361198119853557

Liu, K., Xu, P. X., Wang, F., You, L. Y., Zhang, X. C., Fu, C. L., et al. (2022). Assessment of automatic induction self-healing treatment applied to steel deck asphalt pavement. *Automation Constr.* 133, 104011. doi:10.1016/j.autcon.2021.104011

Mai, D., Turochy, R. E., and Timm, D. H. (2013). Quality control of weigh-in-motion data incorporating threshold values and rational procedures. *Transp. Res. Part C Emerg. Technol.* 36, 116–124. doi:10.1016/j.trc.2013.08.012

Mai, D., Turochy, R. E., and Timm, D. H. (2014). Sensitivity of flexible pavement thickness to traffic factors in mechanistic-empirical pavement design. *J. Transp. Eng.* 140 (12), 04013005. doi:10.1061/(asce)te.1943-5436.0000628

MEPDG Documentation (2010). *Guide for mechanistic-empirical design of new and rehabilitated pavement structures*. Washington, DC: National Cooperative Highway Research Program, Transportation Research Board, National Research Council. Available at: http://onlinepubs.trb.org/onlinepubs/archive/mepdg/guide.htm.

Ministry of Transport of the People's Republic of China (2017). *Specifications for design of highway asphalt pavement*. Beijing, China: JTG D50, China Communications Press.

Ministry of Transport of the People's Republic of China (2014). *Technical standard of highway engineering*. Beijing, China: JTG B01, China Communications Press.

Mohammed, B., Hassan, R., and Alaswadko, N. (2018). The effect of traffic data source on deterioration rates of heavy-duty flexible pavements. *Int. J. Pavement Eng.* 19, 1096–1110. doi:10.1080/10298436.2016.1240562

Peng, A. P., Dan, H. C., and Yang, D. (2019). Experiment and numerical simulation of the dynamic response of bridges under vibratory compaction of bridge deck asphalt pavement. *Math. Problems Eng.* 2019, 1–16. doi:10.1155/2019/2962154

Perez-Acebo, H., Mindra, N., Railean, A., and Roji, E. (2019). Rigid pavement performance models by means of Markov chains with half-year step time. *Int. J. Pavement Eng.* 20 (7), 830–843. doi:10.1080/10298436.2017.1353390

Ren, J., Thompson, R. G., and Zhang, L. H. (2019). Impact of payload spectra of heavy vehicles on pavement based on weigh-in-motion data. *J. Transp. Eng. Part B Pavements* 145 (2), 04019005. doi:10.1061/jpeodx.0000099

Shi, Y., Xiang, Y. S., and Li, M. Y. (2019). Optimal maintenance policies for multi-level preventive maintenance with complex effects. *IISE Trans.* 51 (9), 999–1011. doi:10.1080/24725854.2018.1532135

Song, Y. Z., Wang, X. Y., Wright, G., Thatcher, D., Wu, P., Felix, P., et al. (2019). Traffic volume prediction with segment-based regression kriging and its implementation in assessing the impact of heavy vehicles. *IEEE Trans. Intell. Transp. Syst.* 20 (2), 232–243. doi:10.1109/tits.2018.2805817

Tang, J. J., Chen, X. Q., Hu, Z., Zong, F., Han, C., and Li, L. (2019). Traffic flow prediction based on combination of support vector machine and data denoising schemes. *Phys. A Stat. Mech. its Appl.* 634, 120642. doi:10.1016/j.physa.2019.03.007

Tang, Y., and Huang, S. P. (2019). Assessing seismic vulnerability of urban road networks by a bayesian network approach. *Transp. Res. Part D Transp. Environ.* 77, 390–402. doi:10.1016/j.trd.2019.02.003

Tarefder, R. A., and Hasan, M. A. (2016). Development of weight-in-motion data analysis software. International conference on human factors, software, and systems engineering. *Adv. Intelligent Syst. Comput.* 492, 13–22. doi:10.1007/978-3-319-41935-0_2

Tarefder, R., and Rodriguez-Ruiz, J. I. (2013). WIM data quality and its influence on predicted pavement performance. *Transp. Lett.* 5 (3), 154–163. doi:10.1179/1942786713z.00000000017

Turochy, R. E., Baker, S. M., and Timm, D. H. (2005). Spatial and temporal variations in axle load spectra and impacts on pavement design. *J. Transp. Eng.* 131 (10), 802–808. doi:10.1061/(asce)0733-947x(2005)131:10(802)

Wang, F. Y., Du, L. M., Li, G., and Dong, J. (2019). Research on the influencing factors of residents' travel based on bayesian network. *Int. Conf. Cyber Secur. Intell. Anal. (CSIA), Shengyang, China* 928, 1354–1359. doi:10.1007/978-3-030-15235-2_186

Wang, H., and Zhang, J. (2016). Development of overweight permit fee using mechanistic-empirical pavement design and life-cycle cost analysis. *Transport* 31 (2), 156–166. doi:10.3846/16484142.2016.1191039

Wang, S. L., Huang, W., and Lo, H. K. (2019). Traffic parameters estimation for signalized intersections based on combined shockwave analysis and bayesian Network. *Transp. Res. Part C Emerg. Technol.* 104, 22–37. doi:10.1016/j.trc.2019.04.023

Wang, Y. H., Hancher, D. E., and Mahboub, K. (2007). Axle load distribution for mechanistic-empirical pavement design. *J. Transp. Eng.* 133 (8), 469–479. doi:10.1061/(asce)0733-947x(2007)133:8(469)

Wen, H. Y., Zhang, X., Zeng, Q., and Sze, N. N. (2019). Bayesian spatial-temporal model for the main and interaction effects of roadway and weather characteristics on freeway crash incidence. *Accid. Analysis Prev.* 132, 105249. doi:10.1016/j.aap.2019.07.025

Yin, H. (2015). Full-scale test of thermally induced reflective cracking in airport pavements. *Road Mater. Pavement Des.* 16 (1), 119–132. doi:10.1080/14680629.2014.982691

# Frontiers in Materials

**Investigates the discovery and design of materials for future application**

A multidisciplinary journal that explores the breadth of materials science, engineering and mechanics - from carbon-based materials to smart materials.

---

## Discover the latest Research Topics

See more →


**Frontiers**

Avenue du Tribunal-Fédéral 34
1005 Lausanne, Switzerland
frontiersin.org

**Contact us**

+41 (0)21 510 17 00
frontiersin.org/about/contact